

Published in final edited form as:

Chem Rev. 2011 August 10; 111(8): 5042–5137. doi:10.1021/cr100212h.

Quantum Mechanical Investigations of Organocatalysis: Mechanisms, Reactivities, and Selectivities

Paul Ha-Yeon Cheong[†], Claude Y. Legault[‡], Joann M. Um[§], Nihan Çelebi-Ölçüm[§], and K. N. Houk^{§,*}

[†] Oregon State University, Department of Chemistry, 153 Gilbert Hall, Corvallis, OR 97331-4003 USA

[‡] University of Sherbrooke, Department of Chemistry, 2500 boul. de l'Université, local D1-3029, Sherbrooke (Québec) J1K 2R1 CANADA

[§] University of California Los Angeles, Department of Chemistry and Biochemistry, 607 Charles E. Young Drive East, Los Angeles, CA 90095-1569 USA

Keywords

Computational; DFT; Quantum; Theoretical; Mechanism; Catalysis; Organocatalysis; Stereoselectivity; Diastereoselectivity; Enantioselectivity; Regioselectivity; Asymmetric

1. Introduction

Organocatalysis has captured the imagination of a significant group of synthetic chemists. Much of the mechanistic understanding of these reactions has come from computational investigations or studies involving both experimental and complementary computational explorations. As much as any other area of chemistry, organocatalysis has advanced because of both empirical discoveries and computational insights. Quantum mechanical calculations, particularly with density functional theory (DFT), can now be applied to real chemical systems that are studied by experimentalists; this review describes the quantum mechanical studies of organocatalysis.

The dramatic growth of computational investigations on organocatalysis in the last decade reflects the great attention focused on this area of chemistry since the discoveries of List, Lerner, and Barbas of the proline-catalyzed intermolecular aldol reaction, and by MacMillan in the area of catalysis by chiral amino-acid derived amines. The number of reports on the successful applications of organocatalysts and related mechanistic investigations for understanding the origins of catalysis and selectivities keep growing at a breathtaking pace. Literature coverage in this review is until October 2009, except for very recent discoveries that alter significantly the conclusions based on older literature.

1.1 Computational methods for organocatalysis

Over the last two decades, DFT has become a method of choice for the cost-effective treatment of large chemical systems with high accuracy.¹ Most of the studies reported in this review were carried out using the B3LYP functional with the 6-31G(d) basis set, which is a standard in quantum mechanical calculations. Nevertheless, DFT is experiencing continuing developments of new functionals and further improvements. The availability of many new

*To whom correspondence should be addressed. houk@chem.ucla.edu. Phone: (+1) 310-206-0515. Fax: (+1) 310-206-1843.

functionals and, in particular, the rapidly evolving performance issues of B3LYP have stimulated extra efforts on benchmarking DFT methods for the prediction of key classes of organic reactions.² The well-documented deficiencies of B3LYP include the failure to adequately describe medium-range correlation and photobranched effects,^{3,4} delocalization errors causing significant deviations in $\pi \rightarrow \sigma$ transformations,^{2b,5} and incorrect description of non-bonding and long-range interactions,⁶ which are likely to be key factors in determining stereoselectivities. Benchmark results also show that newer functionals considerably improve some of the underlying issues.²⁻⁷ Recent advances, especially in the treatment of dispersion effects, now offer more reliable models of the reaction profiles and stereoselectivities.

Most benchmarks focus on energetics rather than stereoselectivities. Systematic benchmarking for stereoselectivities requires more sophisticated techniques and averaging over conformations. To date, such benchmarking based upon stereoselectivity is available for only three reactions,⁸ and even there only various basis sets with B3LYP, as well as comparisons of results predicted using enthalpies and free energies. It is not possible to assign error bars for stereoselectivities for the majority of reports discussed in this review. Because stereoisomeric transition structures are very similar species, their relative energies are likely to be calculated accurately, as shown by the good agreement between calculated and experimental values.

More recently Harvey (Harvey, 2010, faraday discussions) has studied two typical organic reactions of polar species (Wittig and Morita-Baylis-Hillman reactions) at different levels of theory.²ⁱ He showed that many standard computational methods, involving B3LYP, are qualitatively useful, but the energetics may be misleading for larger reactive partners; the quantitative prediction of rate constants remains difficult. These studies suggest that although B3LYP provides valuable qualitative insight into the reaction mechanisms and selectivities, the energetics may require testing with higher accuracy methods for complex organic systems. On the other hand, Simón and Goodman found B3LYP to be “only slightly less accurate” than newer methods, and recommended its use for organic reaction mechanisms.⁹

2. Enamine/Iminium Catalysis

2.1. Proline and proline derivatives

2.1.1. Intramolecular aldol reaction—The Hajos-Parrish reaction is sometimes considered to be the first organocatalytic enantioselective transformation to be reported (1971). Two groups, Hajos and Parrish at Hoffmann La Roche¹⁰ and Eder, Sauer, and Wiechert at Schering AG,¹¹ published a series of papers and patents involving these transformations. This discovery made possible the stereoselective synthesis of enediones like the so-called Wieland-Miescher ketone, which are key structural elements of steroids, terpenoid, and taxol. It also paved the way to the growing phenomenon of organocatalysis. List has reviewed the field recently¹² and MacMillan has described his influence on creating the field of organocatalysis.¹³

2.1.1.1. Mechanism of Hajos-Parrish reaction: Four main mechanisms of the C-C bond-forming step have been proposed (Scheme 1). There were two original proposals set forth by Hajos and Parrish. The first is the nucleophilic attack by the exocyclic enol ether to a carbinolamine to displace the catalyst (Mechanism A). The second is a simultaneous proton transfer and nucleophilic attack by an enaminium, assisted by the carboxylate (Mechanism B). Based on the observation of a small non-linear effect, Agami suggested that second molecule of proline may be involved in the proton transfer process from the carboxylic acid (Mechanism C).¹⁴ Finally, a mechanism originally proposed by Jung in 1976 suggested a

nucleophilic attack of the enamine terminus with simultaneous proton transfer to the developing alkoxide involving a single molecule of proline catalyst (Mechanism D).¹⁵

Houk and co-workers reported a detailed DFT investigation of the proposed mechanisms of this reaction.¹⁶ Geometry optimizations were performed at the B3LYP/6-31G(d) level of theory, while energies were computed at the B3LYP/6-31+G(d, p) level of theory with single point PCM solvation corrections for DMSO using HF/6-31+G(d, p) and the UAKS radii.¹⁷ The carbinolamine intermediate that precedes the TS corresponding to mechanism A is found to be higher in energy than the uncatalyzed reaction. Such a transition state would be even higher in energy than this intermediate. Mechanism B is disfavored by ~30 kcal/mol due to the distortion of the enamine from planarity to accommodate proton transfer. Mechanism C is disfavored due to the entropic penalties associated with the involvement of another molecule of proline. Mechanism D is favored energetically; this transition structure is ~10 kcal/mol lower in energy than the uncatalyzed process. The preference for this mechanism stems from the enhanced nucleophilicity of the planar enamine as well as the activation of the carbonyl electrophile by the carboxylic acid.

The entire transformation leading from the attack of the exocyclic ketone by the proline moiety through the aldol transition state and the subsequent hydrolysis of the product iminium has been investigated in detail.¹⁴ More recent kinetic isotope effect experiments and calculations lead to the conclusion that the rate-determining step occurs prior to C–C bond formation.¹⁸

2.1.1.2. Origins of stereoselectivity: The stereoselectivity of the Hajos-Parrish reaction has also been investigated by Houk and coworkers using B3LYP/6-31G(d) level of theory.¹⁹ Two chair Zimmerman-Traxler-like transition states are possible: the *syn* and the *anti* (Figure 1). The *syn* and *anti* refer to orientation of the enamine with respect to the carboxylic acid. The *anti* transition state leads to the formation of the experimentally observed product, while the *syn* leads to the formation of the minor product. The 3.4 kcal/mol preference for the *anti* TS corresponds reasonably well to the experimentally observed stereoselectivity of 95 % *ee* (2.2 kcal/mol). A later study involving a single point at the B3LYP/6-311+G(2df, p) level of theory was shown to reproduce the exact experimental stereoselectivity of 2.2 kcal/mol for the Hajos-Parrish reaction.²⁰

The enantioselectivity of the Hajos-Parrish reaction is directly related to the ability with which each of the transition states can achieve optimal enamine nucleophilicity and provide the greatest electrostatic stabilization to the developing negative charge on the carbonyl electrophile. A planar enamine allows for optimal nucleophilicity to the enamine and experiences minimal geometric distortion to form the iminium upon C–C bond formation. The proton donation from the carboxylic acid moiety and, to a lesser extent, the $\delta^+\text{NCH}\cdots\text{O}^{\delta-}$ electrostatic interactions stabilize the developing alkoxide.

The enamine of the *anti* TS is much more planar than the *syn* TS. This distortion of the *syn* TS arises from the necessity to proton transfer to a more proximal alkoxide, which in turn, results in the distortion of the pyrrolidine ring. In contrast, such distortions are unnecessary in the *anti* TS in which there is ample distance between the carboxylic acid and the developing alkoxide.

The $\delta^+\text{NCH}\cdots\text{O}^{\delta-}$ electrostatic interaction exists for both the *syn* and *anti* TSs. However, the distance is much shorter (2.4 Å) and therefore the interaction is stronger in the *anti* TS, in comparison to the *syn*, where this distance is much longer (3.4 Å). The absolute magnitude of the $\delta^+\text{NCH}\cdots\text{O}^{\delta-}$ interaction is also greater in the *anti* TS than in the *syn*, due to the greater positive charge on the far more advanced developing iminium.

2.1.1.3. Catalysis by proline derivatives: Houk and co-workers have also reported the origins and predictions of stereoselectivities of the Hajos-Parrish reaction catalyzed by a diverse range of proline-derivatives (Scheme 2).²¹ B3LYP/6-31G(d) geometry optimizations followed by B3LYP/6-311+G(2df, p) reproduced the exact enantioselectivities of the derivatives for which the reaction has been reported. This combination of methods yielded excellent correlation between the computed and experimental stereoselectivities (mean absolute error, MAE = 0.1 kcal/mol). The Houk-List model, described later in Scheme 10, provides the basis for the experimentally observed stereoselectivities of all the catalysts in Scheme 2.

4,5-methanoproline: The first computational investigations of proline-derivative catalyzed Hajos-Parrish reaction was reported by a joint collaboration between Houk and Hanessian groups.²⁰ At the time, the Hanessian group had reported the synthesis of *cis*- and *trans*-4,5-methanoprolines as conformationally rigid proline surrogates (**5** and **6**). Interestingly, the Hanessian group discovered that the *cis*-4,5-methanoprolines exhibited similar stereoselectivity and reactivity as proline in the Hajos-Parrish reaction, whereas the *trans*-4,5-methanoproline was a poorer catalyst, both in terms of selectivity and rate.

Bicyclo[3.1.0]hexanes are known to favor the boat conformation over the chair due to the torsional interactions around the fused cyclopropane ring. The computed lowest energy conformations of the *cis*- and *trans*-methanoproline enamines revealed that the *trans*-methanoproline enamine is the expected boat with a significantly pyramidalized amine. The *cis*-methanoproline was also found to be the expected boat; however, the steric repulsion of the carboxylic acid group *syn* to the cyclopropane ring resulted in a rather planar *cis*-methanoproline enamine.

The stereoselectivity of the Hajos-Parrish reactions catalyzed by these methanoprolines is dictated by the native conformational preference of the respective proline derivatives. In the *cis*-methanoproline case, the planar enamine allows for a facile transition to the *anti*, planar iminium transition structure, whereas the realization of the pyramidalized *syn* transition structure would require geometric distortion (Figure 2). This is in contrast to the *trans*-methanoproline, where the naturally pyramidalized enamine requires less geometric distortion to reach the *syn*, pyramidalized iminium transition structure, than the planar *anti*. Despite this conformational bias, *trans*-methanoproline is still *anti*-selective not only due to the stability gained by the more planar iminium of the *anti* transition structure but because of the accentuated interaction between the cyclopropyl methylene hydrogen and the developing alkoxide oxygen.

The observed catalytic ability of the two derivatives can also be explained by the conformational biases. The energy required for the naturally pyramidalized *trans* stereoisomer to achieve the necessary planar iminium arrangement in the aldol transition state is responsible for its comparatively poorer catalytic ability.

Pyrrolidine-2-thioic and dithioic acids: The pyrrolidine-2-thioic acid (**2**) and the closely related pyrrolidine-2-dithioic acid (**3**) feature acid groups that prefer longer ideal proton transfer distances. As expected, there is a substantial penalty for the *syn* transition states for cases where the proton transfer occurs from the sulfur (4.8 kcal/mol), while proton transfer from the oxygen exhibited a smaller preference (2.8 kcal/mol, Figure 3).²¹

Protonated amine: The protonated amine case (**4**), which features a quaternary ammonium cation as the proton donor in lieu of a carboxylic acid moiety, was particularly unique from the other catalysts in that it exhibited a reversal in the stereoselectivity (4.7 kcal/mol preference for the *syn* transition structure, Figure 4).²¹ This reversal is seen to be caused by

two factors: 1) the relief of geometric strain in the *syn* transition structure due to the change in hybridization of the proton donor; 2) and the destabilization of the *anti* transition structure due to the steric interactions between the ammonium ion and the substrate.

Isoxazolidine-3-carboxylic acid: The isoxazolidine-3-carboxylic acid (**7**) is an interesting choice of catalyst, due to the possibility of increased nucleophilicity originating from an α -effect. This catalyst also lacks the ability to stabilize the developing alkoxide via $\delta^+\text{NCH}\cdots\text{O}^{\delta-}$ interactions. The computed activation barrier for the C-C bond formation for this catalyst was $\Delta H^\ddagger = 10.0$ kcal/mol, which was found to be similar to the analogous barrier in proline of 10.0 kcal/mol.²¹ The lack of change in reactivity is most likely due to the fact that the repulsive $\delta^-\text{NO}\cdots\text{O}^{\delta-}$ interactions erode any potential reactivity gained from the α -effect. This same repulsive interaction is also responsible for the lack of any computed stereoselectivity for this catalyst (Figure 5).

5,5-dimethylthiazolidine-4-carboxylic acid (DMTC) and 5,5-dimethyloxazolidine-4-carboxylic acid (DMOC): 5,5-Dimethylthiazolidine-4-carboxylic acid (DMTC, **8**) and the closely related 5,5-dimethyloxazolidine-4-carboxylic acid (DMOC, **9**) were also studied.²¹ DMTC is particularly interesting because since the first reports of intermolecular aldol reactions catalyzed by proline, it has been ear-marked as a promising alternative to proline. The presence of the *gem*-dimethyl groups in both these catalysts create $A^{1,2}$ strain with the carboxylic acid group. The need to accommodate a proximal alkoxide in the *syn* TS forces the slight rotation of the carboxylate towards the *gem*-dimethyl groups as compared to the *anti* TS (Figure 6). This results in the computed greater stereoselectivity of the DMOC (3.1 kcal/mol) as compared to proline (2.1 kcal/mol). The DMTC exhibited the same stereoselectivity as proline, and this decrease in preference is seen to be from the weaker $\delta^+\text{NCH}\cdots\text{O}^{\delta-}$ interaction in DMTC as compared to DMOC.

2.1.1.4. Primary amino acid catalysis: Clemente and Houk studied the stereoselectivity of Hajos-Parrish reaction catalyzed by primary amino acids (Scheme 3).²² Primary amino acids exhibit a slightly different stereoselectivity from proline. In the classic Hajos-Parrish reaction, the enantioselectivity exhibited by the primary amino acids are lower than that catalyzed by proline. However, in cases where there is an alkyl substituent on the exocyclic terminus, primary amino acids are more selective than proline.

Geometry optimizations were performed at the B3LYP/6-31G(d) level of theory, while energies were computed at the B3LYP/6-31+G(d, p) level of theory with single point PCM solvation corrections for DMSO using HF/6-31+G(d, p) and the UAKS radii.

The enamine mechanism is still operative. In the case of the Hajos-Parrish substrate, the stereoselectivity arises from the energetic discrimination between the *syn* and the *anti* enamine cyclizations. The energetic penalty of the *syn* TS is again explained as a consequence of the geometric distortion required to do proton transfer to a more proximal alkoxide. In the case of primary amino acids, the energetic penalty from this distortion is less than that exhibited by proline (1.7 kcal/mol less than proline), because the absence of the constraining pyrrolidine ring alleviates some of the geometric penalty of the *syn* TS (Figure 7).

In the case where the exocyclic terminus is substituted by a methyl group, the stereoselectivity is influenced by the difference in energy between the *Z* or *E* enamines. In the case of proline, the methyl group of the *anti-Z*-enamine experiences steric interaction with the pyrrolidine ring, while the *E*-enamine experiences steric interaction with the approaching cyclopentadione electrophile, leading to overall destabilization of the *anti-Z* transition structure. The *syn* transition structures are higher in energy. This is in sharp

contrast to the phenylalanine *anti Z*-enamine structures, which exhibits little steric interaction between the methyl and the proton of the phenylalanine enamine (Figure 8).

2.1.2. Intermolecular aldol reactions—The intermolecular aldol reaction was reported by List, Lerner, and Barbas, and is the first report of the rebirth of organocatalysis since the discovery of the Hajos-Parrish reaction (Scheme 4).²³

2.1.2.1. Mechanism: The generally accepted mechanism of proline-catalyzed reactions involves the transformation of the starting carbonyl compound to a more nucleophilic enamine (Scheme 5, left cycle). Although the generation of enamine is critical for catalysis, the details of the process are still not well understood.

Patil and Sunoj²⁴ computed a proton-relay mechanism involving two molecules of methanol for the enamine formation between model substrates (dimethylamine and propanal) at the mPW1PW91/6-31G(d) level of theory. The PCM solvation model with UAKS radii was used to include solvent effects (THF) in the energy calculations. Significantly lower activation energies compared to the unassisted pathway (Scheme 6) suggested a facile enamine formation in the presence of protic additives. The catalytic ability of co-catalysts is explained by the improved transition state stabilization due to effective hydrogen bonding.

Clemente and Houk¹⁶ studied the pathway involving the formation of an enamine intermediate for a proline-catalyzed intramolecular aldol reaction with B3LYP/6-31+G(d, p)//B3LYP/6-31G(d). The predicted activation energies for the carbinol amine, iminium and enamine formation are 17.0, 15.3 and 26.2 kcal/mol respectively with respect to separated reactants (Scheme 7). More recently, Sunoj and co-workers²⁵ reported the gas phase free energy profile associated with the formation of the enamine intermediate in the reaction between proline and propanal at the B3LYP/6-31+G(d, p) level of theory. The activation free energies for the formation of carbinolamine, iminium and enamine intermediates are found to be 24.2, 25.1 and 26.2 kcal/mol relative to the separated starting compounds.

Boyd and co-workers reported a DFT investigation of the mechanism of the proline-catalyzed intermolecular aldol reaction between acetone and acetaldehyde.²⁶ B3LYP/6-311+G(2df, p) single point energies based on B3LYP/6-31G(d) geometry optimizations along with solvation corrections using the Onsager model (DMSO, $\epsilon = 46.7$) were used.

Boyd and co-workers report that the most difficult step along the reaction potential energy profile is the initial addition of proline to the donor ketone to form the carbinolamine with a barrier of $\Delta E_{zp}^{\ddagger} = 40.1$ kcal/mol. This was shown to be more difficult than the enamine formation ($\Delta E_{zp}^{\ddagger} = 7.1$ kcal/mol) or the C-C bond formation step ($\Delta E_{zp}^{\ddagger} = 13.7$ kcal/mol) in the gas phase. Once solvation corrections have been accounted for, however, the barrier for initial addition drops to $\Delta E_{zp}^{\ddagger} = 9.7$ kcal/mol, and is more facile than the enamine formation ($\Delta E_{zp}^{\ddagger} = 12.0$ kcal/mol) or the C-C bond formation step ($\Delta E_{zp}^{\ddagger} = 11.1$ kcal/mol). They concluded that the use of high polarity solvent is necessary to stabilize the various zwitterionic intermediates and transition state, as expected of an acid-base mechanism.

Reaction progress kinetic analysis of the proline mediated intermolecular aldol reaction by Blackmond and co-workers²⁷ provided evidence that the enamine formation cannot be rate-determining. The rate depends on the concentrations of both the donor ketone and the acceptor aldehyde. The observed isotope effects supports a role for the carboxyl group in the rate limiting step, which is suggested to be the C-C bond formation.

Only very recently, Gschwind and co-workers²⁸ detected and characterized the enamine intermediates in proline catalyzed aldol reactions for the first time experimentally, and

showed the direct formation of enamine carboxylic acids from oxazolidinones in the solvent dimethylsulfoxide.

The NMR spectroscopic evidence for the formation of oxazolidinone intermediates in the reactions of proline with carbonyl compounds²⁹ has stimulated significant debate over the mechanism of catalysis. List and co-workers characterized the formation of oxazolidinones in terms of a “parasitic equilibrium”; that is, oxazolidinones are not involved in the catalytic cycle, but their formation would still allow for turnover by keeping the catalyst in solution.^{29c} More recently a catalytic role of oxazolidinone have been proposed that involves a key enamine carboxylate intermediate (Scheme 5, right cycle).³⁰

Sunoj and co-workers²⁵ explored the competing enamine and oxazolidinone pathways (Scheme 5) using density functional and ab-initio MP2 calculations. Scheme 8 shows the activation free energies of alternative pathways for the conversion of iminium carboxylate to various key intermediates computed with B3LYP/6-31+G(d, p). The barrier for the formation of the oxazolidinone intermediate by the intramolecular attack of carboxylate to iminium is only 0.7 kcal/mol. Higher activation free energies for the formation of enamine carboxylic acid (12.8) and enamine carboxylate (18.0) suggest an equilibrium composition in favor of the oxazolidinone intermediate, in agreement with the experiments. The C-C bond formation steps for both enamine and oxazolidinone pathways were also examined (Figure 9). The C-C bond formation barriers for the oxazolidinone pathway are higher by 11.6 kcal/mol compared to the enamine pathway, and do not predict the correct stereochemistry of the major product. The resulting oxazolidinone products are also found to be significantly higher in energy than the corresponding iminium products in the enamine pathway. Although the energetics support the enamine pathway, a likely convergence between the enamine and oxazolidinone pathways under the experimental conditions is proposed based on the variance of enantio- and diastereoselectivities under different conditions.

Blackmond and co-workers³¹ carried out experimental studies of the role of base additives in enamine catalysis of aminations and observed an unusual reversal of enantioselectivity, in line with the kinetically controlled outcome of the oxazolidinone pathway.

2.1.2.2. Origins of stereoselectivity

The Zimmerman-Traxler model: In List’s initial paper on the proline-catalyzed intermolecular aldol reaction,²³ the enantioselectivities were rationalized based on the Zimmerman-Traxler transition states (Scheme 9),³² originally described for metal enolate aldol reactions. In this model, the nitrogen of the proline enamine is aiding the proton transfer from the carboxylic acid to the forming alkoxide. The stereoselectivity arises from a switch in the axial or equatorial orientation of the electrophile substituent.

The Houk-List model: Joint efforts by the Houk and List groups resulted in the Houk-List model to explain the origin of stereoselectivity of proline catalyzed intermolecular aldol reactions.^{8,33} In contrast to the Hajos-Parrish reaction where the intramolecular nature of the aldol addition restricts the approach of the electrophile, the carbonyl of the electrophile in the intermolecular case can realize various dihedral angles with respect to the enamine double bond. Calculations from Bahmanyar and Houk indicate that only the transition structures that involve intramolecular proton catalysis are energetically viable. DFT (B3LYP/6-31G(d)) computations of a simple model system involving the proline enamine attack of acetaldehyde revealed that only certain rotamers with a dihedral angle of $\pm 60^\circ$ can participate in the H-bonding. In particular, transition structures with a dihedral -60° were found to be 5–10 kcal/mol higher in energy than those with $+60^\circ$ (Figure 10).

Scheme 10 shows the Houk-List model for predicting the stereoselectivity of proline-catalyzed intermolecular aldol reactions. Transition structures involving the *anti* proline enamine are favored over the *syn*, due to: (1) the greater electrostatic stabilization arising from the $\delta^+\text{NCH}\cdots\text{O}\delta^-$ interaction; (2) the *syn* transition structures suffer from distortion of the pyrrolidine ring to accommodate proton transfer to a more proximal developing alkoxide; and (3) transition structures involving the *syn*-enamine force the substituents at the forming C-C bond to be nearly eclipsed.

The *re* face attack is found to be preferred over the *si* face attack. This minimizes the steric interaction between the aldehyde substituent and the enamine, placing the substituent in a pseudo-equatorial conformation. The *re* face attack also generally features a more perfect staggering of substituents around the forming C-C bond.

The computed transition state geometries reveal that the carboxylic acid proton and enamine nitrogen (N \cdots H distance \sim 2.5 Å) are not arranged to form an ideal Zimmerman-Traxler six-membered ring, as had been originally surmised by List.²³ On the other hand, the remaining five atoms are arranged in a chairlike arrangement. These findings are summarized in the Houk-List model, which can be represented as a Newman projection centered at the forming C-C bond or in the offset Newman arrangement that shows the chairlike arrangement of the five heavy atoms involved in bonding changes (Scheme 10).

The Seebach-Eschenmoser model: More recently, the Seebach-Eschenmoser model has been proposed to explain the origin of selectivity (Scheme 11).³⁰ This model involves the enamine carboxylate as a key reaction intermediate. They suggested anti-addition to the *syn*-enamine rotamer, which leads to the more stable, *exo* isomer of the product oxazolidinone, and ultimately to the experimentally observed stereoisomer of the product.

In order to gauge the accuracies of DFT in reproducing the stereoselectivities of proline-catalyzed aldol reactions, the average absolute errors in calculations for three known aldol reactions were determined.⁸ B3LYP/6-31G(d) was shown to have average absolute errors of approximately \pm 0.5 kcal/mol.

Predictions of stereoselectivities: Houk and Bahmanyar predicted the stereoselectivities of proline-catalyzed intermolecular aldol reactions between cyclohexanone and benzaldehyde.^{8,33} The predictions were computed prior to the experiments, which were in turn performed by Benjamin List. They reported excellent agreement between the quantum mechanical prediction and the experimental results. Subsequent calculations indicated that different predictions were obtained when more extensive conformational searches were performed, and are described in a recent published interview of Houk.³⁴ List also found that the stereochemical results obtained with the proline catalyzed reaction of cyclohexanone and benzaldehyde were highly dependent on adventitious water and temperature, so that the agreement of theory and experiment was rather fortuitous.

2.1.2.3. 5-pyrrolidin-2-yltetrazole: 5-Pyrrolidin-2-yltetrazole is one of the currently most interesting analogues of proline, in particular for reactions when less reactive aldehydes are employed as aldol acceptors (Scheme 12). In addition, although tetrazoles and carboxylic acids have similar $\text{p}K_{\text{a}}$ values, the tetrazole group is much more lipophilic and, unlike proline, does not suffer from solvation issues in organic solvents.

Domingo and co-workers performed a B3LYP/6-31G(d, p) study of the tetrazole-catalyzed intermolecular aldol reaction between acetone and pivaldehyde.³⁵ Solvation energies were computed for DMSO using the PCM method. The tetrazole catalyst can exist in two different tautomers (Scheme 13). The 2-tautomer is more stable than the 3-tautomer form by

2.4 kcal/mol in the gas phase. Solvation corrections increased this difference by 3.3 kcal/mol.

Domingo and co-workers state that the origins of stereoselectivity are similar to the reported proline case by Houk and co-workers. The transition structures involving *anti* enamine attack on the *re* face of the pivaldehyde was favored (Figure 11). However, the most interesting feature of note in this report was the discovery that the free energy of activation of the tetrazole catalyst was lower than that of the prolines. This is a consequence of the larger solvation corrections for the tetrazole transition structures ($\Delta G_{\text{solv}} = 11.1$ kcal/mol) than the proline transition structures ($\Delta G_{\text{solv}} = 7.4$ kcal/mol).

2.1.2.4. Proline amide derivatives: Wu and co-workers have reported the development of a proline amide derivative as a catalyst for the intermolecular aldol reaction of acetone and *p*-nitrobenzaldehyde (Scheme 14).³⁶ These catalysts are of particular interest as a more active and stereoselective catalyst than the parent proline. They yield the same enantioselectivity as the proline aldol reactions.

HF/6-31G(d) geometries with B3LYP/6-31G(d, p) single points were used to compute the transition structures of various proline-amide derivative catalyzed aldol reactions. The computed activation barriers of simple proline amides, which lack a strongly acidic proton, are similar to those catalyzed by proline. As expected, the presence of another H-bond donor decreases the aldol barrier even further, as shown by the transition structure of (1*S*,2*S*)-diphenyl-2-aminoethanol amide derivative (Figure 12). Experimental observations also show that the doubly hydrogen bonded aminoethanol amide derivative is more reactive than proline or the parent proline amide.

The use of (1*S*,2*S*)-diphenyl-2-aminoethanol amide derivative resulted in a substantial increase in stereoselectivity, as compared to proline. This increase in stereoselectivity is said to arise from the steric interaction between the phenyl of the benzaldehyde and the hydroxyl of the aminoethanol in the *si* attack of the *anti* enamine.

Gong and co-workers reported highly selective aldol reactions of ketones with α -keto acids using amides prepared from proline and aminopyridines (Scheme 15).³⁷ B3LYP/6-31+G(d) was used to explain the high enantioselectivity of the reaction.

It was proposed that the pyridine nitrogen of the catalyst could hydrogen bond with the acid, while the amide hydrogen could bind with the α -keto acid at the carbonyl of either the keto or ester group (Scheme 16). Binding at the keto group was calculated to be favored by 2.5 kcal/mol. Single hydrogen bonding of the amide hydrogen with either carbonyl group (and without interaction of the pyridine nitrogen) was calculated to be disfavored by 8.0–8.7 kcal/mol.

The Gong research group also investigated the intermolecular aldol reaction of hydroxyacetone with benzaldehyde, catalyzed by a proline amide (Scheme 17).³⁸ It was found that water influenced the regioselectivity, affording products with enantioselectivities ranging from 91 to 99% ee. Theoretical studies (B3LYP/6-31++G(d, p)//HF/6-31+G(d) with explicit solvation by water) revealed that this is due to the hydrogen bonds formed between the amide oxygen of proline amide, the hydroxy of hydroxyacetone, and water. HF generally gives poor activation energies because of the lack of correlation energy. This may also cause the position of the transition state to be in error. However, geometries with HF are reasonable, if less accurate than B3LYP geometries, so that use of HF for geometries is occasionally employed for large systems.

The *anti* enamine and *anti* enol enamine were predicted to differ in stability by only 0.4 kcal/mol (Scheme 18). In the absence of explicit solvation, the transition state leading to the minor 1,2-diol regioisomer (via the enol enamine) was calculated to be favored over the transition state leading to the major 1,4-diol regioisomer (via the enamine) by 4.3 kcal/mol. This regioselectivity is attributed to the short hydrogen-hydrogen distance of 2.34 Å between an amide hydrogen and hydroxy hydrogen in the disfavored transition state.

With the inclusion of an explicit water molecule, the calculated relative energies of the transition states still favor the experimental 1,2-diol (Figure 13). It was reasoned that the experimentally observed selectivity for the 1,4-diol is attributed to the stabilities of the enamine-water complexes. The 6.6 kcal/mol stability of the *anti* enamine compared to the *anti* enol enamine leads to formation of the favored 1,4-diol.

Okuyama and co-workers observed high stereoselectivities in aldol and Michael addition reactions catalyzed by 4-hydroxyprolinamide alcohols (Scheme 19).³⁹ B3LYP/6-31G(d) calculations were performed to understand the high selectivity observed in the reaction between acetone and benzaldehyde (99% ee).

The *anti* conformation of the enamine was assumed to be the most stable, and attack on the *re*- and *si*-faces of benzaldehyde were calculated. Only one conformation for each of these transition states was located due to steric hindrance of the two *gem*-diphenyl groups of the catalyst (Figure 14). The 5.3 kcal/mol difference between the transition states leading to the major (*R*) and minor (*S*) isomers is in excellent agreement with the experimental results.

2.1.2.5. Primary amino acids: Acyclic primary amino acids have also been discovered to be catalysts for the intermolecular aldol reactions (Scheme 20), as discussed earlier for the Hajos-Parrish reaction.⁴⁰ Simple natural and unnatural primary amino acid derivatives catalyzed the reaction between cyclohexanone and an aldehyde in high yield and enantioselectivities.

Córdoba has reported the origins of stereoselectivity of this reaction using B3LYP/6-31G(d, p) geometry optimizations and B3LYP/6-31+G(2d,2p) single points.⁴¹ Four factors were seen to control the stereoselectivity of this reaction: (1) The C-N bond of the amino acid can rotate in the enamine intermediate, in contrast to the corresponding proline-derived enamine intermediates. (2) $\delta^+ \text{NH} \cdots \text{O}^{\delta-}$ electrostatic interactions between the amine proton and the forming alkoxide are stabilizing. Transition state (*R, R*), which lacks this interaction, is higher in energy by 2–5 kcal/mol (Figure 15). (3) The steric interactions between the aldehyde phenyl and the enamine cyclohexyl are destabilizing. The (*S, S*) transition state is thus more crowded than the corresponding (*S, R*) transition state, which lacks this destabilizing interaction. The same holds true for the (*R, R*) transition state compared to the (*R, S*) transition state. (4) Finally, the methyl substituent of alanine interacts unfavorably with the cyclohexyl ring, destabilizing the (*R, S*) transition state by 3.2 kcal/mol compared to the (*S, R*).

The same group computed the reaction profile for formation of the major (*S, R*) product (Figure 16a). The overall reaction profile is analogous to various proline-catalyzed processes. It is worthy to note that the oxazolidinone is 4.6 kcal/mol more stable compared to the active catalyst enamine (Figure 16b). Córdoba stated that the need for water in the reaction mixture experimentally is to drive the equilibrium towards the enamine from the oxazolidinone.

Blackmond and co-workers later investigated the effect of water in proline-mediated aldol reactions using reaction progress kinetics analysis.^{29e} Their results showed two conflicting roles for water: 1) increasing the total catalyst concentration within the cycle due to the

suppression of spectator species, such as oxazolidinones; 2) decreasing the relative concentrations of key intermediates in the cycle by shifting the equilibrium from the iminium carboxylate back toward proline.

2.1.2.6. Cyclic aminophosphonates - pyrrolidin-2-ylphosphonic acid: Dinér and Amedjkouh reported the aldol reaction of acetone and cyclohexanone derivatives with *para*-nitrobenzaldehyde catalyzed by pyrrolidin-2-ylphosphonic acid (Scheme 21).⁴² This catalyst is the phosphonic acid version of proline, and was studied as a candidate for the *syn*-aldol catalyst.

The reaction involving acetone and *para*-nitrobenzaldehyde has been studied computationally using B3LYP/6-31G(d). The three most important transition structures are shown in Figure 17.

The origins of stereoselectivity for this catalyst are very similar to those for the proline cases. The one notable difference between this catalyst and proline is that the *syn-re* transition state is only 0.9 kcal/mol disfavored compared to the most stable *anti-re*, whereas in proline, this difference is greater (>2 kcal/mol).

All enantioselective organocatalysts known to date yield the *anti*-aldol as major products. The authors hoped that the reduced preference between the *anti* and *syn* enamine preference in the aldol transition state of this catalyst would favor the formation of *syn* aldol in the reaction between benzaldehyde and various cyclohexanone derivatives. However, even with Lewis base additives which enhance the *syn*-aldol selectivity to the reaction mixture, the authors found only modest preference for the *syn* aldol (*syn:anti* ~1:1).

2.1.2.7. Nornicotine: Lovell, Noodleman, and Janda have reported the experimental and theoretical studies of nornicotine aqueous aldol reactions between acetone and substituted benzaldehydes. Notably, proline and pyrrolidine are poor catalysts for the aqueous aldol reactions. The mechanism they proposed for this reaction is shown in Scheme 22.⁴³

Lovell, Noodleman, and Janda propose that the nornicotine catalyst reacts via the enamine pathway, but invoked an unusual transition state in which a molecule of water simultaneously attacks the internal carbon of the enamine olefin and donates a proton to the forming alkoxide. In addition a second molecule of water is suggested to be present in the transition structure that later participates in the hydrolysis of the catalyst. No explanations were offered to justify the necessity for the electrophile addition to the more hindered face of the enamine.

This mechanism is based on their calculations for the model reaction of acetaldehyde and acetone (Scheme 23). However, the authors did not include the 9 kcal/mol higher energy of the enol tautomer of acetone compared to acetone. Furthermore, this high energy pathway, in which the first transition structure is entropically disfavored, was not explained.

Zhang and Houk computed the same aldol reaction in water and proposed an alternative mechanism involving water ionization.⁴⁴ The reaction involves three steps: (1) water autoionization, (2) hydroxide or hydronium-catalyzed conversion of aldehyde or ketone into enol, and (3) C-C bond formation and proton transfer to give the aldol product. The overall process for the reaction of acetone and acetaldehyde using B3LYP/6-311++G(3d,3p)//B3LYP/6-31G(d) and the CPCM solvation model are shown in Scheme 24. Two alternative possible mechanisms—(1) initial proton transfer from the ketone enol to water, and (2) initial proton transfer from the ketone enol to aldehyde—were also computed, but the highest-energy species of these reactions are significantly higher in energy than that of the mechanism shown in Scheme 24. While C-C bond formation was calculated to be the rate-

determining step, formation of the enol or enolate may be rate-determining for more reactive aldehydes.

2.1.3. Mannich reaction—The discovery of the intermolecular aldol reaction soon paved the way for the discovery that additions to various other double bonds would also be possible. The proline-catalyzed direct Mannich reaction is a natural extension of the aldol reaction, and is a highly effective carbon-carbon bond-forming reaction that is used for the preparation of enantiomerically enriched amino acids, amino alcohols, and their derivatives (Scheme 25).⁴⁵

Origin of the reverse enantioselectivity compared to the aldol reaction: The enantioselectivity of the Mannich reaction is opposite that of the aldol reaction. Computational investigations by Houk and co-workers show that the imine acceptor must be situated so as to accommodate proton transfer to nitrogen (Figure 18).⁴⁶ This situates the carbon substituent in the more crowded pseudo-axial position.

The enhanced rate of the Mannich reaction versus the aldol reaction: It is also of interest to note that proline-catalyzed Mannich reactions are often much faster than the corresponding aldol reaction. Hayashi and co-workers have suggested that the more basic imines are more readily activated by the carboxylic acid of proline.⁴⁷

The origin of erosion of diastereoselectivity in the piperidic acid catalyzed Mannich reaction: Barbas' group reported that piperidic acid catalysis gives both *syn* and *anti* diastereomers with high enantioselectivity (Scheme 26).⁴⁸ The diastereomeric ratio of *syn*- versus *anti*-product ranged from 2:1 to 1:1. This unusual change in diastereoselectivity upon the increase in ring size from five to six was investigated computationally by Cheong and Houk.⁴⁸

The C-C bond forming steps involving both piperidic acid and proline enamines of propionaldehyde attacking the *N*-PMP-protected *R*-imino methyl glyoxylate were calculated at the HF level of theory with the 6-31G(d) basis set.

The diastereoselectivity of this reaction is determined by whether the *anti* or *syn* enamine conformer is favored in the transition structure. In the case of proline, the transition structures involving the *anti*-enamine are favored over those that involve the *syn*-enamine. The latter involves distortions of the developing iminium from planarity to accommodate proton transfer, and the computed diastereoselectivity given by the difference in *anti-si* and *syn-si* transition structures is 1.0 kcal/mol.

This differentiation is weakened in the case of piperidic acid – the analogous difference for piperidic acid is only 0.2 kcal/mol (Figure 19). The piperidine ring experiences steric interactions with the *anti* or *syn*-enamines that are different than those of the pyrrolidine ring of proline. The relatively rigid piperidine ring holds the carboxylic acid more rigidly than the more flexible pyrrolidine. This alters electrostatic interactions with the ester of the iminoglyoxylate and with the protonated imine. These differences allow the imine to react via both the *anti* and *syn*-enamine, giving rise to roughly equal amounts of both *syn*- and *anti*-product experimentally and computationally. Although the calculated selectivities are in good agreement with the experiments, it should be noted that various benchmarks show that such small energy differences fall in the error margin of the most of the standard computational methods.²⁻⁷ It is generally assumed, without proof, that these methods are able to predict small differences in the energies of stereoisomeric transition states.

The facial *re* or *si* selectivity of the imine acceptor is governed by the necessity for intramolecular proton transfer and minimization of steric interactions between the imine and the reactive enamine. The *E*-imine is more stable than the *Z*-imine. Transition structures involving intramolecular proton transfer are favored; thus the *re* face attacks necessitate substantial eclipsing of the imine and enamine. Consequently, *anti-re* and *syn-re* transition structures are higher in energy by >1 kcal/mol than the *anti-si* or *syn-si* transition structure for both proline and pipercolic acid.

The Mannich reaction catalyzed by diarylprolinol silyl ethers: Hayashi and co-workers used B3LYP/6-31G(d) to investigate the role of acid additives in the Mannich reaction of imines and acetaldehyde catalyzed by diarylprolinol silyl ethers (Scheme 27).⁴⁹ The catalyst was modeled by 2-methylpyrrolidine and the imine was modeled by *N*-benzoyl-*N*-benzylidenenamine. The lowest energy conformer was calculated to have an *s-cis* geometry around the C=N–C=O bond (Scheme 28). The *s-trans* conformer converged to a transition structure for the rotation of this dihedral. The *Z*-isomer is approximately 30 kcal/mol higher in energy than the *E*. The modeled enamine was calculated to have a small 0.7 kcal/mol preference for an *anti* alkene with respect to the pyrrolidine methyl group. The imine was calculated to favor protonation of the nitrogen versus protonation of the carbonyl oxygen by approximately 7 kcal/mol.

Addition of the acetaldehyde *anti*-enamine to the protonated imine was calculated to be highly exothermic (–31.1 kcal/mol in THF, PCM model) and barrierless. The favored transition structure was modeled by constraining the forming C–C bond at 3.0 Å and plotting the energy versus the dihedral angle around this bond. The optimal geometry was located at a dihedral angle of 140 between the reacting imine and enamine double bonds (Figure 20). Because the addition step is extremely fast, the authors conclude that enaminium formation is the rate-determining step of the reaction.

Wong also investigated a similar Mannich reaction using the same catalyst and concluded that the reaction proceeds through an enol rather than an enamine intermediate (Scheme 29).⁵⁰ The calculated enantioselectivity is in good agreement with experimental results. Wong also proposed that the Michael-aldol condensation, Michael addition, α -amination, α -fluorination, and α -sulfenylation, and α -bromination reactions proceed by an enol intermediate with this catalyst.

The Mannich reaction catalyzed by (S)-1-(2-pyrrolidinylmethyl) pyrrolidine: Li and co-workers used BH&HLYP to explain the opposite diastereoselectivities obtained by (*S*)-1-(2-pyrrolidinylmethyl) pyrrolidine and proline in the direct Mannich reactions between ketimine and isovaleraldehyde reported by Jørgensen and co-workers (Scheme 30).⁵¹ Sketches and relative energies of the lowest energy transition structures for each diastereomeric product are shown in Scheme 31. The (*S*, *S*) and (*R*, *S*) transition structures are higher in energy than the (*R*, *R*) and (*S*, *R*) transition structures due to a disfavored steric interaction between the ketimine protecting group and the pyrrolidinyl moiety of the catalyst. In the (*R*, *R*) and (*S*, *R*) transition structures, the ketimine is attacked from the opposite face of the pyrrolidine group. The stability of the (*R*, *R*) transition state compared to the diastereomeric (*S*, *R*) transition structure is attributed to three factors: (1) larger degree of planarity of the developing iminium in the (*R*, *R*) transition structure, (2) electrostatic stabilization of the imine nitrogen by the catalyst in the (*R*, *R*) transition structure, and (3) better staggering around the forming C–C bond in the (*R*, *R*) transition structure.

Catalysis of the same reaction by proline was then studied computationally and represented the first theoretical study of the Mannich reaction of ketimines. The previous studies had involved reactions of aldimines. The lowest energy transition structures for each

diastereomer are shown in Scheme 32. The C-C bond forming distances are shorter than those calculated for the reactions of aldimines (2.2–2.4 Å) and the proton transfer occurs later in the ketimine reactions. In agreement with experiment, the lowest energy transition structure involves attack of the *anti* enamine on the *si*-face of the ketimine to give the (*R*, *S*) product. This transition structure has good staggering around the C–C forming bond and the iminium is stabilized by the carboxylic acid proton.

The computational design of an anti-selective Mannich organocatalyst: Following on the heels of the study of pipercolic acid catalyzed Mannich reactions, Houk and Barbas reported a joint computational and experimental design of an *anti*-selective organocatalyst (Scheme 33).⁵² The stereoselective formation of *anti*-products necessitates a reversal in the facial selectivity of either the enamine or the imine, compared to the proline-catalyzed reactions. A substituent at the 5-position of the pyrrolidine was used to fix the conformation of the enamine. The acid functionality was placed at the distal 3-position of the ring, to affect control of enamine and imine facial selection in the transition state. To avoid steric interactions between the substituent at the 5-position of the new catalyst and the imine in the transition state, the substituents at 3- and 5-positions were placed in the *trans* configuration. On the basis of these considerations, a new catalyst, (3*R*,5*R*)-5-methyl-3-pyrrolidinecarboxylic acid, was designed. The proposed major transition state of the Mannich reaction catalyzed by the new catalyst is shown in Scheme 33.

The reaction between propionaldehyde and *N*-PMP-protected *R*-imino methyl glyoxylate was studied using HF/6-31G(d) calculations to test the design prior to synthesis. No computed structures were reported in this work. The catalyst was predicted to give 95:5 *anti:syn* diastereoselectivity and ~98% ee for the formation of the (2*S*,3*R*)-product.

The relative contributions of the carboxylic acid and methyl group of the catalyst in directing the stereochemical outcome of the reaction were assessed. Computational studies involving the derivative lacking the 5-methyl group, (*S*)-3-pyrrolidinecarboxylic acid, indicate that the methyl group contributes ~1 kcal/mol toward the *anti*-diastereoselectivity. That is, the stereoselectivity changes to 82:18 *anti:syn* dr and 92% ee when transition structures with the unmethylated catalyst are located. This unmethylated catalyst was also tested in an actual reaction, for the case where R1 = *i*-Pr. This derivative afforded (2*R*,3*S*)-*anti*-product in 95:5 *anti:syn* dr and 93% ee, which is a drop of 0.6 kcal/mol from the 1-catalyzed reaction with the same substrate.

2.1.4. α -Aminoxylation reaction—The proline-catalyzed aminoxylation reaction is a convenient way of oxidizing the α position of carbonyl compounds (Scheme 34).

Three different variations of the mechanism have been proposed (Scheme 35). The proposed mechanisms differed by the degree to which the carboxylic acid or the proline amine participates in the proton-transfer process. The transition state model proposed by Hayashi⁵³ is analogous to the Houk-List model; proton transfer occurs from the carboxylic acid in a “partial-Zimmerman-Traxler” chairlike transition state. Zhong proposed a Zimmerman-Traxler transition state in which the proline amine also facilitates the proton transfer,⁵⁴ while MacMillan proposed an enammonium-mediated ene-like zwitterionic transition state.⁵⁵ These pathways do not exhaust the mechanistic possibilities. Nitrosobenzene dimerizes readily, and analogous pathways involving the proline enamine attack on the nitrosobenzene dimer are also possible. Blackmond has reported the observation of an acceleration of reaction rate for the aminoxylation and the related amination reactions by the products of the reaction.^{56,29f} It was concluded that the autoinduction occurs in these reactions but not in the aldol reaction because of a difference in the rate-determining steps.⁵⁷

The reaction was investigated computationally by the Cordóva,^{58a} Houk^{58b} and Wong^{58c} groups. Cordóva reports that the C-O bond forming step for the major *R*-enantiomer occurs via the *anti* enamine, similar to the model proposed by Hayashi (Scheme 36). Formation of the minor *S*-enantiomer reportedly occurs via addition of the *syn* enamine to the *re*-face of the hydrogen-bound nitrosomethane. The minor transition structure is disfavored by approximately 7 kcal/mol. Attempts to locate a transition structure according to the MacMillan model resulted in structures that are similar to the Hayashi transition structure.

The transition structure for the major *R*-enantiomer computed by the Houk group (Figure 21)^{58b} is similar to that of Cordóva. However, the minor transition structure (*syn*-O) differs in that the *syn* enamine attacks the *si*-face of the hydrogen-bound nitrosobenzene, as opposed to the *re*-face described by Cordóva. The transition structure for the minor enantiomer is 3.3 kcal/mol higher in energy than the most stable transition structure for the major enantiomer. This corresponds to a prediction of 99% *ee* of the product favored experimentally, in reasonable agreement with the experimentally reported *ee* of 97%.

The model proposed by Zhong is found not to be a transition state, but minimizes to more stable transition state *anti*-O. Here the proline amine-proton distance is 2.7 Å, and there is no evidence of proline amine pyramidalization. The enammonium-mediated zwitterionic ene-like transition state proposed by MacMillan, with the carboxylate group *syn* to the proton-transfer face, was not found. The closest enammonium transition structure found was one in which the carboxylate group is *anti* to the proton transfer; it is 32.4 kcal/mol higher in energy than the most stable transition structure. The high barrier is attributed to the poor nucleophilicity of the enammonium olefin and the great energetic penalty accrued by the charge separation.^{58b}

The transition structures involving the nitrosobenzene dimer are disfavored due to the entropic cost of dimerization and the difficulty of a nucleophilic attack on the partially negatively charged oxygen of the nitrosobenzene dimer. The most stable transition structure involving the nitrosobenzene dimer is 24.4 kcal/mol higher than the most stable pathway involving the nitrosobenzene monomer.^{58b}

The transition structures for attack at nitrogen (oxyamination) were generally higher in energy than those for attack at oxygen. The attack at nitrogen to give the (*R*)-hydroxyamination product via transition structure *anti*-N is disfavored by 2.6 kcal/mol. This heteroatom selectivity is also explained by the preferential protonation of the more basic nitrogen. In the absence of Brønsted catalysis, a reversal in heteroatom selectivity is expected. The reaction between the dimethyl enamine of propionaldehyde and nitrosobenzene was computationally shown to favor the attack on the nitrogen.^{58b}

Wong also investigated the reaction and found that the lowest energy transition structures for each enantiomer occur from the *anti* enamine (Scheme 37). The calculated energy difference is large in the gas phase (5.2 kcal/mol), but decreases substantially with the inclusion of solvent effects (1.3 kcal/mol). The pathway subsequent to bond-formation was also computed with one explicit water molecule. It was found that the resulting imine favors a *syn* geometry with respect to the catalyst carboxylate in order to maximize hydrogen bonding.^{58c}

2.1.5. α -Fluorination—Jørgensen used DFT to explain the enantioselectivities of α -fluorination reactions catalyzed by trimethylsilyl diarylprolinol (Scheme 38).⁵⁹ Unlike proline, where the carboxylic acid directs the electrophile to the “top” face of the enamine via hydrogen bonding, the TMS diarylprolinol catalyst directs the electrophile to the “bottom” face of the catalyst due to steric shielding (Scheme 39). It was found that there is

little preference for the *anti* or *syn* enamines of propanal and 3,3-dimethylbutanal (Scheme 40), so transition structures for attack of both *anti* and *syn* enamines were calculated.

Transition structures for the α -fluorination of 3,3-dimethylbutanal by *N*-fluorobenzenesulfonamide (NFSI) were located using B3LYP/6-31G(d). The *syn* and *anti* conformations and *E* and *Z* geometries were considered. The lowest energy transition structures leading to the major (*S*)- and minor (*R*)-enantiomers are shown in Figure 22. The major (*S*)-enantiomer is formed by attack of the *anti-E* enamine from the “bottom” (*si*) face to NFSI. The minor (*R*)-enantiomer is 2.4 kcal/mol higher in energy and is formed by attack of the *syn-E*-enamine from the “bottom” (*re*) face to NFSI. This predicted selectivity (96% *ee*) is in excellent agreement with the enantioselectivity (97% *ee*) observed experimentally. The energy difference is attributed to good staggering around the forming C-F and breaking F-N bonds in the major enantiomer, but eclipsing around these bonds in the minor enantiomer. The transition structure for the major enantiomer of the α -amination of *n*-butanal by diethyl azodicarboxylate (DEAD) was also located, but the stereoselectivity was not discussed.

2.1.6. γ -Amination—The γ -amination of α,β -unsaturated aldehydes by diethyl azodicarboxylate (DEAD), catalyzed by the same TMS-protected diarylprolinol, was studied computationally by Jørgensen (Scheme 41).⁶⁰ The (*R*) enantiomer dominated in these reactions, which is the opposite of what was expected. Density functional theory (B3LYP/6-31G(d) with CPCM solvent corrections) was used to rationalize the stereoselectivity of the reaction. Two low-energy conformers of the enamine were located, *E-s-trans-E* and *E-s-trans-Z* (Scheme 42), which differ in energy by 1.4 kcal/mol. This is consistent with ¹H-NMR observations of a mixture of isomers; the two isomers are believed to readily interconvertible by a protonation/deprotonation mechanism.

The activation energy for γ -amination of the major (*R*) isomer with respect to the *E-s-trans-E* enamine is predicted to be 17.1 kcal/mol, while that of the minor (*S*) enantiomer is 13.0 kcal/mol. The activation energy for α -amination of both enamine conformations is approximately 21 kcal/mol. Given the discrepancy between the calculated selectivity for the (*S*)-enantiomer and the experimental observation of the (*R*)-enantiomer, Diels-Alder cycloaddition barriers of the enamine intermediates were calculated. It was postulated that the resulting Diels-Alder cycloadducts should readily hydrolyze to the γ -aminated aldehyde, and the *E*-geometry of the C2-C3 double bond would be reestablished via a reversible addition mechanism of a nucleophile such as water or the catalyst. The activation energy for the [4+2] cycloaddition of *E-s-cis-E* was calculated to be only 6.7 kcal/mol (11.6 kcal/mol with respect to the lowest energy enamine, Figure 23), while the activation energy for the [4+2] cycloaddition of *E-s-cis-Z* was calculated to be 12.3 kcal/mol (18.1 kcal/mol with respect to the lowest energy enamine). The Diels-Alder reactions were calculated to be exothermic, while the γ -amination reactions were calculated to be endothermic. Thus, calculations predict that the preferred mechanism for γ -amination occurs by a Diels-Alder cycloaddition of the *E-s-cis-E* enamine, followed by hydrolysis to give the (*R*) product. To support the Diels-Alder mechanism, 2-pentenal and the pyrrolidine catalyst were reacted with *N*-methylmaleimide instead of DEAD. The Diels-Alder cycloadduct was isolated.

The Seebach group computed the relative energies of the enamine formed by 2-pentenal, and the iminium formed by 3-phenyl-2-propenal, with TMS-protected diarylprolinol catalyst using B3LYP and MP2 and found that the *anti-all-trans* conformations are most stable (Figure 24).⁶¹ The most stable calculated iminium geometry overlays very well with the crystal structure.

2.1.7. α -Alkylation—The intramolecular catalytic asymmetric α -alkylation of aldehydes was developed by List and co-workers. The synthesis of cyclic aldehydes via proline and 2-methylproline catalyzed cyclizations of acyclic halo-aldehydes are shown in Scheme 43.⁶²

Two items are of particular interest in this reaction: (1) Simple methyl substitution at the 2-position of proline enhanced the stereoselectivity of the reaction, as shown in Scheme 43. (2) Triethylamine accelerates the reaction. Thiel and List reported a computational investigation of this reaction using B3LYP with the 6-31G(d) and LANL2DZ basis sets.⁶³ CHCl₃ solvation effects were taken into account by geometry optimizations using the Onsager model and single point energies using the CPCM method with the UAKS radii. Triethylamine was modeled using trimethylamine.

The reaction proceeds via the enamine nucleophilic displacement of the halogen, analogous to the typical proline mechanisms (Figure 25). The rate and stereo-determining step was considered to be the alkylation step. It is interesting to note that the stabilization of the departing iodide by the carboxylic acid of the catalyst induces a cisoid conformation of the carboxylic acid, while in other reported reactions involving proline, the transoid conformation is preferred. Triethylamine was found to provide a salt bridge between the carboxylic acid and the departing halide.

The stereoselectivity of this reaction arises from preferred cyclization by the *anti* enamine. The basic origin of stereoselectivity remains the same – the cyclization of the *syn* enamine accrues energetic penalties due to the catalyst stabilization of a more proximal developing anion. The calculated 99% *ee* is in good agreement with the experimentally observed 95% *ee*. The enhanced enantioselectivity for the 2-methylproline catalyzed aldol reaction compared to the proline-catalyzed reaction is due to the inherently larger steric interactions between the methyl and the aldehyde substituent in the *syn* transition structure. Again, the calculated 66% *ee* for the proline-catalyzed reaction is in good agreement with the experimental 68% *ee*.

2.1.8. Hydrophosphination—Diaryl prolinols have been used to catalyze the asymmetric hydrophosphination of α,β unsaturated aldehydes (Scheme 44).⁶⁴ The origin of high enantioselectivity was investigated using density functional theory (B3LYP/6-311+G(2d,2p)//B3LYP/6-31G(d, p)). The lowest energy iminium intermediate is in the *E* geometry and is 3.5 kcal/mol lower in energy than the *Z* isomer (Scheme 45). In agreement with experimental observations, the lowest energy transition structure leads to the *S* product. The lowest energy transition structure leading to the minor *R* product is 1.5 kcal/mol higher in energy and also rises from the *E* iminium. Steric repulsion with the bulky group of the catalyst causes this transition state to be disfavored. The lowest energy transition structure that arises from the *Z* iminium is 4.2 kcal/mol higher in energy than the *S* transition state.

2.1.9. Michael addition—Domingo and co-workers used B3LYP/6-31G(d, p) to study the role of (*S*)-5-(pyrrolidin-2-yl)-1*H*-tetrazole in the Michael addition of (i) acetaldehyde to nitroethylene and (ii) acetone to β -nitrostyrene (Scheme 46).⁶⁵ For the former reaction, it was found that the enamine isomers formed by condensation of the catalyst with acetaldehyde differ by only 0.8 kcal/mol (Model A, Scheme 47). All possible modes of addition—of the α and β faces of both the *anti* and *syn* enamines to both faces of nitroethylene—were calculated. The lowest energy transition structure has an activation barrier of 18.7 kcal/mol and occurs by addition of nitroethylene to the β -face of the *anti* conformation of the enamine, with a hydrogen bond between the tetrazole hydrogen and an oxygen on the nitro group.

For the latter reaction, four transition structures—addition of both faces of nitrostyrene to the β -face of both the *anti* and *syn* enamines—were located (Model B). The four lowest energy transition structures for each mode of attack are shown in Scheme 48. In all four transition structures, an *anti* arrangement between the phenyl group of nitrostyrene and the enamine C-C double bond, and a *gauche* arrangement between the enamine and nitrostyrene C-C double bonds are preferred. The configuration of the lowest energy transition structure, TS-*anti-re*, agrees with the experimentally observed major diastereomer. The stability of this transition structure is attributed to favorable electrostatic interactions between the forming iminium and the nitro group, as well as the tetrazole hydrogen and an oxygen on the nitro group. Seebach proposed this arrangement (topological rule) for the transition states of enamine reactions with nitroalkenes.⁶⁶ The *syn* transition structures are approximately 2 kcal/mol higher in energy; the N=O \cdots H-N distances reveal weaker hydrogen bond stabilization.

Sunoj used mPW1PW91 and B3LYP to explore the importance of explicit solvation in computing transition structures for the proline-catalyzed Michael addition of 3-pentanone and cyclohexanone to nitrostyrene (Scheme 49).⁶⁷ Polar protic solvents had experimentally been shown to improve reaction rates and stereoselectivities,⁶⁸ and calculations without explicit solvent molecules failed to reproduce the experimentally observed stereoselectivities. The experimentally observed major diastereomer could arise from addition of the *anti* enamine to the *re*-face of nitrostyrene (TS-*anti-re*) to give the *syn*-(*S*, *R*) product. However, mPW1PW91/6-311G(d, p)/mPW1PW91/6-31G(d) gas phase calculations predict a stereochemical outcome of 6% de (*syn*) and 40% ee in favor of the (*S*, *R*) product for 3-pentanone, and 32% de (*anti*) and 97% ee in favor of the (*R*, *R*) product for cyclohexanone.

With one methanol, calculations still do not fit experiment, but the inclusion of two methanol molecules in a cooperative binding mode results in stereoselectivities that are in good agreement with experimental results. Calculations predict 80% de (*syn*) and 90% ee (*S*, *R*) for 3-pentanone, and 82% de (*syn*) and 59% ee (*S*, *R*) for cyclohexanone. The most favored transition structures for each ketone are shown in Figure 26. Both transition structures involve attack of the *anti* enamine to the *re*-face of nitrostyrene, with two methanol molecules bridging the carboxylic acid group of the catalyst and the nitro group of the alkene. The enamine and nitroalkene C-C π bonds are anti to one another.

Nájera and co-workers used B3LYP/6-31G(d) to explain the stereoselectivity of the Michael addition reaction of nitroalkenes with 1,2-aminoalcohol-derived prolinamide catalysts (Scheme 50).⁶⁹

The reaction was modeled by 3-pentanone, 1-nitropropene, and a truncated 1,2-aminoalcohol catalyst. Four possible modes of attack—attack of the nitropropene on both the *Re*- and *Si*- faces of both the *anti*- and *syn*- enamines were calculated (Scheme 51).

In agreement with the experimental results, the lowest energy transition structure (Table 1, TS *anti, Re*, 15.0 kcal/mol), which occurs via attack of the *Re*-face of the *anti* enamine, gives the major (4*S*,5*R*)-*syn* product. The transition structure that gives the minor (4*R*,5*S*)-*syn* enantiomer occurs by attack of the nitroalkene to the *Si*-face of the *anti* enamine. The computed energy difference between these two transition structures (1.4 kcal/mol \approx 80% *ee*) agrees well with the enantioselectivities obtained experimentally. The *syn, re* and *syn, si* transition structures do not have stabilizing hydrogen bond interactions and therefore have higher calculated activation energies.

Alexakis and co-workers reported a DFT study of the pyrrolidine-type catalyzed conjugate addition of aldehydes to vinyl sulfone and vinyl phosphonate Michael acceptors (Scheme

52).⁷⁰ The reaction of 3,3-dimethylisobutyraldehyde and vinyl sulfone was computed. Because the five lowest-energy minima for the enamine formed by the pyrrolidine catalyst and 3,3-dimethylbutyraldehyde are *anti*, only the transition structures for *si*-face (“bottom”, major) and *re*-face (“top”, minor) attack on the *anti* enamine were considered (Figure 27). In agreement with experiment, *si*-face attack was calculated to be favored ($\Delta G^\ddagger = 6.2$ kcal/mol). The stereoselectivity is attributed to favorable electrostatic interactions between the sulfone oxygens and enamine nitrogen. Compared to the reactant, the negative charge on each sulfone oxygen increases in the transition state, and these oxygens are stabilized by the developing positive charge on the enamine nitrogen. The minor (*re*) transition structure was calculated to be significantly higher in energy ($\Delta G^\ddagger = 13.0$ kcal/mol). The sulfone oxygens in the minor transition structure are far from the enamine nitrogen (4.07 Å), and experience steric hindrance with the bulky group of the catalyst.

A variety of chiral amines based on the pyrrolidine skeleton are shown to catalyze the Michael addition of aldehydes to vinyl ketones.⁷¹ An interesting aspect of the reaction is that the catalyst can equally take part in the nucleophilic activation of the aldehyde by enamine formation, and/or in the electrophilic activation of the vinyl ketone by iminium ion formation. Patil and Sunoj have investigated the competing enamine and iminium pathways in the pyrrolidine catalyzed Michael addition between propanal and methyl vinyl ketone (MVK)(Scheme 53).⁷² The results summarized in Table 2 suggest that the direct Michael addition of the enamine intermediate to MVK is the more likely pathway for the C-C bond formation in this reaction.

2.1.9. Cascade Reactions—Sunoj reported a computational study of the highly stereoselective triple cascade reaction reported by Enders and co-workers (Scheme 54).⁷³ All possible conformers and faces of addition were explored using B3LYP/6-31G(d)//ONIOM2(B3LYP/6-31G(d):AM1). In excellent agreement with the reported results, the lowest energy transition structure for the first step ($\Delta E^\ddagger = 23.4$ kcal/mol with respect to separated reactants) occurs via addition of the *si*-face of nitrostyrene to the *si*-face of the (*E*)-*anti*-enamine to give (*2R*)-methyl-4-nitro-(*3S*)-phenylbutanal (Figure 28). The unusual stability of this transition structure is attributed to a number of favorable electrostatic interactions, including the oxygens of the nitro group with hydrogens on the catalyst, and a short $N^\delta - N^{\delta-}$ distance of only 2.9 Å. The other diastereomeric transition structures do not bear such stabilizing interactions. The next higher-energy transition structure is 5.0 kcal/mol higher in energy; it involves addition of the *re*-face of nitrostyrene to give the (*2R*, *3R*) aldehyde.

The next step, Michael addition of the anion generated from the formed nitroalkane to the iminium of 3-phenyl-2-propenal, was calculated to favor *si*-facial attack of the nitroalkane anion to the *re*-face of the iminium (Figure 29). Like the first transition structure, hydrogen bond stabilization of the nitro oxygens with the catalyst accounts for the relative stability of this transition structure compared to the higher energy conformers. There is a further stabilization arising from the carbonyl oxygen with a pyrrolidine hydrogen. Attack on the *re*-face of the nitroalkane was calculated to be 2.2 kcal/mol higher in energy. This transition structure is not stabilized by any C=O \cdots H interactions.

The final intramolecular aldol cyclization step was calculated to occur in the same geometry as the previous Michael addition step (Figure 30). The most stable transition structure adopts a chair conformation and has the same C=O \cdots H and N–O \cdots H stabilizing interactions found in the previous steps. Other transition structure conformers are at least 9.1 kcal/mol higher in energy.

2.1.11. Morita-Baylis-Hillman Reaction—Santos and co-workers investigated the proline-catalyzed intramolecular Morita-Baylis-Hillman reaction of hept-2-enedial reported by Hong and co-workers (Scheme 55).⁷⁴ In the presence of imidazole as co-catalyst, the enantioselectivity of the reaction improves considerably, but with an inversion of absolute configuration. Santos used DFT calculations to verify the mechanisms proposed by Hong.

The results of the lowest energy proline-catalyzed reaction and proline-catalyzed reaction with imidazole as a co-catalyst are shown in Scheme 56 and Scheme 57, respectively. For the reaction without imidazole: The relative energies of the *anti* and *syn* iminiums formed between proline and hept-2-enedial are 0.0 and 2.2 kcal/mol, respectively, but the favored pathway initially involves rearrangement of the *syn* imine to the enamine with water assistance (TS-taut). This tautomerization is the rate-determining step. The resulting *syn* enamine (with C3-C4 in the *Z* geometry) rotates to the *anti* enamine, which then can cyclize via TS-MBH to give either the (*S*) or (*R*) iminium intermediate. In agreement with experiment, cyclization to the (*S*) product is favored. The *syn* enamine can also cyclize to give either the (*S*) or (*R*) product, but these barriers were calculated to be higher than those of the *anti* enamine.

The four possible cyclizations result in a calculated enantioselectivity of 64%. The experimental range is 5–45%, depending on the solvent.^{74b,75} The most favored MBH transition structure is shown in Figure 31. Overall, the model agrees with the one proposed by Hong, which involves addition of the *re*-face of the *anti*-enamine to the *re*-face of the aldehyde. A significant stabilizing electrostatic interaction for the computed transition structure is seen in the 2.39 Å distance between a proline C5 methylene hydrogen and the developing alkoxide, as is found in the usual Houk-List transition structure for the aldol reaction catalyzed by proline. The corresponding distance is at least 3.10 Å in transition structures involving the *syn* enamine.

The reaction in the presence of imidazole was then studied in order to explain the stereoselectivity reversal. The lowest-energy computed pathway is shown in Scheme 57. Unlike the mechanism in the absence of imidazole, the mechanism with imidazole proceeds favorably via the initially formed *anti*-iminium. Addition of imidazole to the iminium terminus and tautomerization to the *anti*-enamine proceeds with water assistance to give the (*S*) configuration at C3 (TS-addn, Figure 32). The transition structure for addition without water assistance is only 0.4 kcal/mol higher in energy. The transition structures for formation of the (*R*) stereoisomer with and without water are 5.8 and 2.4 kcal/mol higher in energy, respectively.

The carboxylic acid of the proline catalyst activates the terminal aldehyde of the *anti*-enamine (C3-(*S*)), which cyclizes via the “top” (*re*) face of the enamine to the *si*-face of the carbonyl, giving the experimentally observed (*R*) product upon hydrolysis (TS-MBH-(*R*), Figure 32). Cyclization to the (*S*) product was calculated to be 2.4 kcal/mol higher in energy. This transition state proceeds via an axial orientation of the imidazole group, which is less stable than the equatorial conformation found in the (*R*) transition state. The overall predicted stereoselectivity of 93% *ee* agrees with the experimental results (80% *ee* with 0.1 equivalent imidazole, 93% *ee* with 1.0 equivalent imidazole).

The rate-determining transition structure calculated by Santos (TS-addn, Scheme 57 and Figure 32) is similar to the one proposed by Hong with respect to an explanation for the stereochemical outcome (Scheme 58). However, the two models differ with respect to the stabilizing mode of the imidazole. Hong proposed that a protonated catalyst carboxylate directs the nucleophilic imidazole nitrogen toward attack of the iminium carbon, while Santos proposed that the carboxylate interacts with the acidic C-2 hydrogen of the imidazole

and directs the nucleophilic attack. Attempts by Santos to locate transition structures proposed by Hong failed.

2.2. Imidazolidinones

The resurgence of organocatalysis in 2000 was initiated not only by reports of the proline-catalyzed aldol reaction, but also by MacMillan's report of an intermolecular Diels-Alder reaction catalyzed by an imidazolidinone catalyst (Scheme 59).⁷⁶ Since this discovery, imidazolidinone catalysts have catalyzed a number of reaction types in good yields and stereoselectivities.

2.2.1. Structure study—Burley and co-workers⁷⁷ and Seebach and co-workers⁷⁸ have independently reported crystallographic and DFT studies of imidazolidinone catalysts. Burley showed that the lowest energy gas phase conformations of the benzoyl groups predicted by B3LYP/6-31G(d, p) and B3LYP/6-311G(d, p) optimizations of the catalysts shown in Figure 33 are not the same as the conformers that exist in the solid state. This discrepancy can be explained by the fact that the gas phase monomeric structures are stabilized by intramolecular interactions, while the solid state structures are stabilized by intermolecular interactions.

Seebach overlaid the crystal structures of the PF₆ salts formed by (*E*)-1-cinnamaldehyde and three imidazolidinone catalysts with DFT structures and found excellent agreement between the structures (Figure 34).

2.2.2. Alkylation—Houk and co-workers used B3LYP/6-31G(d) calculations to rationalize varying enantioselectivities by MacMillan and co-workers in the alkylation of *N*-methylindole and *N*-methylpyrrole by (*E*)-crotonaldehyde, catalyzed by two imidazolidinone catalysts (Scheme 60).⁷⁹ Tomkinson and co-workers have also reported a solution phase NMR, X-ray crystallographic, and DFT study of the imidazolidinone intermediates.⁸⁰

The lowest energy transition structure for the experimental major (*R*) enantiomer in the reaction catalyzed by the dimethyl substituted imidazolidinone occurs via bonding of the *si*-face of the pyrrole to the *re*-face of the iminium (Figure 35). The lowest energy transition structure for the experimental minor (*S*) enantiomer occurs via bonding of the *re*-face of the pyrrole to the *si*-face of the iminium. A theoretical enantioselectivity of 71% ee was calculated for all low-energy conformers. This corresponds to an activation free energy difference that is 0.5 kcal/mol lower than the experimental observation. The *si*-face of the iminium is shielded by the benzyl group, accounting for the observed preference for attack at the *re*-face. The conformation of the benzyl group is, however, different from that displayed in MacMillan's publication.

Like the previous catalyst, the lowest energy transition structure for the experimental major (*R*) enantiomer in the reaction catalyzed by the *tert*-butyl substituted imidazolidinone occurs via the *si*-face of the pyrrole bonding to the *re*-face of the iminium (Figure 36). The lowest energy transition structure for the experimental minor (*S*) enantiomer occurs via the *re*-face of the pyrrole to the *si*-face of the iminium. A theoretical enantioselectivity of 90% ee was calculated using all low-energy conformers, in excellent agreement with the experimental observation.

The enhanced enantioselectivity compared to the dimethyl substituted catalyst can be explained by the preferred conformations of the ground state iminium ions. In the dimethyl substituted catalyst, the phenyl ring lies over the face of the catalyst due to a stabilizing C-H \cdots π interaction between the phenyl ring and the *cis*-methyl group (Figure 37). Such a stabilizing interaction does not exist in the *t*-butyl substituted catalyst due to the steric bulk

of the *t*-butyl group. The phenyl ring effectively rotates away from the catalyst and blocks the *si*-face of the iminium to a greater extent than the same group of the dimethyl substituted catalyst.

2.2.3. Diels-Alder Cycloaddition—Since MacMillan's first report of the imidazolidinone-catalyzed Diels-Alder cycloaddition reaction, modifications to the catalyst structure have been made in attempts to improve stereoselectivity. Table 3 lists the results of changing substituents on the catalyst. The furyl-substituted catalyst (entry 5) proved to be the most efficient in catalyzing the [4+2] cycloaddition between 4-hexene-3-one. Houk and co-workers carried out B3LYP/6-31G(d) calculations in order to explain the stereoselectivity of the reaction.⁸¹

The uncatalyzed reaction was calculated to have a barrier of 20.9 kcal/mol (TS-*s-cis-exo*, Figure 38). A 1:4.5 *endo:exo* ratio was calculated in the gas phase at 0 °C (1:3.7 in water). Transition structures were also located for the Diels-Alder cycloaddition catalyzed by dimethylamine. A 3.1 kcal/mol *endo:exo* ratio was calculated in the gas phase at 0 °C (4.1:1 in water). The activation energy for the most favored transition structure is 9.8 kcal/mol (Figure 38), significantly lower than that of the uncatalyzed reaction.

Transition structures for the least and most effective imidazolidinone catalysts (dimethyl, entry 1, versus furyl, entry 5) were located. Houk and co-workers predicted an *endo:exo* ratio of 6:1 and >99% ee for the dimethyl substituted catalyst in the gas phase at 0 °C, and 100% *endo* selectivity and >99% ee in water (CPCM model, HF/6-31G(d)//B3LYP/6-31G(d), UAKS cavity model). For the furyl-substituted catalyst, an *endo:exo* ratio of 25:1 and 99% ee was calculated in the gas phase at 0 °C. In water the predicted *endo:exo* ratio increases to 35:1 and the enantioselectivity is still high (>99% ee).

The poor enantioselectivity prediction for the dimethyl substituted catalyst led the authors to propose that the iminium is slowly formed compared to the furyl substituted catalyst. The slow iminium formation would allow for the uncatalyzed background reaction to occur and erode the % ee. Gas phase calculations show that iminium formation with the dimethyl substituted catalyst is endothermic by 7.9 kcal/mol, whereas iminium formation with the furyl substituted catalyst is exothermic by 0.6 kcal/mol. The stability difference is due to strong steric hindrance between the ethyl fragment and dimethyl groups (Figure 39). The closest H–H distances are 1.93 Å and 2.05 Å; the closest H–H distance in the furyl substituted catalyst is 2.22 Å).

In conclusion, good *endo:exo* ratios are predicted by both catalysts, but the enantioselectivities are overestimated. The poor enantioselectivity of the dimethyl substituted catalyst can be explained by steric hindrance between the ethyl group of the ketone and the dimethyl groups of the catalyst. The catalysts decrease the activation energies compared to the uncatalyzed reaction by 11 kcal/mol.

2.2.4. α,β -unsaturated ketone reduction—Density functional theory (B3LYP/6-31G(d)) was used to investigate the stereoselectivity of the organocatalytic transfer hydrogenation of 3-phenyl-2-cyclopentenone (Scheme 61).⁸² Two low energy iminium conformers were located that could lead to the experimentally observed products (Scheme 62). Hydride attack on the “bottom” face of the *E* iminium would lead to the major *R* product, while attack on the “bottom” face of the *Z* iminium would lead to the minor *S* product. In good agreement with experimental results, attack of the *E* iminium was calculated to be favored by 1.1 kcal/mol (76% ee). The selectivity is due to a more favorable C–H $\cdots\pi$ interaction in the favored *R* transition structure.

2.2.5. α -Arylation—Both the Nicolaou⁸³ and MacMillan⁸⁴ groups reported asymmetric intramolecular α -arylation reactions via SOMO-activation (Scheme 63).

Based on geometry, charge, spin density, and molecular orbital analyses of the uncyclized and cyclized radical enamine cation intermediates, Houk and co-workers concluded that the cyclization is best described as a radical mechanism.⁸⁵ In agreement with experiment, radical attack *ortho* to the methoxy group was calculated to be favored over *para* attack. The greater stabilization of the cyclohexadienyl radical by the methoxy group at the 1-position rather than the 3-position provides the basic origin of the selectivity (Figure 40).⁸⁶

An interesting reversal of selectivity occurs when an addition substituent R⁴ is introduced to the aromatic ring (Scheme 64, top). Calculations show that *para*, *meta* cyclization is favored over *ortho*, *meta* cyclization by 2.4–3.4 kcal/mol, in agreement with experiment. The *ortho*, *meta* cyclization barriers were calculated to be unachievable under the reaction conditions due to a destabilization of the *ortho*, *meta* transition states. This destabilization is due to repulsion between R³ and the iminium moiety, which results in a distortion of R³ (Scheme 64, bottom).

3. Lewis/Brønsted base catalysis

3.1. Nucleophilic carbenes

3.1.1. Benzoin condensation and Stetter reaction—The benzoin condensation is a powerful and interesting C-C bond formation, as it implies the use of an aldehyde as a carbon nucleophile.⁸⁷ It was first reported by Wöhler in a version catalyzed by cyanide ion,⁸⁸ and a thiazolium salt catalyzed variant was later reported by Ugai and co-workers.⁸⁹ The mechanism of the thiazolium salt catalyzed benzoin condensation is still a matter of debate, and various hypotheses were proposed in the past 50 years. Bofill and co-workers have even reported the possibility of a biradical mechanism based on AM1 calculations.⁹⁰ Houk and co-workers studied this reaction computationally using DFT and found evidence that the monomer-catalyzed pathway was preferred,⁹¹ which is in accord with the original mechanism proposed by Breslow (Scheme 65).⁹²

Chiral thiazolium and triazolium salts, precursors of their corresponding carbenes, were used with mixed success in order to achieve an asymmetric variant of the benzoin condensation. Houk and co-worker initially studied a small achiral system using B3LYP/6-31G(d). They found that the intramolecular proton transfer is key for controlling the stereoselectivity (Scheme 66).

The C-C bond forming step for four different chiral carbene catalysts (**10–13**, Figure 41), as well as the reaction of a chiral aldehyde (**14**) with an achiral thiazolium derived catalyst (**15**), were studied using ONIOM(B3LYP/6-31G(d):AM1). Energies were computed at B3LYP/6-31G(d).

Catalyst **10**, a triazolium catalyst reported by Enders and co-workers⁹³ to be highly selective, was studied. The two lowest energy transition structures leading to the enantiomeric antipodes are shown in Figure 42. In both structures, the phenyl group of the enolamine is *anti* to the bulky *tert*-butyl group. In the lower energy TS-*re* the aldehyde substituent is positioned *anti* to both the aromatic substituent of the enolamine and the *N*-aryl moiety of the catalyst. They proposed that the *re* addition structure (TS-*re*) is stabilized by the π -aryl-iminium ion interaction, as the distance between the aldehyde aryl group and the triazolium ring is fairly close (~ 3.3 Å). The stereoselectivity was predicted using a Boltzmann distribution of the most stable transition structures within 4 kcal/mol. This gave an enantioselectivity of 98% *ee*, which is in good agreement with experiment (90% *ee*).

Catalyst **11** is a similar thiazolium catalyst reported by Knight and co-workers⁹⁴ that afford the (*S*)-benzoin product from benzaldehyde with low enantioselectivity (11% *ee*). The two lowest energy addition structures are shown in Figure 43. The main difference between the two transition structures is a repulsive interaction between the phenyl group of the aldehyde and the aryl of the catalyst. Moreover, there seems to be a slightly more favorable π -aryl-iminium ion interaction in the *si* transition structure (distance between Ph_{aldehyde}-thiazolium = 3.8 Å) compared to the *re* addition (distance 4.3 Å). These transition states are very similar in energy, and the computed enantioselectivity of 10% *ee* in favor of the *R* product is in fair agreement with the low selectivity observed experimentally (11% *ee*) in favor of the *S* product.

The third catalyst (**12**) studied was reported by Sheehan and co-workers⁹⁵ to give modest enantioselectivity (51% *ee*), and the two lowest energy structures are shown in Figure 44. The main difference is the repulsive interaction between the aryl of the aldehyde and the α -methyl of the catalyst. The computed energies overestimate the enantioselectivity (91% *ee*) in favor of the *R* product.

Catalyst **13**, reported by Enders and co-workers,⁹⁶ has many possible conformational isomers, but all located transition structures showed the same conformation of the chiral dioxirane ring. The two lowest energy transition structures leading to the *R* and *S* product are shown in Figure 45. In both structures, the chiral dioxane ring is in a chair conformation with the triazolium in an axial position and the phenyl in an equatorial position. The main difference between the *re* and *si* is the repulsive interaction between the aldehyde aryl and the phenyl ring of the catalyst in the *re* structure. The computed enantioselectivity is >99% *ee* in favor of the *R* product, higher than the experimentally observed 75% *ee*. Enders and co-workers have however reported a decrease in enantioselectivity with longer reaction times, possibly explained by the benzoin product racemization.

Finally, they computed the transition structures of an intramolecular condensation of a chiral aldehyde **14** using a simple achiral thiazolium derivative (**15**) reported by Hachisu and co-workers.⁹⁷ The four possible transition structures are shown in Figure 46. The transition structures leading to the minor product (*si* attack) are clearly disfavored, as the thiazolium moiety and the ester groups are eclipsing each other. Of the two transition structures leading to the experimentally observed product (*re* attack), the *exo* transition state is slightly favored, as an unfavorable interaction between the methyl in the *endo*-position and the ring exists in the *endo* transition state. The energy difference of 6.6 kcal/mol predicts an exclusive formation of the *R, S* isomer, in agreement with the >20:1 selectivity observed experimentally.

A reaction that is closely related to the benzoin condensation is the Stetter reaction, which involves the C-C coupling between aldehydes and an appropriate Michael acceptor. The suggested mechanisms of these related reactions are similar; only the second aldehyde of the benzoin condensation is replaced by a similar conjugate acceptor. Hawkes and Yates investigated a model asymmetric Stetter reaction using B3LYP/6-31G(d) on the basis of Breslow's mechanism for benzoin condensation.⁹⁸ They located a low energy intermolecular proton transfer pathway that yields the Breslow intermediate with an overall barrier of 13.1 kcal/mol (Scheme 67), competing with the high energy intramolecular 1,2-hydrogen shift transition state (39.1 kcal/mol). The overall reaction profile is consistent with benzoin condensation: the stereo- and rate-determining step is the C-C coupling (34.4 kcal/mol). Unlike the benzoin condensation, the C-C coupling in the Stetter reaction occurs in a two step process, in which C-C bond formation precedes proton transfer. The authors suggested that the stereoselectivity is governed by the steric interactions of the enolamine *N*-

substituents with the Michael acceptor and the exact conformation of the enolamine, which can be adjusted by tailoring the carbene substituents.

3.1.2. Transesterification—Widely used *N*-heterocyclic carbenes (NHCs) have recently been shown to be excellent catalysts for transesterification reactions. Nolan and co-workers have demonstrated their use in the rapid transesterification of a vinyl acetate.⁹⁹ Hedrick and co-workers have reported similar methodologies, and have noted their potential as catalysts for the living polymerization of cyclic esters.¹⁰⁰ The actual mechanism of action of the NHC in the transesterification is still a matter of debate. Hu and co-workers computationally studied the possible pathways for the transesterification reaction,¹⁰¹ using B3LYP and the cc-pVDZ basis set. The mechanism involving a neutral tetrahedral intermediate (Scheme 68) was found to be the most favorable.

The pathway involving the nucleophilic attack of the NHC to the carbonyl carbon, resulting in a 2-acylimidazolium intermediate, was found to be unfavorable. They also studied different alcohols and carbenes derivatives, and found qualitative agreement between the relative energies of the tetrahedral intermediates (TD) and the experimentally observed conversions.

3.1.3. Oxidation/protonation of α,β -unsaturated aldehydes—Scheidt and co-workers gave experimental and computational evidence for the ability to divert product distributions in the esterification of α,β -unsaturated aldehydes catalyzed by *N*-heterocyclic carbenes. (Scheme 69).¹⁰² Prior to this report, manipulation of reaction conditions to favor the saturated product remained elusive.¹⁰³ All known reports had favored either solely the oxidized product, or mixtures of the two products.

A test of the reaction in toluene, dichloromethane, tetrahydrofuran, and methanol shows a reversal of product selectivity as the solvent polarity increases. In toluene, the saturated product dominates (approximately 2 or 3:1), while in methanol the oxidized product dominates (up to 12:1). To understand the divergent pathways, the reaction enthalpies of the competing steps—hydride loss from the tetrahedral intermediate (Scheme 70, ΔH_3) and 1,2-proton shift from the tetrahedral intermediate (ΔH_2) — were calculated in methanol and dichloromethane using density functional theory (M06-2X/6-311+G(2df, p)/M06L/MIDI! (6D)/Auto, SM8 solvation model and a single explicit methanol molecule). The results are shown in Table 4. The first step, addition of the catalyst to the aldehyde (ΔH_1), is calculated to be exothermic in both methanol and dichloromethane. In good agreement with experimental results, hydride loss from the tetrahedral intermediate to generate the cationic acyl azolium intermediate ($\Delta H_3 = 3.7$) is more favorable than a 1,2-proton shift ($\Delta H_2 = 6.1$) in methanol. In contrast, hydride loss in dichloromethane is significantly disfavored ($\Delta H_3 = 13.7$), while a proton shift becomes more facile ($\Delta H_2 = 2.7$). This difference is attributed to the sensitivity of the cationic intermediate to solvation. The oxidation pathway dominates in protic solvents, whereas the saturation pathway dominates in nonpolar solvents.

3.1.4. Biomimetic oxidation of aldehydes—Pyruvate ferredoxin oxireductase (PFOR), along with co-factor thiamine pyrophosphate and a $[\text{Fe}_4\text{S}_4]$ cluster, catalyzes the oxidative decarboxylation of pyruvate.¹⁰⁴ Studer and co-workers were guided by PFOR activity in the development of a reaction system of 2,2,6,6-tetramethyl piperidine *N*-oxyl radical (TEMPO) and thiazolium carbene to mediate the oxidation of aldehydes (Scheme 71).¹⁰⁵ The proposed mechanism is shown in Scheme 72.

The structure of the intermediate radical cation (**RC**) was studied using several DFT methods (PBEh/TZVP, B2LYP/TZVP, and B2LYP/TZVPP). Both enol (**RC-enol**) and keto (**RC-keto**) forms were calculated (Figure 47). The enol form was calculated to be more

stable than the keto form by 12.8, 9.6, and 11.4 kcal/mol using PBEh/TZVP, B2LYP/TZVP, and B2LYP/TZVPP, respectively. The electronic structures shown in Figure 47 are in agreement with the calculated spin density distributions.

3.2. DMAP catalysts

3.2.1. Mechanism of the DMAP catalyzed acylation—4-(Dimethylamino)pyridine (DMAP) is an efficient catalyst for the acylation of alcohols and amines. Zipse and co-workers computationally studied the simplest acylation of alcohols with DMAP.¹⁰⁶ The currently accepted mechanism involves the facile nucleophilic addition of DMAP to acetic anhydride to form an acylpyridinium cation, followed by a rate-limiting formation of the ester from this intermediate (Scheme 73). A stoichiometric quantity of an auxiliary base, such as triethylamine, is required to regenerate the catalyst.

The identity of the base in the rate limiting step is a matter of debate, as the acetate counterion, triethylamine or a second DMAP molecule could be involved. In order to confirm the mechanism and clarify this issue, Zipse and co-workers have done computational and kinetic studies on the simple DMAP catalyzed acetylation of alcohols. The gas phase enthalpy diagram for the accepted mechanism is shown in Scheme 74.

As experimentally observed, the rate determining step is found to be the trans acylation of the alcohol. Single point solvation corrections were calculated for different solvents, and the results are in qualitative agreement with experimental findings that show polar solvents tend to slow down the reaction. The trans acylation step is always found to be the rate determining step, even with solvation. Other possible pathways were calculated and found to be energetically less favorable.

The identity of the base implicated in the trans acylation step was still unanswered. Some previous evidence suggests that the acetate anion plays an important role, based on the low reactivity of acylpyridinium salts containing less basic anions.¹⁰⁷ Using kinetic studies, they found strong evidence that triethylamine does not participate in the rate-limiting trans acylation reaction, in agreement with the role of the acetate anion as the actual base.

It has been shown that increasing the steric bulk of the anhydride leads to decreased reaction rates. The G3(MP2)B3 compound method was used to calculate the reaction enthalpies of acyl transfer to cyclohexanol by a variety of anhydrides (Table 5).¹⁰⁸ The reaction enthalpy is independent of the choice of anhydride, with only a 1.2 kcal/mol difference between the most reactive acetic anhydride and least reactive pivalic anhydride. Thus it was concluded that the experimental rate differences intrinsically lie in the activation barriers. The rate of the catalyzed reaction is more sensitive to the steric bulk of the anhydride than the rate of the uncatalyzed reaction. This different response has implications for the kinetic resolution of alcohols.

3.2.2. Conformational analysis of chiral DMAP derivatives—Although no mechanistic studies have been reported concerning the acylation or resolution of chiral alcohols using chiral DMAP derivatives, some interesting studies have been reported concerning the properties of such chiral bases. The design of a chiral DMAP derivative requires a chiral environment around the DMAP nitrogen to effect stereoselectivity, but not enough to hinder the catalysis. Numerous groups have sought to exploit π - π interactions (Scheme 75) to achieve such a feat. Aside from providing a chiral control element, such interactions were also proposed to enhance the rate of the reactions via stabilization of the acylpyridinium intermediate. In order to better understand these proposals, Zipse and co-workers have performed a general study concerning the role of π - π interactions in DMAP derivative catalysis.¹⁰⁹

Zipse studied a number of DMAP derivatives in which π - π interactions could occur (**17–19**, Scheme 76). In order to account for dispersion interactions, an extensive study of different theoretical methods was performed. Zipse concluded that a conformational search at MP2/6-31G(d)//HF/3-21G level followed by SCS-MP2/6-311+G(d, p)//MP2/6-31G(d) refinements on the lowest energy conformations led to the best quality results. In an earlier publication, they found a correlation between the relative stability of the acyl pyridinium intermediates and the $C_{\text{acyl}}-N_{\text{pyridinium}}$ bond length.¹¹⁰ With the exception of the pyridine acyl intermediate, with a C-N bond of 1.54 Å, all the other catalysts were found to have almost identical bond lengths, around 1.47–1.49 Å. Interestingly, an inspection of the different conformations of catalyst **18**, all possessing very different degree of π - π interactions, showed mostly identical C-N bond lengths. They thus concluded the interaction does not seem to greatly stabilize the acyl pyridinium species.

3.2.3. Stabilities of *N*-acyl DMAP derivatives—Zipse showed that some correlation could be found between the relative stabilities of the acyl pyridinium species and the catalytic activity.^{111,112} In order to address the relative stabilities of acyl pyridinium intermediates, they computed the isodesmic reaction shown in Scheme 77 for a number of catalysts. This strategy was also used by Han and co-workers in order to evaluate the relative efficiency of new DMAP derivative **22**.¹¹³ The reaction enthalpies of select catalysts were compared with the measured half life for the equation shown in Scheme 78. The results are shown in Table 6.

The nucleophilic base 4-pyrrolidinopyridine (**PPY**) has long been known catalyze acyl transfer reactions more efficiently than DMAP.¹¹⁴ The 3-alkyl-4-guanidinyldiopyridines are moderately more effective than PPY in acyl transfer reactions (**23–24**),^{111a} while 4-dialkylaminopyridines (**DMAP**, **PPY**, **16**)¹⁰⁹ and 3,4-dialkylaminopyridines (**21**),^{111b,114} are among the most effective DMAP-type catalysts. Han showed that 3,4,5-trialkylaminopyridine catalyst **22** is approximately 10% more effective than **16**.

Yamada and co-workers reported their own conformational study concerning the DMAP derivative **20** (Figure 48), used as a catalyst for the resolution of chiral alcohols and amidines.¹¹⁵ In the neutral form, the chiral sidearm at the 3 position is found to be freely rotating. Upon the formation of a pyridinium salt, however, the side arm favors conformation **A**, thus blocking the top face. This was independently verified by NMR. They have computed the two lowest energy conformations at B3LYP/6-31G(d) of the *isobutyryl* acylpyridinium and showed that **A** is favored by 1.0 kcal/mol. **B** is disfavored due to repulsive interactions between the *tert*-butyl and the *isobutyryl* groups.

3.2.2. Structural analysis of *N*-acetylated DMAP salts—Schreiner and co-workers studied the salt formation between acetylated DMAP and CH_3CO_2^- , CF_3CO_2^- , and Cl^- , using experimental and computational techniques (Figure 49).¹¹⁶ B3LYP/6-311+G(d, p) (PCM, dichloromethane)//B3LYP/6-31G(d) was used for the calculations. The anions can be stabilized by hydrogen bonding interactions (**I** and **II**, Figure 50), nucleophilic interactions (**IV–VI**), or a mixture of both (**III**).

Complex I was calculated to be the preferred structure for salts **25–27**, while complex II was the preferred structure for **28**. IR and NMR spectra, crystal structure analyses, and experiments with deuterated DMAP support complex II as the preferred geometry for the chloride salt (**28**). However, experimental evidence supports the conclusion that III is the preferred geometry for **25–27**, even though it is approximately 2 kcal/mol higher in energy. The authors concluded that the bidentate anions might be able to guide an alcohol to the reaction center via hydrogen bonding interactions (Figure 51).

3.3. Cinchona type catalysts

Despite their use as versatile organocatalysts,¹¹⁷ cinchona alkaloids have received little attention computationally, most probably due to their large size and flexibility. However, some mixed spectroscopic and computational studies have been reported in the literature relating the conformations of various cinchonidine derivatives (Figure 52). Baiker and co-workers reported a NMR and computational study of the conformational behavior of cinchonidine in different solvents.¹¹⁸ More recently, they also reported a mixed VCD spectroscopy and computational study of O-phenyl cinchonidine.¹¹⁹ Zaera and co-workers reported a mixed NMR and computational study of the effect of protonation of cinchonidine.¹²⁰ Lastly, Szöllösi and co-workers have reported a similar mixed study on the conformational behavior of *py*-hexahydrocinchonidine.¹²¹

3.3.1. Staudinger reaction—Lectka and co-workers developed an efficient cinchona alkaloid catalyzed methodology for the asymmetric synthesis of β -lactams (Scheme 79).¹²² The catalyst of choice in this case is benzoylquinine (**BQ**)

In order to rationally design and optimize their catalyst, they performed molecular mechanics conformational searches on the base-ketene adducts. They had some success using this method, as they obtained qualitative agreement between the enantioselectivities observed and the relative energies between the different diastereomers.¹²³

3.3.2. Decarboxylation of Naproxen—Due to the high demand of non-steroidal anti-inflammatory drugs (NSAID), such as naproxen and ibuprofen, there is a growing interest in the efficient syntheses of these compounds (Figure 53).

The synthesis reported by Brunner and Schmidt¹²⁴ relies on a cinchona catalyzed asymmetric decarboxylation as the critical stereodetermining step (Scheme 80) and has been the subject of a short computational study by Strassner and co-workers.¹²⁵ To explain the decarboxylation step, Brunner and Schmidt proposed a two step mechanism involving a decarboxylation/ketimine formation followed by an enantioselective protonation of the ketimine by the catalyst.

Strassner and co-workers computationally studied the decarboxylation step using B3LYP/6-31G(d)/AM1 level and Onsager solvation corrections. They have found that a concerted decarboxylation/protonation mechanism was energetically more favorable than the stepwise pathway. The transition structures leading to both enantiomers are shown in (Figure 54). The formation of the (*S*)-enantiomer is favored by 3.7 kcal/mol, in good agreement with experiment. They explain this difference by the better H-bonding arrangements in the transition state leading to the *S* enantiomer.

3.3.3. Sulfinylation—The synthesis of chiral sulfinates by Ellman et. al. involves the use of cinchona alkaloids in the dynamic kinetic resolution (DKR) of racemic sulfinyl chlorides (Scheme 81).¹²⁶ In this methodology, the Ellman group used a catalytic amount of quinidine as well as an excess of proton sponge in order to neutralize the forming HCl in the reaction. A similar methodology, but using stoichiometric amounts of a cinchona alkaloid was developed earlier by Toru and co-workers.¹²⁷

These methodologies require the fast racemization of sulfinyl chlorides under the reaction conditions, as well as an acceleration of the sulfinylation step by the base. Maseras and co-workers have studied these two issues computationally using trimethylamine as a base model. They initially studied the mechanism of racemization of different sulfinyl derivatives.¹²⁸ The calculations were done using B3LYP with the 6-31G(d) and LANL2DZ(ECP) basis sets for the first and second row elements, respectively. The

inversion barriers of sulfinyl chloride and methyl sulfinite were found to be too high (63.4 kcal/mol) to occur under experimental conditions (Scheme 82).

The computed pathways for the inversion in the presence of trimethylamine were found to be substantially lower in energy and experimentally feasible. For the case of the sulfinyl chloride, the inversion barrier is lowered to 22.9 kcal/mol in the presence of the base. The analogous barrier for the methyl sulfinite is 42.7 kcal/mol, too high for racemization to occur, hence these products keep their optical activity after their formation, as observed experimentally.

A comparison of the uncatalyzed and base catalyzed inversion transition states led some insights (Figure 55). The major difference observed comes a more important elongation of the S-X bond (X = Cl, OMe) in the base catalyzed structures. These results show the importance of the base in the dynamic kinetic resolution.

More recently Maseras and co-workers also studied the effect of the base on the actual sulfinylation step.¹²⁹ They have also investigated several different mechanisms for this reaction, as shown in Scheme 83. They used the same method described for the earlier calculations, but included single point solvation corrections for toluene using CPCM.

Uncatalyzed and base-catalyzed pathways were both calculated for the neutral mechanism (Scheme 83a) and the energy diagram is illustrated in Figure 56. **TS-add** was considered the stereodetermining step. The intermediate between **TS-add** and **TS-elim** was not investigated.

Assistance of the trimethylamine greatly stabilizes the addition step **TS-add**. This is due to the strong coordination of the base in the proton transfer process (Figure 57). Moreover, this results in a greater nucleophilicity of the alcohol. The close proximity of the base to the chiral sulfur center in this critical step also explains the high enantioselectivities observed by Ellman and co-workers.

The ion pair mechanism (Scheme 83b) was also studied, and the addition step was also found to be the rate determining step. The TSs involving one or two amines are shown in Figure 58.

It is interesting to note that the chloride anion is not fully dissociated and maintains interaction with the sulfur atom, resulting in an octahedral complex. The energies show the uncatalyzed addition of the alcohol to the sulfinyl ammonium to be unfavorable (40.9 kcal/mol). However, the base assisted mechanism leads to a free energy of activation similar to what was observed for the neutral mechanism (14.4 kcal/mol). From those results, it is hard to rule out a single mechanism. However, it should be noted that the use of bulkier bases would disfavor the ion-pair mechanism.

3.3.4. α -Bromination—Recently, Lectka and co-workers also developed an asymmetric catalysis for the α -chlorination of acid halides, using cinchona alkaloid derivatives.¹³⁰ In an effort to widen the scope of the method, they extended it to α -bromination (Scheme 84).¹³¹ Unfortunately, this new methodology led to lower enantioselectivities on larger scale. They thus resorted to computational studies to assist in the optimization of their methodology.¹³²

Using molecular mechanics to guide their designs, they replaced the benzoylquinine (**BQ**) by a proline-quinine conjugate (**ProQ**). This new catalyst led to improved enantioselectivities.

Brominating agent **29a** was replaced by brominating agent **29b** to achieve enhanced selectivities. Computational studies of the bromination step for brominating agents **29a** and **29b**, using benzoyl quinine (**BQ**) as the catalyst, were employed with the IMOMO variation of ONIOM(HF/3-21G(d):AM1). The *si* and *re* TSs for the bromination using **29b** are shown in Figure 59.

The strong asymmetry in the $C_{\text{enolate}}\text{-Br-C}_{29a}$ clearly shows that these are late, product-like, transition states. The electrostatic interactions with the quinuclidine hydrogens stabilize the forming negative charge on the brominating agent. The energetic preference for the *si* addition originates from a repulsive van der Waals contact between the enolate α -hydrogen and the C-H hydrogen α to the benzoyl in the catalyst in the *re* TSs. The calculated enantioselectivity of 87% *ee* is in close agreement with the experimental value of 88% *ee*.

The transition structures for the bromination using **29a** are shown in Figure 60. They share similar geometries as the one found for **29b**. The preference for the *si* addition seems to originate from a better stabilization of the enolate oxygen through 3-point H-bond network with the quinuclidine ring. In addition, there is a destabilizing van-der-Waals contact between the ketene enolate phenyl and the quinoline methoxy in the unfavored *re* addition. The calculated enantioselectivity of 99% *ee* is an overestimation of the 78% *ee* experimentally observed, but the low selectivity is thought to be due to competing product racemization.

Molecular dynamics on the lowest energy TSs found for the α -bromination using **29a** and **29b** were performed in order to monitor the time needed for the phenolate to be oriented suitably for the trans acylation. They have found that this process for **29a** took 8.5 ps, more than twice as much as for **29b** (3.6 ps), giving further evidence to the possible competition between epimerization and trans acylation.

3.4. Pyridine *N*-oxide 3.4.1. Strecker reaction

The Strecker reaction is an efficient method to rapidly access α -amino acids through the formation of the corresponding α -amino nitriles. Asymmetric versions have been developed using different catalysts. In particular, amine *N*-oxides have been found to be efficient catalysts for this reaction, affording the desired α -amino nitriles under mild conditions.¹³³ Hu and co-workers have computationally studied the methodology shown in Scheme 85 using small models.¹³⁴ The calculations were done using B3LYP/6-31G(d) and solvation energy corrections using PCM.

The two mechanisms of the uncatalyzed reaction were initially studied. In pathway a, H_3SiCN first isomerizes to isocyanide, then adds to the imine, forming the α -amino nitrile (Scheme 86). Alternatively, the isomerization to the experimentally observed α -amino nitrile occurs after addition of the H_3SiCN to the imine (pathway b, Scheme 86).

The two pathways are very similar energetically (Figure 61). Both addition transition states involve simultaneous silyl transfer to the nitrogen and the cyanide (or isocyanide) addition to the imine carbon.

The reaction profiles for the pyridine *N*-oxide catalyzed process reveal some striking differences (Scheme 87). The catalyzed process features a stepwise formation of the initial *N*-oxide- H_3SiCN -imine complex, not concerted as in the uncatalyzed process. While the original mechanistic proposal involved a bis-pyridines *N*-oxide chelating to the silicon, only mono ligated complexes were found computationally (**33** and **Int1a**).

The relative energy profiles are shown in Figure 62. Complexation of the *N*-oxide lowers slightly the isomerization process from nitrile to isonitrile, compared to the uncatalyzed process. More importantly, the complexation of the *N*-oxide enhances the nucleophilicities of isocyano and cyano group, resulting in a remarkable facilitation of the addition step in both cases. This is due to the strong donor ability of the *N*-oxide. They did not however study the stereochemical aspects of the reactions.

3.5. Sulfides

3.5.1. Sulfur Ylide Mediated Epoxidations—Aggarwal and co-workers have recently developed an asymmetric epoxide synthesis methodology based on the addition of sulfonium ylides to carbonyl compounds (Scheme 88).¹³⁵ Although a metal catalyst is needed in the overall reaction process, the actual epoxidation proceeds through organocatalysis.

The mechanism of the parent reaction is well established. Aggarwal has shown that the preference for *trans*-epoxides arises because the *anti*-betaine formation is irreversible, while the formation of the *syn*-betaine is reversible (Scheme 89).

Previous theoretical studies concerning the epoxidation using sulfonium ylides were either done using very small models (CH₂=SH₂ and formaldehyde)¹³⁶ or on larger models without reliable solvation corrections.¹³⁷ Aggarwal thus conducted a computational study of the transition states of this methodology, involving realistic model molecules with solvation effects.¹³⁸ They studied the reaction of a phenyl stabilized ylide (PhCH=SMe₂) with benzaldehyde at the B3LYP/6-311+G(d, p)//B3LYP/6-31G(d) level. Polarizable continuum-Poisson solvation corrections were applied during the geometry optimizations and on single points.

The lowest energy TSs for the addition of the ylide to the aldehyde all proceed through a *gauche* (cisoid type) conformation (Scheme 90). This maximizes the stabilizing coulombic interactions between the sulfonium and the forming alkoxide in the addition step. In a smaller model system the following *trans* cyclization is greatly favored (Scheme 91). Hence, the rotation from the *gauche* staggered conformation to the *anti* staggered conformation must be taken into account in the overall reaction process.

The epoxidation energy profile is shown in Figure 63. It is of interest to note that the rotation is the rate determining step. In the formation of the *trans* stilbene oxide, the addition is found to be irreversible, whereas the formation of the *cis* stilbene oxide this is reversible due to the fact that the rotation is difficult.

The calculations are in accord with their kinetic and crossover experiments. These results are particularly interesting as experiments could not have predicted the rotational barrier following the addition to be critical in the reaction process.

More recently, they have also reported the development of an epoxidation methodology using amide stabilized ylides.¹³⁹ Although the reported methodology is stoichiometric, previous work by Seki and co-workers have reported a catalytic methodology giving moderate enantioselectivities in which the sulfur ylides are generated in situ from diazoacetamide with catalytic chiral binaphthylsulfide and copper(II) acetylacetonone.¹⁴⁰ In both methodologies, the reaction is found to afford exclusively the *trans* epoxide. In order to better understand this reactivity, they have done crossover experiments and found that in contrast to the phenyl stabilized ylides, the addition of amide stabilized ylides is reversible in both *syn* and *anti* pathways. They have then used calculations to determine if the origin of this reversibility is due to change in the barrier for rotation or cyclization. The calculations

were done at the B3LYP/6-311+G(d, p)//B3LYP/6-31G(d) level including a continuum description of ethanol as the solvent. The energy profile is shown in Figure 64.

With these ylides, the elimination step, leading to the formation of the epoxides, was found to be the rate limiting step. The elimination leading to the *trans* epoxide is favored, as the elimination leading to the *cis* product exhibit repulsive interactions between the phenyl ring and amide group. These results are in accord with the crossover experiments. This difference in energetics can be attributed to the greater stabilization of the ylide afforded by the amide group, in comparison to the poorer phenyl.

Aggarwal has also reported a theoretical study discussing the importance of the leaving group ability in the reaction. Various ammonium, oxonium, phosphonium and sulfonium ylides were studied.¹⁴¹ Studies of epoxidations using ammonium show that high barriers to ring closure are due to the poor leaving group ability of the amine.¹⁴²

The theoretical work of Aggarwal focused on the understanding of the reactivity and diastereoselectivity, but studies of enantioselectivities are comparatively rare. Goodman and coworkers have recently reported a computational study¹⁴³ regarding the enantioselectivity in the epoxidation reaction catalyzed by the sulfides **35**, developed by Metzner and coworkers,¹⁴⁴ and **36**, by the Goodman group (Scheme 92).¹⁴⁵

Calculations with B3LYP/6-31G(d) first explored the initial ylide conformations. While both sulfides give good enantioselectivities, there was little conformational preference. The transition states of the addition step of the ylides to the aldehyde adopt a cisoid (*gauche*) conformation, similar to the lowest energy addition transition states found by Aggarwal (Figure 65).

For sulfide **36**, the computed enantio- and diastereoselectivities from the relative energies of the four possible addition TSs correlate well with experiment. However, for sulfide **35**, they found that the enantioselectivity is controlled by the addition step, but the diastereoselectivities are controlled by the cyclization, as shown by Aggarwal. The cyclization step for the *trans* diastereomer for the reaction with catalyst **35** is indeed lower in energy by 1–6 kcal/mol, confirming that the enantioselectivity is controlled by the addition step for the *trans* epoxide. The detailed origin of the enantioselectivities observed was not reported.

3.5.2. Cyclopropanation—In relation to the ylide based organocatalytic epoxide synthesis, a homologous variant leading to polysubstituted cyclopropanes has been developed by Tang and Dai (Scheme 93).¹⁴⁶ Of particular interest is the access of both enantiomer of the product through the use of *endo* or *exo* camphor based sulfides.

The reaction works under catalytic conditions and leads to good yields and enantioselectivities, with both *endo* and *exo* sulfides leading to the enantiomeric antipodes. Interestingly, the free hydroxyl group on the chiral sulfide is necessary for reactivity – simple dialkylsulfides or the methoxy protected variant of the chiral sulfide did not yield any desired products (Scheme 94). In order to understand this particular reactivity and explain the relative and absolute stereoselectivity of the reaction, Wu and co-workers performed computational studies.

The calculations were done using B3LYP with either 6-31+G(d) or 6-31G(d) basis sets for the hydrogen, carbon and oxygen and LANL2DZ(ECP) for sulfur and silicon. Single point solvation corrections were done using the IEFPCM model(THF). The model system is shown in Scheme 95. For the *exo*-ylide, methyl acrylate was studied ($R_1 = H$), and methyl cinnamate ($R_1 = Ph$) was used for the *endo*-ylide.

The TSs of the addition step for the *exo*-ylide and methyl acrylate are shown in Figure 66. The addition step is found to be the rate- and stereodetermining step, as the cyclization is extremely facile. The chiral sulfide hydroxyl group directs the methyl acrylate in an *s-cis* conformation by H-bonding.

The two transition structures (**TS8** and **TS9**) leading to the wrong diastereomer are both in an eclipsed conformation around the forming C-C bond. An almost staggered conformation is found in the most stable transition structures (**TS6** and **TS7**), leading to the major products. However, in the structure leading to the minor enantiomer, a steric interaction is found between the *cis* hydrogen of C3 and the hydrogens of the chiral ylide. The authors also explain the greater stability of **TS6** by solvation effects. **TS6** has the largest surface area, and is more prone to experiencing greater solvation effects.

The calculations predict a diastereoselectivity of 99:1 in favor of the *anti* product in 93% *ee*, which is in good agreement with experiment (>99:1 *anti:syn*, 95% *ee*).

The transition structures of the addition step of *endo*-ylide with methyl cinnamate are shown in Figure 67; they show similarities to the addition transition structures found for the *exo*-ylide.

Again, a strong H-bond with the ylide hydroxyl group orients the electrophile, in this case methyl cinnamate. A staggered conformation is found in **TS10** and **TS11**, while an almost eclipsed conformation is found for the transition structures (**TS12** and **TS13**), leading to the wrong diastereomer. A strong steric contact is observed in the transition structures (**TS10** and **TS12**), leading to the minor enantiomer. The computed energies favor the *anti* product by 98:2 in 93 % *ee*, which is in good agreement with experiment (>99:1 *anti:syn*, 74% *ee*).

3.5.3. Aziridination—A related reaction to sulfur ylide mediated epoxidations and cyclopropanations is the synthesis of aziridines from the reaction of sulfur ylides with imines (Scheme 96). As in epoxidations and cyclopropanations, the reaction starts with the addition of the ylide to the imine to form both *anti* and *syn* betaines. The *transoid* betaine conformers then undergo a ring closure to give the *trans* and *cis* aziridines, respectively.

Robiette has investigated this reaction involving semi-stabilized (R = Ph) and stabilized (R = CO₂Me) sulfur ylides using the B3LYP/6-31G(d) methodology.¹⁴⁷ The optimizations were performed in a continuum solvent with a dielectric constant of 37.5 D and a solvent probe radius of 2.179 Å to represent acetonitrile, one of the common solvents used in these reactions. Energies were obtained from single point calculations at the B3LYP/6-311+G(d, p)(CH₃CN) level. In the case of semi-stabilized ylides, the betaine formation is found to be irreversible. The steric strain induced by the *N*-sulfonyl group in the addition transition state determines the stereochemical outcome of the reaction. The *transoid* approach is favored in the case of *syn* betaine formation, and the *cisoid* mode of addition for the *anti* transition state (Figure 68). The observed low *trans* selectivity is explained by the stabilizing Coulombic interactions and stabilization by favorable C-H...O interactions in the *cisoid anti* addition transition state. In the case of stabilized ylides, the addition and rotation steps are reversible, and ring closure is found to be the rate- and selectivity-determining step. The computed energies of *syn* and *anti* ring-closure transition structures (16.1 and 16.5 kcal/mol relative to the separated reactants) predict a low selectivity in favor of the *cis* aziridine formation. Similarly, the observed low *cis* selectivity is accounted for by the steric strain in the elimination generated by the formation of the *cis* aziridine as compared to the *trans* aziridine.

Sunoj and co-workers have also studied the reaction between substituted ylides and an aldimine bearing a CO₂Me group on the nitrogen atom using the B3LYP/6-31G(d) level of theory with the polarizable continuum model (SCRF-PCM).¹⁴⁸ The single-point energies were calculated using the 6-311G(d, p) basis set in acetonitrile continuum. They found that the stabilized (R = COMe) and semistabilized (R = Ph) ylides all follow a *cisoid* addition path leading to *trans* aziridines via *anti* betaine intermediates. Sunoj and Robiette agree on the more pronounced steric effects than electronic factors in favoring *cisoid* and *transoid* addition modes, and the rate- and selectivity-determining step is the addition for semistabilized ylides and elimination for stabilized ylides.

Janardanan and Sunoj later reported a density functional theory investigation of the factors controlling enantio- and diastereoselectivities in asymmetric aziridination reactions by the addition of chiral bicyclic sulfur ylides to substituted aldimines (97).¹⁴⁹ The B3LYP/6-311G(d, p)(acetonitrile)//B3LYP/6-31G(d) calculations were used to construct the energy profiles given in Figure 69. In the case of stabilized ylides, although the enantioselectivity is determined in the addition step, the energetics of the diastereoselectivity-determining elimination step affects the predicted %ee values (Figure 69). A cumulative effect of electronic and steric interactions in the diastereomeric transition states (Figure 70) controls the stereochemical outcome of the reaction.

The nature of the N-protecting group on aldimines (CO₂Me and SO₂Me) is found to play an important role for the diastereoselectivities (Figure 69, a vs. b). The reversal of diastereoselectivity is explained by the differences in steric interactions of the N-protecting group. The orientation of SO₂Me oxygens in **Y1-TSelim-RS** shows an unfavorable interaction with the COMe oxygen (Figure 70a), whereas in the case of CO₂Me substituted imine (Figure 70b, **Y2-TSelim-RS**), this repulsion is minimized due to the planar geometry around the carbonyl carbon.

3.6. Phosphines

3.6.1. Hydroalkoxylation of methyl vinyl ketone—Phosphines are found to be efficient catalysts for the hydroalkoxylation of α - β unsaturated ketones (Scheme 98).¹⁵⁰ This allows ready access to β -hydroxy ketones, and provides a useful alternative to the typical aldol or sequential epoxidation/reduction of enones.

Interestingly, little retro-aldol or ketalization products are produced in the phosphine catalyzed hydroxylation reaction, whereas these are common side products in the analogous base (hydroxide) catalyzed systems. Li and co-workers investigated these interesting reactivity differences and studied the addition of methanol to methyl vinyl ketone catalyzed by trimethylphosphine with MP2.¹⁵¹ Geometry optimizations were done using the 6-31+G(d) basis set, and energies were computed using the 6-311+G(2df,2p) basis set. In order to account for solvation, the geometry optimizations were done using CPCM and UAHF radii.

The reaction is stepwise. The first step is the formation of the base (or nucleophile), and the second stage is the actual hydroalkoxylation step (Scheme 99).

In the first step, phosphine facilitates the formation of the methoxide anion by either pathway 1a or pathway 1b. In the former process, the proton transfer from MeOH to intermediate **37** is found to be the rate determining step with an activation energy of 26.6 kcal/mol. Calculations show that the direct deprotonation is disfavored by 15.7 kcal/mol.

The hydroalkoxylation can proceed through the base-catalyzed mechanism (pathway 2a) or a direct S_N2 mechanism (pathway 2b). The base catalyzed mechanism is favored over the

S_N2 mechanism by 29.2 kcal/mol. The most difficult step in the reaction was the proton transfer from MeOH to **38** with a barrier of 18.1 kcal/mol. They conclude that the use of polar solvents is key in this reaction as this stabilizes the catalytically important methoxide anion.

3.6.2. Allenolate additions—Phosphine catalyzed [3 + 2] and [2 + 2 + 2] annulations of allenolates and various electrophiles have been developed recently.¹⁵² While these reactions are closely related, contrasting regioselectivities were observed depending on the nature of the electrophilic partner. The mechanisms are shown in Scheme 100.

Dudding and co-workers investigated the regioselectivities observed in the annulation process with methyl acrylate, *N*-Tosyl benzaldimine, and benzaldehyde using B3LYP/6-31G(d).¹⁵³ Trimethylphosphine was used as a model for the tri-*N*-butylphosphine. CPCM solvation corrections for benzene were computed.

The cycloadditions for all substrates are stepwise; concerted [3 + 2] cyclization transition structures are not found. The initial C-C bond formation is rate limiting, and these are shown in Figure 71. The computed 95:5 product ratio in favor of the α addition is in agreement with experiment.

The difference in energy between the two transition structures can be summarized by the following: First, a stronger $\delta^+P \cdots O^{\delta-}$ electrostatic interaction is found in the transition state leading to the α addition (TS α). The phosphorous oxygen distance is shorter in the α addition (3.31 Å) compared to the γ (3.44 Å). Second, shorter and more symmetric hydrogen bonds are observed for the α addition. Finally, the gauche conformation around the forming C-C bond in the α addition is found to minimize more ideally the steric interactions (44°) compared to the γ addition (27°).

The transition state leading the α addition product is quite similar to the structure observed for the addition to methyl acrylate (Figure 72). A strong $\delta^+P \cdots O^{\delta-}$ electrostatic interaction (3.35 Å) and two stabilizing hydrogen bonds (2.16 Å and 2.58 Å) are found. A gauche conformation around the C-C forming bond (58°), minimizing steric interactions is also observed. Moreover, an anomeric effect involving the donation of the imine lone pair to the S-O σ^* enhances the $\delta^+P \cdots O^{\delta-}$ electrostatic interaction.

On the other hand, the transition state leading to the γ addition product exhibits a weaker $\delta^+P \cdots O^{\delta-}$ electrostatic interaction (3.77 Å). The free energy difference of 1.2 kcal/mol between these structures corresponds to a α : γ ratio of 86:14, which is consistent with experiment.

Lastly, the transition structures found for the additions to benzaldehyde are shown in Figure 73. In this case, the γ addition is favored by 3.6 kcal/mol (CHCl₃), leading to a ratio of 99.8:0.2, in accord with experiment. Interestingly a stronger $\delta^+P \cdots O^{\delta-}$ electrostatic interaction is observed for the α addition (2.60 Å vs. 3.11 Å) as well as relatively similar hydrogen bonds in both transition structures. However, an important difference arises in the dihedral angle around the forming bond. A staggered gauche conformation is found for the more stable α addition, whereas an almost eclipsed conformation is found for the γ addition, leading to greater steric interactions. This can also be observed by the comparison of the forming C-C bond lengths, being noticeably longer for the γ addition.

The full mechanism of the PMe₃-catalyzed [3+2] cycloaddition of 2,3-butadienoate and methyl acrylate was investigated both by the Kwon and Dudding and by the Yu groups (Scheme 101).¹⁵⁴ Kwon used B3LYP/6-31G(d) with CPCM single point corrections (benzene) to account for solvation energies, while Yu used B3LYP/6-31+G(d) with the same

solvent correction method. Kwon concluded that the first C-C bond formation step (**TS-CC1**) is the rate-determining step, with $\Delta G_{\text{act}} = 17.9$ kcal/mol, while Yu concluded that either addition of the catalyst to the allenolate (**TS-add1**) or **TS-CC1** is the rate-determining step, depending on the phosphine. Both Kwon and Yu agree that intramolecular proton transfer from the α - to β -carbon of the allenolate is unfeasible under the reaction conditions (calculated $\Delta G_{\text{act}} = 37.6$ kcal/mol and 39.6 kcal/mol, respectively). Rather, water assists the [1,2] migration by a protonation-deprotonation mechanism (**TS-prot** and **TS-deprot**). Yu and co-workers used isotopic labeling experiments in combination with DFT calculations to confirm the catalytic role of water.¹⁵⁵ The barriers for water catalyzed [1,2]-hydrogen shift were computed to be significantly lower, approximately 8 kcal/mol.

Yu calculated the mechanism for formation of a 1,3-dipole generated by PMe_3 and alkynoate (Scheme 102). Without water assistance, the [1,3]-proton shift of the catalyst-alkynoate zwitterion intermediate has a calculated activation free energy barrier of 52.8 kcal/mol (**TS-1,3**). A water-assisted protonation-deprotonation mechanism occurs with a significantly lower barrier of 26.7 kcal/mol (**TS-deprot**; **TS-prot** could not be located and was presumed to be nearly barrierless).

Yu and co-workers have observed an unexpected [3+2] cycloadduct in the reaction of 2-methyl-2,3-butadienoate with dimethyl fumarate under the co-catalysis of phosphine and water (Scheme 103).¹⁵⁶ The 2-methylallenolate is thought to act as a three-carbon synthon generated through a [1,4]-proton shift process to yield the unexpected product. Geometry optimizations and single-point CPCM solvation corrections at the B3LYP/6-31+G(d) level located a highly energy-demanding intramolecular [1,4]-proton transfer transition state with an activation enthalpy of 40.8 kcal/mol. The water-catalyzed [1,4]-hydrogen shift is found to be much easier, requiring only 23.9 kcal/mol activation enthalpy (Scheme 104). These results revealed a reasonably low energy pathway for the formation of the unexpected product.

3.6.3. Morita-Baylis-Hillman reaction—The Morita-Baylis-Hillman (MBH) reaction has been a well-known carbon-carbon bond-forming reaction for nearly 40 years,¹⁵⁷ yet computational studies of the reaction have only appeared in the literature in the last 4 years. One of the earliest computational reports, by Xu, investigated the PMe_3 -catalyzed reaction of acrylonitrile and ethanal using B3LYP/6-311+G(d) using Tomasi's IEF-PCM solvent model for CH_2Cl_2 .¹⁵⁸ The calculated mechanism and relative free energies are shown in Scheme 105.

In agreement with experimental studies, the rate-determining step was predicted to be proton transfer from the carbon α to the cyano group of the catalyst-alkene-aldehyde adduct to the alkoxide (**zwitter-II** to **zwitter-III** via **TS-H⁺**). However this barrier is extremely high (63.2 kcal/mol) and involves a four-membered transition state (Figure 74).

3.7. Other Amine Catalysts

3.7.1. Morita-Baylis-Hillman reaction—One year after Xu's publication of phosphine-catalyzed MBH reactions, Aggarwal and Harvey reported a DFT study of the reaction catalyzed by tertiary amines.¹⁵⁹ Kinetic data support mechanism in which the rate-determining step involves proton transfer from the α -carbon,¹⁶⁰ addition of the aldehyde, which had been proposed earlier.¹⁶¹ Autocatalysis in the absence of protic solvents and rate acceleration in the presence of protic solvents had also been observed. The nature of the rate-determining step, the mechanism of proton transfer in protic and aprotic solvents, and the origin of rate enhancement in the presence of alcohols were the focus of Aggarwal and Harvey's study. The B3LYP/6-311+G(d, p) (THF)//B3LYP/6-31+G(d) (THF) lowest energy pathways shown in Scheme 106.

Both in the presence and absence of methanol, the rate-determining step is intramolecular proton transfer from the α -carbon to an alkoxide (**TS-H⁺**). For the non-alcohol pathway, the aldehyde adds twice to form hemiacetal intermediate **hemi-I**, from which proton transfer occurs via a six-membered transition state. For the alcohol catalyzed pathway, proton transfer occurs via a six-membered transition state with assistance from the alcohol. The intramolecular proton transfer via a four-membered transition state was calculated to be significantly higher in energy, 46.6 kcal/mol. All three transition structures are shown in Figure 75. These results are consistent with experimental observations and kinetic isotope effect studies.

Similar to Aggarwal and Harvey, He and co-workers calculated the MBH reaction of acrolein and formaldehyde catalyzed by NMe₃ using B3LYP/6-311++G(d, p).¹⁶² Results of gas phase and CPCM (MeOH) calculations show that the intramolecular proton transfer is the rate-determining step, with activation energies of 45.8 and 35.1 kcal/mol, respectively, with respect to separated reactants. The calculated energies with one explicit methanol molecule is shown in Scheme 107. He found that explicit solvation with methanol significantly reduces the energies of zwitterionic intermediates and lowers the barrier for proton transfer (**TS-H⁺**), causing to the C-C bond forming step (**TS-ald**) to be rate-determining. These results appear to contradict Harvey and Aggarwal's results, but the former authors noted that reactive aldehydes should have lower barriers for C-C bond formation (without effecting the proton transfer barrier), resulting in a change in the rate-determining step.

In the same year that Aggarwal and Harvey's report was published, Sunoj reported a mPW1K/6-31+G(d) study of the MBH reaction of methyl vinyl ketone and benzaldehyde catalyzed by diazabicyclo[2.2.2]octane (DABCO).¹⁶³ Single-point energy calculations using the IEF-PCM model (DMSO) were applied. In agreement with Aggarwal and Harvey, Sunoj concluded that the rate-determining step of the reaction involves proton transfer from the zwitterion intermediate generated upon C-C bond formation. While this proton transfer was proposed to occur via a four membered transition state with $\Delta G^\ddagger = 70.0$ kcal/mol (Figure 76), the authors did note that calculations on a model reaction between acrolein, formaldehyde, and NMe₃ with explicit water molecules significantly reduces the barrier to 39.1 kcal/mol.

Most recently, Sunoj showed that the inclusion of two explicit co-catalyst molecules—including water, methanol, and formic acid—significantly lowers the activation energy for the C-C bond formation and proton transfer steps.¹⁶⁴ Stabilization of the proton transfer is more effective than stabilization of the C-C bond formation. This difference is even more pronounced in the aza-MBH reaction compared to the MBH reaction.

3.7.2. 3-Alkynoate isomerization to chiral allenates—The Brønsted base catalyzed 1,3-proton shift is a useful deprotonation-reprotonation reaction the preparation of allenes from alkynes.¹⁶⁵ Prior to a report by Huang and Tan,¹⁶⁶ only one asymmetric isomerization, catalyzed by a cinchona alkaloid derivative, had been reported.¹⁶⁷ Propyne is ~2 kcal/mol more stable than propa-1,2-diene; thus at equilibrium the isomerization yields depend on the relative stabilities of the alkyne and allene. Huang and Tan used a guanidine organocatalyst to effect the isomerization of 3-alkynoates to chiral allenates in good yields and enantioselectivities (Scheme 108).

The relative stabilities of four alkyne/allene pairs were calculated using B3LYP/6-31G(d, p). A comparison of the calculated and experimental results is shown in Table 7. The calculated relative stabilities qualitatively correlate with the experimental results. The thiophen-2-yl alkynoate, which gives the lowest allenate isomerization yield (39%), shows the smallest

energy difference between the two isomers (3.0 kcal/mol). The *N*-phthalamido alkynoate, which gives the highest isomerization yield (94%), shows the highest energy difference between the two isomers (6.0 kcal/mol). No discussion of the enantioselectivity was given.

3.7.3. Knoevenagel condensation—The condensation of aldehydes and activated methylenic groups, also known as the Knoevenagel condensation, was studied by Corma and co-workers (Scheme 109).¹⁶⁸ Proton affinities of seven amine catalysts were computed using B3LYP/6-31G(d, p) in order to attempt a correlation between catalyst basicity and reaction rates. The experimental turnover frequencies (TOF) and calculated proton affinities (energy difference between protonated and unprotonated species) are shown in Table 8.

Not surprisingly, the addition of methyl groups to parent **39** results in an increase in proton affinity (compare **39** with **40** and **41**). Catalyst **43**, which differs from **40** by an additional methylene bridge, has a higher proton affinity than **40**. This difference is rationalized by a geometry that allows better interaction with both nitrogens and the proton in **43** (1.06 Å and 1.93 Å) compared to **40** (1.02 Å and 2.52 Å).

A reasonable correlation between proton affinity and catalyst activity could be made for catalysts **40**, **39**, **42**, and **45**. However, **41**, which has a similar proton affinity as **40** (251.5 versus 250.9), has a lower TOF. Catalysts **43** and **44**, which have significantly higher proton affinities compared to **40**, also react with a lower TOF. The low activity of **41** might be explained by steric hindrance of proton abstraction by the four methyl groups. The low activity of **44** and **43** might also be due to steric factors, but another possible explanation is that the high proton affinities of these catalysts cause the protonation of the alkoxy intermediate to be disfavored (**TS-prot**, Scheme 110). The activation energies for each step in Scheme 110 for catalysts **40** and **44** were computed with HF/3-21G in order to clarify the cause of poor reactivity. The results are shown in Table 9.

Despite the high proton affinity of **44**, the activation energy for deprotonation of ethyl cyanoacetoacetate is high (22.4 kcal/mol). This high barrier can be explained by steric hindrance by the methyl groups. While the barrier for protonation of the oxyanion intermediate by DMPMH⁺ is barrierless, the corresponding barrier with **44**-H⁺ is 4.1 kcal/mol. This difference can again be explained by steric interference by the methyl groups of **44**. In conclusion, both proton affinity and the steric ability to abstract protons contribute to the high reactivity of diamine catalysts.

4. Lewis/Brønsted acid/hydrogen bond catalysis

Organocatalysts may not accelerate reactions to the large extent that metal catalysts do, but they are attractive alternatives due to their environmentally benign nature, effectiveness in water, and general lack of product inhibition. Lewis (hydrogen-bonding) and Brønsted (proton-transfer) acid organocatalysts explored to date involve (thio)ureas, diols, phosphoric acids, oxazaborolidines, guanidinium/amidinium ions, and bispidine.

4.1 Urea and thiourea-based organocatalysis

The co-crystallization of *N*, *N'*-diarylureas with acetone was observed as early as 1976.¹⁶⁹ Over one decade later, Etter and co-workers co-crystallized diarylureas with substrates bearing a variety of Lewis basic functional groups, including ketones, ethers, sulfoxides, triphenylphosphine oxides, and nitroaromatics.¹⁷⁰ The ability of a single urea molecule to bind substrates by double H-bonding has led to many uses in organocatalysis.

4.1.1. Diels-Alder cycloaddition—One of the earliest theoretical studies of thioureas involves Diels-Alder cycloadditions. Schreiner used DFT to explain the experimental

stereoselectivity in the *N, N'*-bis[3-(trifluoromethyl)phenyl]thiourea-catalyzed cycloaddition of *N*-acyloxazolidinone with cyclopentadiene (Scheme 111).¹⁷¹

Model calculations (B3LYP/6-311+G(d, p)//B3LYP/cc-pVTZ on C, H, O, and N; B3LYP/6-311+G(d, p)//B3LYP/3-21G(d) on S) show that the most favored binding mode of the catalyst involves a *syn* relationship between the carbonyl groups, even though the *anti* geometry is preferred for the ground state conformation of the uncomplexed species (Figure 77). The efficiency of the catalyst was attributed to hydrogen bonding with both carbonyl oxygens of the substrate.

A study of the catalysis of the cycloaddition between methyl vinyl ketone and cyclopentadiene by *N, N'*-bis[3,5-(trifluoromethyl)phenyl]thiourea and by water reveals that thioureas are effective catalysts even in the presence of water (Table 10).¹⁷² Gas phase calculations show that the thiourea reduces the activation barrier with respect to the uncatalyzed reaction by 2 kcal/mol, which correlates with the observed 9-fold rate acceleration. Catalysis by two explicit water molecules is less effective, reducing the barrier by only 0.5 kcal/mol.

Fu explored the same reaction with geometry optimizations at the DFT, rather than semi-empirical, level of theory (Table 11).¹⁷³ In all cases, the *endo* transition state with the *s-cis* conformation of the dienophile is most stable. It had already been observed that the transition states of the uncatalyzed cycloaddition between methyl vinyl ketone and dienes are concerted, but asynchronous.^{174,175,176,177} This asynchronicity is enhanced in the thiourea-catalyzed transition states, and is even greater in the case of BF₃. Similarly, thiourea decreases the barrier by 3.2 kcal/mol, while BF₃ barriers are decreased by 11.2 kcal/mol. An increased charge transfer between the diene HOMO and dienophile LUMO explains both the increased asynchronicity and the decreased reaction barriers.

Brinck used B3LYP and B2PLYP to study diene and dienophile substituent effects on the thiourea-catalyzed Diels-Alder reaction (Scheme 112).¹⁷⁸ A synergistic effect between the substituents and catalyst was found, resulting in overall reduced activation barriers of up to 6 kcal/mol. The substituent-mediated reactions display more asynchronous transition structures than the unsubstituted reactions, which led to the investigation of a stepwise Michael-type mechanism. While the Michael product is 23 kcal/mol less stable than the Diels-Alder product, the small difference between the Michael addition and concerted Diels-Alder transition structures (1.3 kcal/mol) suggests that a stepwise mechanism might compete with the concerted.

4.1.2. Claisen rearrangement—The catalysis of Claisen rearrangements of allyl vinyl ethers by water¹⁷⁹ or thiourea¹⁸⁰ has been known for over a decade, but a computational investigation of the thiourea-catalyzed reaction was only recently reported by Strassner and co-workers (Scheme 113).¹⁸¹

Computational analysis of the uncatalyzed rearrangement shows that the lowest energy pathway proceeds through an *s-cis* geometry of the ester carbonyl (Scheme 114). The barriers for the catalyzed (3,3)-rearrangement steps with respect to the catalyst-substrate complexes are reduced by 4.0 kcal/mol for the *s-trans* conformation and increased by 0.2 kcal/mol *s-cis* conformation (Scheme 115). The doubly hydrogen-bonded *s-trans* transition state is more stable than singly hydrogen-bonded *s-cis* transition state, making the *trans* pathway more favorable, and offering only a 3.1 kcal/mol free energy activation barrier reduction over the uncatalyzed reaction. It is likely that substantially greater charge transfer in the transition state will be required for acceleration by hydrogen-bonding catalysts to be effective.

4.1.3. Strecker reaction—The thiourea-catalyzed asymmetric hydrocyanation of imines (Strecker reaction) reported by Jacobsen is highly enantioselective and has a significant substrate scope.^{182,183,184,185} In a preliminary study Jacobsen reported that the urea functionality is responsible for catalysis and that the imine favorably binds with the urea hydrogens in the ground state (Figure 78).¹⁸⁶

More recently, a detailed kinetic and computational investigation by the same group showed instead that the catalyst promotes the reaction by generating an iminium/cyanide ion pair.¹⁸⁷ The rate-determining step involves rearrangement of the catalyst-iminium-cyanide complex prior to addition of the cyanide to the iminium. The enantioselectivity is attributed to a larger stabilization of the iminium in the transition structure leading to the major (*R*) enantiomer (Figure 79).

4.1.4. Nucleophilic oxirane opening—Schreiner envisioned that diarylthioureas could mimic biological epoxide hydrolases in detoxifying living cells (Scheme 116).¹⁸⁸ The authors were pleased to find that when methyl oxirane was reacted with a range of nucleophiles and 10 mol% *N, N'*-bis[3,5-(trifluoromethyl)phenyl]thiourea in both CH₂Cl₂ and water, the aqueous reactions were accelerated as large as 200-fold and in excellent yields (Table 12).

The thiourea-catalyzed and uncatalyzed reactions of ethylene oxide and NH₃ in water, CH₂Cl₂, and in the gas phase were studied at the DFT level. Of the possible hydrogen bonding interactions between the reactants (Scheme 117), the binding of a single water molecule with thiourea (binding energy = 6.0 kcal/mol) is more favorable than its interaction with oxirane or another water molecule (binding energies = 2.8 and 1.1 kcal/mol, respectively). However, thiourea binds with oxirane (binding energy = 7.0 kcal/mol) even more strongly than it does with water.

As the H-bonding ability of the solvent increases (gas phase → DCM → water, Table 13), the transition states become earlier and less asynchronous. The activation barriers decrease in the same order. These calculations show that the significant rate acceleration of nucleophilic oxirane opening is due to a strong and preferential catalyst-oxirane interaction, which is enhanced in water relative to weaker solvating systems.

Connon and co-workers proposed that *N*-tosyl-*N'*-aryl-(thio)ureas should be more effective hydrogen bonding catalysts than their diaryl-(thio)urea counterparts due to their higher acidities.¹⁸⁹ The calculated interaction energies of phenyl oxirane with these catalysts show that binding of the proposed catalysts is indeed more favorable than the diarylthiourea (Scheme 118).

The favorable binding energies led to a survey of the catalyzed addition of 1,2-dimethylindole to phenyloxirane (Table 14). The designed catalyst proved to be remarkably effective, catalyzing the reaction where all tested (thio)urea catalysts failed (entries 2–4), and showing higher activity than a tosyl sulfonamide organocatalyst (entry 5).

4.1.5. Tetrahydropyranilation—Schreiner presented the first acid-free organocatalytic tetrahydropyran (THP) protection of alcohols (Scheme 119).¹⁹⁰ The mechanism of this remarkably efficient reaction (turnover numbers of 100,000 at 0.001 mol% catalyst loading) was elucidated using DFT and coupled cluster computations.

The pre-organization of reactants is favored for the catalyzed reaction compared to the uncatalyzed reaction by nearly 15 kcal/mol (Figure 80). The activation for the uncatalyzed reaction is prohibitively high, in agreement with experiment. The thiourea catalyst

remarkably lowers the activation barrier. The computed transition structure of the catalyzed reaction also shows that the catalyst is positioned away from the alcohol R group, explaining the ease of protecting even bulky tertiary alcohols.

4.1.6. Pictet-Spengler-type cyclization—In 2007 Jacobsen reported the highly effective use of thiourea catalysis in the asymmetric Pictet-Spengler-type cyclization of β -indolyl ethyl hydroxylactams (Scheme 120).¹⁹¹ Possible mechanisms are shown in Scheme 121. The enhanced reactivity of alkylated lactams ($R = CH_3$) versus saturated lactams ($R = H$) led to the proposal that an S_N2 -type reaction is not operative. The authors proposed that the catalyst promotes cyclization by abstracting a chloride in an S_N1 -type rate-determining step. Subsequent addition of the indole to the N -acyliminium ion (S_N1 -type A) or via a spiroindoline intermediate followed by alkyl migration (S_N1 -type B) would afford the final product. Enantioinduction would be established by the closely associated catalyst-chloride complex.

To gain further support of the proposed mechanism, B3LYP/6-31G(d) was used to optimize three ground state structures: (1) catalyst-ionized hydroxylactam, (2) catalyst-chlorolactam via carbonyl, and (3) catalyst-chlorolactam via chloride (Figure 81). All attempts to locate a complex in which the thiourea is bound to the carbonyl of the ionized lactam (#1) failed to converge. While the catalyst can bind to the carbonyl of the chlorinated lactam (#2), this leads to an unproductive mechanism. Finally, a complex in which the thiourea binds to the chloride of the hydroxylactam (#3) was located. In a recent work, Danishefsky was able to isolate the azaspiroindolenine intermediate of the Pictet-Spengler reaction.¹⁹²

4.2 Diols

TADDOLs have been used as metal chiral auxiliaries and stoichiometric enantiodifferentiating reagents for over a century.¹⁹³ Rawal's discovery of the acceleration of hetero-Diels-Alder cycloaddition reactions by TADDOLs stimulated their uses as organocatalysts in recent years.^{194,195}

4.2.1 TADDOL-catalyzed Diels-Alder cycloaddition—Wu and co-workers employed QM/MM methods to analyze the cycloaddition of Danishefsky's diene with benzaldehyde (Scheme 122).¹⁹⁶ Danishefsky's diene was modeled by 1,3-dimethoxy-1,3-butadiene.

Various H-bonding interactions between TADDOL and benzaldehyde were investigated (Figure 82). Of these binding modes, the *trans* complex was established as the mode of catalysis.

The transition structures of the uncatalyzed reaction ($\Delta E^\ddagger = 20.2$, Figure 83) shows that the cycloaddition is concerted but asynchronous; the *endo* mode of attack is preferred; the nucleophilic terminus of the diene attacks the carbonyl carbon.

The computed transition structures of the catalyzed reaction with all three catalysts explain the experimentally observed enantioselectivities. The 1-naphthyl substituted catalyst, which experimentally gives the highest yield and *ee*, was calculated to give the lowest activation barrier of the three catalysts—6.0 and 2.5 kcal/mol lower than the lowest energy transition structures for the phenyl and 2-naphthyl substituted catalysts, respectively. The 1-naphthyl substituted catalyst was also calculated to promote the largest selectivity for the *si*-face attack and most effectively enhance the *endo* versus *exo* selectivity with respect to the uncatalyzed reaction. The lowest energy transition structure for the cycloaddition by the 1-naphthyl substituted catalysts is shown in Figure 84.

The stabilization of the Diels-Alder transition state by the catalysts is attributed to a significant charge transfer from the donor diene to the dienophile-catalyst acceptor complexes (0.47–0.49e). The transition states bear zwitterionic character, and the H-bond to the carbonyl oxygen stabilizes the developing negative charge.

The quadrant diagram shown in Figure 85 explains the energetic preference for the *si*-face approach. The aromatic moieties of TADDOL protrude “out” in quadrants II and IV (gray). A *si*-approach would place the reactants in unhindered quadrants I and III, while a *re*-approach would place the reactants in hindered quadrants II and IV. The 1-naphthyl moieties of the most efficient catalyst would protrude more than the phenyl or 2-naphthyl groups of the other catalysts, causing an increased barrier for the *re*-approach for the 1-naphthyl catalyst, and explaining the larger observed enantioselectivity.

One year later Houk and co-workers reported a fully quantum mechanical study of two TADDOL-catalyzed hetero-Diels-Alder cycloaddition reactions involving Rawal-type dienes (Scheme 123).¹⁹⁷ The catalyst was initially modeled by 1,4-butanediol and was predicted to bind most favorably in a cooperative binding mode (Figure 86). Gómez-Bengoa also studied the binding modes of double hydrogen bond donors at the B3LYP and MP2/6-311++G(d, p) levels and found that the cooperative binding mode is favored for the Diels-Alder reaction.¹⁹⁸ Both reactions were found to be *endo*-selective. The catalyst efficiency is attributed to a charge stabilization of the zwitterionic transition state by the hydrogen bonds.

The Houk group then reported the use of ONIOM (B3LYP/6-31G(d):AM1) calculations to explain the origin of enantioselection in the reaction of 1-dimethylamino-3-*tert*-butyldimethylsiloxy butadiene and benzaldehyde.¹⁹⁹ The two lowest energy transition structures for *si*-face (favored) and *re*-face (disfavored) are given in (Figure 87). Both structures show *endo* selectivity and are highly asynchronous. The *re*-face transition structure shows that the hydrogen atoms of the naphthyl groups are within van der Waals radius of the diene moiety. The *si*-face attack does not suffer these repulsions, and furthermore, benefits from CH- π stabilization between the aldehyde CH and a pseudo-equatorial naphthyl ring. The calculated 1.5 kcal/mol difference between these two transition structures corresponds to an *S*:*R* product ratio of 97:3 at -40°C , which is in good agreement with the experimentally observed ratio of 99:1. To account for dispersion interactions, single point energy calculations were performed on the ONIOM geometries. MPWB1K/6-31G(d) and M06-2X/6-31+G(d) results show a 2.4 and 3.4 kcal/mol selectivity, respectively, for the *si*-face transition state, overestimating the selectivity substantially.

4.2.2 Biphenylene diol-catalyzed oxirane opening—Lewis acid catalysis by 1,8-biphenylene diol was first discovered by Hine and co-workers in the opening of phenyl glycidyl ether by diethylamine.²⁰⁰ Soon after, Maruoka and co-workers employed the same type of catalyst to promote carbonyl reductions, the Mukaiyama aldol reaction, Michael addition of silyl ketene acetals to α , β -unsaturated ketones, and the Claisen rearrangement.²⁰¹ Several years later Kelly furthered the scope of catalysis by applying it to the Diels-Alder cycloaddition.²⁰²

Fujimoto investigated the nucleophilic ring-opening of oxirane by ammonia, catalyzed by 1,8-biphenylene diol and various monodentate acids (Table 15).²⁰³ Calculations at both the B3LYP/6-31G(d) and MP2/6-311++G(d, p) levels confirm that the bidentate diol catalyzes the nucleophilic ring-opening more effectively than the monoacids by over 5 kcal/mol (Figure 88). A computational molecular orbital analysis showed that the H-bonded catalyst promotes charge transfer from the oxirane to the catalyst, thereby enhancing its electrophilicity and decreasing electronic repulsion with the attacking nucleophile.

4.2.3 Fluorination—Pliego envisioned the design of an organocatalyst that would accelerate S_N2 reactions more effectively than polar aprotic solvents do.²⁰⁴ A thorough research of potential catalyst structures suggested 1,4-benzenedimethanol as the most promising catalyst. The binding mode is shown in Scheme 124.

MP2/6-31+G(d)//HF/6-31G(d) calculations of the uncatalyzed reactions of ethyl chloride and acetate in DMSO reveal S_N2 and E2 free energy barriers of 26.1 kcal/mol and 31.9 kcal/mol, respectively, which means the E2 reaction does not compete with the S_N2 reaction. The 1,4-benzenedimethanol catalyst decreases these barriers by 4.3 kcal/mol and 3.5 kcal/mol, respectively.

It was calculated that the same catalyst could enhance the S_N2 reaction of fluoride ion with 2-chlorobutane.²⁰⁵ Experimentally these two reactants lead to 90% elimination and only 10% S_N2 product. The calculated free energy barriers of the uncatalyzed reaction in DMSO are nearly identical for all four reactions (Scheme 125). Calculations of the catalyzed reaction show that the elimination process barrier is reduced by 1.8–3.1 kcal/mol and the S_N2 by 3.7 kcal/mol. Figure 89 shows that the $\text{OH}\cdots\text{F}$ distance in the S_N2 transition structure is at least 0.1 Å shorter than that of the E2 transition structures. These reduced activation barriers predict a 100 fold increase in the total reaction rate ($S_N2 + \text{E2}$) and a change in the S_N2 :E2 product ratio from 10:90 to 40:60.

4.3 Phosphoric acid catalysis

Like TADDOL, the role of BINOL as a hydrogen-bond donor catalyst was not discovered until recent years when Schaus and co-workers discovered its catalytic power in the Morita-Baylis-Hillman reaction.^{206,207} The phosphoric acid analog was then demonstrated by the Terada and Akiyama groups to catalyze Mannich-type reactions.²⁰⁸ These successes launched the use of dialkylphosphoric acid organocatalysts in a large array of asymmetric reactions.²⁰⁹

4.3.1 Mannich Reaction—Two nearly-simultaneous computational investigations of the BINOL-based phosphoric acid catalyzed Mannich reaction were reported in 2007.^{210,211} In the first report, Terada and co-workers used DFT to explain the mechanism and stereoselectivity of the addition of acetylacetone to aldimines (Scheme 126).

Preliminary computational analysis had shown that the catalyst-imine complex is controlled by the bulky X substituents of phosphoric acid. Four different adducts which place the imine groups away from these bulky groups two—with the *trans* imine and two with the *cis* imine—were envisioned and investigated (Figure 90).

Attempts to locate hydrogen-bonded complex *cis*-2 were unsuccessful, presumably due to unfavorable interactions between the Boc group and phosphoric acid oxygens. Of the other three optimized structures, *trans*-1 is more stable than *trans*-2 and *cis*-1 by 0.8 and 6.9 kcal/mol, respectively. The imine carbon in complexes in *trans*-2 and *cis*-1 is completely shielded by either of the aromatic X groups. The same carbon in *trans*-1 is exposed to stereospecific attack. It was hypothesized that if *trans*-1 could freely rotate around the N-H bond, the observed enantioselectivity would presumably be destroyed. Indeed, experimental replacement of the Boc group with a benzyl and methyl ester resulted in significantly lower enantioselectivities of 26% and 6%, respectively, supporting the mechanism of the Mannich reaction via complex *trans*-1.

Yamanaka and co-workers reported experimental and theoretical investigation of an analogous chiral Brønsted acid catalyzed Mannich-type reaction of silyl enolates with aldimines (Table 16).

BH and HLYP/6-31G(d) model calculations show that the reaction occurs by a dicoordination pathway (Scheme 127). The reaction was found to be a Brønsted acid-catalyzed process in which the rate-determining proton transfer from phosphate to the imine occurs prior to nucleophilic addition.

The *re*-face and *si*-face attacks were modeled to explain the origin of enantioselectivity (Figure 91). In agreement with experiment, *re*-face attack (TS-*re*) is 5.7 kcal/mol more stable than *si*-face attack (TS-*si*). TS-*re* possesses an aromatic stacking interaction between the catalyst and iminium *N*-aryl group, which fixes the iminium geometry for attack by the nucleophile. The magnitude of the aromatic stabilization depends on the substitution, which explains why the 4-nitrophenyl substituent enhances reaction rates and selectivities. TS-*si* is disfavored due to a steric hindrance between the 4-nitrophenyl group of the catalyst and either the trimethylsilyl group of the nucleophile or the aromatic group of the aldimine electrophile.

4.3.2. Acid-catalyzed 1,3-Dipolar cycloadditions—Gong and co-workers synthesized spiro[pyrrolidin-3,3'-oxindole] derivatives in high enantiopurity via a 1,3-dipolar cycloaddition of methyleneindolines with azomethine ylides formed from aldehydes and amino esters in the presence of chiral phosphoric acids (Scheme 128).²¹³

B3LYP/6-31G(d) calculations were performed to explain the high regio- and stereoselectivity. The lowest energy transition structure (Figure 92) corresponds to the experimentally obtained major regio- and stereoisomer. Both the methyleneindoline and the azomethine ylide are hydrogen-bonded to the catalyst. The transition structure that gives the minor enantiomer is 1.5 kcal/mol higher in energy and does not benefit from hydrogen bond stabilization to the same extent; the P=O...HN distance is 4.75 Å. The stability of the major transition structure compared to the transition structure that gives the minor regioisomer is attributed to a favorable π - π interaction between the oxo-indole ring and the conjugated esters in the former transition structure. The distance between these moieties is only ~3.0 Å.

4.3.3. Biginelli reactions—The same group synthesized dihydropyrimidinethiones in excellent enantioselectivities via Biginelli and Biginelli-type reactions catalyzed by phosphoric acid organocatalysts (Scheme 129).²¹⁴ ONIOM calculations were used to explain the stereo- and regioselectivity of the reaction. First, the imine resulting from condensation of the aldehyde and thiourea was calculated to favor the *E* geometry by 6.2 kcal/mol, arising from steric repulsion between the sulfur atom and phenyl ring. Two activation modes were then considered (Scheme 130): (1) activation of the imine by the phosphoric acid OH to generate a zwitterionic iminium salt, and stabilization of the enol proton by the oxygen of the OH group, and (2) activation of the imine by the phosphoric acid proton to generate a zwitterionic iminium salt, and stabilization of the enol proton by the oxygen of the P=O group. All possible modes of attack for both pathways were calculated.

The lowest energy transition structure follows mechanism B and involves attack of the *Re*-face of the imine by the *Si*-face of the enol (TS-(*S*)). This leads to the experimentally observed major (*S*) product. In contrast, the lowest energy transition structure that gives the minor (*R*) enantiomer (TS(*R*)) was calculated to occur via mechanism A. The hydrogen bond distances between the enol and phosphoric acid in TS-(*R*) are shorter than those of TS-(*S*) and is believed to account for the 1.1 kcal/mol difference between these two enantiomeric transition structures.

4.3.4. Reductive aminations—The Goodman²¹⁵ and Himo²¹⁶ groups independently reported theoretical studies on chiral phosphoric acid-catalyzed imine reductions by

Hantzsch ester. Goodman used ONIOM(B3LYP/6-31G(d):UFF) followed by single point calculations (MPWB1K/6-31G(d, p), PCM solvation model for toluene) to investigate the mechanism and stereoselectivity of the reaction. Of the possible mechanisms, protonation of the imine by the phosphate OH and stabilization of the Hantzsch ester NH by the phosphate oxygen was calculated to be favored significantly (Scheme 131).

In the case of Rueping's catalyst ($\text{Ar}^2 = 3,5\text{-}(\text{CF}_3)_2\text{-Ph}$),²¹⁷ the transition structures favor the *Z* geometry of the imine, even though the ground state *E* conformation was calculated to be favored over the *Z* by 2.9 kcal. The lowest energy transition structure gives the experimentally observed *R*-product and is 1.1 kcal/mol lower in energy than the lowest energy transition structure that gives the *S*-product. This difference is attributed to a destabilizing interaction between a CF_3 group of the catalyst and the aromatic group on the imine nitrogen ($\text{Ar}^1 = \text{Ph}$) in the minor *S*-transition structure. For MacMillan's catalyst ($\text{Ar}^2 = \text{SiPh}_3$)²¹⁸, the lowest energy transition structure that gives the favored *R*-product also bears the *Z* conformation. Unlike Rueping's catalyst, the lowest energy transition structure that gives the minor *S*-product is in the *E* conformation. This minor transition structure was calculated to be 2.7 kcal/mol higher in energy than the major *R*-transition structure. Although no explanation for the stereoselectivity was given for the stabilization of the *E* transition structure, a general model that explains the stereoselectivity of the *Z* transition structures was given (Figure 93).

Himo used B3LYP/6-311+G(2d,2p) to explain the kinetic resolution of α -branched imines (Scheme 132). For $\text{R}_L = \text{Ph}$ and $\text{R}_S = \text{Me}$, the *Z* imine was calculated to be 3.7 kcal/mol higher in energy than the *E* imine. Eight transition structures—*Re*- and *Si*-face hydride attack of both the *E* and *Z* isomers of each imine diastereomer—were considered. The naphthyl groups were modeled by phenyl groups; the carboxyethyl groups of the Hantzsch ester were modeled by carboxymethyl groups; $\text{Ar}^2 = 2,4,6\text{-trimethylphenyl}$.

Unlike Goodman's results, the lowest energy transition structures leading to the major *S*-product and minor *R*-product arise from the *E* imine. This difference is not surprising, considering that different imines—conjugated aromatic and aliphatic branched—were studied by both groups. The lowest energy transition structures are shown in Figure 94. In the major (*S*) transition structure, R_L ($\text{R}_L = \text{Ph}$) points away from the phosphate, minimizing steric interactions with the mesityl group of the catalyst. The *para*-methoxyphenyl group on the imine nitrogen is parallel with one ester group of the Hantzsch ester (at approximately 3.5 Å) and one *ortho*-proton of the protecting group has a weak stabilizing interaction with a phosphate oxygen (2.27 Å). The 1.8 kcal/mol destabilization of the minor (*R*) transition structure is attributed to steric clashing between the *para*-methoxyphenyl group and a mesityl group on the catalyst (shortest H–H distance is 2.27 Å).

Goodman recently studied the Friedel-Crafts reactions of indole with *N*-acyl and *N*-tosylimines catalyzed by BINOL-phosphoric acid derivatives and discussed in detail the energy dependence of the *Z/E*-imine conformations in the transition state on the nitrogen substituent.²¹⁹ *N*-phenyl ketimines prefer a *Z*-conformation in the transition state, whereas, *N*-benzyl aldimines adopt an *E*-conformation. The highest preference for the *E*-imine is calculated for *N*-acylimines.

4.3.5. Hydrophosphonylation—Shi and co-workers used ONIOM(B3LYP/6-31G(d):AM1) to investigate the hydrophosphonylation reaction of imines (Scheme 133).²²⁰ A reaction screening showed that other aromatic groups on the catalyst— $\text{Ar} = 4\text{-NO}_2$ or $4\text{-CF}_3\text{C}_6\text{H}_4$ —cause both the reaction yield and enantioselectivity to drop. It was also found that changing the phosphonate from an ethyl ester to an isopropyl ester causes the

enantioselectivity to increase from 43% to 52%. Finally, a benzothiazole protecting group causes an almost complete loss of stereoselectivity.

Unlike the results of the Akiyama study, the mono-coordination pathway was calculated to be higher in energy than the di-coordination pathway. The calculated mechanism shown in Scheme 134. All energies are with respect to separated reactants. The rate-determining transition structures involve addition of the phosphonate to protonated imines (*R*)-int and (*S*)-int. The 5.2 kcal/mol stability of the (*R*)-TS compared to the (*S*)-TS is overestimated, but gives a qualitative picture of the origin of enantioselectivity. The difference is mainly attributed to steric interference between a mesityl group of the catalyst and the *para*-methoxyphenyl group in the (*S*)-TS, which causes the *para*-methoxyphenyl group to distort from planarity (Figure 95). In agreement with experimental trends, the effect of changing the diethyl phosphite to diisopropyl phosphite resulted in a calculated 6.8 kcal/mol difference between the major and minor rate-determining transition structures.

The rate-determining transition structures for the benzothiazole-protected imine were also calculated. In excellent agreement with the experimental results, the major *R*-TS was calculated to be only 0.1 kcal/mol more stable than the minor *S*-TS. There is no significant difference in the geometries of the enantiomeric transition structures, and the disfavored interactions between the 3,3'-substituents of the catalyst and *para*-methoxyphenyl group of the transition structures in Figure 95 do not exist in the benzothiazole transition structures (Figure 96).

4.4 Oxazaborolidines

Although it could be argued that boron-containing molecules are not organocatalysts, oxazaborolidines have had significant impact on asymmetric synthesis as chiral Lewis-acid catalysts and the origins of stereoselectivities has received ample attention from computational chemists as discussed in this section. Oxazaborolidines, also known as CBS (Corey-Bakshi-Shibata) catalysts, were discovered to reduce carbonyl compounds with excellent enantioselectivities one decade ago.^{221,222} Derivatives of this catalyst, including recent applications of the protonated salt, have been employed in catalytic enantioselective alkynylations,²²³ Diels-Alder reactions,^{224,225,226} cyanosilylation of aldehydes,²²⁷ Michael additions,²²⁸ and vinylogous Mukaiyama aldol reactions.²²⁹

4.4.1. Carbonyl reductions—Between 1991 and 1996 Nevalainen provided a series of *ab initio* studies that confirmed Corey's mechanistic theories of oxazaborolidine-catalyzed carbonyl reductions (Scheme 135). A computational explanation was given for the experimental formation of oxazaborolidine aggregates²³⁰ and the role of Lewis basic solvents in reducing the aggregation.²³¹ The favored coordination mode of BH₃ to the catalyst²³² as well as the proper ketone-oxazaborolidine complex geometry²³³ were also elucidated.

Li and co-workers provided a more recent series of theoretical investigations on the chiral oxazaborolidine²³⁴ and sulfur-containing chiral oxazaborolidine²³⁵ catalyzed reduction of carbonyl compounds at the HF/6-31G(d) level. The same group also used HF/6-31G(d) and B3LYP/6-31G(d) to investigate the enantioselective reduction of keto oxime ethers (3-cyclohexene-1,2-dione-1-oxime).²³⁶ Despite these successful investigations, transition structures explaining the observed enantioselectivities were not calculated. Numerous semiempirical studies have addressed this issue.²³⁷ This review focuses on high level DFT investigations which explain the general origin of enantioselectivity of these reductions.²³⁸

General Mechanism: Consistent with Corey's observations and earlier calculations, Alagona found that the *cis* oxazaborolidine-borane-THF complexation is exothermic ($\Delta G =$

-1.9 kcal/mol). The *trans* coordination is disfavored because of the highly strained pyrrolidine ring conformation ($\Delta G = +9.9$ kcal/mol, Figure 97). The geometry of the *cis* adduct closely resembles that of the crystal structure obtained by Corey.²³⁹ Coordination of BH_3 to the catalyst shifts electron density from nitrogen to the exocyclic boron, enhancing the nucleophilicity of the hydrides, and increasing the Lewis acidity of the endocyclic boron.

The ketone binds the *cis* catalyst- BH_3 complex from the less hindered convex face. Only two of four possible coordination geometries converged to a local minimum at the B3LYP/6-31G(d) level, each leading to opposite faces of hydride transfer (Figure 98). The *si* face attack is the preferred mode of hydride transfer because the transition state has a chairlike conformation, whereas the transition state of the *re* face attack adopts a boatlike conformation.

The Meyer group investigated the same catalyst in the reduction of 2',5'-dimethylphenyl isopropyl ketone.²⁴⁰ Experimental and calculated ^{13}C kinetic isotope effect measurements were in excellent agreement with each other and provide strong evidence that the rate-determining step is hydride transfer to the carbonyl carbon. The computed enantiomeric transition structures show that the gem-diphenyl groups on the catalyst have little effect on the placement of the R_L and R_S groups. Rather, the phenyl groups serve to constrain the conformation of the bicyclic catalyst and dictate the coordination of the ketone.

Tang and co-workers used B3LYP/6-31G(d, p) to explain the experimental selectivities obtained by a similar diamide catalyst (Scheme 136).²⁴¹ The reaction was found to proceed via four steps, with the rate-determining step being the transfer of hydrogen from the catalyst-ketone complex to acetophenone (Figure 99). In agreement with experimental results, the activation free energy for *re*-face attack was calculated to be favored over *si*-face attack by 1.2 kcal/mol. The difference is attributed to different amounts of repulsion between the ketone substituent that is closest to the catalyst and the catalyst substituents. The spatial structures of both transition structures show that the phenyl group of the *re*-face transition state is further away from the catalyst system than the methyl group of the *si*-face transition state.

4.4.2. Reduction of glycosyl α -ketoesters—Grison and co-workers obtained good experimental diastereoselectivities in the CBS-catalyzed reduction of glycosyl α -ketoesters (Table 17).²⁴² However, if one considers the glycosyl group as larger than the ester moiety, Corey's model predicts the opposite stereoselectivity than that which was obtained experimentally. Suspecting that the chiral centers of the glycosyl group may influence the asymmetric induction, Ruiz-Lopéz modeled the reaction at the B3LYP/6-31G(d) level to explain the origin of diastereoselectivity.²⁴³

Model calculations with various substitution patterns at C4 and C5 show that the C4 configuration determines the product configuration, and disubstitution at C5 enhances the stereoselectivity. Consistent with Alagona's calculations, the lowest energy pathway involves a *cis* coordination of the borane to the catalyst, binding of the carbonyl to the same face, and hydride transfer via the *si* face of the carbonyl carbon (Scheme 137).

Catalysis of the glycosyl α -ketoester reduction by an achiral oxazaborolidine was calculated in order to explain the influence of the sugar moieties on the asymmetric reduction (Scheme 138). Unlike the previous calculations, the lowest energy transition structures for each enantiomeric reduction proceeds via the *top* face of the catalyst. The authors suggest that unlike TS-*exo-anti* in Scheme 137 which is favored because R_L (CO_2Me) is *trans* to the B-Me group, the analogous TS-*exo-anti* for a sugar (Me is substituted by a sugar) is disfavored

because the dihedral around the adjacent carbonyls must distort from a planar conjugation to avert clashing between the ester and B- Me groups.

Further calculations of a mismatched chiral catalyst (which would favor the *S* product) and the α -ketoester (which favors the *R* product) show that induction by the catalyst dominates, yielding the *S* product, which is opposite to that which would have been predicted by Corey's model (Scheme 139).

4.4.3. Alkynylation—Li and co-workers performed a two-part DFT investigation on the oxazaborolidine catalyzed alkynylation of aldehydes (Scheme 140).^{244,245}

As in the carbonyl reductions, the aldehyde can potentially bind to the catalyst-alkynylborane adduct in four possible geometries—*exo-anti*, *exo-syn*, *endo-anti*, or *endo-syn*—leading to either the *R*- or *S*-alcohol product (Scheme 141). Binding of the aldehyde to the catalyst-alkynylborane complex is exothermic for three out of four complexes, with the *exo/anti* geometry being the most stable adduct. Mulliken charge measurements and an NBO analysis show charge transfer from the carbonyl to alkynyl moiety upon complexation. The lowest energy adduct, *exo-anti*, has the largest stabilization interaction energy among the four complexes (23.1 versus 13.6, 18.9, and 21.2 kcal/mol).

The alkyne transfer transition state was calculated to be that of the rate-determining step of the catalytic cycle. The *exo-anti* transition state is the lowest energy geometry for the alkyne transfer, forming a six-membered twist chair transition state (Figure 100). An NBO analysis of these transition structures showed that the breaking B-C bond is weakest and the forming C-C interaction is strongest in the *exo-anti* conformation compared to the other geometries, facilitating the transfer of the alkyne moiety the most in this transition state. The calculated activation energies for the *exo-syn*, *endo-anti*, and *endo-syn* are 11.4, 11.7, and 11.3 kcal/mol, respectively.

4.4.4. Diels-Alder cycloaddition—Li investigated the cationic oxazaborolidine catalyzed Diels-Alder reaction developed by Corey's group (Scheme 142).²⁴⁶ B3LYP/6-31G(d) was applied to all proline ring hydrogens. B3LYP/6-31G(d, p) was applied to all other atoms. Model calculations of both the uncatalyzed and catalyzed reactions (Scheme 143) show that the *exo/s-cis* pathway is preferred, yielding the *S* product. The authors concluded that the uncatalyzed reaction is concerted, but the catalyzed reaction is stepwise, with the rate-determining step being addition of the catalyst-methylacrolein complex to cyclopentadiene to form a zwitterionic intermediate.

More recently, Paddon-Row and co-workers investigated the same class of reactions in order to explain the origins of enantioselectivity proposed by Corey (Scheme 144).²⁴⁷ Key features of Corey's models include: (1) a preferred *s-trans* C=C-C=O conformation of the dienophile, (2) π stacking between the dienophile and the *exo*-phenyl group at C-5 of the catalyst, and (3) catalyst binding to the oxygen *anti* lone pair (with respect to the double bond) and formyl hydrogen in the case of aldehydes, versus catalyst binding to the *syn* oxygen lone pair and α -hydrogen of ketones, esters, and carboxylic acids. These different binding modes expose opposite faces of the dienophile and explain the opposite enantioselectivities observed experimentally.

MPW1K/6-31+G(d, p)//B3LYP/6-31G(d) calculations for seven catalyzed cycloadditions are in qualitative agreement with experimentally observed selectivities (Table 18) and agree with Corey's pre-transition state models. An alternative coordination mode for ester dienophiles that does not involve a CH \cdots O bond was found, which was calculated to be significantly favored over the Corey model (Figure 101). In the new model, binding of the

anti lone pair of the tethering carbonyl oxygen is predicted to be favored due to relief of repulsion interactions with the alkoxy oxygen center. Such a stabilization does not occur when the *syn* lone pair of the methyl ester carbonyl is bound to the catalyst.

The same group then reinvestigated the reaction computed by Li in order to determine if the aldehyde does indeed bind to the catalyst in an *s-cis* conformation, which is at odds with Corey's model.²⁴⁸ Two major changes were made in the latter investigation, the first being that the enantiomeric ratio was determined by the activation free energies of the cycloaddition, rather than on the stabilities of the catalyst-carbonyl complexes. This modification is valid because it had been shown that complexation is rapidly reversible on the NMR timescale.²⁴⁹ Second, it was argued that the model catalyst was oversimplified because π -stacking of one of the C-5 phenyl groups plays a role in the stereochemical outcome of the reaction. Thus, the experimental catalyst was employed in the calculations, with the only change being the replacement of the *o*-tolyl group with a phenyl group.

The reactions of five dienophiles with 1,3-butadiene were calculated using B3LYP/6-31G(d). All possible coordination modes and conformations were considered. As shown in Table 19, the predicted enantioselectivities are in excellent agreement with experimentally observed results. The poor selectivity predicted in entry 5 is attributed to the modeling of both the bulky 2-*tert*-butyl-1,4-benzoquinone and 2-triisopropylsilyloxy-1,3-butadiene with simpler 2-methyl-1,4-benzoquinone and 1,3-butadiene, respectively. In four out of five cases, the computational results reinforce Corey's model of stereoselectivity. It was also found that the minor enantiomer is largely formed through a coordination of the dienophile to the concave (*endo*) face of the catalyst, and thus catalyst designs that favor this mode of binding should enhance selectivities.

4.4.5. Diels-Alder cycloaddition catalyzed by *N*-sulfonylated oxazaborolidines

—Several groups have reported *ab initio* and DFT investigations^{250,251} of the coordination of aldehydes to model *N*-sulfonylated oxazaborolidines catalysts in the asymmetric Diels-Alder cycloaddition reactions of α , β -unsaturated aldehydes with simple dienes²⁵² and in Mukaiyama aldol reactions (Figure 102).^{253,254} It was consistently found that the two lowest-energy coordination modes involve a binding of the aldehyde to the “top” face of the catalyst.

Wong explored the full (*S*)-tryptophan-derived catalyst using DFT methods to explain the role of the tryptophan moiety of the reaction (Scheme 145).²⁵⁵

Corey had attributed the remarkable selectivities of the Diels-Alder cycloaddition to three stabilizing interactions (Scheme 146): (1) donor-acceptor interaction between the endocyclic boron of the catalyst and the carbonyl oxygen of acrolein, (2) H-bond between the formyl hydrogen of acrolein and the ring oxygen of the catalyst, and (3) π -stacking between the tryptophan and acrolein groups.

Wong proposed the same type of stabilizing interactions, but with modifications: the acrolein can adopt an *s-cis* or *s-trans* conformation, and the formyl hydrogen can bond with either the ring oxygen (as Corey had proposed) or a sulfonyl oxygen. This gives rise to four possible complexes. MP2/6-31G(d)//PW91PW91/6-31G(d)+ZPE calculations show that the most stable complex has an *s-trans* acrolein geometry, and the aldehyde hydrogen binds to the sulfonyl oxygen (Figure 103). The binding energy is 6.9 kcal/mol. The other complexes are at least 3.8 kcal/mol higher in energy. The acrolein and tryptophan moieties are separated by 3.15 Å, indicative of a π -stacking interaction. An NBO analysis showed a strong decrease of electron population in the indole moiety by 0.13–0.16 e, indicating that the indole group acts as a π donor.

Calculations show that the binding of *s-trans* bromoacrolein to a model catalyst is selective for the sulfonyl oxygen mode over the ring oxygen mode by 2.3 kcal/mol (Figure 104). A similar selectivity of 1.4 kcal/mol is predicted for *s-cis*-bromoacrolein. In addition, *s-trans*-bromoacrolein has a larger binding energy with indole than *s-cis*-bromoacrolein (Figure 105). Both the strong CH \cdots O=S interaction and *trans*-acrolein \cdots tryptophan π - π stacking interactions explain the excellent experimental enantioselectivities.

5. Bifunctional catalysis

5.1. Thioureas

5.1.1. Michael addition of ketones to nitroalkenes—Three groups have reported theoretical studies of thiourea-based asymmetric Michael addition reactions.²⁵⁶ The first report, by Tsogoeva and Schmatz, investigates a thiourea/cyclohexanediamine catalyst, in which the amine moiety enhances the nucleophilicity of the ketone by enamine formation, and the thiourea moiety enhances the electrophilicity of the nitro-olefin through hydrogen bonding (Scheme 147).²⁵⁷

While it had been proposed by Takemoto and accepted by most groups that both oxygens of the nitro moiety are involved in H-bonding with the thiourea (Figure 106),²⁵⁸ Tsogoeva and Schmatz found that the doubly bonded transition state is *less* stable than the singly bonded transition state by 1.3 kcal/mol at the B3LYP/6-31G+(d, p) level. Inclusion of zero-point and thermal corrections reverses this stability (the doubly bonded structure is 1.5 kcal/mol more stable), but it was reasoned that this structure cannot undergo Michael addition for steric reasons.

Transition state geometries and relative energies calculated by Tsogoeva and Schmatz are shown in Figure 107. DFT calculations at various basis sets show a preference for the *R* transition state, which leads to the formation of the major product. This is attributed to a tighter H-bonding interaction between the thiourea and nitro-olefin, as seen in the transition H-bond distances, and repulsive electrostatic interactions between the phenyl and oxygen in the minor *S* transition state.

5.1.2. Michael addition of 1,3-dicarbonyls to nitroalkenes—Pápai and co-workers pursued a DFT investigation of the organocatalyzed Michael addition of 1,3-dicarbonyls to nitroolefins (Scheme 148).^{256b}

Of the five lowest-energy catalyst conformations, only one conformation was found to favor a double H-bond coordination with either the nitro-olefin (proposed by Takemoto) or the dicarbonyl (Figure 108). The binding energies of the nitro-olefin (R^2 =Ph) and dicarbonyl (R^1 =Me) with the catalyst are 7.6 and 7.3 kcal/mol, respectively, implying no preference for formation of either complex. Both possible routes leading to the experimentally observed major *R* enantiomer were thus explored (Scheme 149).

The conjugate addition transition structures leading to the major *R* enantiomer for pathways (A) and (B) are given in Figure 109. The conjugate addition activation barrier (gas phase, B3LYP/6-311++G(d, p)) with respect to separated reactants for the catalyst-dicarbonyl complex pathway (B) was calculated to be only 2.2 kcal/mol, while the barrier for the catalyst-nitro-olefin complex pathway (A) was found to be 4.9 kcal/mol. In both pathways, transition structures leading to the minor *S* enantiomer is less stable than those of the *R* enantiomer (2.6 and 2.4 kcal/mol for the former and latter pathways, respectively). The instability of the *S* transition structure is due to eclipsing in the C-C forming bonds, unlike the *R* transition structures, in which the forming bonds are staggered.

Chen and co-workers investigated similar thiourea bifunctional catalysts that contain both a chiral center and chiral axis (Scheme 150).²⁵⁹ The bis-3,5-trifluoromethylphenyl group was replaced by hydrogen. A total of four pathways—both enantiomers of each catalyst—were calculated using B3LYP/6-311++G(d, p)//B3LYP/6-31G(d). The calculations show that the stereocenter is established at the C–C bond forming step, but subsequent proton transfer is the rate-determining step. The activation energies for these steps with respect to each catalyst-substrate complex are given in Table 20.

All of the calculated energies agree with experimental stereoselectivities. C–C bond formation (**TS-CC**) and proton transfer (**TS-PT**) by catalyst A favor the *S*-enantiomer over the *R*-enantiomer by 1.6 kcal/mol and 2.7 kcal/mol, respectively. Likewise, C–C bond formation and proton transfer by catalyst B favor the *R*-enantiomer over the *S*-enantiomer by 1.3 kcal/mol and 9.7 kcal/mol, respectively.

The enantioselectivities were rationalized by changes in the catalyst dihedral angles in going from the ground state to the transition states (Table 21). Dihedral angle N1–C2–N3–C4 of catalyst A, which favors the *S*-product, changes by 7° in the *S*-transition state, as opposed to 15° in the minor *R*-transition state. The same dihedral angle of catalyst B, which favors the *R*-product, changes by 14° in the *R*-transition state, as opposed to 21° in the minor *S*-transition state. The authors conclude that the enantioselectivity depends on a geometrical match or mismatch of the catalyst's axis of chirality with the center of chirality.

Zhong and co-workers recently developed a highly enantioselective domino Michael–Henry reaction catalyzed by a cinchona alkaloid derived thiourea catalyst to furnish highly functionalized bicyclo[3.2.1]octanes with four stereogenic centers (Scheme 151).²⁶⁰ The B3LYP/6-31G(d) calculations revealed a new catalytic activation mode for the thiourea catalyst (Figure 110). Unlike the previously proposed “dual activation model” by Takemoto,²⁵⁸ this mode shows activation of the 1,3-dicarbonyl substrates by the thiourea group and an acidic proton in the phenyl ring, and at the same time tertiary amine activation of the nitro group, which promotes the domino reaction with excellent stereoselectivity. The lowest energy transition structure, shown in Figure 110, favors the formation of the (*R*, *S*)-enantiomer compared to the (*S*, *R*)-enantiomer by 5.7 kcal/mol.

5.1.3 Michael addition of α -aryl and α -alkyl cyanoacetates to vinyl ketones—

Chen and co-workers explored the thiourea catalyzed Michael addition of α -aryl and α -alkyl cyanoacetates to vinyl ketones (Scheme 152).²⁶¹

The major *S* enantiomer is produced by a *re*-face attack of the *Z*-enolate of the cyanoacetate (Figure 111, top), while the undesired *R* enantiomer is produced by a *si*-face attack of the *E*-enolate of the cyanoacetate. (Figure 111, bottom). The *R* enantiomer is believed to be disfavored because of steric clashing between the vinyl ketone and cyanoacetate alkyl/aryl groups.

5.1.4. Michael addition of 1,3-dicarbonyls to azodicarboxylates (α -amination)

—Liu and co-workers investigated the enantioselective α -amination of 1,3-dicarbonyl compounds to azodicarboxylates catalyzed by a bifunctional urea (Scheme 153).²⁶²

All possible pathways—both *re*-face (major) and *si*-face (minor) attack of the dicarbonyl via (1) binding of the dicarbonyl to the urea moiety and the azodicarboxylate to the protonated tertiary amine, and (2) binding of the azodicarboxylate to the urea moiety and the dicarbonyl to the tertiary amine—were considered. The calculated lowest energy transition structures leading to both enantiomeric products are in qualitative with experimental results (Figure 112).²⁶³ The origin of enantioselection was not discussed.

Liu and co-workers used B3LYP/6-311++G(d, p)//B3LYP/6-31G(d) to explain the mechanism and stereoselectivity of α -amination reactions catalyzed by a urea-based bifunctional organocatalyst (Scheme 154).²⁶⁴ The dicarbonyl was modeled by 2-acetylcyclopentanone, the aromatic ring of the catalyst was replaced by hydrogen, and the *tert*-butyl carboxylates were replaced with methyl carboxylates. Two activation modes of the substrates were considered (Figure 113): in mechanism A, the urea moiety activates the dicarbonyl while the tertiary amine activates the azodicarboxylate; in mechanism B, the urea moiety activates the azodicarboxylate while the tertiary amine activates the dicarbonyl. Mechanism A is favored, with a rate-determining activation barrier of 2.7 kcal/mol. This step involves nucleophilic attack of the enolate to the azodicarboxylate. The corresponding activation barrier for mechanism B is 7.8 kcal/mol. An enantiomeric excess of >99% ee was calculated, which is in reasonable agreement with the experimental results.

5.1.5. Michael addition of amines to $\alpha\beta$ -unsaturated compounds—

Aminoindanol-derived thioureas are shown to catalyze the addition of hydroxylamines to pyrazole crotonate derivatives yielding β -aminoacids with high enantioselectivities.²⁶⁵ Simón and Goodman studied the mechanism of the reaction with quantum mechanical methods in order to elucidate the role of the catalyst.²⁶⁶ Geometry optimizations were performed with the B3LYP/6-31G(d, p) in toluene using the implicit PCM solvation model and UFF cavity scheme. Energies were further refined with single point energy calculations at the MPWB1K/6-31G(d, p) level with solvent included implicitly by PCM model and UAKS cavity definition. Two possible pathways were explored using a simplified model of the catalyst (Figure 114). Mechanism A explains the stereochemical outcome of the reaction as a consequence of a H-bond between the hydroxyl group of the chiral catalyst and the oxygen in the nucleophile (Figure 114a). In mechanism B, the catalyst takes active part in proton transfer by a proton switch mechanism (Figure 114b), rather than simply stabilizing the anions via a H-bond network.

The calculations with the model hydroxy-thiourea catalyst showed that the transition states corresponding to mechanism B are 3–4 kcal/mol lower in energy than the transition structures located for mechanism A. Hybrid QM/MM ONIOM calculations on mechanism B with the real catalyst resulted in 1.6 kcal/mol energy difference between the enantiomeric transition states favoring the (*S*) enantiomer, in agreement with the experiments.

5.1.6. Enolization—Computational methods were used to design a bifunctional thiourea catalyst that accelerates enolization in non-H-bonding organic solvents such as dichloromethane.²⁶⁷ The catalyst incorporates both a basic amine for deprotonation and hydrogen donors to stabilize the forming enolate. Based on HF/6-31+G(d) transition states of the urea and methanol catalyzed enolization, 3D structural databases were searched by the computer program CAVEAT. A cyclohexenone was identified as an appropriate linker between the urea and amine moieties (Scheme 156). After further design and functionalization, a linear thiourea/amine was synthesized and accelerated the enolization five-fold. This work demonstrates the promise of using computational methods as a foundation for catalyst design.

5.1.7. Alcoholysis of cyclic anhydrides—Chen reported highly enantioselective alcoholysis of *meso*-cyclic anhydrides by a bifunctional thiourea catalyst (Scheme 157).²⁶⁸ B3LYP/6-31G(d) calculations show that the transition state model leading to the major enantiomer (Figure 115) is 7.0 kcal/mol lower in energy than the complex leading to the minor isomer. The transition state is stabilized by hydrogen bonding interactions between a thiourea hydrogen and the developing alkoxide, and the amine with the adding alcohol.

5.1.8. Ring-opening polymerization—Zhang and co-workers investigated the ring-opening polymerization of D-lactide by a bifunctional thiourea organocatalyst (Scheme 158).²⁶⁹ Both a concerted and stepwise mechanism were calculated using B3LYP/6-311++G(d, p) (PCM, CH₂Cl₂)/B3LYP/6-31G(d) (Scheme 159). In both cases, the rate-determining step were calculated to be very high—at least 37 kcal/mol with respect to separated reactants—suggesting that the uncatalyzed reaction is energetically unfeasible.

The concerted and stepwise mechanisms of the catalyzed reaction were then calculated. Unlike the uncatalyzed reaction, the stepwise pathway is favored over the concerted, with transition state energies of 11.5 kcal/mol and 32.1 kcal/mol, respectively, with respect to separated reactants (25.8 kcal/mol and 46.4 kcal/mol, respectively, with respect to the catalyst-methanol-D-lactide complex). A sketch of the rate-determining transition structure for the stepwise mechanism is shown in Figure 116. The catalyst activates the lactide for ring-opening by three hydrogen bond interactions. A covalent binding mechanism involving acyl transfer to the catalyst was also calculated, but this pathway is higher in energy.

5.2 Guanidines

Guanidinium and amidinium cation catalysts have successfully promoted highly enantioselective C-C bond forming reactions, first pioneered by Corey in the Strecker reaction.²⁷⁰ Numerous applications have followed, including in catalysis of the Diels-Alder reaction,²⁷¹ (aza)-Henry reaction,^{272,273} amination of 1,3-dicarbonyl compounds,²⁷⁴ and ring-opening-metathesis polymerization.²⁷⁵

5.2.1. Strecker reaction—Han and co-workers used DFT (B3LYP/6-31G(d)) to investigate the mechanism of the bicyclic guanidine-catalyzed Strecker reaction (Scheme 160)²⁷⁶ because Corey had claimed that HCN does not react with *N*-benzhydrylbenzaldimine at 10°C and theoretical groups had confirmed a high energy barrier for this addition but a lower energy pathway for the HNC addition,^{277,278} Han modeled and proposed two possible reaction pathways: HCN isomerizes to HNC, which adds to methanimine to yield aminonitrile (Pathway A, Scheme 161), or HCN adds to methanimine to afford aminoisoacetoneitrile, which then isomerizes to aminonitrile (Pathway B).

The calculated free energy profile is shown in Figure 117. Pathway A (red) is lower in energy is lower in energy than pathway B (blue). Formation of aminoisoacetoneitrile **51** is predicted to be unfavorable. A high energy transition structure for the isomerization of intermediate **49b** to **49a** was located. These calculations suggest that the Strecker reaction most likely proceeds through hydrogen isocyanide.

5.2.2. Ring-opening polymerization—Rice and co-workers investigated two proposed mechanisms for the ring-opening polymerization of L-lactide using guanidine-based catalyst 1,5,7-triazabicyclo[4.4.0]dec-5-ene (TBD, Scheme 162).²⁷⁹ Their mechanism was based on earlier calculations performed by Goodman on the ring-opening polymerization of lactones in the presence of TBD.²⁸⁰ The first mechanism involves both nucleophilic ring-opening of the lactide and proton donation to the opened alkoxide by the catalyst (“dual lactide activation”/“nucleophilic catalytic mechanism”), while the second mechanism involves hydrogen bond activation of both the lactide and alcohol nucleophile by the catalyst (“Lactide and alcohol H-bond activation”/“acid-base catalytic mechanism”). Geometries were optimized using MPW1K/6-31G+(d) with the CPCM model (dichloromethane). Single point calculations were carried out with MPW1K/aug-ccpVTZ.

The reaction was initially modeled with guanidine as the catalyst. The first mechanism—ring-opening of the lactide prior to alcohol addition—was found to be significantly disfavored. The rate-determining step is the addition of the alcohol and the activation energy

is 18.6 kcal/mol with respect to separated reactants (19.9 kcal/mol with respect to complexed starting materials). The second mechanism proceeds via a significantly lower-energy pathway. The rate-determining step is the addition of the alcohol to the lactone, with a barrier of only 6.0 kcal/mol with respect to separated reactants (13.3 kcal/mol with respect to complexed starting materials).

Having established the preferred mechanism, the rate-determining step of the hydrogen-bonded pathway was recalculated with the full experimental catalyst (TBD). This change resulted in a nearly barrierless reaction, with an activation energy of 0.3 kcal/mol with respect to separated reactants (7.9 kcal/mol with respect to complexed starting materials). This rate-determining step is shown in Figure 118.

Similar to the results of Rice and co-workers in their earlier work on lactones, Simón and Goodman showed that the transition structures corresponding to acid-base catalytic pathway are energetically favored over the ones corresponding to the nucleophilic catalytic reaction by more than 7 kcal/mol in Gibbs free energy computed with B3LYP/6-311++G(d, p) (CH₂Cl₂)/B3LYP/6-31+G(d).²⁸⁰ However, a peculiar feature of the process is that the catalyst surprisingly failed to catalyze the ring-opening polymerization of the more reactive butyrolactone. Calculations showed that unlike the reactions of 5- and 6-ring lactones, Gibbs free energy barriers for nucleophilic addition of TBD to butyrolactone and methanol acid-base addition are within 1 kcal/mol, presumably due to the strain in the starting material favoring the former (Scheme 163). Nucleophilic addition of TBD to butyrolactone leads to the formation of a stable amide-like intermediate (1.3 kcal/mol), trapping the catalyst, as the energy barrier to form the product from this intermediate is very high (37.9 kcal/mol).

5.2.3. Michael addition of 1,3-dicarbonyls to nitroalkenes—The Nájera group reported good enantioselectivities for the conjugate addition of 1,3-dicarbonyls to nitroalkenes catalyzed by a *trans*-cyclohexanediamine-benzimidazole catalyst in the presence of TFA (Scheme 164).²⁸¹ Two coordination modes of the catalyst—(1) the di-coordinated dicarbonyl nucleophile (Figure 119, top), and (2) the di-coordinated nitroalkene electrophile (Figure 119, bottom)—were calculated. The mechanism involving the coordinated nucleophile was calculated to be favored, in agreement with the activation mode reported by Pápai and co-workers for the cyclohexanediamine-thiourea-catalyzed Michael addition reaction.^{256b} The approximately 3 kcal/mol difference between the major *R* and minor *S* transition structures agrees well with the experimental enantioselectivities.

5.2.4. Acetonitrile hydrolysis—1,5,7-Triazabicyclo[4.4.0]dec-5-ene (TBD) has been shown by Sun and co-workers to be an effective catalyst for the hydrolysis of acetonitrile (Scheme 165).²⁸² The full mechanism of the uncatalyzed and catalyzed reactions were carried out with B3LYP/6-311++G(d, p) and MP2/6-311++G(d, p).²⁸³ The rate-determining step of the uncatalyzed reaction is the first step—addition of water to acetonitrile (Scheme 166). This barrier is extremely high, 58.3 kcal/mol and 64.7 kcal/mol using B3LYP and MP2, respectively, as expected for such four-center transition states.

The catalyzed reaction was then calculated with B3LYP (Scheme 167). The activation energy for the first hydrolysis step (27.6 kcal/mol) is 30.7 kcal/mol lower in energy than that of the uncatalyzed reaction. Unlike the uncatalyzed reaction, the rate-determining step is the loss of ammonia after the second hydrolysis step (35.3 kcal/mol). This rate-limiting barrier is 23.0 kcal/mol lower in energy than the rate-limiting barrier of the catalyzed reaction. This difference would likely change if solvent effects were considered for these gas phase calculations. Nevertheless, the calculations show that TBD is effective in reducing the barrier for the hydrolysis reaction. The mechanism is similar to that of the TBD and methanol-catalyzed ring-opening polymerization (Scheme 162, bottom).

5.3. Proline Derivatives

5.3.1. Epoxidation—The asymmetric epoxidation of α , β -unsaturated ketones by *tert*-butyl hydroperoxide (TBHP) and β -amino alcohol catalysts have been studied by the Lattanzi and co-workers (Scheme 168).²⁸⁴ Catalyst screening and testing of reaction conditions led to the hypothesis that the catalyst plays a dual role in the reaction. The proposed mechanism is shown in Scheme 169. The catalyst deprotonates TBHP to form an ion pair, and the TBHP anion attacks the α , β -unsaturated ketone to generate an intermediate that is stabilized by the hydroxy group of the catalyst.

Two low-energy conformers were located for each cyclic catalyst—one in which the hydroxyl hydrogen is bonded to the *cis* hydrogen on the ammonium, and one in which the hydroxyl hydrogen is bonded to the *trans* hydrogen on the ammonium. In all three cases, the *cis* conformation is preferred, which the authors argue contributes to the experimentally observed enantioselectivities. The *cis* and *trans* conformers of the pyrrolidine catalyst are shown in Figure 120. The acyclic ammonium shows only a 0.6 kcal/mol energy difference for the two lowest energy conformers, which may explain the poor experimental selectivities.

In order to better understand the structure of the ion pair and explain the experimental enantioselectivities, the protonated proline, azetidine, piperidine, and 2-methylpropylamine catalysts (Table 22) were studied using density functional theory (B3LYP/6-31G(d)).

5.3.2. Transfer hydrogenation—Schreiner and co-workers used a proline-derived diamide catalyst to achieve moderate yields and enantioselectivities in the asymmetric transfer hydrogenation of ketimines with trichlorosilane (Scheme 170).²⁸⁵ B3PW91/cc-pVDZ was used to rationalize the mechanism and stereoselectivity. The aromatic groups of the ketimine were modeled by methyl groups, while the methyl group of the ketimine was modeled by a hydrogen. The adamantane group of the catalyst was replaced with hydrogen.

The calculated activation enthalpy of the uncatalyzed reaction involving a four-center transition state is very high, 40.0 kcal/mol (Figure 121, top), while the calculated activation enthalpy of the catalyzed reaction is 19.1 kcal/mol (Figure 121, bottom). The role of the catalyst is to coordinate the trichlorosilane and serve as a proton donor to the imine. The high free energy barriers (59.7 and 47.1 kcal/mol for the uncatalyzed and catalyzed reactions, respectively) suggest that alternate mechanisms should be explored.

5.4. Amine-amides

5.4.1. Aldol reaction—Recently Feng and co-workers introduced amino acids into the bispidine framework to catalyze the aldol and Michael addition reactions (Scheme 171).²⁸⁶ These reports represent the first effective use of bispidine as an organocatalytic core. The L-phenylalanine-derived bispidine catalyst proved to be extremely effective in catalyzing the aldol reaction between acetone and methylethylketone with α -ketophosphonates, α -ketoesters, and α , α -dialkoxyketones in up to 97% isolated yield and 97% ee. The size of the phosphonates and esters and electronic nature of the aromatic ketone has very little effect on yields and enantioselectivities.

The transition states for the aldol addition between methyl benzoylformate and acetone were modeled theoretically. In agreement with experiment, the transition structure leading to the major *R*-product was calculated to be nearly 4 kcal/mol lower in energy than that of the minor product (Figure 122). The origin of enantioselectivity is attributed to a preferential conformation in both the major and minor transition states in which the phenyl group of the catalyst shields the *si* face of the enamine. The favored transition state shows a shorter

distance between the protonated catalyst and the keto group compared to that of the disfavored transition state, indicating a stronger hydrogen bond interaction.

Feng and Hu achieved good yields and enantioselectivities in the secondary amine amide organocatalyzed asymmetric nitroaldol reaction of α -ketophosphonates (Scheme 172).²⁸⁷ The transition structures for the major (*R*) and minor (*S*) enantiomers were located using HF/3-21G(d) (Figure 123). A 3.7 kcal/mol energy difference was calculated for the two transition structures. The major transition structure benefits from stronger stabilizing hydrogen bond interactions compared to the minor transition structure. This is seen by a comparison of various hydrogen bond distances: the nitro group oxygens and piperidine hydrogen distances are 1.63 Å and 2.43 Å in the major transition state versus 1.67 Å and 2.77 Å in the minor transition state; and the carbonyl group of the ketophosphonate is separated from an amide hydrogen by 1.59 Å in the major transition state as opposed to 1.79 Å in the minor. However, the phosphonate oxygen of the minor transition state is significantly more stabilized compared to the major transition state, with O-H bond distances of 1.56 Å and 1.83 Å, respectively.

5.4.2. Michael addition of ketones to nitroalkenes—The L-4-fluorophenylglycine-derived bispidine catalyst was shown to be extremely effective for catalyzing the Michael addition of ketones to nitroolefins (Scheme 173).²⁸⁸ Electron-rich, electron-deficient, and fused aromatic rings have little effect on reactivity and selectivity.

The Michael addition of acetone to nitrostyrene catalyzed by L-phenylglycine derived bispidine was modeled computationally.²⁸⁸ For both the favored (*re*) and disfavored (*si*) faces of attack, two possible modes were considered (Figure 124). In mode A, TBBP participates in an intramolecular bond, freeing one hydroxyl group to protonate the catalyst, which activates the nitroalkene. In mode B, one hydrogen of TBBP protonates the catalyst, while the second hydrogen activates the nitroalkene. Mode A was calculated to be favored for the *re* and *si* transition structures by 4.7 and 4.3 kcal/mol, respectively.

The computational results show that *re*-face attack of the nitroolefin is favored by 2.2 kcal/mol (Figure 125). The selectivity is attributed to a stronger hydrogen bond between the protonated catalyst and nitroolefin in the favored transition structure, as indicated by the shorter distance.

5.5. Cinchona alkaloids

While cinchona alkaloids were described in Section 3.3, this current section focuses more specifically on cinchonas that appear to display a dual activating mode in organocatalysis.

5.5.1. Michael addition—The bifunctional cinchona catalyzed Michael addition of ketoesters and phenyl maleimide was studied by Cucinotta and Gervasio (Scheme 174).²⁸⁹ Molecular dynamics, ab initio methods, and quantum mechanical/molecular mechanic (QM/MM) approaches were used to investigate the mechanism. The catalytic cycle based on the calculations is shown in Scheme 175. Molecular dynamics and cluster analysis were used to locate the lowest energy binary (complex I) and ternary (complex II) complexes. Four ternary complexes were located that are within 2 kcal/mol of each other. These structures differ in the nature of the hydrogen bond interactions between the protonated quinuclidine, the catalyst hydroxyl group, and the ketoester anion. Activation energy calculations for C–C bond formation from each of these 4 complexes show that the complexation mode shown in Figure 126 is the most favored.

The transition structures for C–C bond formation were located using QM/MM (nudged elastic band technique, NEB). The most favored transition state shown in Figure 126 (left),

and gives the same major stereoisomer that was observed experimentally. The enolate is stabilized by the protonated quinuclidine, while the maleimide is stabilized by the hydroxyl group of the catalyst. A transition state that does not involve activation by the hydroxyl group was calculated to be nearly 10 kcal/mol higher in energy, which supports arguments for the bifunctional role of the catalyst. The rigid hydrogen bond network is responsible for the high diastereoselectivities.

Finally, B3LYP/6-311+G(d, p) calculations on a model system show that hydrogen bond donation to the maleimide significantly lowers the energy of the transition state for C-C bond formation (Figure 127).

5.5.2. Alcohol Desymmetrization—Chin and Song developed a sulfonamide-based cinchona alkaloid bifunctional catalyst to effect the desymmetrization of *meso*- anhydrides in excellent yields and enantioselectivities (Scheme 176).²⁹⁰ Analogs of the enantiomeric transition states for five experimental substrates were modeled using B3LYP/6-31G(d).²⁹¹ All calculations show a stabilization of the developing alkoxide by the sulfonamide hydrogen and the quinuclidine nitrogen acting as a general base in accepting the methanol hydrogen (Figure 128). While no explanation was given for the origin of stereoselectivity, the calculated relative energies of the enantiomers do agree with the experimental results.

5.5.3. [1,3]-rearrangements—Cinchona derivatives catalyze [1,3]-sigmatropic *O*- to *N*-rearrangements of allylic trichloroacetimidates to give the corresponding trichloroacetamides via a two-step S_N2' mechanism (Scheme 177).^{292,293} Houk and co-workers used M05-2X/6-31+G(d, p)(CPCM-toluene)//B3LYP/6-31G(d) calculations to show that the availability of H-bonding interaction between the catalyst and the substrate determines the fast reacting enantiomer and the stereochemical outcome of the reaction (Figure 129).²⁹³

5.6. Dipeptides

5.6.1. Hydrocyanation—In 1981, Inoue and co-workers reported the enantioselective hydrocyanation of aldehydes employing a cyclic dipeptide catalyst cyclo[(*R*)-His-(*R*)-Phe] or cyclo[(*S*)-His-(*S*)-Phe] (Scheme 178).²⁹⁴ This catalyst was designed to be a small molecule alternative to the enzyme hydroxynitrilase lyase (oxynitrilase) that catalyzes the identical reaction. Highest enantioselectivity is observed under heterogeneous (gel) reaction conditions. In methanol no enantioselectivity is observed. Furthermore, asymmetric autoinduction was reported.²⁹⁵

DFT and MP2 methods, molecular mechanics, and molecular dynamics were used to elucidate the mechanism and origin of stereoselectivity and autoinduction. The active catalytic species was shown to be a dimer, with activation by the imidazole rather than the dipeptide moiety. This is consistent with experiments in which second order rate dependence with respect to the catalyst concentration was found.²⁹⁶ Dynamic studies in the gas-phase and non-polar solvent show that the dimer is stable; in contrast, simulation in MeOH showed dissociation of the dimer, consistent with loss of stereoselectivity observed experimentally. The key step involves delivery of the nucleophile and stabilization of the developing negative charge by imidazole groups in the transition state (Figure 130). DFT and MP2 results suggest that extended edge-to-face π -interaction between the catalyst dimers and substrates are critical for catalysis and selectivities.

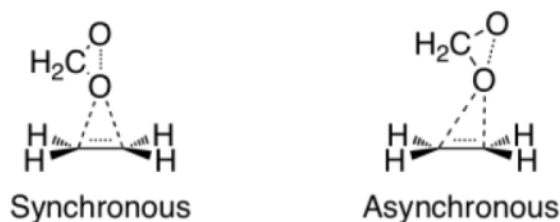
5.7. Brønsted Acids

5.7.1. Additions of phenols and protected amines to olefins—In 2006, He and co-workers demonstrated that trifluoromethanesulfonic acid (TfOH) can effectively catalyze

additions of phenols and amides to alkenes (Scheme 179), which complement the commonly applied methods involving transition-metal or main-group metal catalysts.²⁹⁷ Yu and co-workers used B3LYP/6-31G(d) calculations to gain insight into the mechanism of catalysis of these reactions.²⁹⁸ They found that TfOH activates the nucleophilic additions through a concerted but highly asynchronous eight-membered-ring transition state. The computed activation free energy for the addition of phenol to cyclohexene is 29.4 kcal/mol relative to the separated reactants. The methoxy substituent decreases this barrier to 27.3 kcal/mol, whereas the nitro substituent causes an increase in the activation free energy by 2.4 kcal/mol. The addition of tosylamide to cyclohexene is found to have a higher activation free energy compared to that of phenols (35.8). The authors also showed that the double-bond migration can compete with the addition reaction. The relative reactivities of the phenols towards addition determine the extent of these two competitive processes.

6. Epoxidation by Dioxiranes

The enantioselective direct oxidation of alkenes is a highly exploited method to access enantioenriched epoxides. The in situ formation of a chiral dioxirane from a ketone and Oxone (potassium peroxymonosulfate), which can then undertake the epoxidation of alkenes, is especially effective. The epoxidation mechanism involving dioxiranes has been studied numerous times computationally. To account for experimental results, a spiro transition state has been proposed. Earlier theoretical works on the epoxidation of alkenes by dioxirane have focused on simple models and have consistently supported the preference of a spiro transition state.²⁹⁹



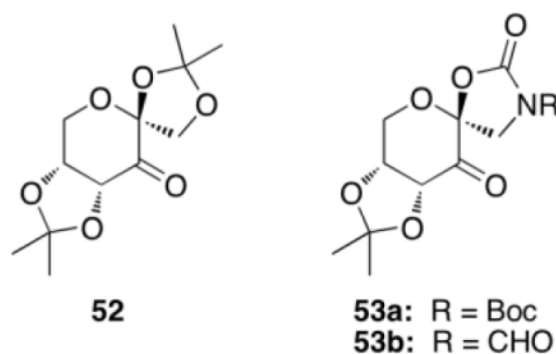
However, there has been some debate concerning the asynchronicity of epoxidation process, as different theoretical models have given different answer relating to the synchronicity of the reaction. MP2 and CASSCF calculations have favored highly asynchronous transition states, while B3LYP and several high-level ab initio have led to a more synchronous formation of the two C-O bonds. Bach and co-workers have concluded after a thorough study of the epoxidation of ethylene with dioxirane that the potential energy surface is very flat, and that the unsymmetrical transition state is slightly favored.^{299e}

Of particular interest here is the study concerning the stereoselectivity aspects of the epoxidation using dioxiranes. Houk and co-workers have studied computationally the stereoelectronic effects found in the alkene epoxidation using fluorinated dioxiranes.³⁰⁰ Using initially dioxirane derived from fluoroacetaldehyde, they found that the TS of epoxidation in which the fluoro substituent is *anti* to the dioxirane oxygen atom that is not transferred is the most favorable (Figure 132, **TS17**). This conformation minimizes electrostatic repulsion between the oxygen with the greater developing negative charge. A natural bond orbital analysis confirmed the electrostatic origin of this conformational preference, as there was no significant difference between bond orders for the forming and breaking bonds and the different TSs.

Both equatorial and axial oxygen transfer for the axial and equatorial fluoro substituents of 2-fluorocyclohexanone dioxirane were studied (Figure 133). **TS20** and **TS21** show both *syn*

and *anti* oxygen transfer using the axial-2-fluorocyclohexanone dioxirane. The large energy difference between **TS20** and **TS21** originates from a stabilization of **TS20** by 5.2 kcal/mol (compared to the cyclohexanone equivalent TS), due to the optimal position of the fluoro substituent *anti* to the oxygen, in order to minimize electrostatic interactions. Moreover, a weak F-H interaction is found in **TS20**. **TS22** and **TS23** are found to be both disfavored due to the electrostatic F-O repulsions. The axial-*anti* transfer (**TS21**) is found to be further disfavored due to the steric interactions between the alkene and the axial hydrogens of the cyclohexanone. The experimental results expressed in Scheme 180³⁰¹ could result from epoxidation with equatorial attack *syn* to the fluorine.

The methodology developed by Shi and co-workers is also of particular interest in the field of enantioselective epoxidation using chiral dioxiranes. Their systems rely on chiral ketones derived from fructose (**52** and **53**), which are transformed into their dioxirane homolog through reaction with Oxone. The chiral dioxiranes then proceed to stereoselectively oxidize the unsymmetrical alkene. The original catalyst **52** was found to be more effective with *trans*-disubstituted and tri-substituted alkenes, while the oxazolidinone **53a** has been found more recently to be effective with *cis*- and terminal alkenes.³⁰²



Singleton and co-workers have studied the process of enantioselection by Shi's catalysts computationally.³⁰³ They also measured experimental kinetic isotope effects (KIE) to compare with computed values for the different optimized transition structures. They initially calculated the epoxidation of *trans*- β -methylstyrene using a model dioxirane **A** and the dioxirane derived from catalyst **52**. Epoxidation using the unhindered reagent **54** led to what they considered the "natural" asynchronicity conformation TS (Figure 134).

Multiple TS conformations were found for the epoxidation using the chiral dioxirane derived from **52**, some selected conformations are illustrated in Figure 135. However, calculation of the KIEs of these TSs and comparison to the experimentally observed values points to **TS24** as the most realistic conformation. Interestingly, this conformation is found to be the most energetically favored and shows the most "natural" asynchronicity when compared with the transition structure found for **A**. The structure obtained is in accord with the model proposed by Shi. In contrast, **TS25** shows divergence from the optimal asynchronicity, and some steric interaction between the styrene methyl and the axial pyran hydrogen. Moreover, **TS26**, which lead to the minor enantiomer, is found to diverge widely from the ideal conformation, as it is not even truly in a spiro TS.

They then proceeded to study the epoxidation of styrene using the dioxirane derived from catalyst **53b**. In the case of styrene, four possible TSs are illustrated in Figure 136. The two lowest TSs leading to both enantiomers (**TS27** and **TS29**) are both found to position the phenyl of the styrene on the same side as the oxazolidinone. The asynchronicity of the reaction, favoring a longer C-O forming bond on the side of the phenyl, thus then minimizes

the interaction between the phenyl and oxazolidinone in **TS27** and **TS29**. In contrast, shorter C-O bond on the alkene terminal carbon causes repulsive interactions with the latter and the oxazolidinone in **TS28** and **TS30**. The calculated selectivity is in accord with the experimentally observed stereoselectivity.

They then computed the epoxidation of 1-phenyl-cyclohexene. This specific substrate is interesting due to the widely different selectivities observed depending on the catalyst used, as seen in Scheme 181. The authors did not report TSs using catalyst **52**, as they supposed that a conformation similar to **TS24** in Figure 135 would be greatly favored, and would explain the high selectivity. However, they reported the two lowest structures leading to both enantiomeric antipodes for the epoxidation using catalyst **53b** (Figure 137). The energy difference found correlates well with the low stereoselectivity observed.

They explain the small difference of energy between the two enantiomeric TSs by the fact that in **TS32**, the asynchronicity causes steric interactions of the alkene hydrogen with the oxazolidinone. Conversely, this asynchronicity minimizes the steric clash of the phenyl group in **TS31** with the same oxazolidinone. It is worth noting that the phenyl group is rotated away from conjugation in **TS31** by 28°, which seems to indicate that the conjugation of the phenyl group with the alkene is not important in order to stabilize the epoxidation process.

7. Conclusions and Outlook

The experimental study of organocatalysis has accelerated enormously since the writing of this review began, and the computational investigations of these reactions have increased in number and sophistication as well. As described in the introduction, B3LYP with modest basis sets continues to be used routinely for the study of organocatalysis, but deficiencies in this functional have been discovered. This is especially true for reaction thermochemistries and in cases where dispersion effects influence weak interactions between groups.⁶ Newer, more highly parameterized functionals such as Truhlar's M0X series, especially M06-2X, and now M08 for organic reactions, are being used routinely. More accurate, but also more expensive methods, like SCS-MP2 and double hybrid functionals like B2PLYP are being used with increasing frequency. The role of dispersion is likely to be important in controlling stereoselectivities of many reactions, and the addition of dispersion corrections to density functionals is now highly recommended.^{7e,o}

While it is important to use intrinsically accurate methods, solvation energies also have an important role for energetics and selectivities, especially due to the fact that organocatalysis is always performed in the condensed phase. CPCM, SMD, and other continuum-based models are continually being improved, but still may have appreciable errors, especially for ions.^{304,2i} Caution must always be exercised in using solvation models, especially for predictions.

Finally, it has been shown by Singleton that dynamic effects may alter regioselectivities; his prime example involves hydroborations.³⁰⁵ While MD may be necessary to quantify selectivities, the cases where this is true generally involve reactions with very low activation barriers.

Computational modeling will continue to complement experimental investigations to provide understanding and new vistas of organocatalysis.

Acknowledgments

We are grateful to the National Institute of General Medical Sciences, National Institutes of Health (GM 36700, K.N.H.); Novartis/ACS (J.M.U.); and NSERC PDF fellowship (C.Y.L.) for support of this work.

References

1. (a) Koch, W.; Holthausen, MC. *A Chemist's Guide to Density Functional Theory*. Wiley-VCH; Weinheim, Germany: 2001. (b) Curtis LA, Raghavachari K, Redfern PC, Pople JA. *J Chem Phys*. 1997; (106):1063.
2. (a) Wheeler SE, Moran A, Pieniazek SN, Houk KN. *J Phys Chem A*. 2009; 113:10376. [PubMed: 19711937] (b) Pieniazek SN, Clemente FR, Houk KN. *Angew Chem, Int Ed*. 2008; 47:7746. (c) Ess DH, Houk KN. *J Phys Chem A*. 2005; 109:9542. [PubMed: 16866406] (d) Guner V, Khuong KS, Leach AG, Lee PS, Bartberger MD, Houk KN. *J Phys Chem A*. 2003; 107:11445. (e) Wodrich MD, Cominboeuf C, Schreiner PR, Fokin AA, Schleyer PvR. *Org Lett*. 2007; 9:1851. [PubMed: 17417862] (f) Jones GO, Guner VA, Houk KN. *J Phys Chem A*. 2006; 110:1216. [PubMed: 16435782] (g) Izgorodina EI, Brittain DRB, Hodgson JL, Krenske EH, Lin CY, Namazian M, Coote ML. *J Phys Chem A*. 2007; 111:10754. [PubMed: 17887739] (h) Dkhissi A, Duc er JM, Blossley R, Pouchan C. *J Comput Chem*. 2009; 30:1179. [PubMed: 18785244] (i) Harvey JN. *Faraday Discuss*. 2010; 145:487.
3. (a) Wodrich MD, Corminboeuf C, Schleyer PvR. *Org Lett*. 2006; 8:3631. [PubMed: 16898778] (b) Wodrich MD, Wannere CS, Mo Y, Jarowski PD, Houk KN, Schleyer PvR. *Chem Eur J*. 2007; 13:7731. (c) Grimme S, Steinmetz M, Korth M. *J Chem Theory Comput*. 2006; 3:42. (d) Schreiner PR, Fokin AA, Pascal RA, de Meijere A. *Org Lett*. 2006; 8:3635. [PubMed: 16898779] (e) Stefan G. *Angew Chem, Int Ed*. 2006; 45:4460. (g) Schreiner PR. *Angew Chem, Int Ed*. 2007; 46:4217.
4. Paul W, Timothy C. *J Comput Chem*. 2004; 25:725. [PubMed: 14978715]
5. (a) Grimme S, Steinmetz M, Korth M. *J Org Chem*. 2007; 72:2118. [PubMed: 17286442] (b) Rokob TA, Hamza A, Papai I. *Org Lett*. 2007; 9:4279. [PubMed: 17854198]
6. (a) Zhao Y, Truhlar DG. *J Chem Theory Comput*. 2006; 3:289. (b) Zhao Y, Truhlar DG. *J Chem Theory Comput*. 2005; 1:415. (c) Zhao Y, Truhlar DG. *Phys Chem Chem Phys*. 2005; 7:2701. [PubMed: 16189582]
7. (a) Zhao Y, Truhlar DG. *Org Lett*. 2006; 8:5753. [PubMed: 17134264] (b) Zhao Y, Truhlar DG. *J Phys Chem A*. 2006; 110:10478. [PubMed: 16942053] (c) Zhao Y, Truhlar DG. *J Phys Chem A*. 2004; 108:6908. (d) Schwabe T, Grimme S. *Phys Chem Chem Phys*. 2007; 9:3397. [PubMed: 17664963] (e) Schwabe T, Grimme S. *Acc Chem Res*. 2008; 41:569. [PubMed: 18324790] (f) de Jong GT, Bickelhaupt FM. *J Phys Chem A*. 2005; 109:9685. [PubMed: 16866421] (g) Izgorodina EI, Coote ML, Radom L. *J Phys Chem A*. 2005; 109:7558. [PubMed: 16834125] (h) Quintal MM, Karton A, Iron MA, Boese AD, Martin JML. *J Phys Chem A*. 2006; 110:709. [PubMed: 16405344] (i) Zhao Y, Gonzalez-Garcia N, Truhlar DG. *J Phys Chem A*. 2005; 109:2012. [PubMed: 16833536] (j) Amin EA, Truhlar DG. *J Chem Theory Comput*. 2007; 4:75. (k) White BR, Wagner CR, Truhlar DG, Amin EA. *J Chem Theory Comput*. 2008; 4:1718. (l) Zhao Y, Truhlar DG. *J Phys Chem A*. 2008; 112:1095. [PubMed: 18211046] (m) Zhao Y, Truhlar DG. *Acc Chem Res*. 2008; 41:157. [PubMed: 18186612] (n) Zhao Y, Truhlar DG. *J Chem Theory Comput*. 2009; 5:324. (o) Korth M, Grimme S. *J Chem Theory Comput*. 2009; 5:993. (p) Zheng J, Zhao Y, Truhlar DG. *J Chem Theory Comput*. 2006; 3:569. (q) Tishchenko O, Zheng J, Truhlar DG. *J Chem Theory Comput*. 2008; 4:1208. (r) Yang K, Zheng J, Zhao Y, Truhlar DG. *J Chem Phys*. 2010; 132:164117. [PubMed: 20441268]
8. Bahmanyar S, Houk KN, Martin HJ, List B. *J Am Chem Soc*. 2003; 125:2475. [PubMed: 12603135]
9. Sim n L, Goodman JM. *Org Biomol Chem*. 2011; 9:689. [PubMed: 20976314]
10. (a) Hajos, ZG.; Parrish, DR. DE. 2102623. Jul 29. 1971 (b) Hajos AG, Parrish DR. *J Org Chem*. 1974; 39:1615.
11. (a) Eder, U.; Sauer, G.; Wiechert, R. DE. 2014757. Oct 7. 1971 (b) Eder U, Sauer G, Wiechert R. *Angew Chem, Int Ed Eng*. 1971; 10:496.

12. (a) List B. *Angew Chem Int Ed.* 2010; 49:1730. For earlier reviews, see: (b) List B. *Chem Rev.* 2007; 107:5413. (c) List B. *Chem Commun.* 2006:819. (d) List B, Houk KN. *Acc Chem Res.* 2004; 37:487. (e) List B. *Adv Synth Catal.* 2004; 346:1021.
13. MacMillan DWC. *Nature.* 2008; 455:304. [PubMed: 18800128]
14. Puchot C, Samuel O, Dunach E, Zhao S, Agami C, Kagan HB. *J Am Chem Soc.* 1986; 108:2353.
15. Jung ME. *Tetrahedron.* 1976; 3:2, 3.
16. Clemente FR, Houk KN. *Angew Chem Int Ed.* 2004; 43:5766.
17. For a study on the accuracy of DFT in predicting thermochemistries of the aldol, Mannich, and aminooxylation reactions, see: Wheeler SE, Moran A, Pieniazek SN, Houk KN. *J Phys Chem A.* 2009; 113:10376. [PubMed: 19711937]
18. Zhu H, Clemente FR, Houk KN, Meyer MP. *J Am Chem Soc.* 2009; 131:1632. [PubMed: 19191687]
19. Bahmanyar S, Houk KN. *J Am Chem Soc.* 2001; 123:12911. [PubMed: 11749554]
20. Cheong PH-Y, Houk KN, Warriar JS, Hanessian S. *Adv Synth Catal.* 2004; 346:1111.
21. Cheong PH-Y, Houk KN. *Synthesis.* 2005; 9:1533.
22. Clemente FR, Houk KN. *J Am Chem Soc.* 2005; 127:11294. [PubMed: 16089458]
23. List B, Lerner RA, Barbas CF III. *J Am Chem Soc.* 2000; 122:2395.
24. Patil MP, Sunoj RB. *J Org Chem.* 2007; 72:8202. [PubMed: 17900139]
25. Sharma AK, Sunoj RB. *Angew Chem, Int Ed.* 2010; 49:6373.
26. Rankin KN, Gauld JW, Boyd RJ. *J Phys Chem A.* 2002; 106:5155.
27. Zotova N, Broadbelt LJ, Armstrong A, Blackmond DG. *Bioorg Med Chem Lett.* 2009; 19:3934. [PubMed: 19362473]
28. Schmid MB, Zeitler K, Gschwind RM. *Angew Chem, Int Ed.* 2010; 49:4997.
29. (a) Pihko PM, Laurikainen KM, Usano A, Nyberg AI, Kaavi JA. *Tetrahedron.* 2006; 62:317. (b) Hartikka A, Arvidsson PI. *Eur J Org Chem.* 2005:4287. (c) List B, Hoang L, Martin HJ. *Proc Natl Acad Sci USA.* 2004; 101:5839. [PubMed: 15073330] (d) de Arriba ÁLF, Simón L, Raposo C, Alcázar V, Morán JR. *Tetrahedron.* 2009; 65:4841. (e) Zotova N, Franzke A, Armstrong A, Blackmond D. *J Am Chem Soc.* 2007; 129:15100. [PubMed: 18001021] (f) Iwamura H, Mathew SP, Blackmond DG. *J Am Chem Soc.* 2004; 126:11770. [PubMed: 15382893]
30. Seebach D, Beck AK, Badine DM, Limbach M, Eschenmoser A, Treasurywala AM, Hobi R, Prikoszovich W, Linder B. *Helv Chim Acta.* 2007; 90:425.
31. Blackmond DG, Moran A, Hughes M, Armstrong A. *J Am Chem Soc.* 2010; 132:7598. [PubMed: 20465280]
32. Zimmerman HE, Traxler MD. *J Am Chem Soc.* 1957; 79:1920.
33. Hoang L, Bahmanyar S, Houk KN, List B. *J Am Chem Soc.* 2003; 125:16. [PubMed: 12515489]
34. Bachrach, SM. *Computational Organic Chemistry.* Wiley; New York: 2007.
35. Arno M, Zaragoza RJ, Domingo LR. *Tetrahedron: Asymmetry.* 2005; 16:2764.
36. (a) Tang Z, Jiang F, Yu TL, Cui X, Gong LZ, Mi AQ, Jiang YZ, Wu YD. *J Am Chem Soc.* 2003; 125:5262. [PubMed: 12720423] (b) Tang Z, Jiang F, Cui X, Gong LZ, Mi AQ, Jiang YZ, Wu YD. *Proc Nat Acad Sci.* 2004; 101:5755. [PubMed: 15079057]
37. Xu X-Y, Tang Z, Wang Y-Z, Luo S-W, Cun L-F, Gong L-Z. *J Org Chem.* 2007; 72:9905. [PubMed: 18004868]
38. Chen X-H, Luo S-W, Tang Z, Cun L-F, Mi A-Q, Jiang Y-Z, Gong L-Z. *Chem Eur J.* 2007; 13:689.
39. Okuyama Y, Nakano H, Watanabe Y, Makabe M, Takeshita M, Uwai K, Kabuto C, Kwon E. *Tet Lett.* 2009; 50:193.
40. (a) Córdova A, Zou W, Ibrahim I, Reyes E, Engqvist M, Liao WW. *Chem Commun.* 2005:3586. (b) Amedjkouh M. *Tetrahedron: Asymmetry.* 2005; 16:1411. (c) Dziedzic P, Zou W, Háfren J, Córdova A. *Org Biomol Chem.* 2006; 4:38. [PubMed: 16357992] (d) Córdova A, Zou W, Dziedzic P, Ibrahim I, Reyes E, Xu Y. *Chem Eur J.* 2006; 12:5383. Correction: Córdova A, Zou W, Dziedzic P, Ibrahim I, Reyes E, Xu Y. *Chem Eur J.* 2006; 12:5175. (e) Klussmann M, Iwamura H, Mathew SP, Wells DH Jr, Pandya U, Armstrong A, Blackmond DG. *Nature.* 2006; 441:621. [PubMed: 16738656]

41. Bassan A, Zou W, Reyes E, Himo F, Córdova A. *Angew Chem Int Ed.* 2005; 44:7028.
42. Diner P, Amedjkouh M. *Org Biomol Chem.* 2006; 4:2091. [PubMed: 16729122]
43. Dickerson TJ, Lovell T, Meijler MM, Noodleman L, Janda KD. *J Org Chem.* 2004; 69:6603. [PubMed: 15387581]
44. Zhang X, Houk KN. *J Am Chem Soc.* 2005; 70:9712.
45. (a) List B. *J Am Chem Soc.* 2000; 122:9336. (b) List B, Pojarliev P, Biller WT, Martin HJ. *J Am Chem Soc.* 2002; 124:827. [PubMed: 11817958] (c) Pojarliev P, Biller WT, Martin HJ, List B, Synlett. 2003:1903. (d) Yang JW, Stadler M, List B. *Angew Chem Int Ed.* 2007; 46:609.
46. Bahmanyar S, Houk KN. *Org Lett.* 2003; 5:1249. [PubMed: 12688731]
47. Hayashi Y, Urushima T, Shoji M, Uchimaru T, Shiina I. *Adv Synth Catal.* 2005; 347:1595.
48. Cheong PH-Y, Zhang H, Thayumanavan R, Tanaka F, Houk KN, Barbas CF III. *Org Lett.* 2006; 8:811. [PubMed: 16494447]
49. Hayashi Y, Okano T, Itoh T, Urushima T, Ishikawa H, Uchimaru T. *Angew Chem Int Ed.* 2008; 47:9053.
50. Wong CT. *Tetrahedron.* 2009; 65:7491.
51. (a) Li H, Fu A, Shi H. *J Mol Catal A: Chem.* 2009; 303:1. (b) Zhuang W, Saaby S, Jørgensen KA. *Angew Chem Int Ed.* 2004; 43:4476.
52. Zhang H, Mitsumori S, Utsumi N, Imai M, Garcia-Delgado N, Mifsud M, Albertshofer K, Cheong PH-Y, Houk KN, Tanaka F, Barbas CF III. *J Am Chem Soc.* 2008; 130:875. [PubMed: 18163619]
53. Hayashi Y, Yamaguchi J, Hibino K, Shoji M. *Tetrahedron Lett.* 2003; 44:8293.
54. Zhong G. *Angew Chem Int Ed.* 2003; 42:4247.
55. Brown SP, Brochu MP, Sinz CJ, MacMillan DWC. *J Am Chem Soc.* 2003; 125:10808. [PubMed: 12952459]
56. (a) Mathew SP, Iwamura H, Blackmond DG. *Angew Chem.* 2004; 116:3379. (b) Iwamura H, Wells DH, Mathew SP, Klussmann M, Armstrong A, Blackmond DG. *J Am Chem Soc.* 2004; 126:16312. [PubMed: 15600319] (c) Mathew SP, Klussmann M, Iwamura H, Wells DH Jr, Armstrong A, Blackmond DA. *Chem Commun.* 2006:4291.
57. Zotova N, Moran A, Armstrong A, Blackmond DG. *Adv Synth Catal.* 2009; 351:2765. and references therein.
58. (a) Córdova A, Sundén H, Bøgevig A, Johansson M, Himo F. *Chem Eur J.* 2004; 10:3673. (b) Cheong PH-Y, Houk KN. *J Am Chem Soc.* 2004; 126:13912. [PubMed: 15506738] (c) Wong H, Yang C, Han K. *Struc Chem.* 2006; 17:97.
59. (a) Dinér P, Kjærsgaard A, Lie MA, Jørgensen KA. *Chem Eur J.* 2008; 14:122. Four groups independently reported the organocatalyzed α -fluorination reaction of aldehydes in the same year: (b) Beeson TD, MacMillan DWC. *J Am Chem Soc.* 2005; 127:8826. [PubMed: 15954790] (c) Steiner DD, Mase N, Barbas CF III. *Angew Chem Int Ed.* 2005; 44:3706. (d) Enders D, Hüttl MRM. *Synlett.* 2005:991. (e) Marigo M, Fielenbach D, Braunton A, Kjærsgaard A, Jørgensen KA. *Angew Chem Int Ed.* 2005; 44:3703.
60. Bertelson S, Marigo M, Brandes S, Dinér P, Jørgensen KA. *J Am Chem Soc.* 2006; 128:12973. [PubMed: 17002394]
61. Groselj U, Seebach D, Badine DM, Schweizer WB, Beck AK. *Helv Chim Acta.* 2009; 92:1225.
62. Vignola N, List B. *J Am Chem Soc.* 2003; 126:450. [PubMed: 14719926]
63. Fu A, List B, Thiel W. *J Org Chem.* 2006; 71:320. [PubMed: 16388651]
64. Ibrahem I, Hammar P, Vesely J, Rios R, Eriksson L, Córdova A. *Adv Synth Catal.* 2008; 350:1875.
65. Arnó M, Zaragoza RJ, Domingo LR. *Tetrahedron: Asymmetry.* 2007; 18:157.
66. Seebach D, Golinski J. *Helv Chim Acta.* 1981; 64:1413.
67. Mahendra PP, Sunoj RB. *Chem Eur J.* 2008; 14:10472.
68. (a) List B. *Tetrahedron.* 2002; 58:5573. (b) Enders D, Seki A. *Synlett.* 2002; 1:26. (c) Betancort JM, Barbas CF III. *Org Lett.* 2001; 3:3737. [PubMed: 11700126] (d) Mase N, Thayumanavan R, Tanaka F, Barbas CF III. *Org Lett.* 2004; 6:2527. [PubMed: 15255682]
69. Almasi D, Alonso DA, Gómez-Bengoia E, Nagel Y, Nájera C. *Eur J Org Chem.* 2007:2328.

70. Sulzer-Mossé S, Alexakis A, Mareda J, Bollot G, Bernardinelli G, Filinchuk Y. *Chem Eur J.* 2009; 15:3204.
71. Melchiorre P, Jørgensen KA. *J Org Chem.* 2003; 68:4151. [PubMed: 12762713]
72. Patil MP, Sunoj RB. *Chem Asian J.* 2009; 4:714. [PubMed: 19353592]
73. (a) Shinisha CB, Sunoj Raghavan B. *Org Biomol Chem.* 2008; 6:3921. [PubMed: 18931798] (b) Enders D, Huttli MRM, Grandoal C, Raabe G. *Nature.* 2006; 441:861. [PubMed: 16778886]
74. (a) Duarte FJS, Cabriat EJ, Frenking G, Santos AG. *Chem Eur J.* 2009; 15:1734.(b) Chen SH, Hong BC, Su CF, Sarshar S. *Tetrahedron Lett.* 2005; 46:8899.
75. (a) Basavaiah D, Rao AJ, Satyanarayana T. *Chem Rev.* 2003; 103:811. [PubMed: 12630854] (b) Basavaiah D, Rao KV, Reddy RJ. *Chem Soc Rev.* 2007; 36:1581. [PubMed: 17721583]
76. Ahrendt KA, Borths CJ, MacMillan DWC. *J Am Chem Soc.* 2000; 122:4243.
77. Burley JC, Gilmour R, Prior TJ, Day GM. *Acta Cryst.* 2008; C64:010.
78. Groselj U, Schweizer WB, Ebert M-O, Seebach D. *Helv Chim Acta.* 2009; 92:1.
79. (a) Gordillo R, Carter J, Houk KN. *Adv Synth Catal.* 2004; 346:1175.(b) Austin JF, MacMillan DWC. *J Am Chem Soc.* 2002; 124:1172. [PubMed: 11841277]
80. Brazier JB, Evans G, Gibbs TJK, Coles SJ, Hursthouse MB, Platts JA, Tomkinson NCO. *Org Lett.* 2009; 11:133. [PubMed: 19061422]
81. Gordillo R, Houk KN. *J Am Chem Soc.* 2006; 128:3543. [PubMed: 16536527]
82. Gutierrez O, Iafe RG, Houk KN. *Org Lett.* 2009; 11:4298. [PubMed: 19722547]
83. Nicolaou KC, Reingruber R, Sarlah D, Bräse S. *J Am Chem Soc.* 2009; 131:2086. Correction: *J. Am. Chem. Soc.* 2009, 131, 6640. [PubMed: 19173649]
84. Conrad JC, Kong J, Laforteza BN, MacMillan DWC. *J Am Chem Soc.* 2009; 131:11640. [PubMed: 19639997]
85. Um JM, Gutierrez O, Schoenebeck F, Houk KN, MacMillan DWC. *J Am Chem Soc.* 2010; 132:6001. [PubMed: 20387888]
86. For ortho-selective radical additions to aromatics, see: (a)Tiecco M, Testaferri L, Abramovitch RA. *Reactive Intermediates.* Plenum PressNew York1983; 3:61.(b) Guadarrama-Morales O, Mendéz F, Miranda LD. *Tetrahedron Lett.* 2007; 48:4515.(c) Muchowski JM, Cho IS, Jaime-Figueroa S, Artis RD. *J Org Chem.* 1994; 59:2456.For a study of the stability of cyclohexadienyl radicals, see: (d) Birch AJ, Hinde AL, Radom L. *J Am Chem Soc.* 1980; 102:4074.
87. For a recent review on carbene catalysts, see: Moore JL, Rovis T. *List B. Asymmetric Organocatalysis.* Springer VerlagHeidelberg2010:77–144.
88. Wöhler F, Liebig J. *Ann Pharm.* 1832; 3:249.
89. Ugai T, Tanaka S, Dokawa S. *J Pharm Soc Jpn.* 1943; 63:269.
90. (a) López Calahorra F, Castells J, Domingo L, Martí J, Bofill JM. *Heterocycles.* 1994; 37:1579.(b) Martí J, López Calahorra F, Bofill JM. *J Mol Struct (Theochem).* 1995; 339:179.
91. Dudding T, Houk KN. *Proc Nat Acad Sci.* 2004; 101:5770. [PubMed: 15079058]
92. Breslow R. *J Am Chem Soc.* 1958; 80:3719.
93. Enders D, Kallfass U. *Angew Chem, Int Ed.* 2002; 41:1743.
94. Knight RL, Leeper FJ. *Tetrahedron Lett.* 1997; 38:3611.
95. Sheehan J, Hara T. *J Org Chem.* 1974; 39:1196.
96. (a) Enders D, Breuer K, Teles JH. *Helv Chim Acta.* 1996; 79:1217.(b) Enders, D.; Breuer, K. *Comprehensive Asymmetric Catalysis.* Vol. 3. Springer-Verlag; Heidelberg, Germany: 1999. p. 1093(c) Teles JH, Breuer K, Enders D, Gielen H. *Synth Commun.* 1999; 29:1.
97. Hachisu Y, Bode JW, Suzuki K. *Adv Synth Catal.* 2004; 346:1097.
98. Hawkes KJ, Yates BF. *Eur J Org Chem.* 2008:5563.
99. (a) Grasa GA, Kissling RM, Nolan SP. *Org Lett.* 2002; 4:3583. [PubMed: 12375893] (b) Grasa GA, Guveli T, Singh R, Nolan SP. *J Org Chem.* 2003; 68:2812. [PubMed: 12662057]
100. (a) Nyce GW, Lamboy JA, Connor EF, Waymouth RM, Hedrick JL. *Org Lett.* 2002; 4:3587. [PubMed: 12375894] For reviews in NHC-catalyzed polymerization reactions, see: (b) Dove AP, Pratt RC, Lohmeijer BGG, Culkun DA, Hagberg EC, Nyce GW, Waymouth RM, Hedrick JL.

Polymer. 2006; 47:4018.(b) Coulembier O, Gegée P, Hedrick JL, Dubois P. *Prog Polym Sci.* 2006; 31:723.

101. Lai C-L, Lee HM, Hu C-H. *Tetrahedron Lett.* 2005; 46:6265.
102. Maki BE, Patterson EV, Cramer CJ, Scheidt KA. *Org Lett.* 2009; 11:3942. [PubMed: 19645427]
103. See Chan A, Scheidt KA. *Org Lett.* 2005; 7:905. and references therein. [PubMed: 15727471]
104. Ragsdale SW. *Chem Rev.* 2003; 103:2333. [PubMed: 12797832]
105. Guin J, De Sarkar S, Grimme S, Studer A. *Angew Chem Int Ed.* 2008; 47:8727.
106. Xu S, Held I, Kempf B, Mayr H, Steglich W, Zipse H. *Chem Eur J.* 2005; 11:4751.
107. (a) Guibe-Jampel E, Le Corre G, Wakselman M. *Tetrahedron Lett.* 1979; 20:1157.(b) Kattinig E, Albert M. *Org Lett.* 2004; 6:945. [PubMed: 15012071] (c) Lamaty G, Mary F, Roque JP. *J Chim Phys Phys-Chim Biol.* 1991; 88:1793.
108. Fischer CB, Xu S, Zipse H. *Chem Eur J.* 2006; 12:5779.
109. Wei Y, Held I, Zipse H. *Org Biomol Chem.* 2006; 4:4223. [PubMed: 17312979]
110. Held I, Villinger A, Zipse H. *Synthesis.* 2005; 9:1425.
111. (a) Heinrich MR, Klisa HS, Mayr H, Steglich W, Zipse H. *Angew Chem Int Ed.* 2003; 42:4826. (b) Held I, Xu S, Zipse H. *Synthesis.* 2007; 8:1185.(c) Held I, Larinov E, Bozle C, Wagner F, Zipse H. *Synthesis.* 2009; 13:2267.
112. Zipse has also calculated the methyl cation affinities of commonly used nitrogen and phosphorous-based organocatalysts. See: (a) Wei Y, Sastry N, Zipse H. *J Am Chem Soc.* 2008; 130:3473. [PubMed: 18288837] (b) Wei Y, Singer T, Mayr H, Sastry GN, Zipse H. *J Comput Chem.* 2008; 29:291. [PubMed: 17570129] The same group reported the performance of computational methods in describing zwitterionic adducts between NMe₃ and PMe₃ with methyl vinyl ketone. See: Wei Y, Bandaru S, Maryasin B, Sastry N, Zipse H. *J Comput Chem.* 2009; 30:2617. [PubMed: 19373894]
113. (a) Singh S, Das G, Singh OV, Han H. *Org Lett.* 2007; 9:401. [PubMed: 17249772] (b) Singh S, Das G, Singh OV, Han H. *Tetrahedron Lett.* 2007; 48:1983.
114. (a) Steglich W, Höfle G. *Tetrahedron Lett.* 1970; 54:4727.(b) Hassner A, Krepski LR, Alexanian V. *Tetrahedron.* 1978; 34:2069.
115. (a) Yamada S, Yamashita K. *Tetrahedron Lett.* 2008; 49:32.(b) Yamada S, Misono T, Iwai Y, Masumizu A, Akiyama Y. *J Org Chem.* 2006; 71:6872. [PubMed: 16930040] (c) Yamada S, Misono T, Iwai Y. *Tetrahedron Lett.* 2005; 46:2239.(d) Yamada S, Noguchi E. *Tetrahedron Lett.* 2002; 42:3621.
116. Lutz V, Glatthaar J, Würtele C, Serafin M, Hausmann H, Schreiner PR. *Chem Eur J.* 2009; 15:8548.
117. (a) Marcelli T, van Maarseveen JH, Hiemstra H. *Angew Chem Int Ed.* 2006; 45:7496.(b) Tan SK, Chen Y, Hang J, Tang L, McDaid P, Deng L. *Acc Chem Res.* 2004; 37:621. [PubMed: 15311961] (c) Hoffmann HMR, Frackenpohl J. *Eur J Org Chem.* 2004:4293.(d) Kacprzak K, Gawroskik J. *Synthesis.* 2001; 7:961.
118. Bürgi T, Baiker A. *J Am Chem Soc.* 1998; 120:12920.
119. Vargas A, Bonalumi N, Ferri D, Baiker A. *J Phys Chem A.* 2006; 110:1118. [PubMed: 16420016]
120. Olsen RA, Borchardt D, Mink L, Agarwal A, Mueller LJ, Zaera F. *J Am Chem Soc.* 2006; 128:15594. [PubMed: 17147361]
121. Szöllösi G, Chatterjee A, Forgó P, Bartók M, Mizukami F. *J Phys Chem A.* 2005; 109:860. [PubMed: 16838957]
122. Taggi AE, Hafez AM, Wack H, Young B, Ferraris D, Lectka T. *J Am Chem Soc.* 2002; 124:6626. [PubMed: 12047183]
123. Taggi AE, Hafez AM, Dudding T, Lectka T. *Tetrahedron.* 2002; 58:8351.
124. Brunner H, Schmidt P. *Eur J Org Chem.* 2000:2119.
125. Drees M, Kleiber L, Wemer M, Strassner T. *Eur J Org Chem.* 2002:2405.
126. Peltier HM, Evans JW, Ellman JA. *Org Lett.* 2005; 7:1733. [PubMed: 15844893]

127. Shibata N, Matsunaga M, Nakagawa M, Fukuzumi T, Nakamura S, Toru T. *J Am Chem Soc.* 2005; 127:1374. [PubMed: 15686360]
128. Balcells D, Maseras F, Khiar N. *Org Lett.* 2005; 6:2197. [PubMed: 15200319]
129. Balcells D, Ujaque G, Fernandez I, Khiar N, Maseras F. *J Org Chem.* 2006; 71:6388. [PubMed: 16901120]
130. (a) France S, Wack H, Taggi AE, Hafez AM, Wagerle TR, Shah MH, Cusich CL, Lectka T. *J Am Chem Soc.* 2004; 126:4245. [PubMed: 15053614] (b) Wack H, Taggi AE, Hafez AM, Drury WJ III, Lectka T. *J Am Chem Soc.* 2001; 123:1531. [PubMed: 11456741] (c) France S, Weatherwax A, Lectka T. *Eur J Org Chem.* 2005; 3:475.
131. Hafez AM, Taggi AE, Wack H, Esterbrook J, Lectka T. *Org Lett.* 2001; 3:2049. [PubMed: 11418046]
132. Dogo-Isonagie C, Bekele T, France S, Wolfer J, Weatherwax A, Taggi AE, Paull DH, Dudding T, Lectka T. *Eur J Org Chem.* 2007:1091.
133. (a) Liu B, Feng X, Chen F, Zhang G, Cui X, Jiang Y. *Synlett.* 2001; 10:1551.(b) Jiao Z, Feng X, Liu B, Chen F, Zhang GL, Jiang Y. *Eur J Org Chem.* 2003:3818.
134. Su Z, Hu C, Qin S, Feng X. *Tetrahedron.* 2006; 62:4071.
135. Aggarwal VK, Alonso E, Hynd G, Lydon KM, Palmer MJ, Porcelloni M, Studley JR. *Angew Chem Int Ed.* 2001; 40:1430.
136. Volatron F, Eisenstein O. *J Am Chem Soc.* 1987; 109:1.
137. (a) Lindvall MK, Koskinen AMP. *J Org Chem.* 1999; 64:4595.(b) Myllymäki VT, Lindvall MK, Koskinen AMP. *Tetrahedron.* 2001; 57:4629.
138. Aggarwal VK, Harvey JN, Richardson J. *J Am Chem Soc.* 2002; 124:5747. [PubMed: 12010049]
139. Aggarwal VK, Charmant JPH, Fuentes D, Harvey JN, Hynd G, Ohara D, Picoul W, Robiette R, Smith C, Vasse J-L, Winn CL. *J Am Chem Soc.* 2006; 128:2105. [PubMed: 16464113]
140. Imashiro R, Yamanaka T, Seki M. *Tetrahedron: Asymmetry.* 1999; 10:2845.
141. Aggarwal VK, Harvey JN, Robiette R. *Angew Chem Int Ed.* 2005; 44:5468.
142. Robiette R, Conza M, Aggarwal VK. *Org Biomol Chem.* 2006; 4:621. [PubMed: 16467935]
143. Silva MA, Bellenie BR, Goodman JM. *Org Lett.* 2004; 6:2559. [PubMed: 15255690]
144. Zanardi J, Leriverend C, Aubert D, Julienne K, Metzner P. *J Org Chem.* 2001; 66:5620. [PubMed: 11485494]
145. (a) Winn CL, Bellenie BR, Goodman JM. *Tetrahedron Lett.* 2002; 43:5427.(b) Winn C, Goodman JM. *Tetrahedron Lett.* 2001; 42:7091.
146. Deng X-M, Cai P, Ye S, Sun X-L, Liao W-W, Li K, Tang Y, Wu Y-D, Dai L-X. *J Am Chem Soc.* 2005; 128:9730. [PubMed: 16866528]
147. Robiette R. *J Org Chem.* 2006; 71:2726. [PubMed: 16555826]
148. Janardanan D, Sunoj RB. *Chem Eur J.* 2007; 13:4805.
149. Janardanan D, Sunoj RB. *J Org Chem.* 2008; 73:8163. [PubMed: 18842028]
150. Stewart IC, Bergman RG, Toste FD. *J Am Chem Soc.* 2003; 125:8696. [PubMed: 12862443]
151. Wang X, Li S, Jiang Y. *J Phys Chem A.* 2005; 109:10770. [PubMed: 16863126]
152. For examples, see: (a) Zhang C, Lu X. *J Org Chem.* 1995; 60:2906.(b) Zhu G, Chen Z, Jiang Q, Xiao D, Cao P, Zhang X. *J Am Chem Soc.* 1997; 119:3836.(c) Wilson JE, Fu GC. *Angew Chem, Int Ed.* 2006; 45:1426.(d) Zhu XF, Lan J, Kwon O. *J Am Chem Soc.* 2003; 125:4716. [PubMed: 12696883] (e) Tran YS, Kwon O. *Org Lett.* 2005; 7:4289. [PubMed: 16146409] (f) Wurz RP, Fu GC. *J Am Chem Soc.* 2005; 127:12234. [PubMed: 16131196] (g) Evans CA, Miller SJ. *J Am Chem Soc.* 2003; 125:12394. [PubMed: 14531667] (h) Wang LC, Luis AL, Agapiou K, Jang HY, Krische MJ. *J Am Chem Soc.* 2002; 124:2402. [PubMed: 11890765] (i) Frank SA, Mergott AJ, Roush WR. *J Am Chem Soc.* 2002; 124:2404. [PubMed: 11890766]
153. Dudding T, Kwon O, Mercier E. *Org Lett.* 2006; 8:3643. [PubMed: 16898781]
154. (a) Xia Y, Liang Y, Chen Y, Wang M, Jiao L, Huang F, Liu S, Li Y, Yu ZX. *J Am Chem Soc.* 2006; 129:3470. [PubMed: 17319666] (b) Mercier E, Fonovic B, Henry C, Kwon O, Dudding T. *Tetrahedron Lett.* 2007; 48:3617.(c) Liang Y, Liu S, Xia Y, Li Y, Yu ZX. *Chem Eur J.* 2008; 14:4361.

155. Xia Y, Liang Y, Chen Y, Wang M, Jiao L, Huang F, Liu S, Li Y, Yu Z-X. *J Am Chem Soc.* 2007; 129:3470. [PubMed: 17319666]
156. Yu X-Z. *Synlett.* 2009; 6:905.
157. (a) Baylis, AB.; Hillman, MED. Offenlegungsschrift 2155113. US Patent. 3,743,669. 1972. *Chem Abstr.* 1972; 77:34174q.(b) Morita K, Suzuki Z, Hirose H. *Bull Chem Soc Jpn.* 1968; 41:2815.
158. Xu J. *THEOCHEM.* 2006; 767:61.
159. Robiette R, Aggarwal VK, Harvey JN. *J Am Chem Soc.* 2007; 129:15513. [PubMed: 18041831]
160. (a) Aggarwal VK, Fulford SY, Lloyd-Jones GC. *Angew Chem Int Ed.* 2005; 44:1706.(b) Price KE, Broadwater SJ, Jung HM, McQuade DT. *Org Lett.* 2005; 7:147. [PubMed: 15624999] (c) Price KE, Broadwater SJ, Walker BJ, McQuade DT. *J Org Chem.* 2005; 70:3980. [PubMed: 15876086] (d) Buskens P, Klankermayer J, Leitner W. *J Am Chem Soc.* 2005; 127:16762. [PubMed: 16316203]
161. (a) Hill JS, Isaacs NS. *J Phys Org Chem.* 1990; 3:285.(b) Hill JS, Isaacs NS. *J Chem Res.* 1988:330.(c) Hill JS, Isaacs NS. *Tetrahedron Lett.* 1986; 27:5007.
162. Fan J-F, Yang C-H, He L-J. *Int J Quantum Chem.* 2009; 109:1311.
163. Roy D, Sunoj RB. *Org Lett.* 2007; 9:4873. [PubMed: 17924642]
164. (a) Roy D, Patel C, Sunoj RB. *J Org Chem.* 2009; 74:6936. [PubMed: 19697897] (b) Roy D, Sunoj RB. *Chem Eur J.* 2008; 14:10530.
165. For examples, see: (a) Jung ME, Node M, Pfluger RW, Lyster MA, Lowe JA III. *J Org Chem.* 1982; 47:1150.(b) Jung ME, Lowe JA III, Lyster MA, Node M, Pfluger RW, Brown RW. *Tetrahedron.* 1984; 40:4751.(c) Yasukouchi T, Kanematsu K. *Tetrahedron Lett.* 1989; 30:6559. (d) Ma D, Yu Y, Lu X. *J Org Chem.* 1989; 54:1105.
166. Liu H, Leow D, Huang K-W, Tan C-H. *J Am Chem Soc.* 2009; 131:7212. [PubMed: 19422238]
167. Oku M, Arai S, Katayama K, Shioiri T. *Synlett.* 2000:493.
168. Climent MJ, Corma A, Domínguez I, Iborra S, Sabater MJ, Sastre G. *J Catal.* 2007; 246:136.
169. Tel RM, Engberts JBFN. *J Chem Soc Perkin Trans.* 1976; 2:483.
170. (a) Etter MC, Panunto TW. *J Am Chem Soc.* 1988; 110:5896.(b) Etter MC, Urbańczyk-Lipkowska Z, Zia-Ebrahimi M, Panunto TW. *J Am Chem Soc.* 1990; 112:8415.(c) Etter MC. *Acc Chem Res.* 1990; 23:120.(d) Etter MC. *J Phys Chem.* 1991; 95:4601.
171. Schreiner PR, Wittkopp A. *Org Lett.* 2002; 4:217. [PubMed: 11796054]
172. Schreiner PR. *Chem Soc Rev.* 2003; 32:289. [PubMed: 14518182]
173. Fu AP, Thiel W. *Theochem-J Mol Struct.* 2006; 765:45.
174. Loncharich RJ, Brown FK, Houk KN. *J Org Chem.* 1989; 54:1129.
175. Bernardi F, Bottoni A, Field MJ, Guest MF, Hillier IH, Robb MA, Venturini A. *J Am Chem Soc.* 1988; 110:3050.
176. Houk KN, Lin YT, Brown FK. *J Am Chem Soc.* 1986; 108:554.
177. Sauer J, Sustmann R. *Angew Chem, Int Ed Engl.* 1980; 19:779.
178. Linder M, Brinck T. *Org Biomol Chem.* 2009; 7:1304. [PubMed: 19300814]
179. Severance DL, Jørgensen WL. *J Am Chem Soc.* 1992; 114:10966.
180. Curran DP, Lung HK. *Tetrahedron Lett.* 1995; 36:6647.
181. Kirsten M, Rehbein J, Hiersemann M, Strassner T. *J Org Chem.* 2007; 72:4001. [PubMed: 17477575]
182. Sigman MS, Vachal P, Jacobsen EN. *Angew Chem, Int Ed.* 2000; 39:1279.
183. Sigman MS, Jacobsen EN. *J Am Chem Soc.* 1998; 120:4901.
184. Su JT, Vachal P, Jacobsen EN. *Adv Synth Catal.* 2001; 343:197.
185. Vachal P, Jacobsen EN. *Org Lett.* 2000; 2:867. [PubMed: 10754690]
186. Vachal P, Jacobsen EN. *J Am Chem Soc.* 2002; 124:10012. [PubMed: 12188665]
187. Zuend SJ, Jacobsen EN. *J Am Chem Soc.* 2009; 131:15358. [PubMed: 19778044]
188. Kleiner CM, Schreiner PR. *Chemical Communications.* 2006:4315. [PubMed: 17047852]
189. Fleming EM, Quigley C, Rozas I, Connon SJ. *J Org Chem.* 2008; 73:948. [PubMed: 18173286]
190. Kotke M, Schreiner PR. *Synthesis.* 2007; 5:779.

191. Raheem IT, Thiara PS, Peterson EA, Jacobsen EN. *J Am Chem Soc.* 2007; 129:13404. [PubMed: 17941641]
192. Trzuppek JD, Li C, Chan C, Crowley BM, Heimann AC, Danishefsky SJ. *Pure Appl Chem.* 2010; 82:1735. [PubMed: 20711493]
193. Frankland PF, Twiss DF. *Journal of the Chemical Society, Transactions.* 1904; 85:1666.
194. Huang Y, Rawal VH. *J Am Chem Soc.* 2002; 124:9662. [PubMed: 12175197]
195. Huang Y, Unni AK, Thadani AN, Rawal VH. *Nature.* 2003; 424:146. [PubMed: 12853945]
196. Zhang X, Du H, Wang Z, Wu Y-D, Ding K. *J Org Chem.* 2006; 71:2862. [PubMed: 16555843]
197. Gordillo RD, Anderson TCD, Houk KN. *Org Lett.* 2007; 9:501. [PubMed: 17249797]
198. Gómez-Bengoia E. *Eur J Org Chem.* 2009:1207. It was reported that the preferred binding mode depends on the polarity of the carbonyl group. As the polarity increases, as in enamine aldol reactions, the bifurcated binding mode becomes favored.
199. Anderson CD, Dudding T, Gordillo R, Houk KN. *Org Lett.* 2008; 10:2749. [PubMed: 18507392]
200. Hine J, Linden SM, Kanagasabapathy VM. *J Org Chem.* 1985; 50:5096.
201. Ooi T, Takahashi M, Maruoka K. *J Am Chem Soc.* 1996; 118:11307.
202. Kelly TR, Meghani P, Ekkundi VS. *Tetrahedron Lett.* 1990; 31:3381.
203. Omoto K, Fujimoto H. *J Org Chem.* 2000; 65:2464. [PubMed: 10789458]
204. Pliego JR. *J Mol Catal A-Chem.* 2005; 239:228–234.
205. Pliego JR, Pilo-Veloso D. *J Phys Chem B.* 2007; 111:1752. [PubMed: 17266358]
206. McDougal NT, Schaus SE. *J Am Chem Soc.* 2003; 125:12094. [PubMed: 14518986]
207. McDougal NT, Trevellini WL, Rodgen SA, Kliman LT, Schaus SE. *Adv Synth Catal.* 2004; 346:1231.
208. (a) Akiyama T, Itoh J, Yokota K, Fuchibe K. *Angew Chem.* 2004; 116:1566. [PubMed: 15022235] (b) Uraguchi D, Terada M. *J Am Chem Soc.* 2004; 126:5356. [PubMed: 15113196]
209. (a) Rowland GB, Rowland EB, Liang Y, Perman JACAJ. *Org Lett.* 2007; 9:2609. [PubMed: 17547413] (b) Rueping M, Ieawsuwan W, Antonchick AP, Nachtsheim BJ. *Angew Chem, Int Ed.* 2007; 46:2097. (c) Storer RI, Carrera DE, Ni Y, MacMillan DWC. *J Am Chem Soc.* 2006; 128:84. [PubMed: 16390133] (d) Chen XH, Xu XY, Liu H, Cun LF, Gong LZ. *J Am Chem Soc.* 2006; 128:14802. [PubMed: 17105279] (e) Terada M, Machioka K, Sorimachi K. *Angew Chem, Int Ed.* 2006; 45:2254. (f) Uraguchi D, Sorimachi K, Terada M. *J Am Chem Soc.* 2005; 127:9360. [PubMed: 15984850] (g) Rueping M, Sugiono E, Azap C, Theissmann T, Bolte OL. *Org Lett.* 2005; 7:3781. [PubMed: 16092874] (h) Hoffmann S, Seayad AM, List B. *Angew Chem, Int Ed.* 2005; 44:7424. (i) Lu M, Lu Y, Zhu D, Zeng X, Li X, Zhong G. *Angew Chem Int Ed.* 2010; 49:8588.
210. Gridnev IDK, Sorimachi MK, Terada M. *Tetrahedron Lett.* 2007; 48:497.
211. Yamanaka M, Itoh J, Fuchibe K, Akiyama T. *J Am Chem Soc.* 2007; 129:6756. [PubMed: 17477527]
212. Uraguchi D, Terada M. *J Am Chem Soc.* 2004; 126:5356. [PubMed: 15113196]
213. Chen X-H, Wei Q, Luo S-W, Xiao H, Gong L-Z. *J Am Chem Soc.* 2009; 131:13819. [PubMed: 19736987]
214. Li N, Chen X-H, Song J, Luo S-W, Fan W, Gong L-Z. *J Am Chem Soc.* 2009; 131:15301. [PubMed: 19785440]
215. Simón L, Goodman JM. *J Am Chem Soc.* 2008; 130:8741. [PubMed: 18543923]
216. Marcelli T, Hammar P, Himo F. *Adv Synth Catal.* 2009; 351:525.
217. Rueping M, Sugiono E, Azap C, Theissmann T, Bolte M. *Org Lett.* 2005; 7:3781. [PubMed: 16092874]
218. Storer RI, Carrera DE, Ni Y, MacMillan DWC. *J Am Chem Soc.* 2006; 128:84. [PubMed: 16390133]
219. Simón L, Goodman JM. *J Org Chem.* 2010; 75:589. [PubMed: 20039624]
220. Shi F-Q, Song B-A. *Org Biomol Chem.* 2009; 7:1292. [PubMed: 19300812]
221. Corey EJ, Bakshi RK, Shibata S. *J Am Chem Soc.* 1987; 109:5551.
222. Corey EJ, Bakshi RK, Shibata S, Chen C-P, Singh VK. *J Am Chem Soc.* 1987; 109:7925.

223. Corey EJ, Cimprich KA. *J Am Chem Soc.* 1994; 116:3151.
224. Corey EJ, Loh T-P. *J Am Chem Soc.* 1991; 113:8966.
225. Payette JN, Yamamoto H. *J Am Chem Soc.* 2007; 129:9536. [PubMed: 17630749]
226. Corey EJ, Shibata T, Lee TW. *J Am Chem Soc.* 2002; 124:3808. [PubMed: 11942799]
227. Ryu DH, Corey EJ. *J Am Chem Soc.* 2005; 127:5384. [PubMed: 15826176]
228. Liu D, Hong S, Corey EJ. *J Am Chem Soc.* 2006; 128:8160. [PubMed: 16787080]
229. Boeckman RK, Pero JE, Boehmier DJ. *J Am Chem Soc.* 2006; 128:11032. [PubMed: 16925414]
230. (a) Nevalainen V. *Tetrahedron: Asymmetry.* 1991; 2:1133.(b) Nevalainen V. *Tetrahedron: Asymmetry.* 1992; 3:921.(c) Nevalainen V. *Tetrahedron: Asymmetry.* 1993; 4:1505.(d) Nevalainen V. *Tetrahedron: Asymmetry.* 1993; 4:1597.(e) Nevalainen V. *Tetrahedron: Asymmetry.* 1994; 5:387.(f) Nevalainen V. *Tetrahedron: Asymmetry.* 1994; 5:395.
231. (a) Nevalainen V. *Tetrahedron: Asymmetry.* 1991; 2:827.(b) Nevalainen V. *Tetrahedron: Asymmetry.* 1992; 3:933.(c) Nevalainen V. *Tetrahedron: Asymmetry.* 1994; 5:289.
232. Nevalainen V. *Tetrahedron: Asymmetry.* 1992; 3:1441.
233. (a) Nevalainen V. *Tetrahedron: Asymmetry.* 1991; 2:63.(b) Nevalainen V. *Tetrahedron: Asymmetry.* 1991; 2:429.(c) Nevalainen V. *Tetrahedron: Asymmetry.* 1992; 3:1563.
234. (a) Li M, Xie R, Hu C, Wang X, Tian A. *Int J Quantum Chem.* 2000; 78:245.(b) Li M, Xie R, Tian S, Tian A. *Int J Quantum Chem.* 2000; 78:252.(c) Li M, Xie R, Hu X, Tian A. *Int J Quantum Chem.* 2000; 78:261.
235. (a) Li M, Tian A. *THEOCHEM.* 2001; 544:25–35.(b) Li M, Tian A. *THEOCHEM.* 2001; 544:37–47.
236. (a) Li M, Zheng W, Yang F, Tian A. *Int J Quantum Chem.* 2001; 81:291.(b) Li M, Zheng W, He R, Tian A. *Int J Quantum Chem.* 2003; 93:294.(c) Li M, Zheng W, Tian A. *Int J Quantum Chem.* 2003; 93:307.(d) Zheng W, Li M, Tian A. *THEOCHEM.* 2003; 634:253.(e) Zheng W, Li M, Tian A. *THEOCHEM.* 2004; 668:13.
237. (a) Jones DK, Liotta DC, Shinkai I, Mathre DJ. *J Org Chem.* 1993; 58:799.(b) Linny LP, Self CR, Williams IH. *J Chem Soc, Chem Commun.* 1994:1651.(c) Linny LP, Self CR, Williams IH. *Tetrahedron: Asymmetry.* 1994; 5:813.(d) Bach J, Berenguer R, Farras J, Garcia J, Meseguer J, Vilarrasa J. *Tetrahedron: Asymmetry.* 1995; 6:2683.(e) Shen Z, Huang W, Feng J, Zhang Y. *Tetrahedron: Asymmetry.* 1998; 9:1091.(f) Puigjaner C, Vidal-Ferran A, Moyano A, Pericas MA, Riera A. *J Org Chem.* 1999; 64:7902.(g) Bringmann G, Hinrichs J, Kraus J, Wuzik A, Schulz T. *J Org Chem.* 2000; 65:2517. [PubMed: 10789465] (h) Fan JF, Wang QX, Yun-Xiang L. *THEOCHEM.* 2004; 674:49.(i) Gondos GP I. *Int J Quantum Chem.* 2001; 84:253.(j) Tlahuextl M, Tapia-Benavides AR, Flores-Parra A, Contreras R, Tlahuext H, Cruz EM. *Heteroat Chem.* 2005; 16:513.
238. (a) Harb W, Ruiz-Lopez MF, Coutrot F, Grison C, Coutrot P. *J Am Chem Soc.* 2004; 126:6996. [PubMed: 15174869] (b) Alagona G, Ghio C, Tomasi S. *Theor Chem Acc.* 2004; 111:287.(c) Alagona GGC, Persico C, Tomasi S. *J Am Chem Soc.* 2003; 125:10027. [PubMed: 12914466] (d) Sun L, Tang M, Wang H, Wei D, Liu L. *Tetrahedron: Asymmetry.* 2008; 19:779.
239. Corey EJ, Azimioara M, Sarshar S. *Tetrahedron Lett.* 1992; 33:3429.
240. Saavedra J, Stafford SE, Meyer MP. *Tetrahedron Lett.* 2009; 50:1324.
241. Sun L, Tang M, Wang H, Wei D, Liu L. *Tetrahedron: Asymmetry.* 2008; 19:779.
242. Grison C, Coutrot F, Coutrot P. *Tetrahedron.* 2002; 58:2735.
243. Harb W, Ruiz-Lopéz MF, Coutrot F, Grison C, Coutrot P. *J Am Chem Soc.* 2004; 126:6996. [PubMed: 15174869]
244. Li M, He R. *THEOCHEM.* 2003; 629:197.
245. Li M, He R. *THEOCHEM.* 2003; 629:209.
246. Pi Z, Li S. *J Phys Chem A.* 2006; 110:9225. [PubMed: 16854037]
247. Paddon-Row MN, Kwan LCH, Willis AC, Sherburn MS. *Angew Chem Int Ed.* 2008; 47:7013.
248. Paddon-Row MN, Anderson CD, Houk KN. *J Org Chem.* 2009; 74:861. [PubMed: 19067584]
249. Corey EJ, Loh T-P, Roper TD, Azimioara MD, Noe MC. *J Am Chem Soc.* 1992; 114:8290.

250. (a) Nevalainen V. *Tetrahedron: Asymmetry*. 1993; 4:1565.(b) Nevalainen V. *Tetrahedron: Asymmetry*. 1994; 5:767.(c) Ugglar R, Nevalainen V, Sundberg MR. *Tetradron: Asymmetry*. 1996; 7:2725.
251. Salvatella L, Ruiz-Lopéz MF. *J Am Chem Soc*. 1999; 121:10772.
252. Corey EJ, Loh T-P, Roper TD, Azimioara MD, Noe MC. *J Am Chem Soc*. 1992; 114:8290.
253. Kiyooka S-I. *Rev Heteroat Chem*. 1997; 17:245.
254. Corey EJ, Cywin CL, Roper TD. *Tetrahedron Lett*. 1992; 33:6907.
255. Wong MW. *J Org Chem*. 2005; 70:5487. [PubMed: 15989330]
256. (a) Yalalov DA, Tsogoeva SB, Schmatz S. *Adv Synth Catal*. 2006; 348:826.(b) Hamza A, Schubert G, Soos T, Papai I. *J Am Chem Soc*. 2006; 128:13151. [PubMed: 17017795] (c) Liu TY, Li R, Chai Q, Long J, Li BJ, Wu Y, Ding LS, Chen YC. *Chem Eur J*. 2006; 13:319.
257. Wei S, Yalalov DA, Tsogoeva SB, Schmatz S. *Catal Today*. 2007; 121:151.
258. Okino T, Hoashi Y, Furukawa T, Xu X, Takemoto Y. *J Am Chem Soc*. 2005; 127:119. [PubMed: 15631461]
259. Chen D, Lu N, Zhang G, Mi S. *Tetrahedron: Asymmetry*. 2009; 20:1365.
260. Tan B, Lu Y, Zeng X, Chua PJ, Zhong G. *Org. Lett*. 2010; 12:2682. [PubMed: 20469881]
261. Liu T-Y, Li R, Chai Q, Long J, Li B-J, Wu Y, Ding L-S, Chen Y-C. *Chem Eur J*. 2007; 13:319.
262. Zhu R, Zhang D, Wu J, Liu C. *Tetrahedron: Asymmetry*. 2007; 18:1655.
263. Xu X, Yabuta T, Yuan P, Takemoto Y. *Synlett*. 2006; 1:137-140.
264. (a) Zhu R, Zhang D, Wu J, Liu C. *Tetrahedron: Asymmetry*. 2007; 18:1655.(b) Xu X, Yabuta T, Yuan P, Takemoto Y. *Synlett*. 2006; 1:137.
265. Sibi MP, Itoh K. *J Am Chem Soc*. 2007; 129:8064. [PubMed: 17552527]
266. Simón L, Goodman JM. *Org Biomol Chem*. 2009; 7:483. [PubMed: 19156313]
267. Zhu Y, Drueckhammer DG. *J Org Chem*. 2005; 70:7755. [PubMed: 16149809]
268. Wang S-X, Chen F-E. *Adv Synth Catal*. 2009; 351:547.
269. Zhu R-X, Wang R-X, Zhang D-J, Liu C-B. *Aust J Chem*. 2009; 62:157.
270. Corey EJ, Grogan MJ. *Org Lett*. 1999; 1:157. [PubMed: 10822552]
271. Schuster T, Kurz M, Göbel MW. *J Org Chem*. 2000; 65:1697. [PubMed: 10814142]
272. Nugent BM, Yoder RA, Johnston JN. *J Am Chem Soc*. 2004; 126:3418. [PubMed: 15025457]
273. Sohtome Y, Hashimoto Y, Nagasawa K. *Adv Synth Catal*. 2005; 347:1643.
274. Terada M, Nakano M, Ube H. *J Am Chem Soc*. 2006; 128:16044. [PubMed: 17165751]
275. Lohmeijer BGG, Pratt RC, Leibfarth F, Logan JW, Long DA, Dove A, Nederberg PF, Choi J, Wade C, Waymouth RM, Hedrick JL. *Macromolecules*. 2006; 39:8574.
276. Li J, Jiang W-Y, Han K-L, He G, Zhong, Li C. *J Org Chem*. 2003; 68:8786. [PubMed: 14604345]
277. Arnaud R, Adamo C, Cossi M, Milet A, Vallee Y, Barone V. *J Am Chem Soc*. 2000; 122:324.
278. Walch SP, Bakes ELO. *Chem Phys Lett*. 2001; 346:267.
279. Chuma A, Horn HW, Swope WC, Pratt RC, Zhang L, Lohmeijer BGG, Wade CG, Waymouth RM, Hedrick JL, Rice JE. *J Am Chem Soc*. 2008; 130:6749. [PubMed: 18454532]
280. Simón L, Goodman JM. *J Org Chem*. 2007; 72:9656. [PubMed: 17997577]
281. Almasi D, Alonso DA, Gómez-Bengoa E, Nájera C. *J Org Chem*. 2009; 74:6163. [PubMed: 19627118]
282. Huang SY, Ma J, Li JP, Zhao N, Wei W, Sun YH. *Catal Commun*. 2008; 9:276.
283. Ma J, Zhao N, Xia F, Wei W, Sun YH. *THEOCHEM*. 2009; 911:40.
284. Russo A, Lattanzi A. *Eur J Org Chem*. 2008:2767.
285. Zhang Z, Rooshenas P, Hausmann H, Schreiner PR. *Synthesis*. 2009:1531.
286. (a) Liu J, Yang Z, Wang Z, Wang F, Chen X, Liu X, Feng X, Su Z, Hu C. *J Am Chem Soc*. 2008; 130:5654. [PubMed: 18380434] (b) Yang Z, Liu J, Liu X, Wang Z, Feng X, Hu C. *Adv Synth Catal*. 2008; 350:2001.
287. Chen X, Wang J, Zhu Y, Shang D, Gao B, Liu X, Feng X, Su Z, Hu C. *Chem Eur J*. 2008; 14:10896.

288. Yang Z, Liu J, Liu X, Wang Z, Feng X, Su Z, Hu C. *Adv Synth Catal.* 2008; 350:2001.
289. Cucinotta CS, Kosa M, Melchiorre P, Cavalli A, Gervasio FL. *Chem Eur J.* 2009; 15:7913.
290. Rho HS, Oh SH, Lee JW, Lee JY, Chin J, Song CE. *Chem Commun.* 2008:1208.
291. Oh SH, Rho HS, Lee JW, Lee JE, Youk SH, Chin J, Song CE. *Angew Chem Int Ed.* 2008; 47:7872.
292. Kobbelgaard S, Brandes S, Jørgensen KA. *Chem-Eur J.* 2008; 14:1464.
293. Çelebi-Ölçüm N, Aviyente V, Houk KN. *J Org Chem.* 2009; 74:6944. [PubMed: 19689147]
294. (a) Inoue S, Oku JI. *J Chem Soc, Chem Commun.* 1981:229.(b) Tanaka K, Mori A, Inoue S. *J Org Chem.* 1990; 55:181.
295. (a) Danda H, Nishikawa H, Otaka K. *J Org Chem.* 1991; 56:6740.(b) Danda H. *Synlett.* 1991:263. (c) Kogut EF, Thoen JC, Lipton MA. *J Org Chem.* 1998; 63:4604.
296. Shvo Y, Becker GM, Elgavi A. *Tetrahedron: Asymmetry.* 1996; 7:911.
297. Li Z, Zhang J, Brouwer C, Yang C-G, Reich NW, He C. *Org. Lett.* 2006; 8:4175. [PubMed: 16956180]
298. Li X, Ye S, He C, Yu Z-X. *Eur J Org Chem.* 2008:4296.
299. (a) Bach RD, Glukhovtsev MN, Gonzalez C, Marquez M, Estevez CM, Baboul AG, Schlegel HB. *J Phys Chem A.* 1997; 101:6092.(b) Houk KN, Liu J, DeMello NC, Condroski KR. *J Am Chem Soc.* 1997; 119:10147.(c) Crehuet R, Anglada JM, Cremer D, Bofill JM. *J Phys Chem A.* 2002; 106:3917.(d) Bach RD, Dmitrenko O, Adam W, Schambony S. *J Am Chem Soc.* 2003; 125:924. [PubMed: 12537490] (e) Dmitrenko O, Bach RD. *J Phys Chem A.* 2004; 108:6886.
300. Armstrong A, Washington I, Houk KN. *J Am Chem Soc.* 2000; 122:6297.
301. Armstrong A, Hayter BR. *Chem Commun.* 1998:621.
302. (a) Tian H, She Z, Shu L, Yu H, Shi Y. *J Am Chem Soc.* 2000; 122:11551.(b) Tian H, She Z, Xu J, Shi Y. *Org Lett.* 2001; 3:1929. [PubMed: 11405747]
303. Singleton DA, Wang Z. *J Am Chem Soc.* 2005; 127:1929.
304. Cramer CJ, Truhlar DG. *Acc Chem Res.* 2008; 41:760.
305. Oyola Y, Singleton DA. *J Am Chem Soc.* 2009; 131:3130. [PubMed: 19215077]

Biographies



K. N. Houk received his Ph.D. at Harvard with R. B. Woodward. He has taught at Louisiana State University, the University of Pittsburgh, and UCLA since 1986. From 1988–1990, he was Director of the Chemistry Division of the National Science Foundation. He is the Saul Winstein Chair in Organic Chemistry at UCLA.



Paul Ha-Yeon Cheong was born in 1979 in Taegu, Korea. In 2001 he received his A.B. degree from Bowdoin College. He did his Ph.D. research with K. N. Houk at UCLA, and collaborated with Paul Wender, Timothy Jamison, Gregory Fu, Carlos Barbas, and Dean Toste during that time and a postdoc afterwards. In 2009, he joined the faculty at Oregon State University.



Claude Y. Legault received his B.Sc. in chemistry from Université de Sherbrooke (Canada) in 1999. He did his Ph.D. research as an NSERC and FQRNT scholar with Professor André B. Charette at Université de Montréal. He then worked under Professor K. N. Houk at UCLA as an NSERC postdoctoral fellow. In 2008, he joined the Department of Chemistry at Université de Sherbrooke.



Joann M. Um received her B.A. in biochemistry at Columbia University in 1999 and an M.S. in chemistry at University of California, Berkeley in 2001. She spent four years as a synthetic organic chemist at both Merck Research Laboratories and Genentech, Inc. before coming to UCLA to complete Ph.D. studies in computational organic chemistry under Professor K. N. Houk.



Nihan Çelebi-Ölçüm received her B.S. degree in chemistry at Bođaziçi University in 1997, and M.S. degree in computational and theoretical chemistry at Université Henri Poincaré (Nancy, France) in 1999. She completed her Ph.D. under the direction of Viktorya Aviyente at Bođaziçi University before joining the Houk group at UCLA as a postdoc in 2009.

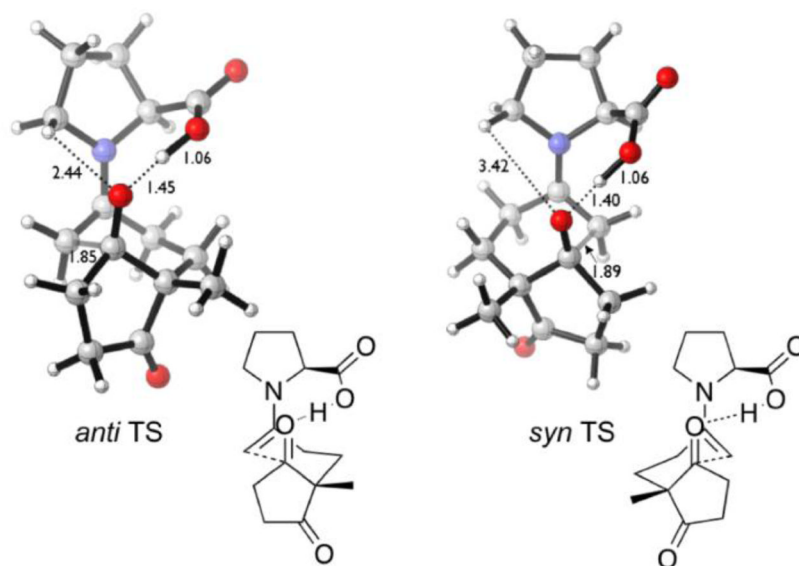


Figure 1. The computed *anti* and *syn* transition structures of proline-catalyzed Hajos-Parrish reaction

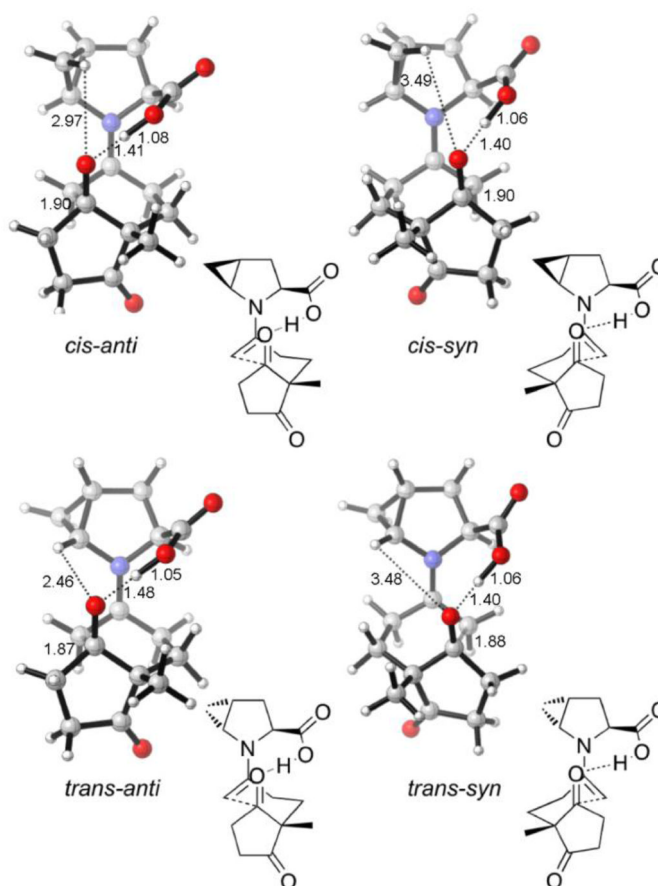


Figure 2.
The computed *anti* and *syn* transition structures of 4,5-methanoproline (**5**, **6**)-catalyzed Hajos-Parrish reactions.

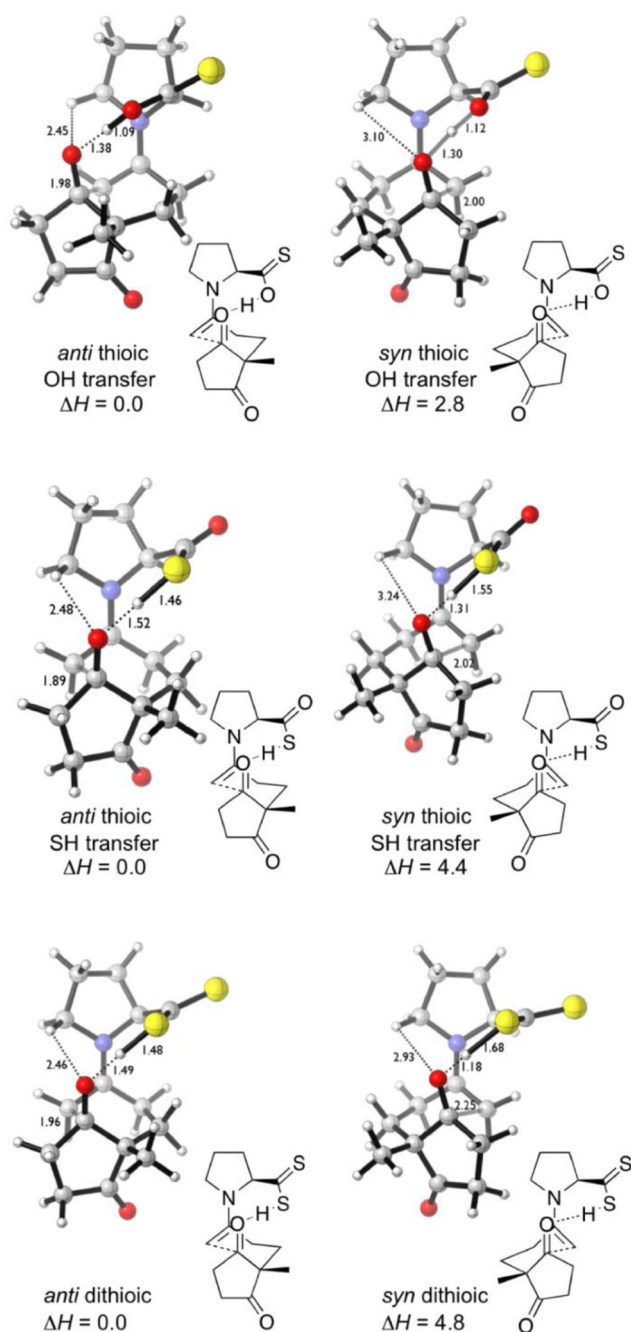


Figure 3. The computed *anti* and *syn* transition structures of thioic acid (2) and dithioic acid (3) catalyzed Hajos-Parrish reactions.

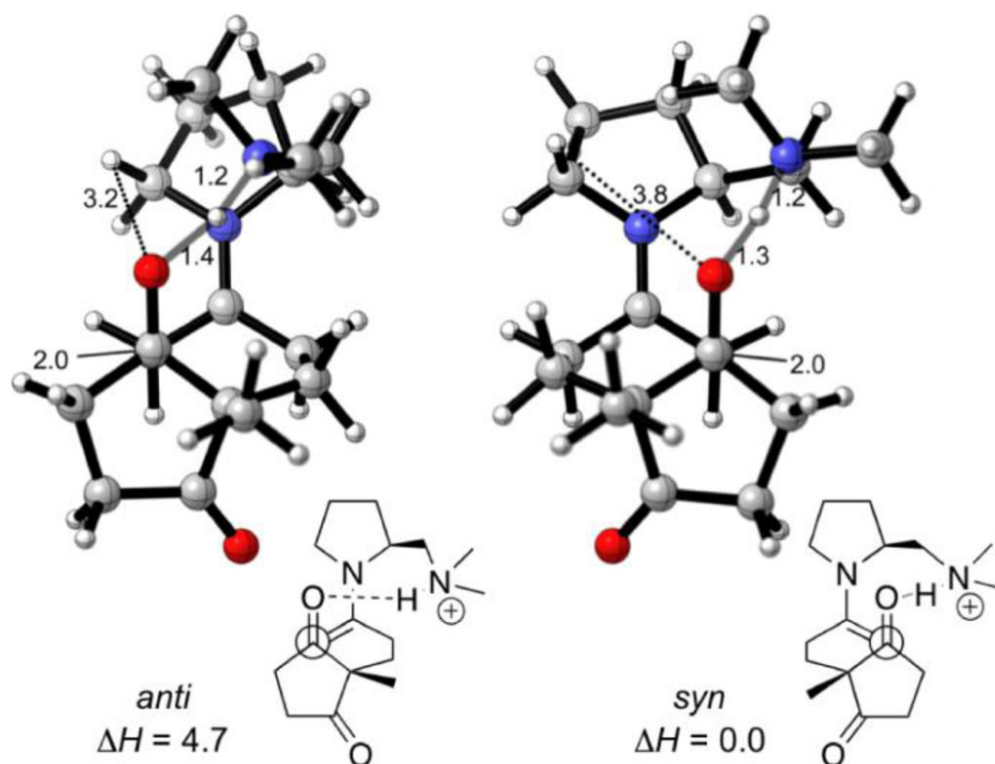


Figure 4. The computed *anti* and *syn* transition structures of quaternary ammonium (**4**) catalyzed Hajos-Parrish reactions.

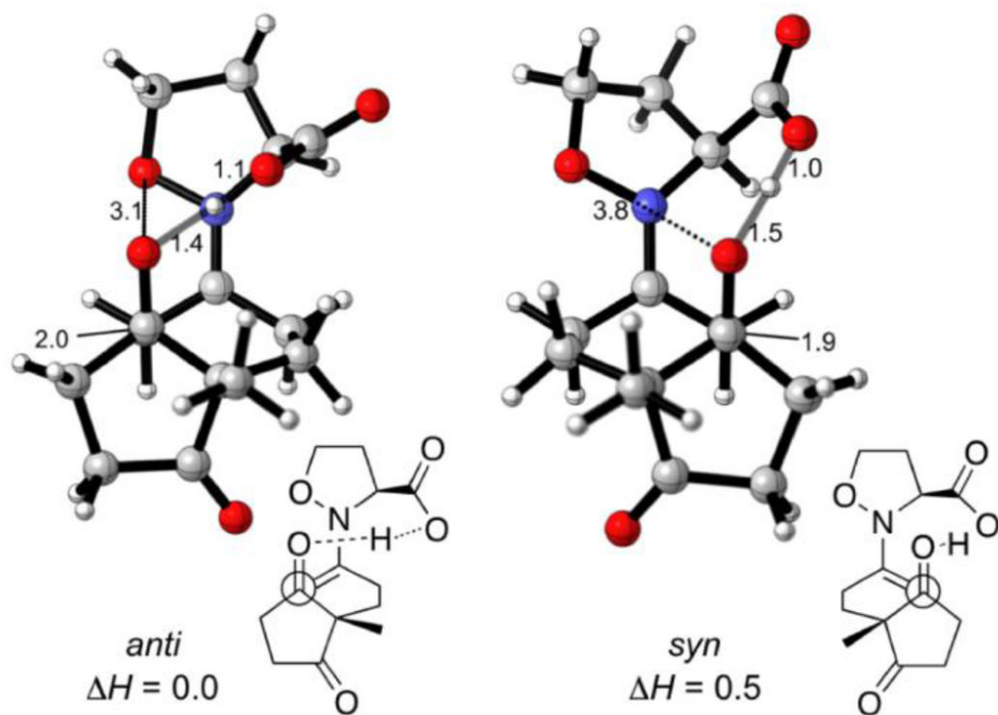


Figure 5. The computed *anti* and *syn* TSs of isoxazolidine-3-carboxylic acid (**7**) catalyzed Hajos-Parrish reactions.

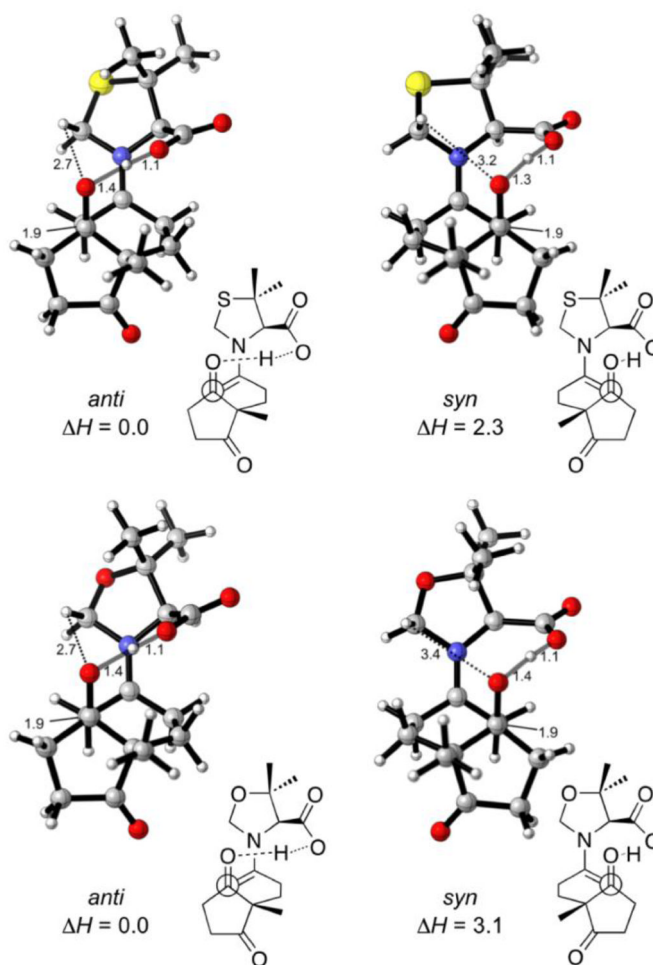


Figure 6. The computed *anti* and *syn* TSs of 5,5-dimethylthiazolidine-4-carboxylic acid (DMTC) and 5,5-dimethyloxazolidine-4-carboxylic acid (DMOC) catalyzed Hajos-Parrish reactions.

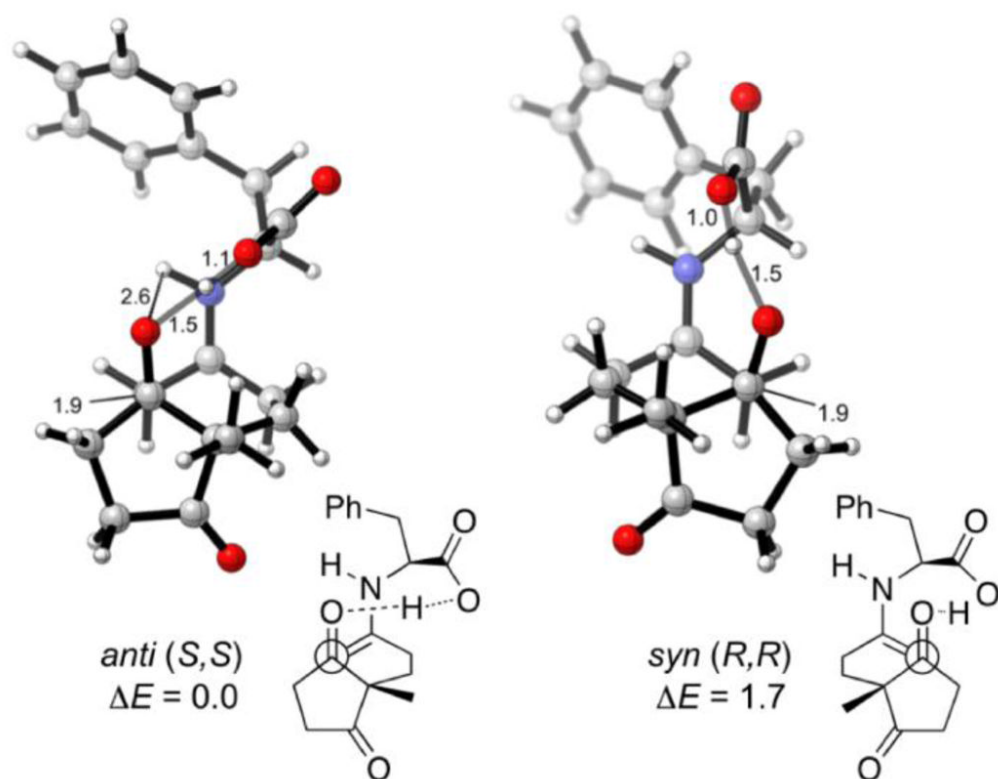


Figure 7.
Phenylalanine catalyzed Hajos-Parrish reaction.

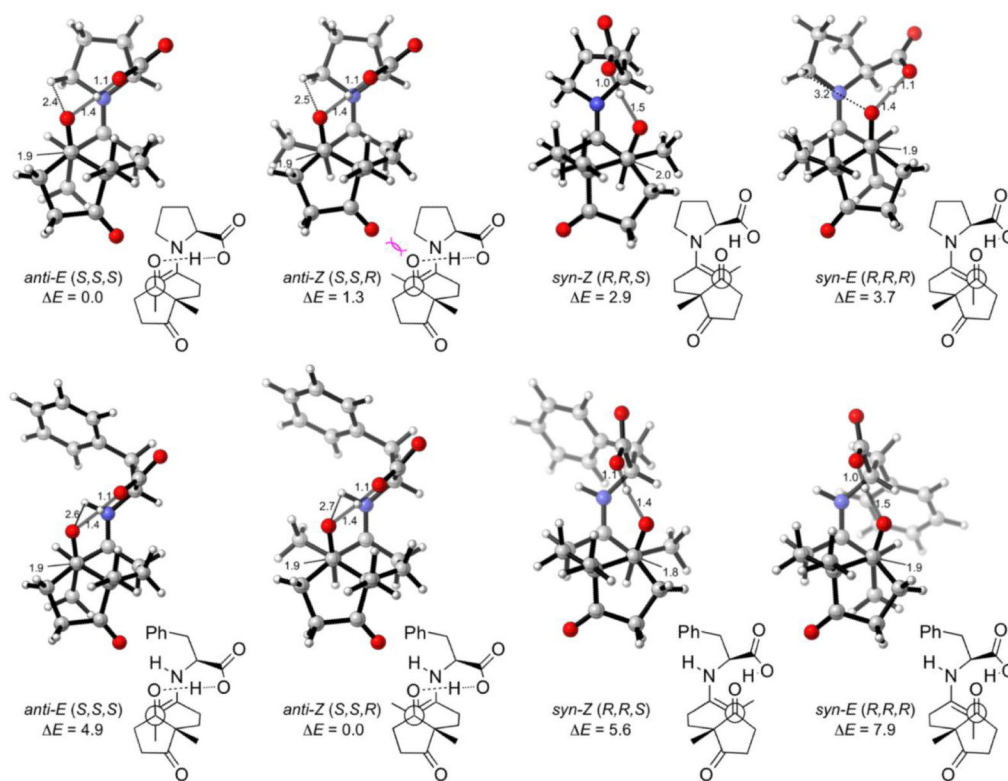


Figure 8. Proline and phenylalanine catalyzed asymmetric intramolecular aldol condensation.

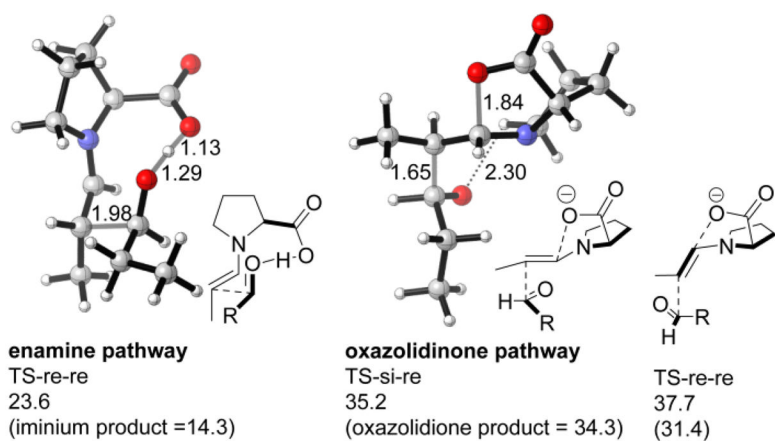


Figure 9. Gibbs free energies of activation (ΔG^\ddagger , kcal/mol) for the C-C bond formation in the enamine and oxazolidinone pathways calculated with B3LYP/6-31+G(d, p). Free energies of iminium and oxazolidinone products (ΔG , kcal/mol) are given in parenthesis.

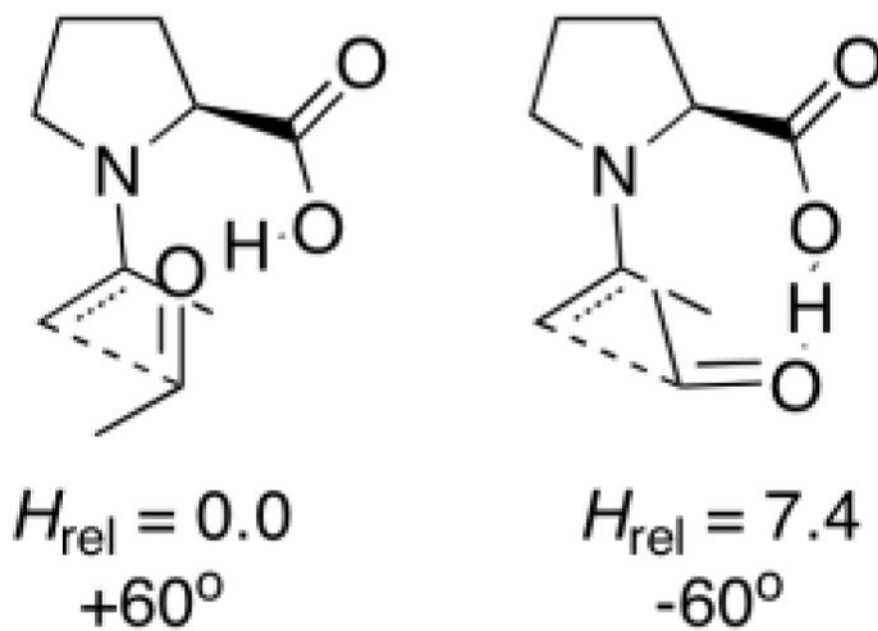


Figure 10. Rotameric *anti-re* transition structures of the intermolecular aldol reaction between acetone and acetaldehyde, catalyzed by proline.

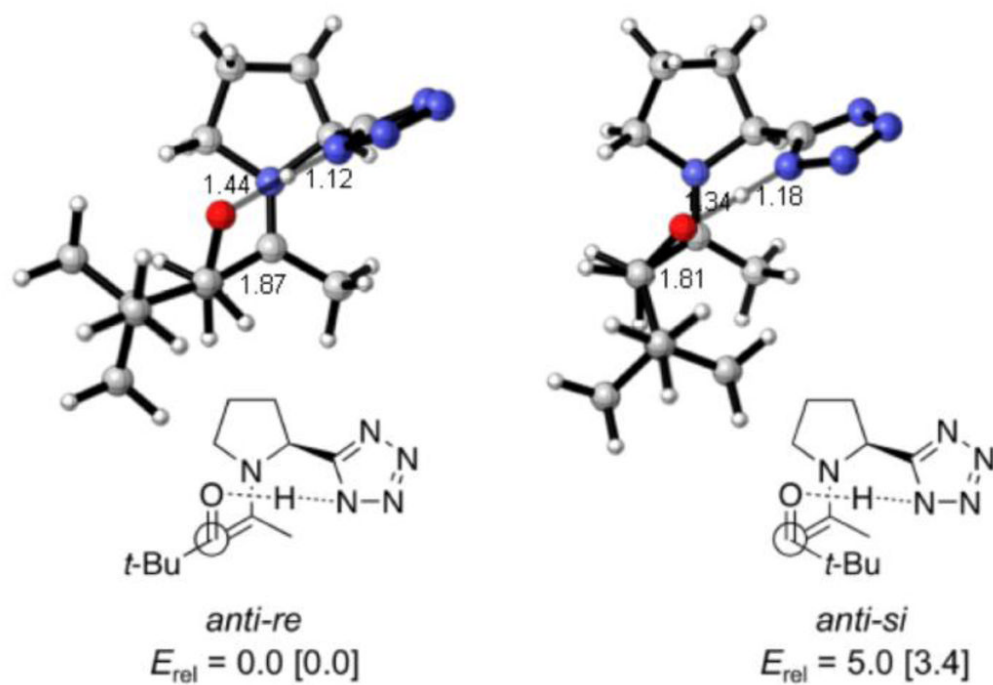


Figure 11. *Anti-re* and *anti-si* TSs of the intermolecular aldol reaction between acetone and pivaldehyde, catalyzed by proline and 5-pyrrolidin-2-yltetrazole. DMSO values in brackets.

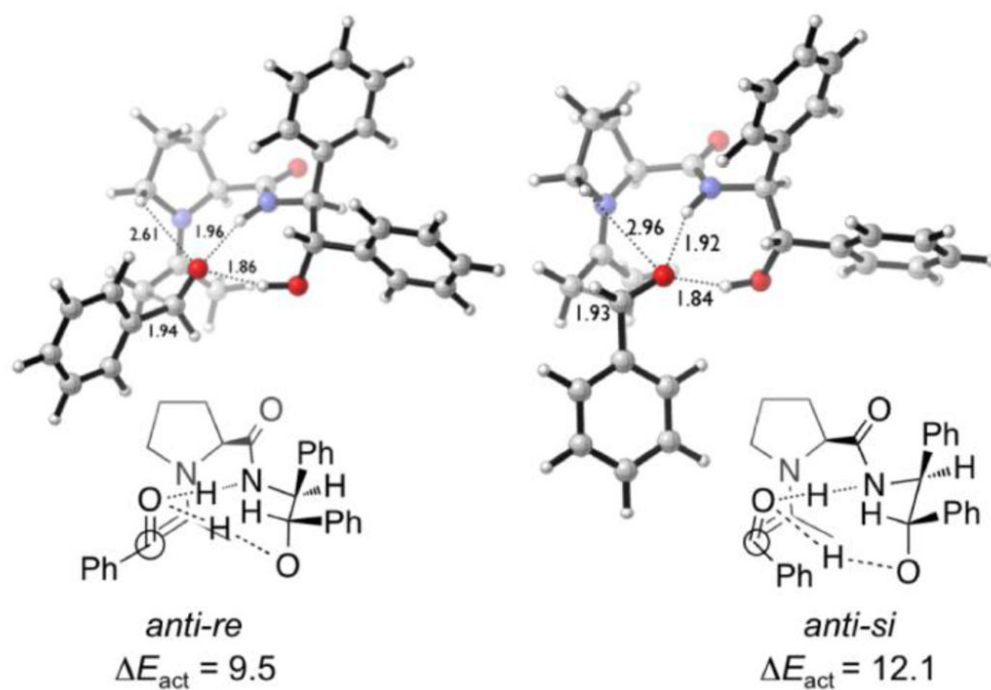


Figure 12. *Anti-re* and *anti-si* transition structures of the intermolecular aldol reaction between acetone and benzaldehyde, catalyzed by (1*S*,2*S*)-diphenyl-2-aminoethanol amide proline derivative.

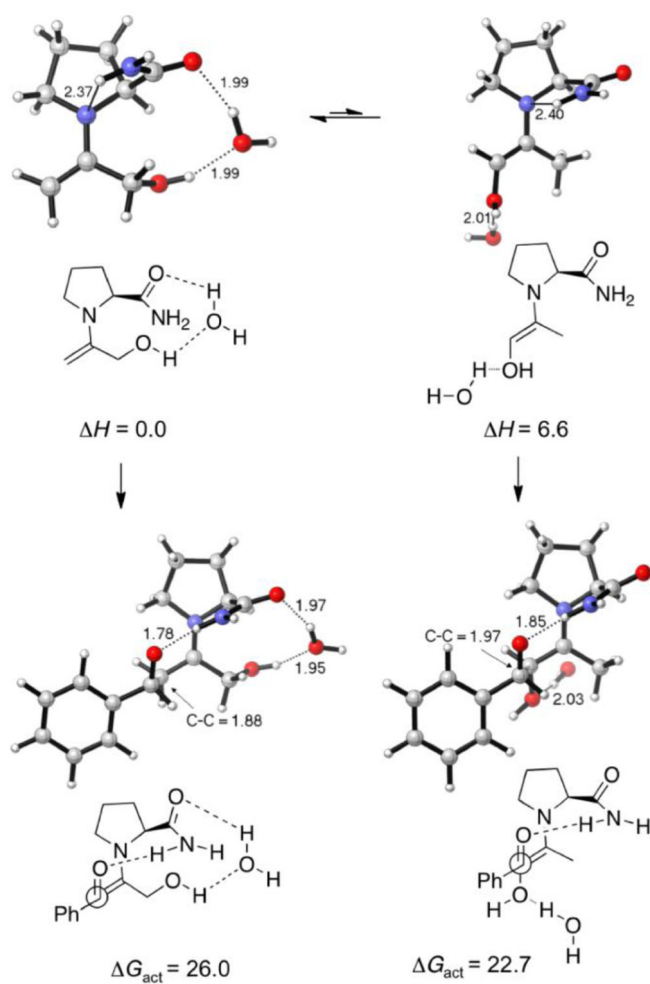


Figure 13.
Aldol reaction of benzaldehyde and hydroxyacetone catalyzed by proline amide.

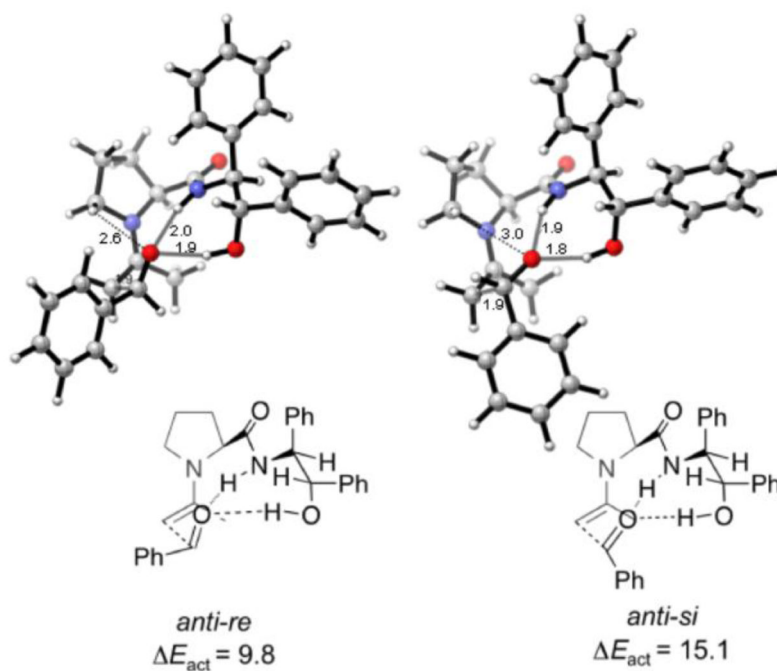


Figure 14. *anti-re* and *anti-si* transition structures for the prolineamide-catalyzed aldol reaction.

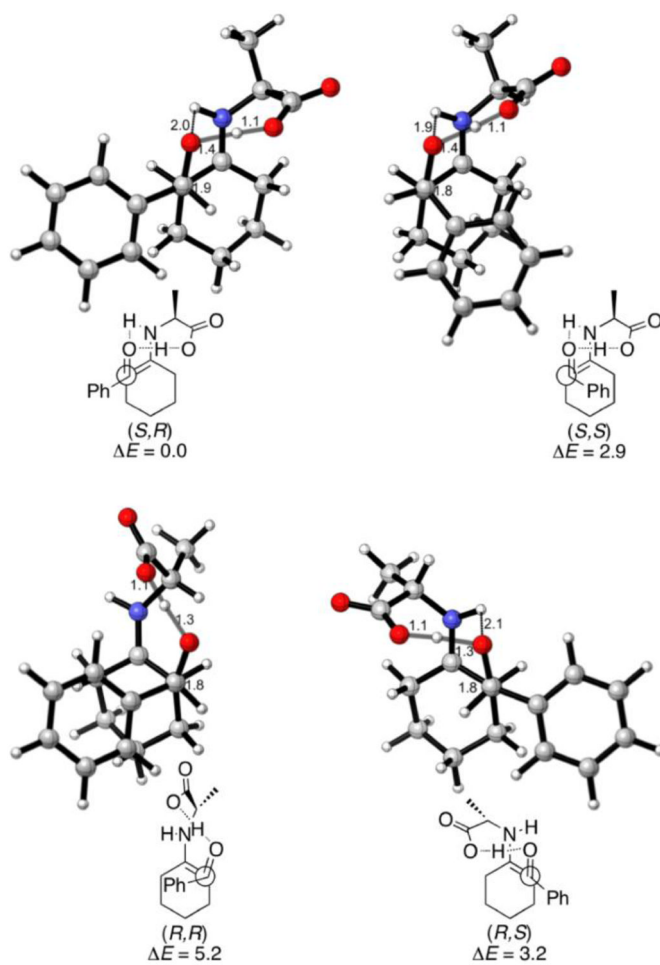


Figure 15.
 (S,R) , (S,S) , (R,R) , and (R,S) TSs for the reaction between cyclohexanone enamine of alanine and benzaldehyde

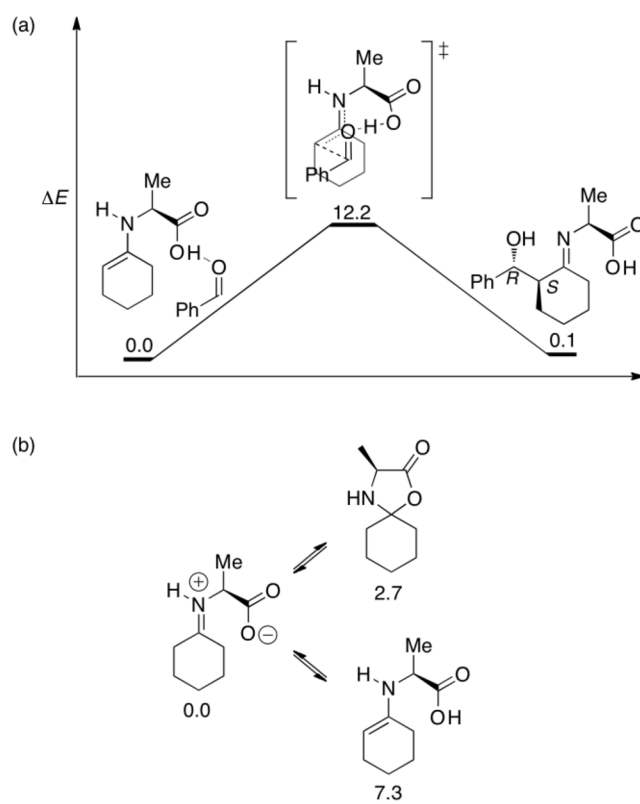


Figure 16. (a) Overall reaction profile for primary amino acid catalyzed aldol reaction. (b) Relative energies of oxazolidinone and enamine (kcal/mol).

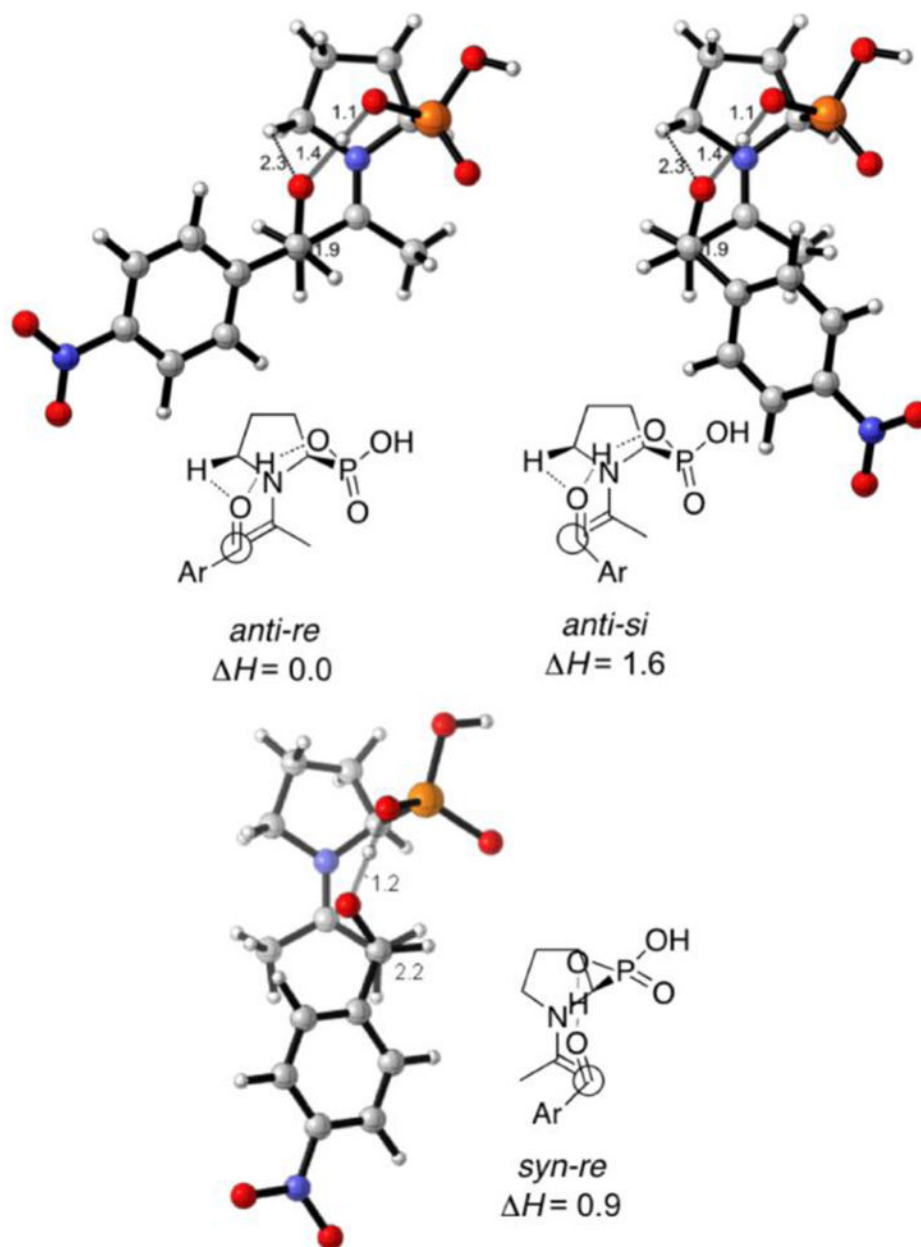


Figure 17.
The most stable *anti-re*, *anti-si*, and *syn-re* transition structures.

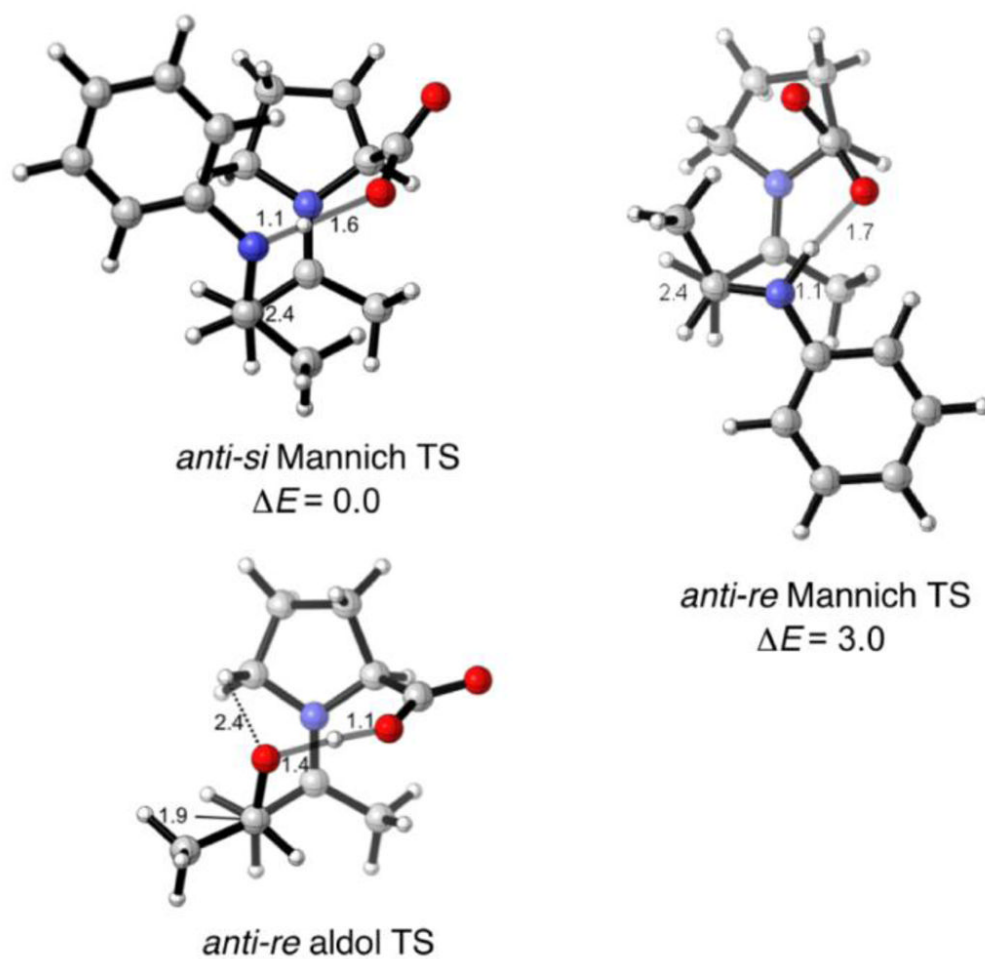


Figure 18. The *anti-re* and *-si* TSs of the Mannich reaction, and *anti-re* TS of the aldol reaction catalyzed by proline.

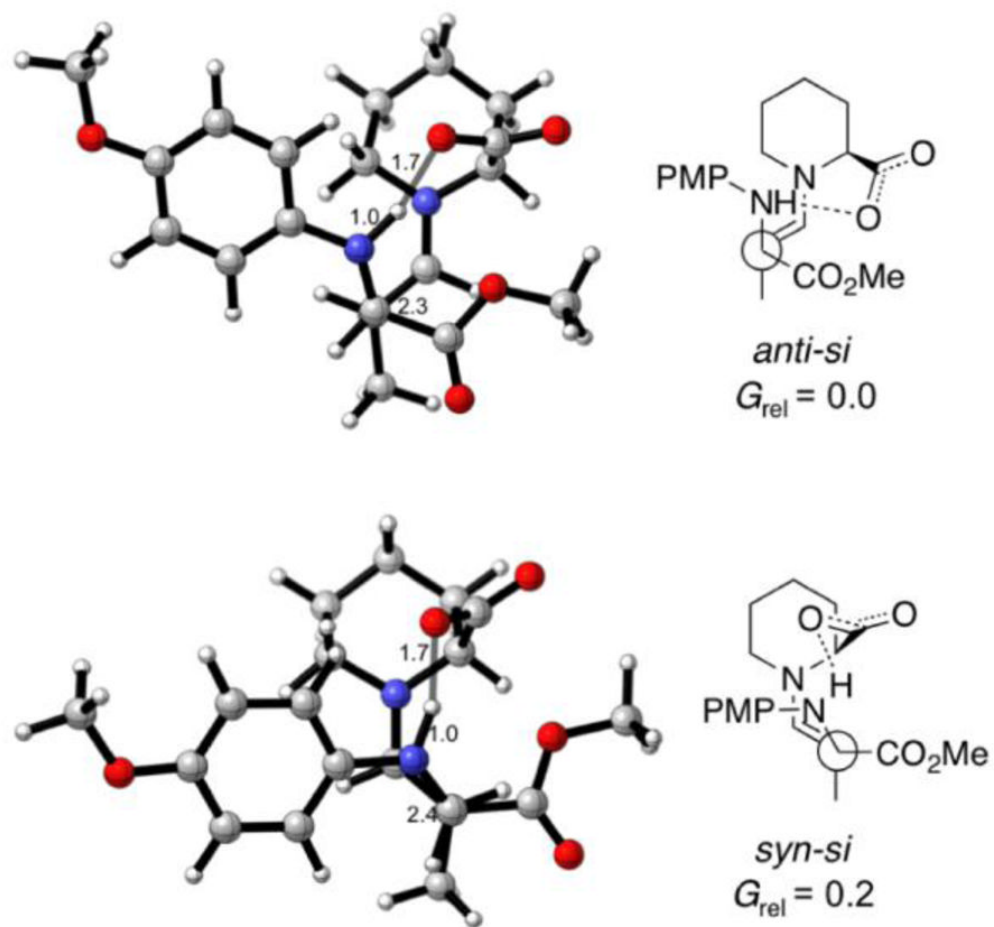


Figure 19. The *anti-si* and *syn-si* transition structures of Mannich reaction catalyzed by pipercolic acid.

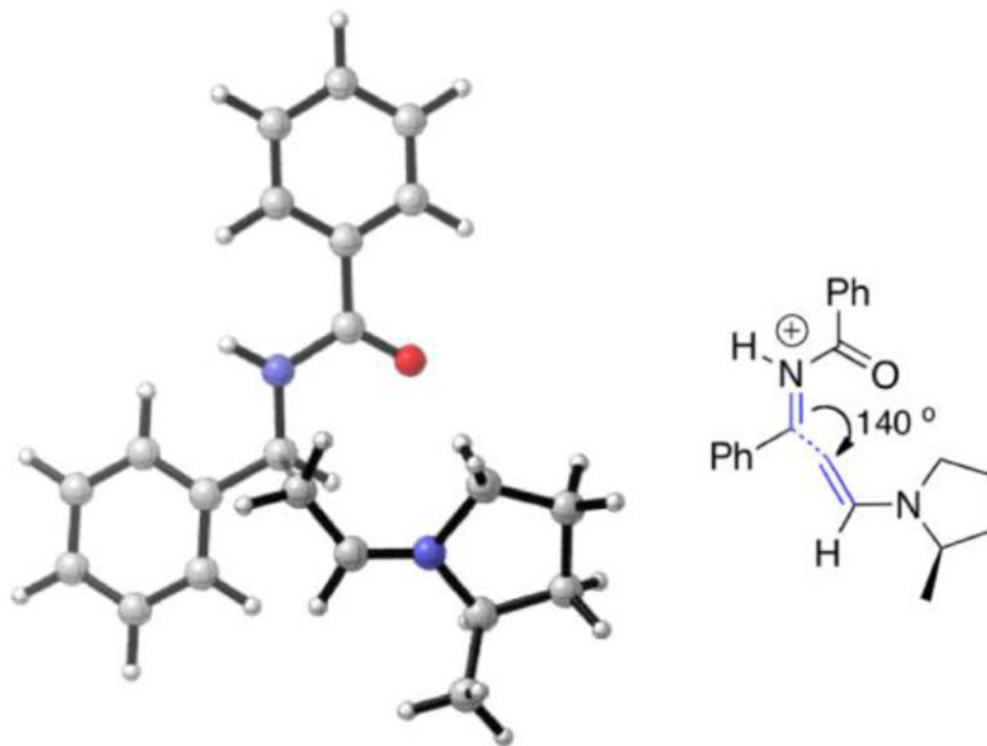


Figure 20. Transition state model for Mannich reaction of acetaldehyde and protonated *N*-benzoyl iminium.

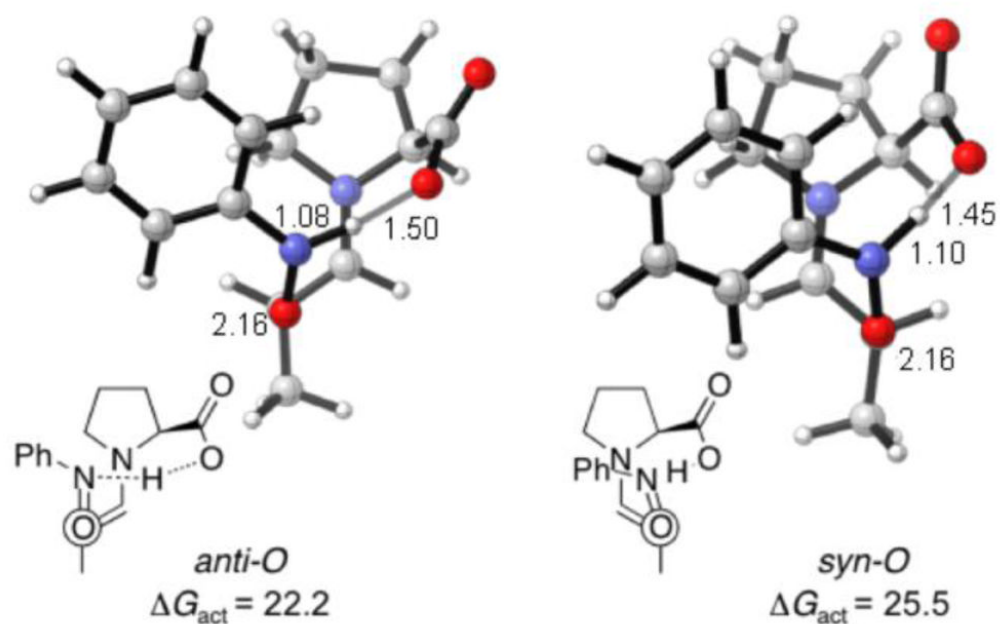


Figure 21. B3LYP/6-31G(d) transition structures for the α -aminoxylation reaction. Activation energies include HF/6-31+G(d, p) DMSO, PCM model, UAKS radii solvation.

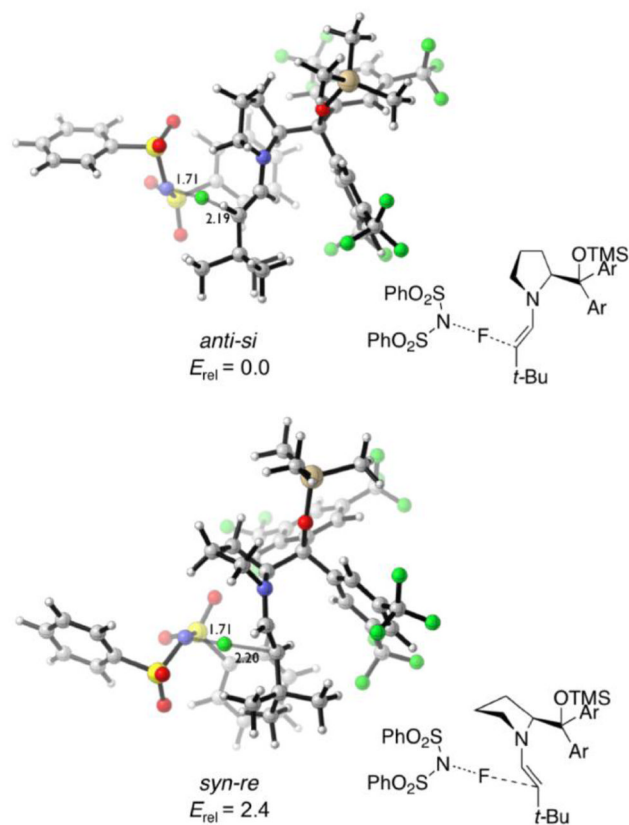


Figure 22. Lowest energy transition structures for the α -fluorination of 2,2-dimethylbutanal.

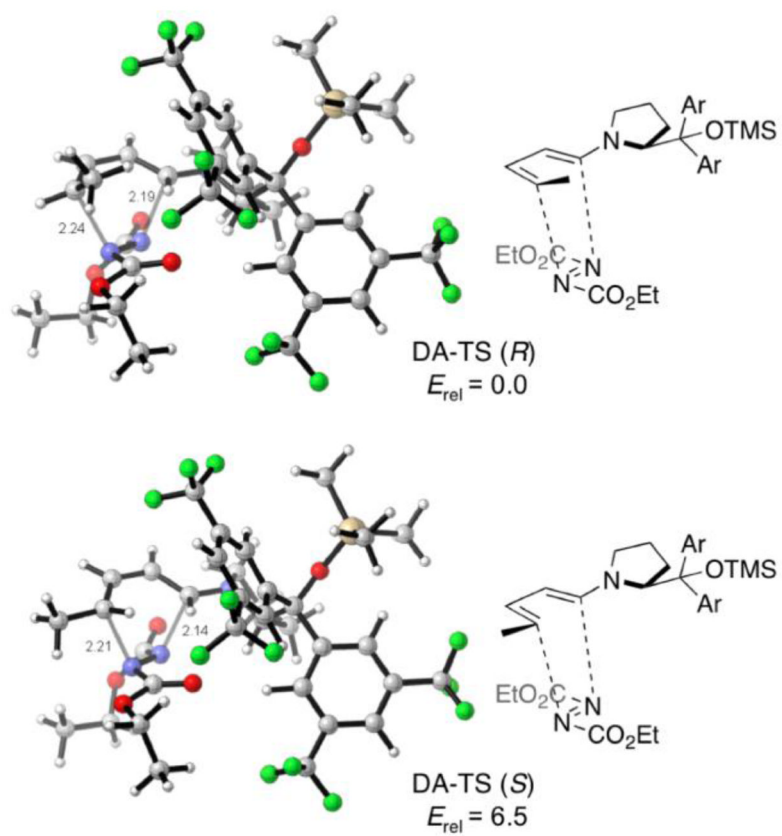


Figure 23. Lowest energy transition structures for the [4+2] cycloaddition of enamines and DEAD.

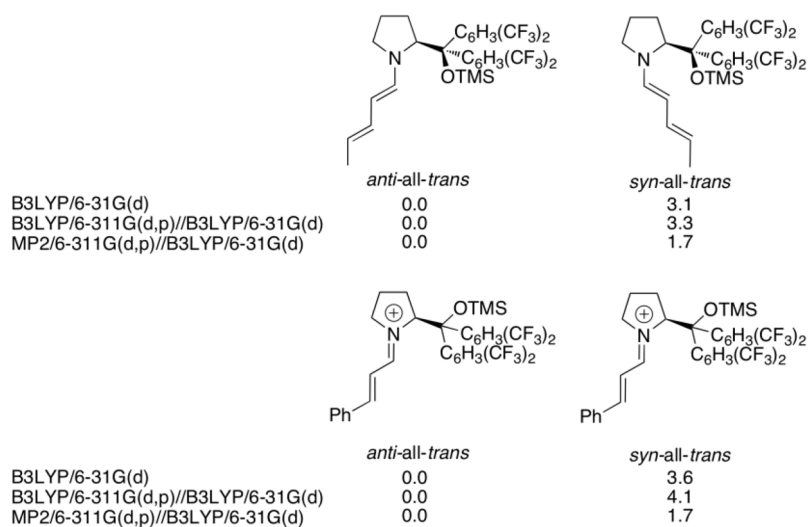


Figure 24.
DFT gas phase relative energies calculated by Seebach and co-workers (ref 47).

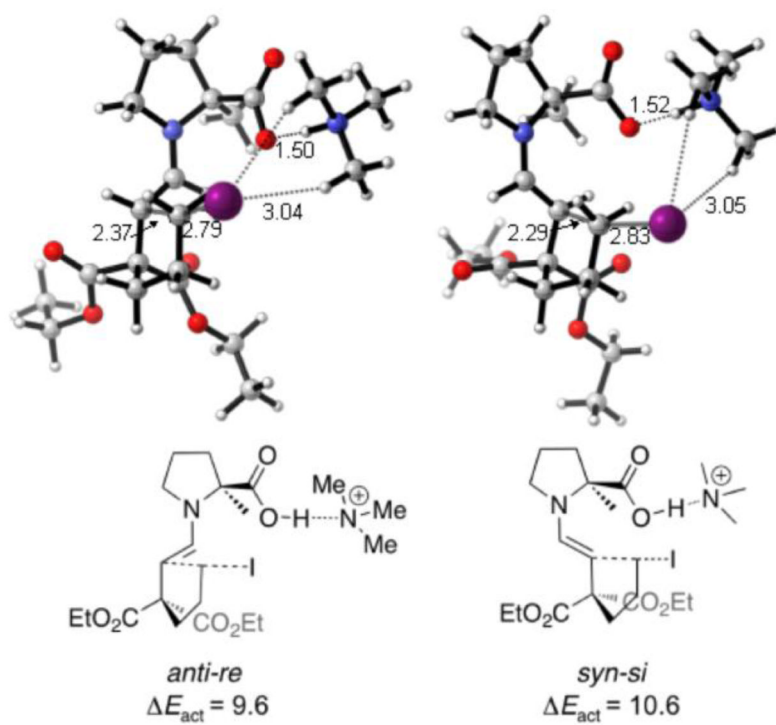


Figure 25.
The two lowest energy alkylation transition structures involving 2-methylproline and trimethylamine

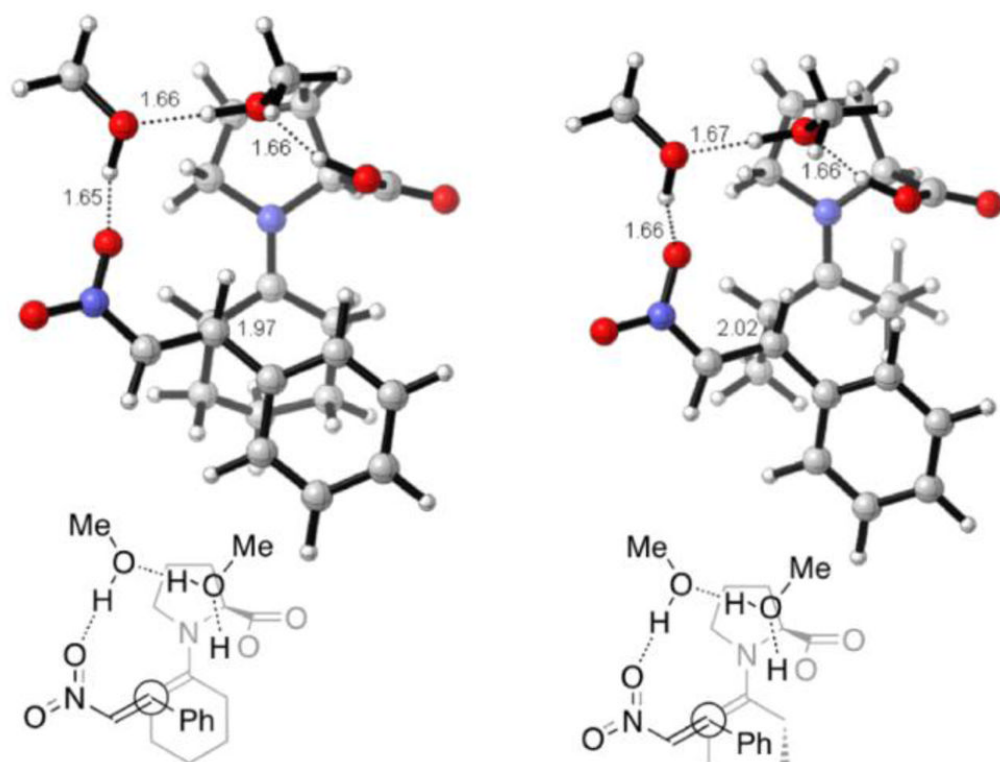


Figure 26. Lowest energy transition structures for the proline catalyzed Michael addition of nitrostyrene and cyclohexanone (left) and 3-pentanone (right), with 2 explicit water molecules.

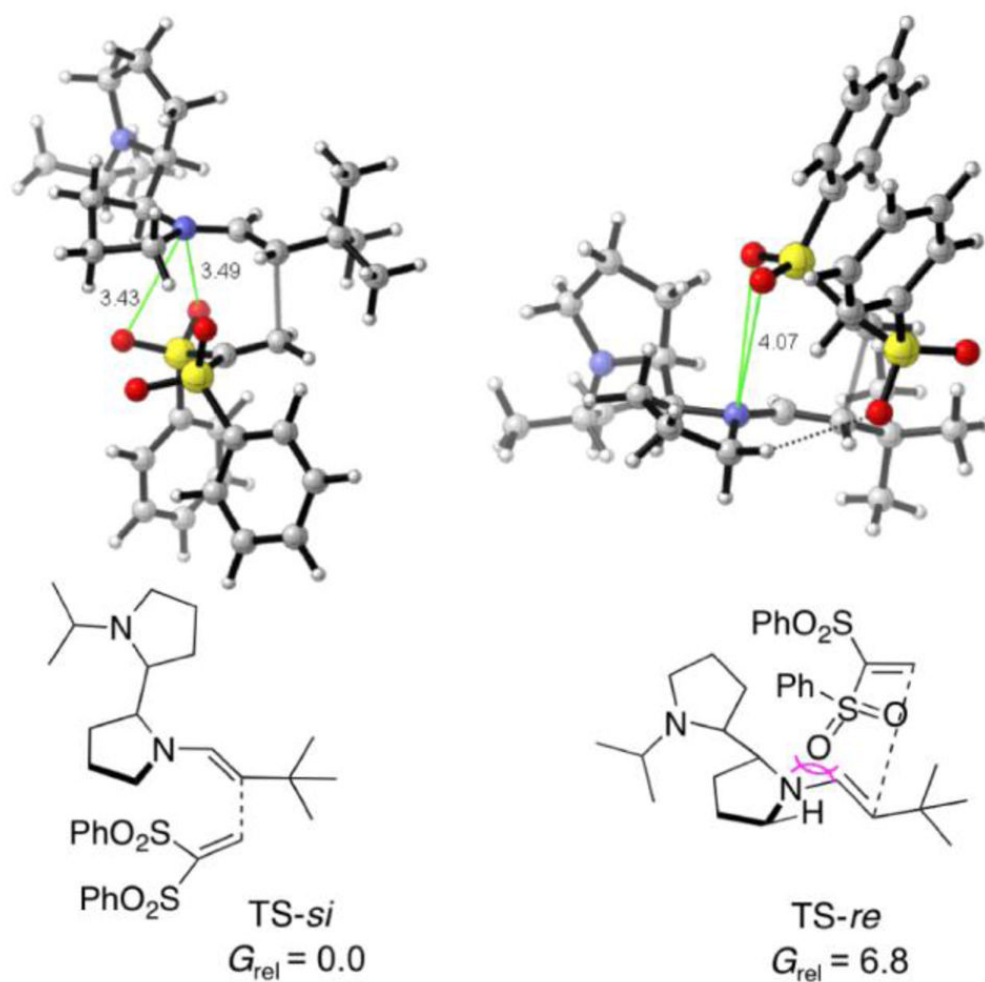


Figure 27. Michael addition transition structures for the addition of 3,3-dimethylisobutyraldehyde to a vinyl disulfone.

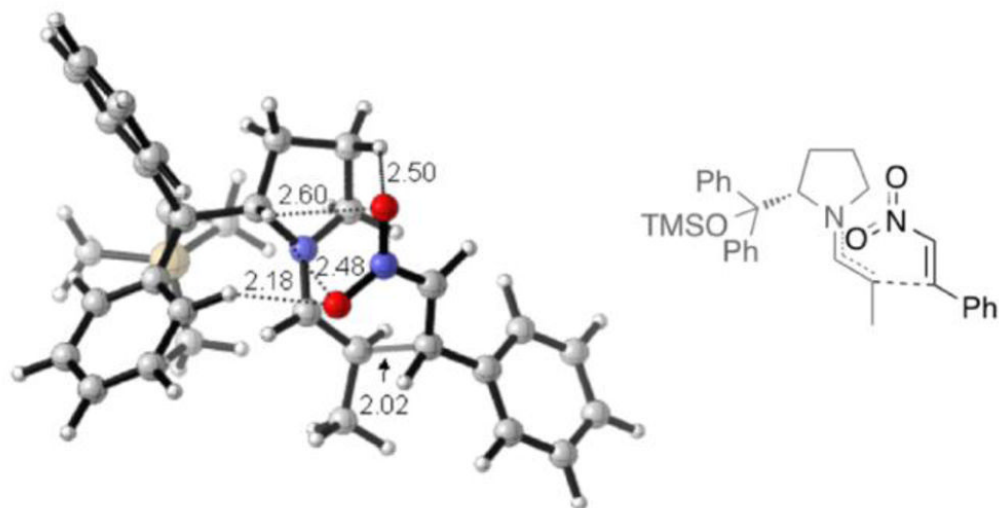


Figure 28.
First Michael addition transition structure in the cascade sequence of Scheme 54.

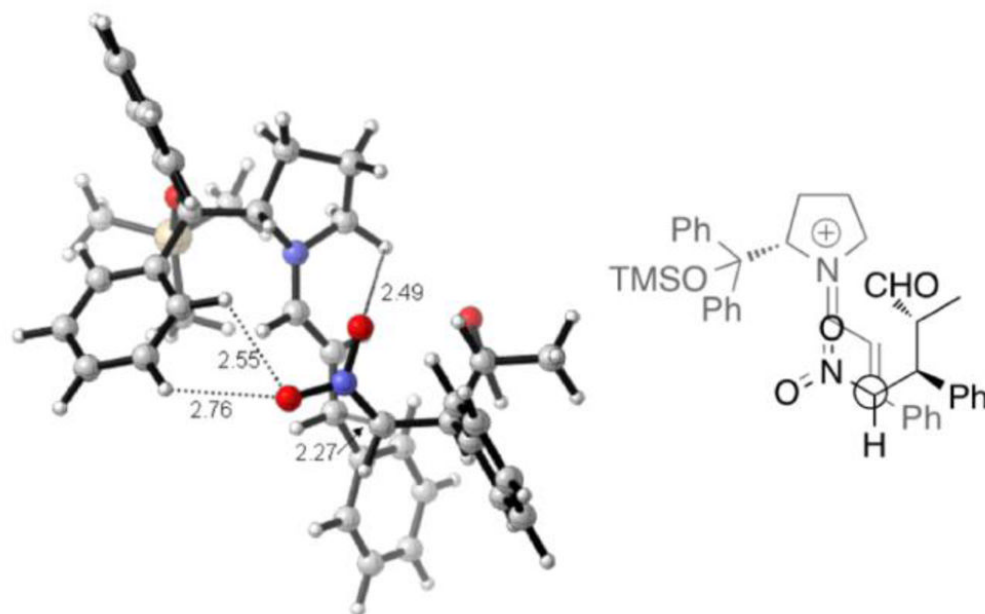


Figure 29.
Second Michael addition transition structure in the cascade sequence

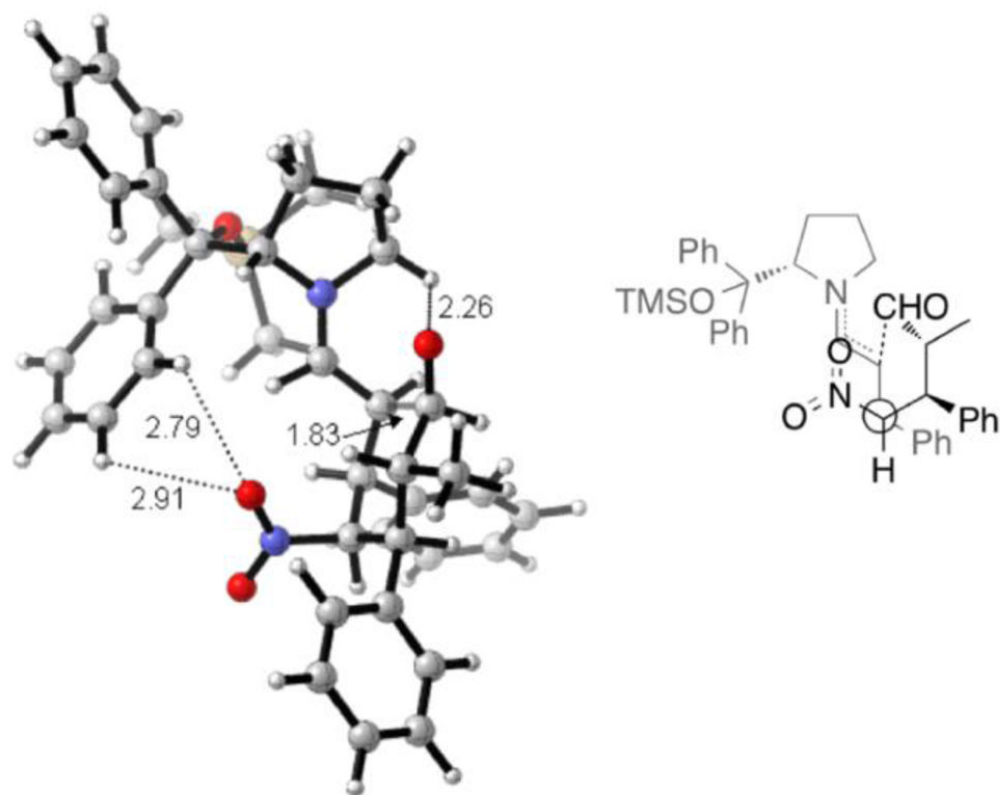


Figure 30.
Intramolecular aldol cyclization in the cascade sequence

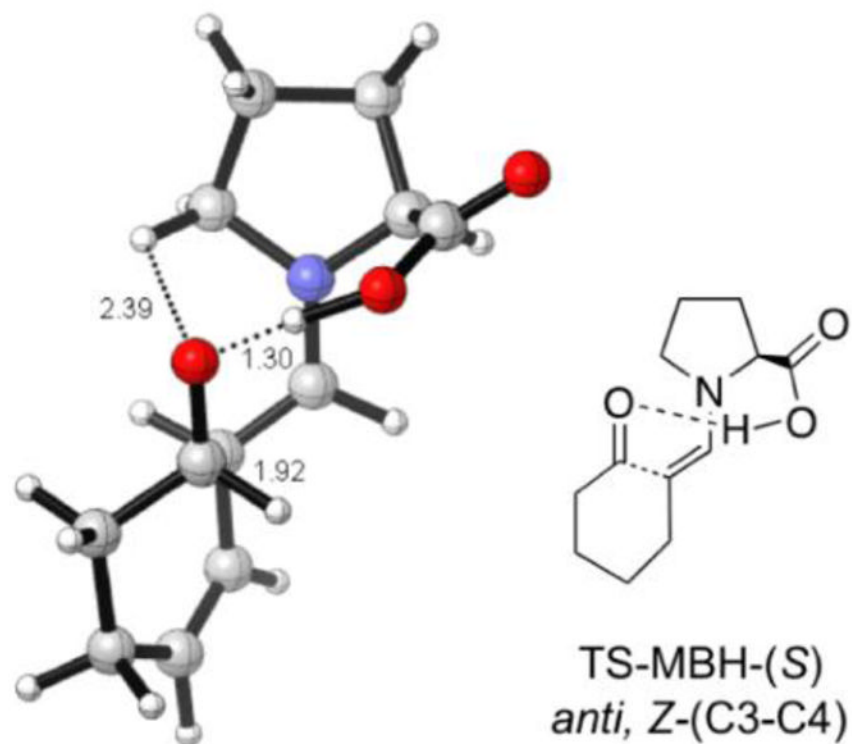


Figure 31. B3LYP/6-31G(d, p) major cyclization transition structure for the proline-catalyzed intramolecular Morita-Baylis-Hillman reaction.

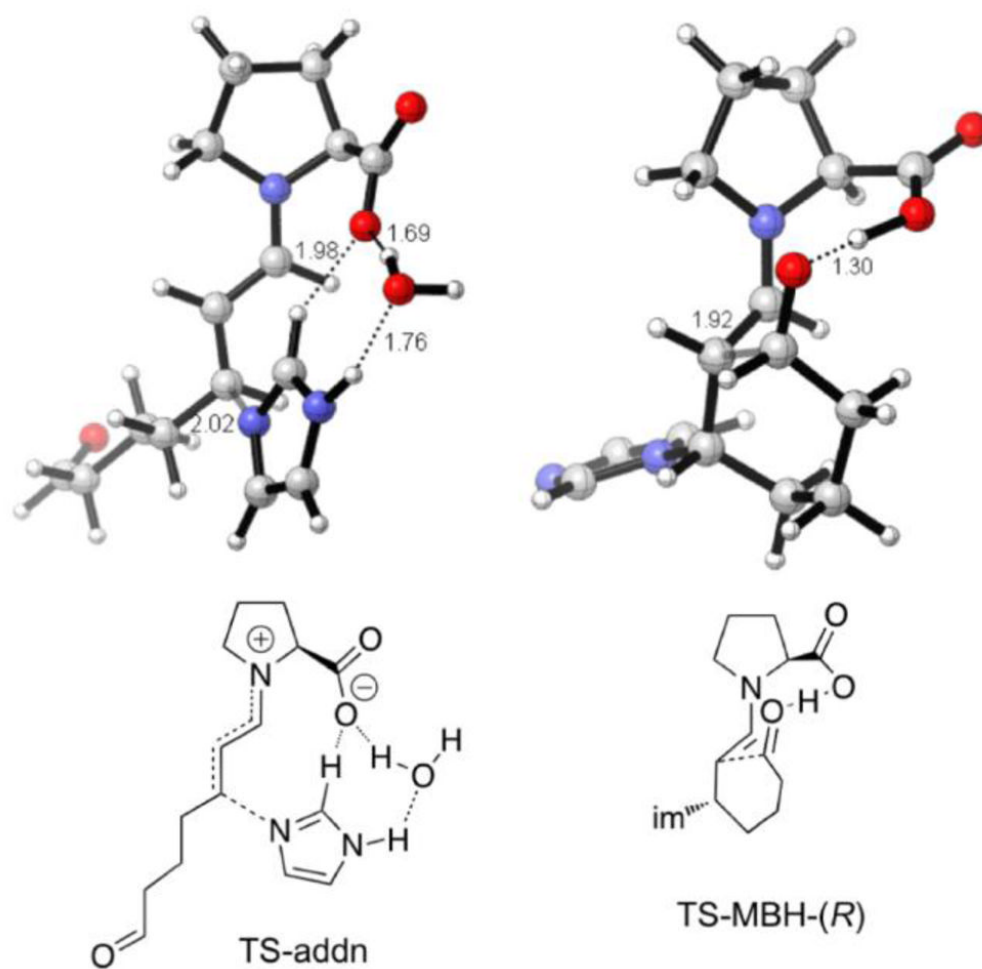


Figure 32. B3LYP/6-31G(d, p) major transition structures for the proline-catalyzed imidazole addition and intramolecular Morita-Baylis-Hillman. (im=imidazole).

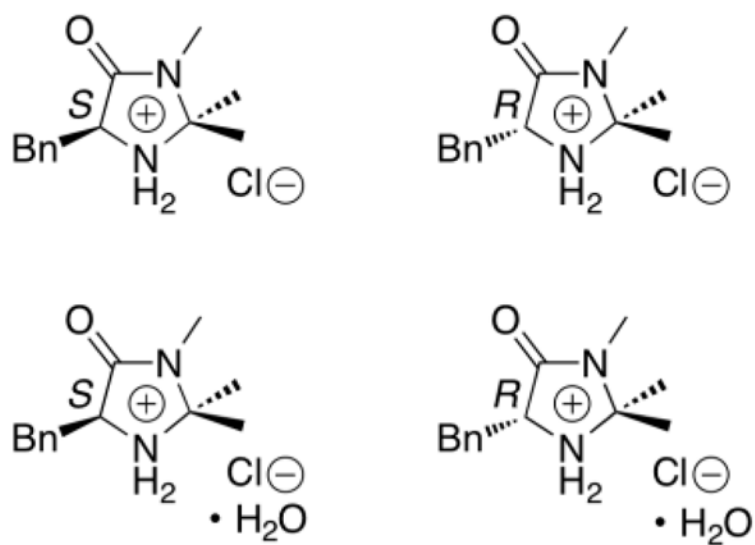


Figure 33.
Imidazolidinone catalysts studied by Burley and co-workers.⁷⁷

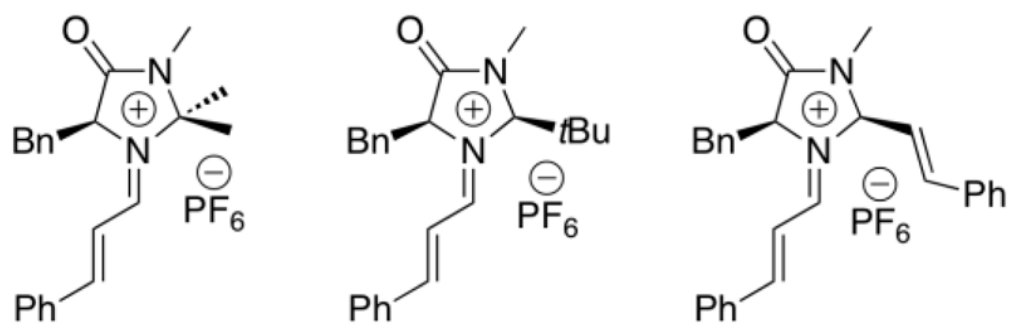


Figure 34. Imidazolidinones investigated by Seebach and co-workers.⁷⁸

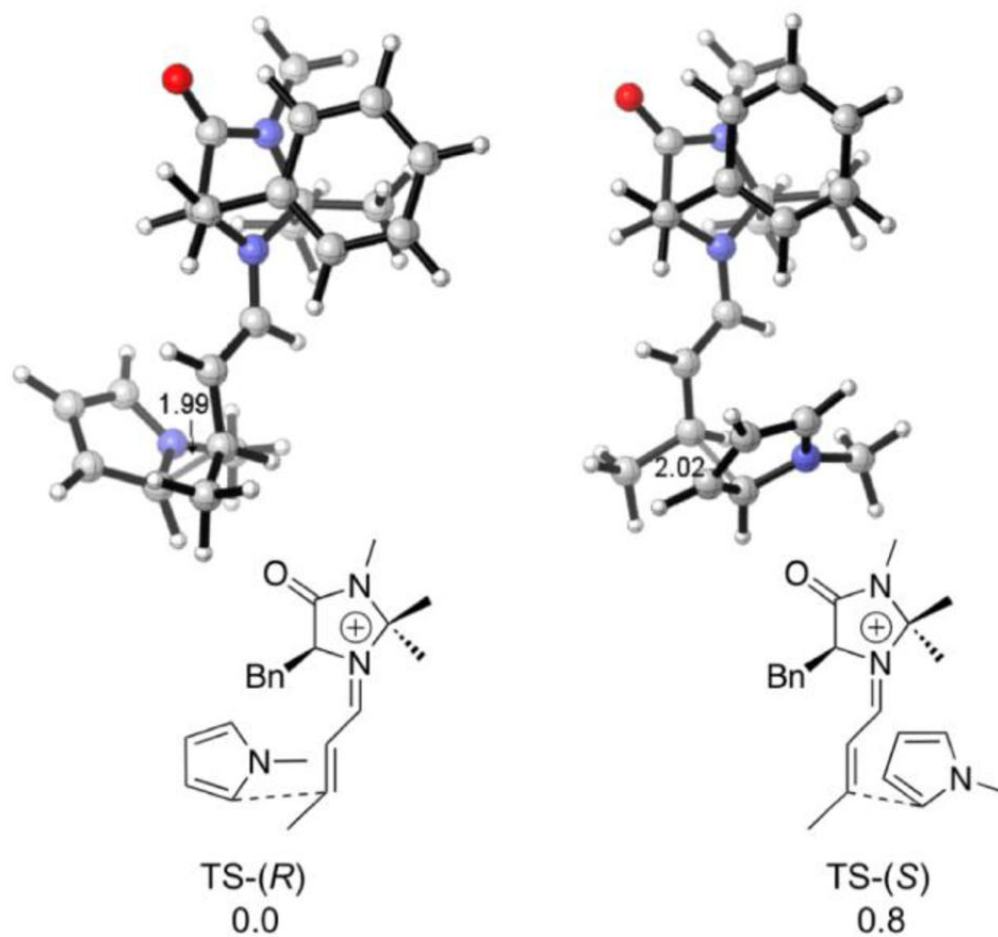


Figure 35. Lowest energy transition structures and relative energies for imidazolidinone-catalyzed alkylation of *N*-methylpyrrole.

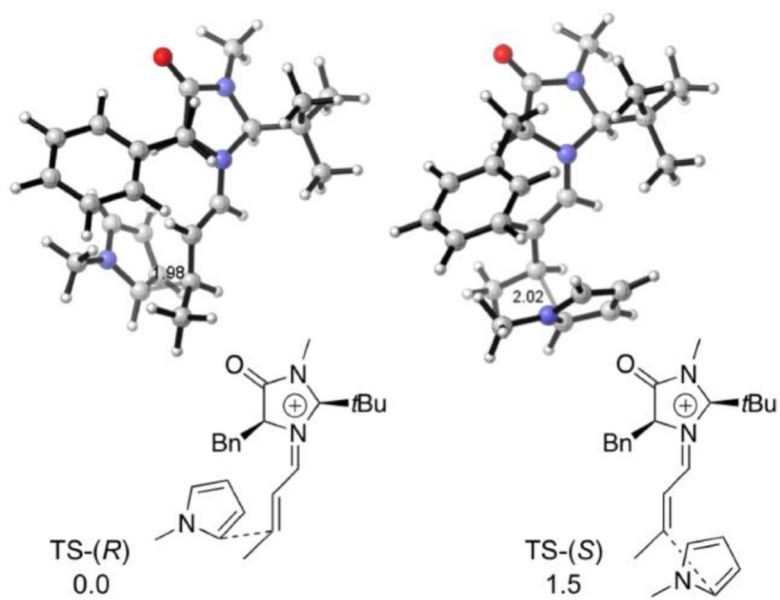


Figure 36. Lowest energy transition structures and relative energies for imidazolidinone-catalyzed alkylation of *N*-methylpyrrole.

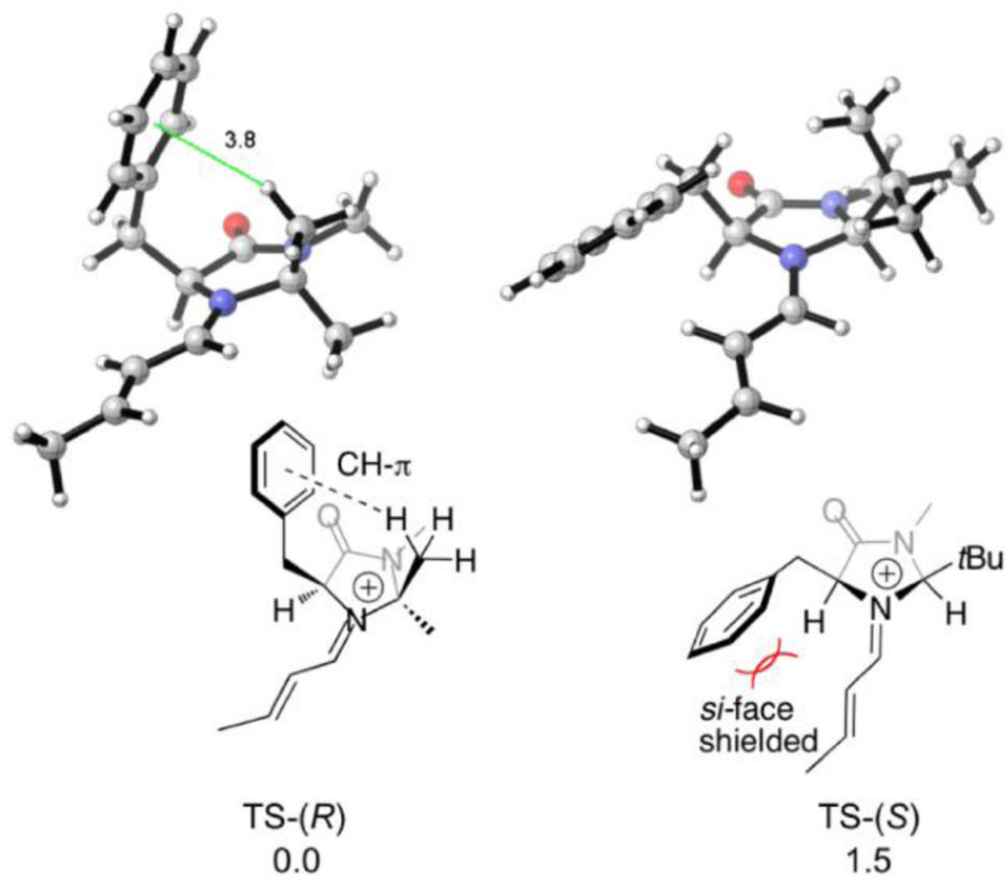


Figure 37.
Most stable conformers of dimethyl and *tert*-butyl substituted iminiums.

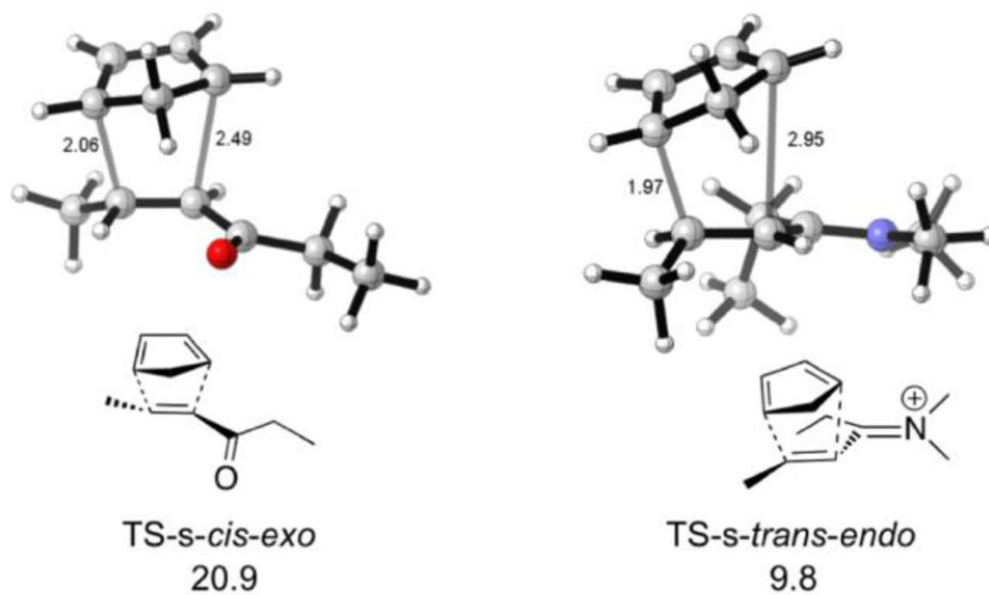


Figure 38. Uncatalyzed and *N,N*-dimethylamine-catalyzed Diels-Alder cycloaddition transition structures and activation energies (B3LYP/6-31G(d)) of cyclopentadiene and 4-hexene-3-one.

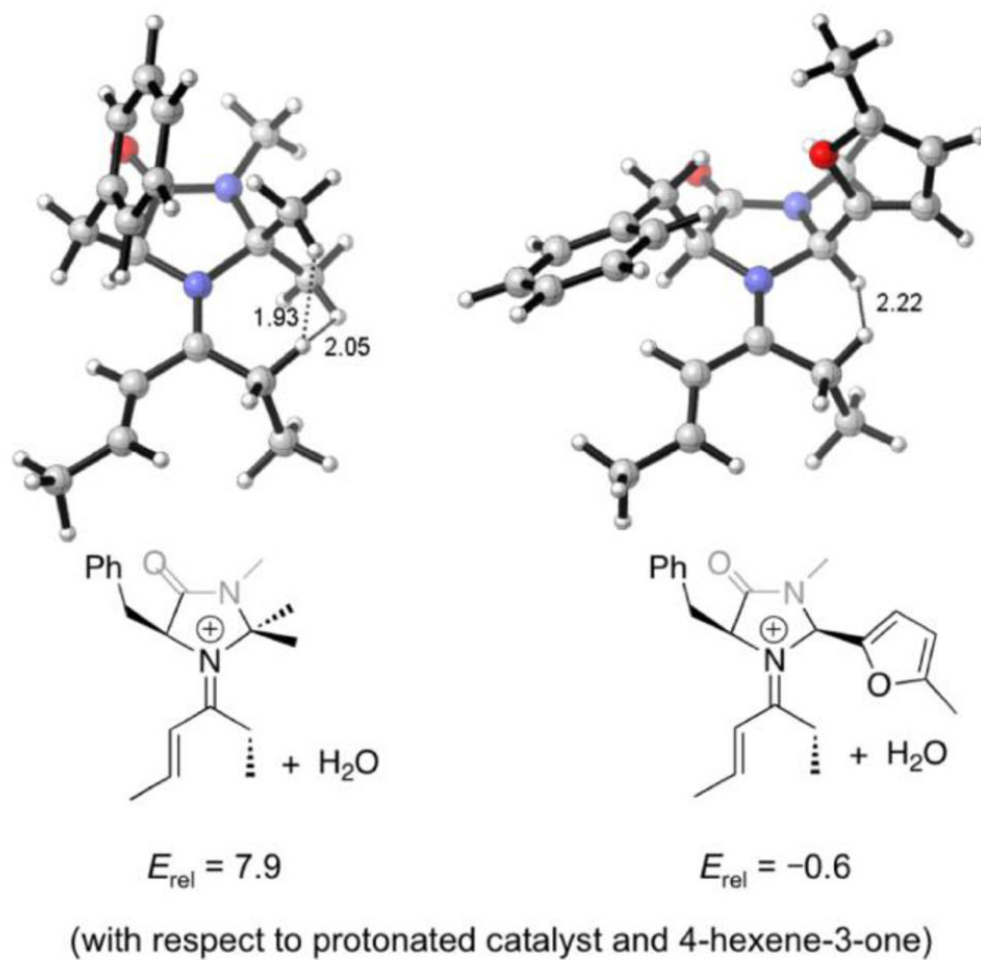


Figure 39.
Lowest energy iminium conformers.

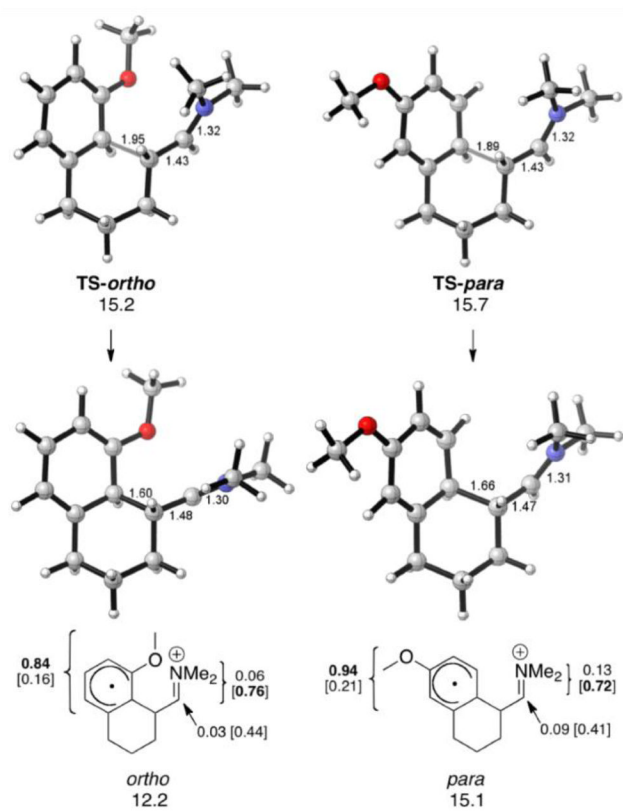


Figure 40. Intramolecular α -arylation transition structures and cyclized radical cations (UB3LYP/6-31G(d) ΔG values for aqueous solution at 268 K; optimizations in CPCM water). Spin densities, followed by Mulliken charges in brackets.

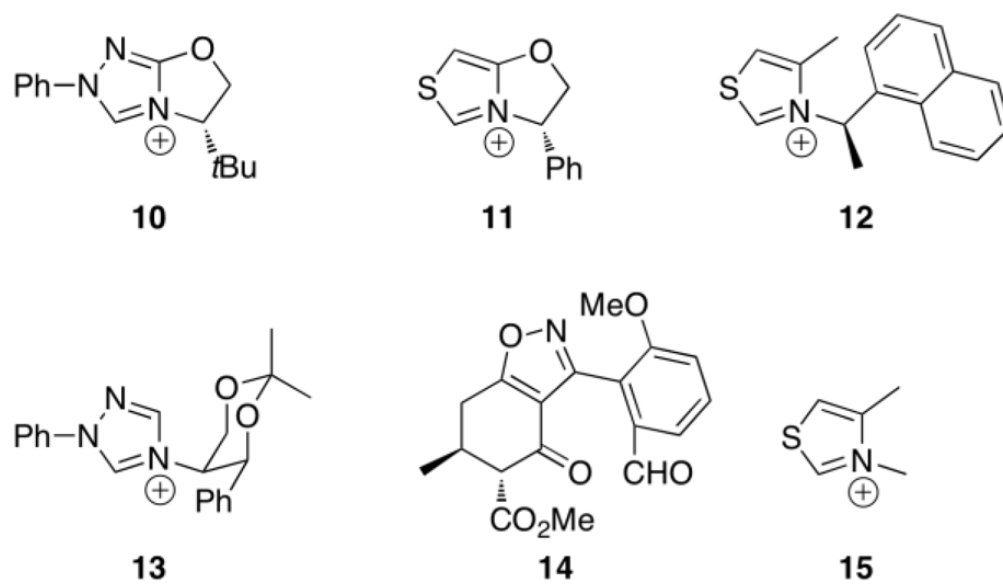


Figure 41. Chiral catalysts (**10–13**, **15**) and aldehyde (**14**) studied in the benzoin condensation.

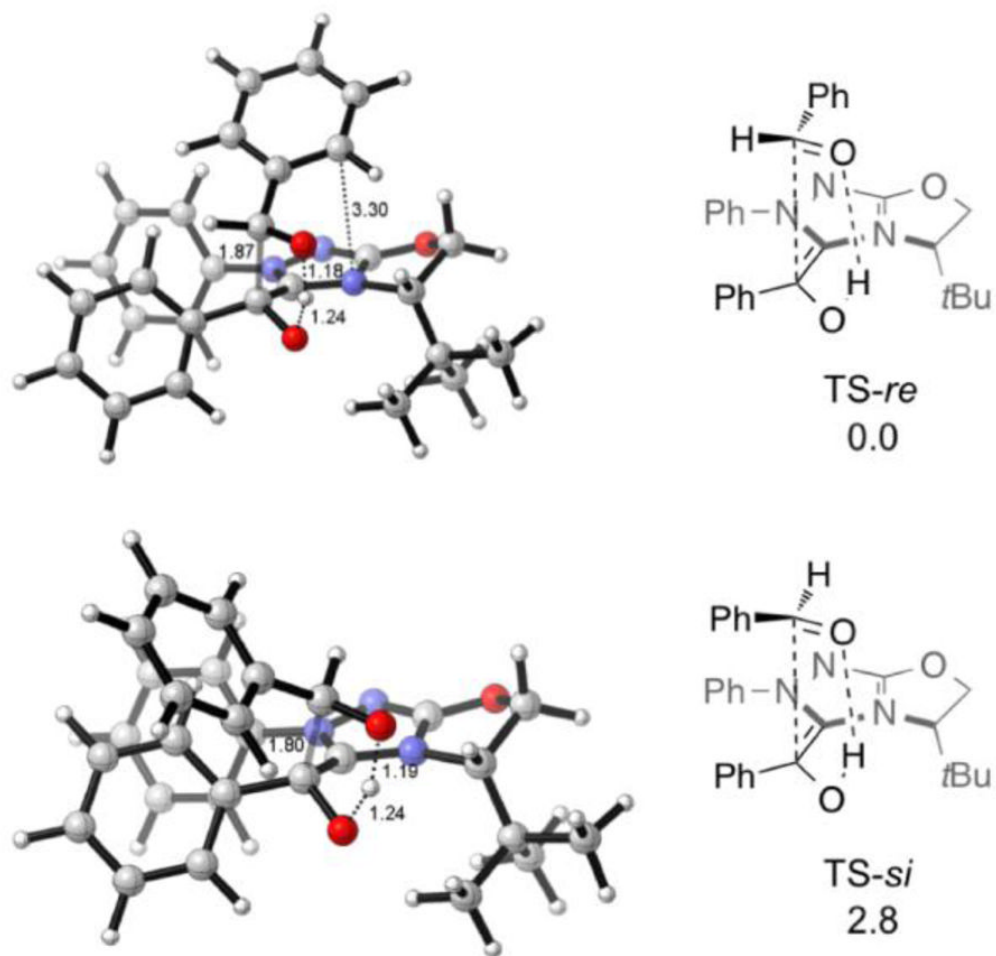


Figure 42.
Lowest energy transition structures for the addition with catalyst **10**.

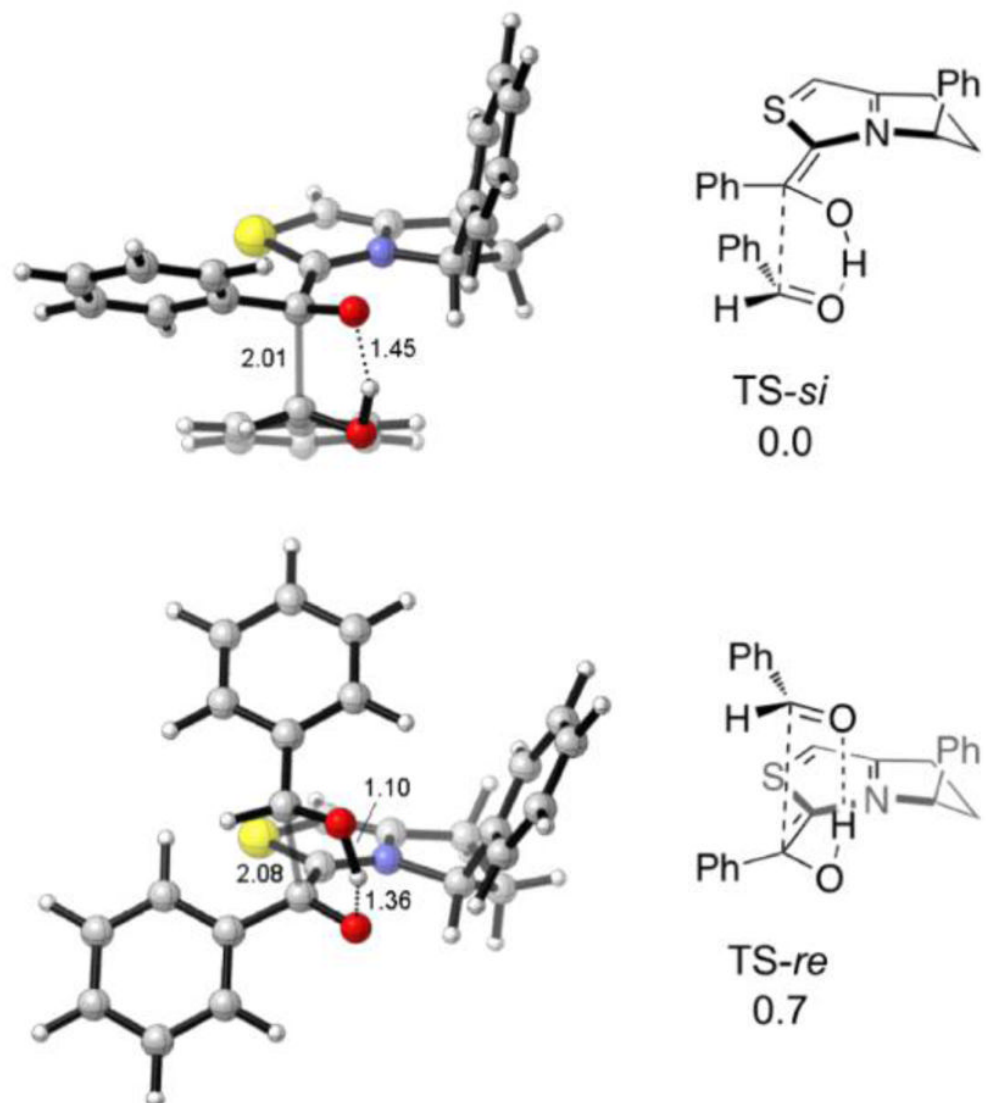


Figure 43.
Lowest energy transition structures for the addition with catalyst **11**.

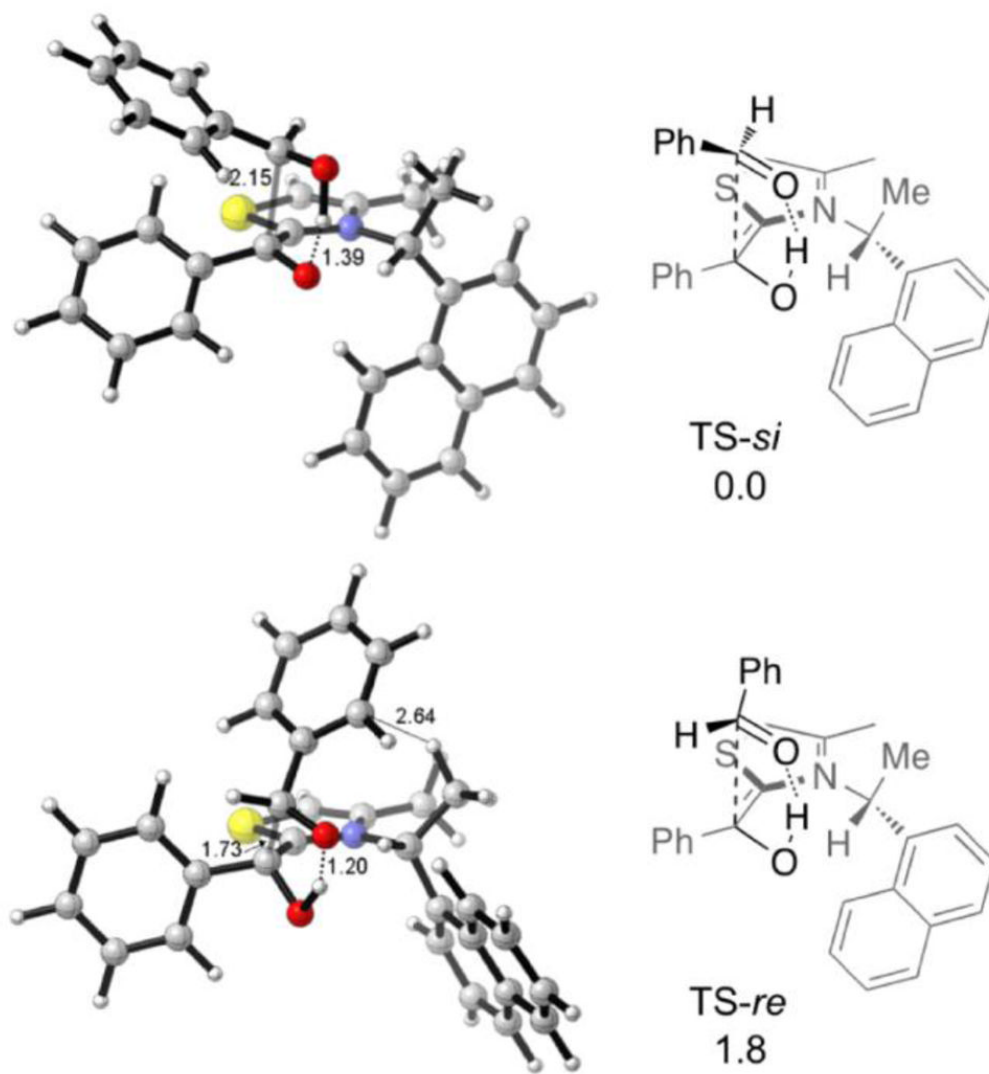


Figure 44.
Lowest energy TSs for the addition with catalyst 12.

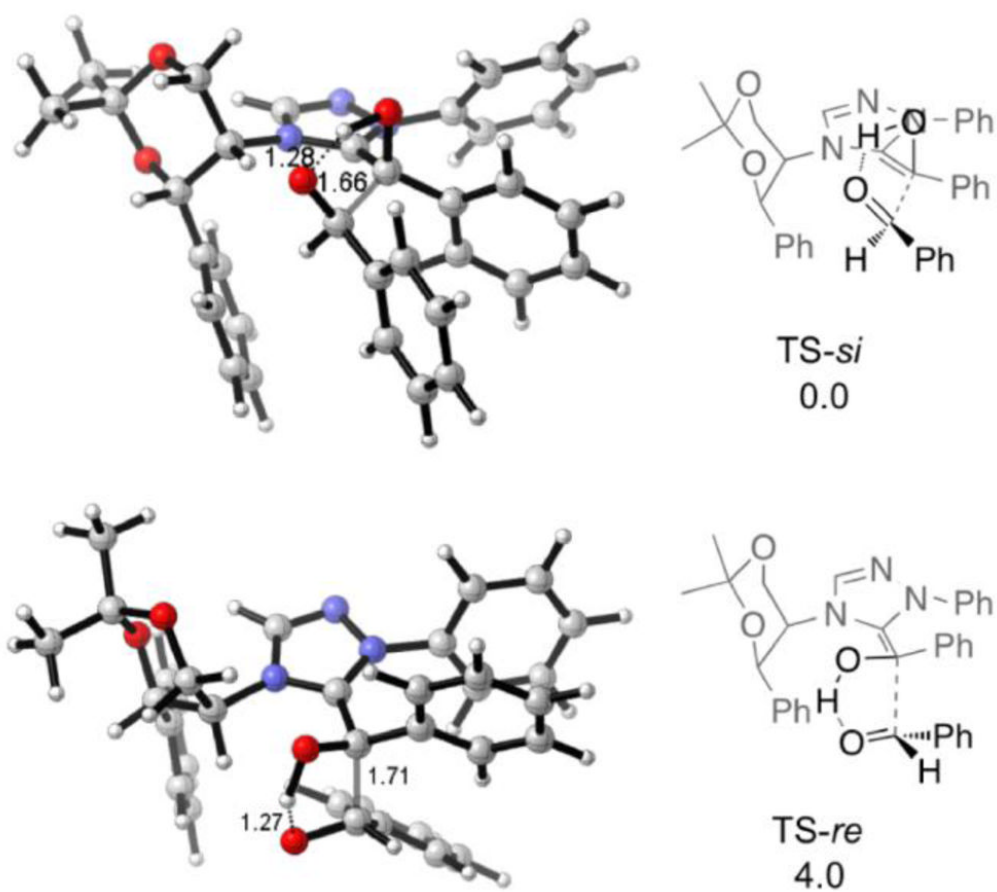


Figure 45.
Lowest energy transition structures for the addition with catalyst **13**.

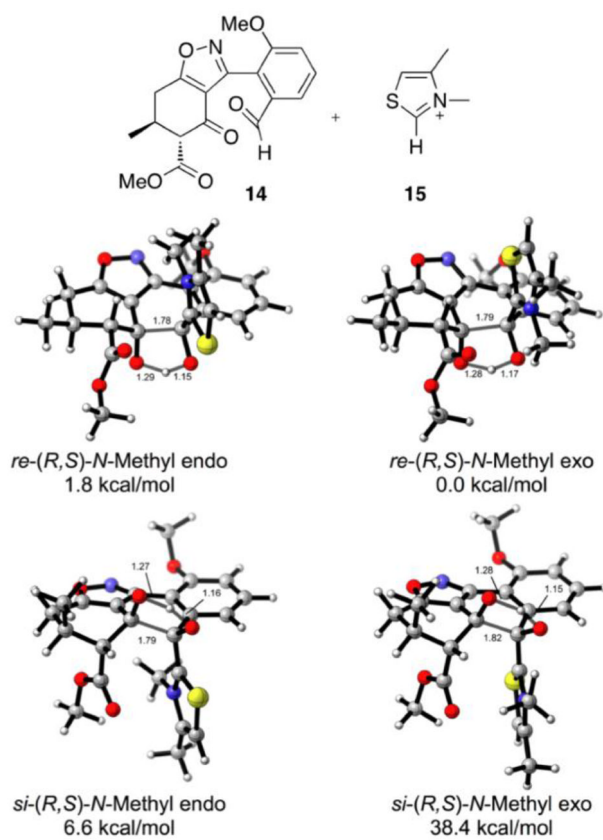


Figure 46. Transition structures for the intramolecular crossed aldehyde-ketone benzoin condensation.

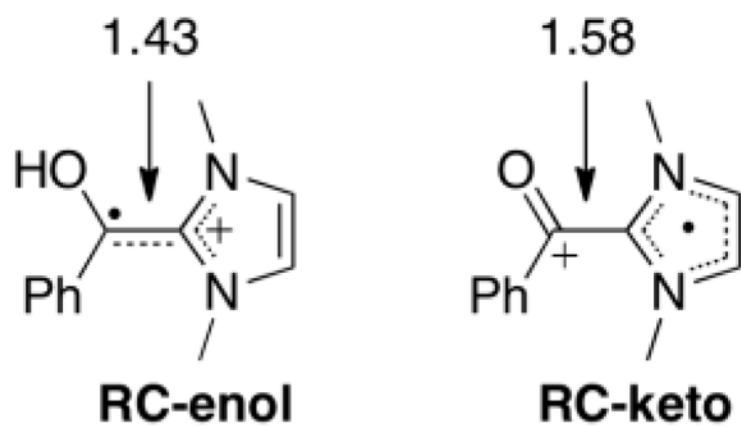


Figure 47. Lewis structures and PBEh/TZP bond distances of enol (**RC**) and keto (**RC'**) forms of intermediate radical cation.

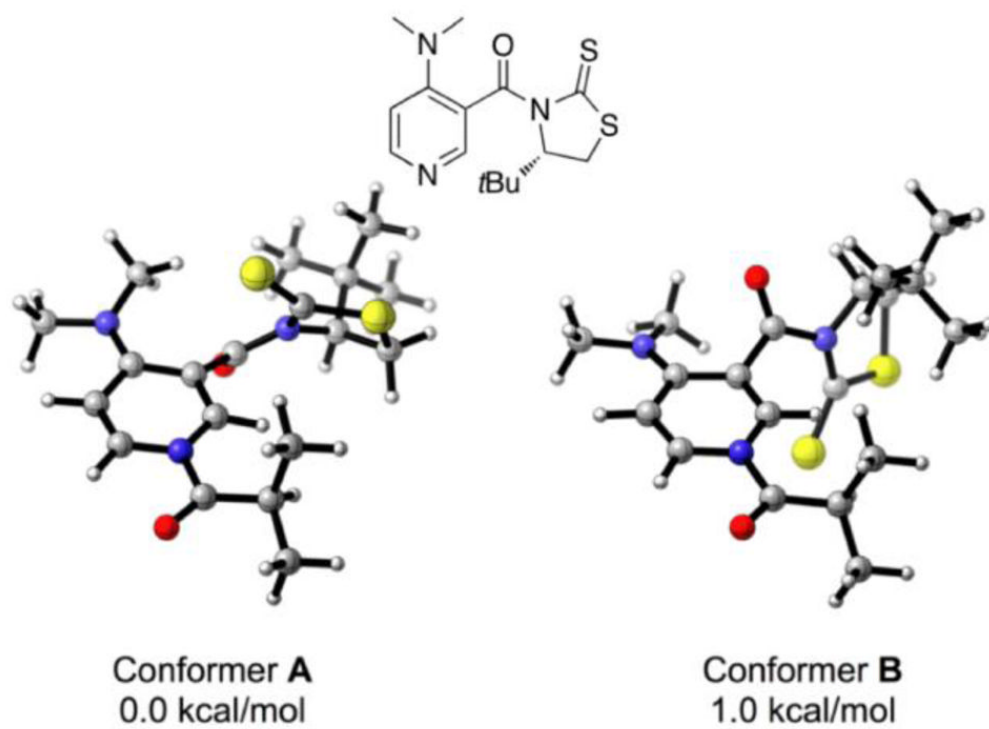


Figure 48. The computed lowest energies conformations of a chiral catalyst developed by Yamada and co-workers.

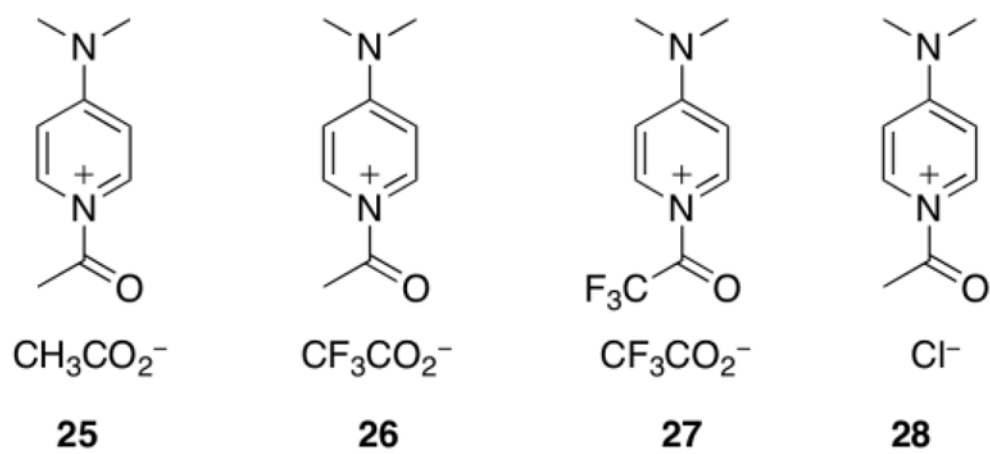


Figure 49.
Acetylated DMAP salts studied by Schreiner.

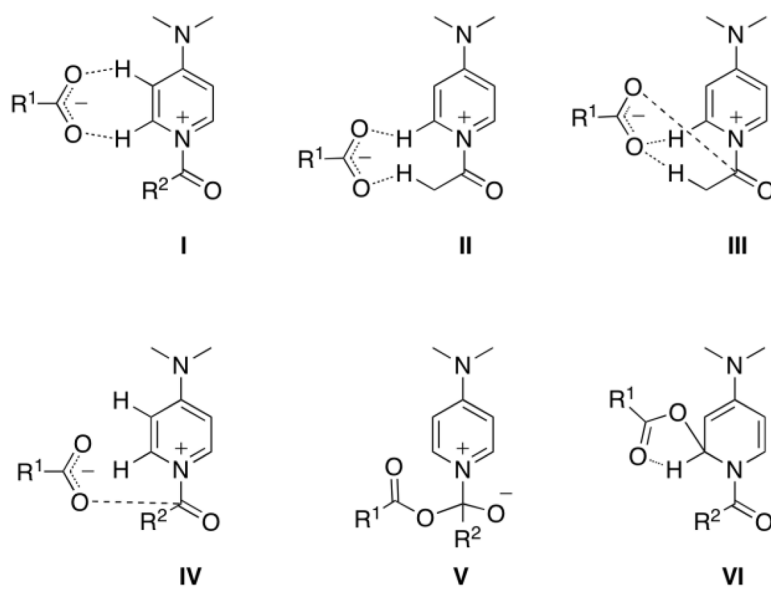


Figure 50.
Salt formation between acetylated DMAP and various anions.

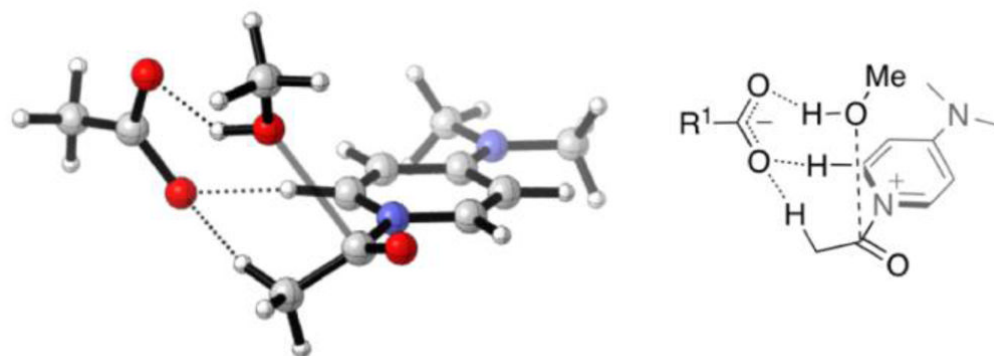


Figure 51.
Alcohol addition to **25** via complex III

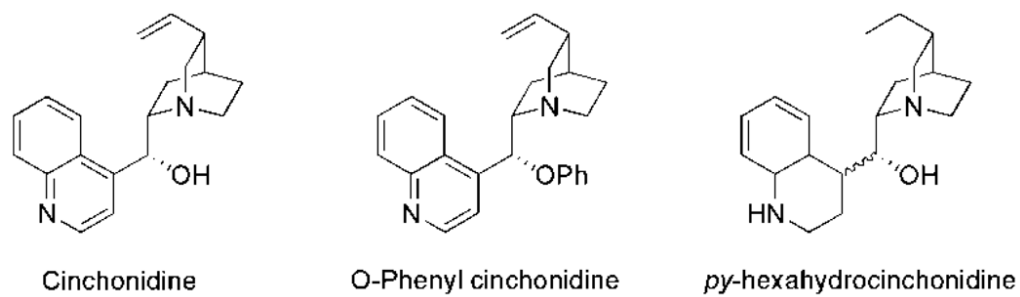


Figure 52.
Various cinchonidine derivatives.

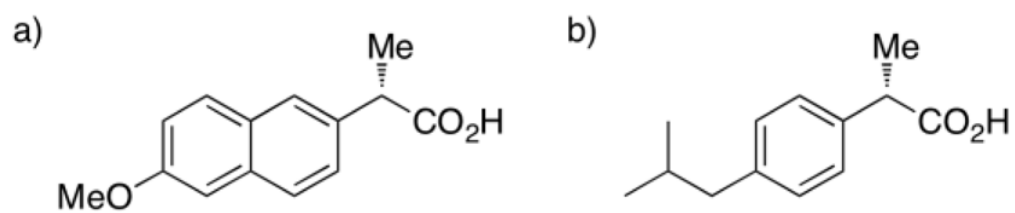


Figure 53.
Two popular NSAID drugs. a) Naproxen; b) ibuprofen.

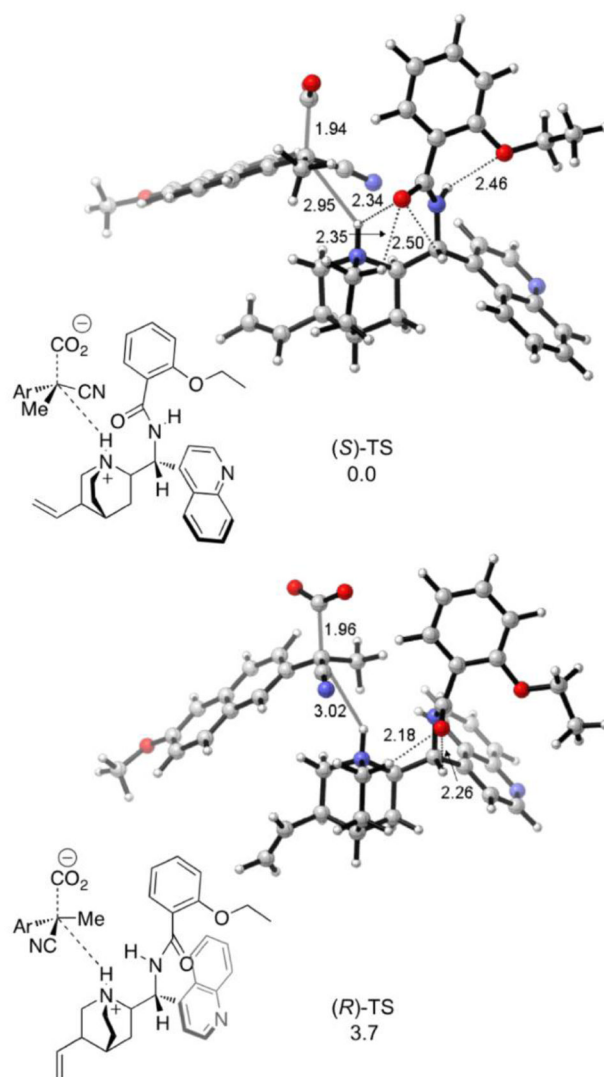


Figure 54.
The concerted decarboxylation/protonation TSs.

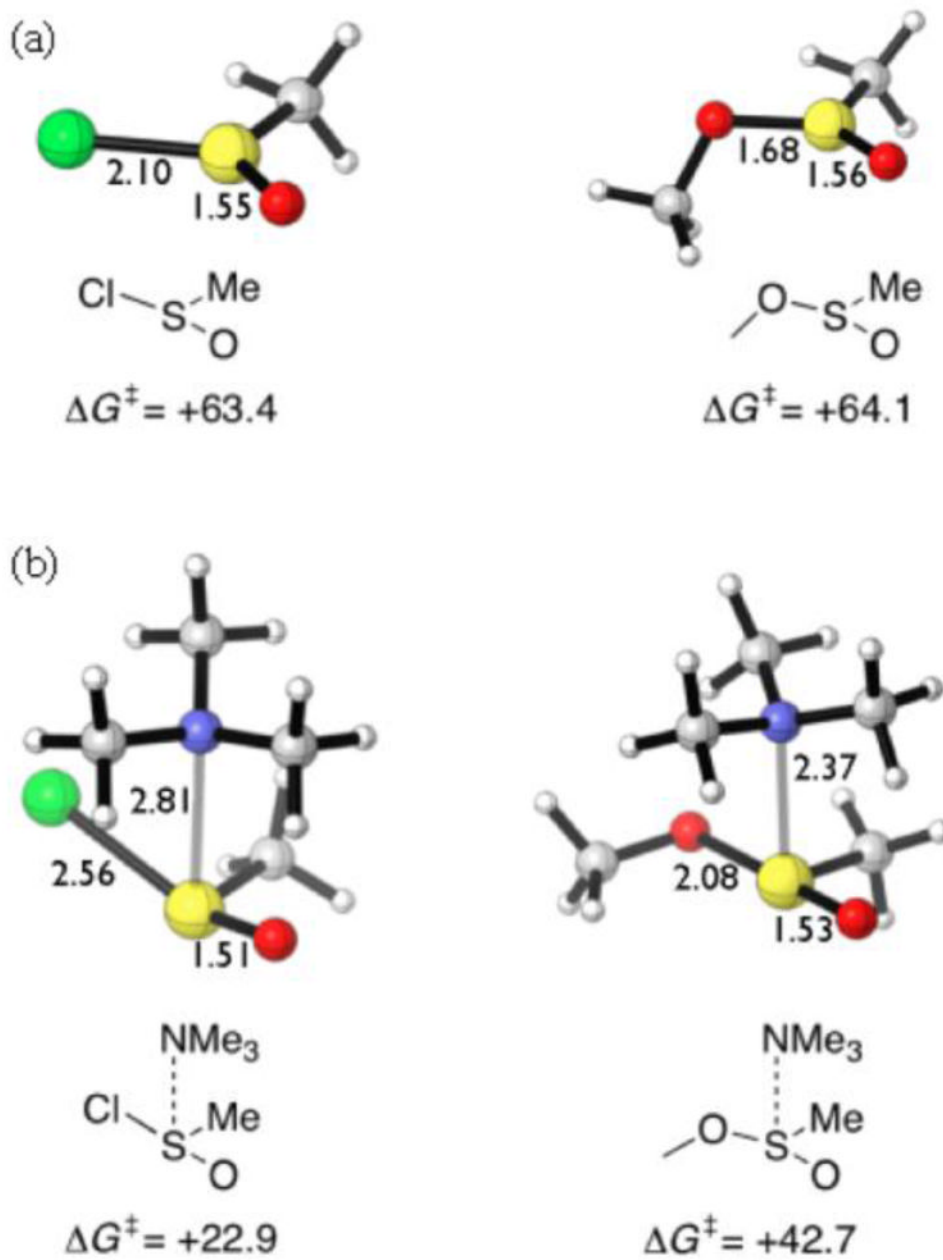


Figure 55. Transition structures for the (a) base-free and (b) base catalyzed inversions.

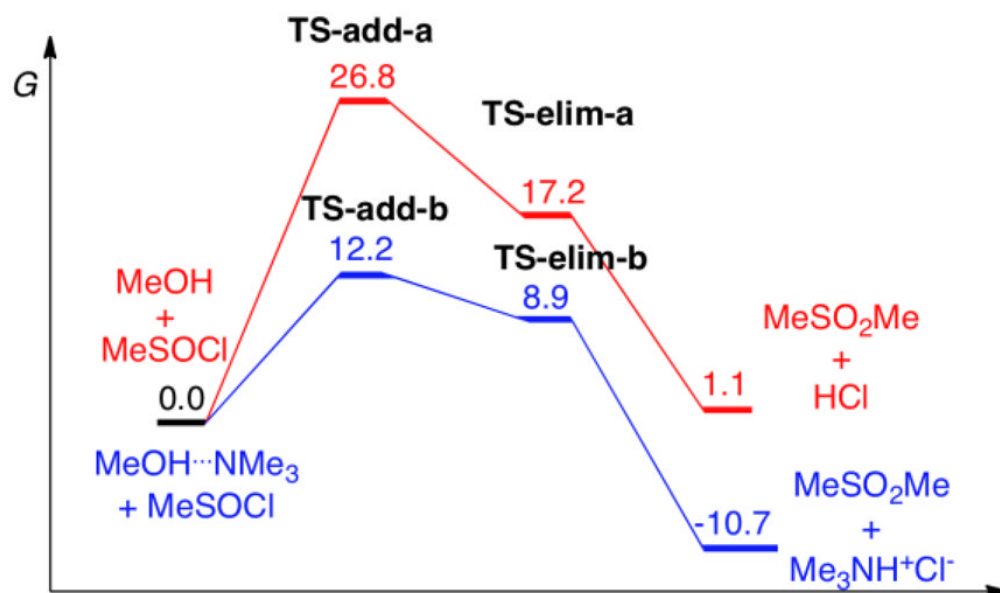


Figure 56.
Free energy diagram for base-free and base-assisted pathways for the neutral mechanism.

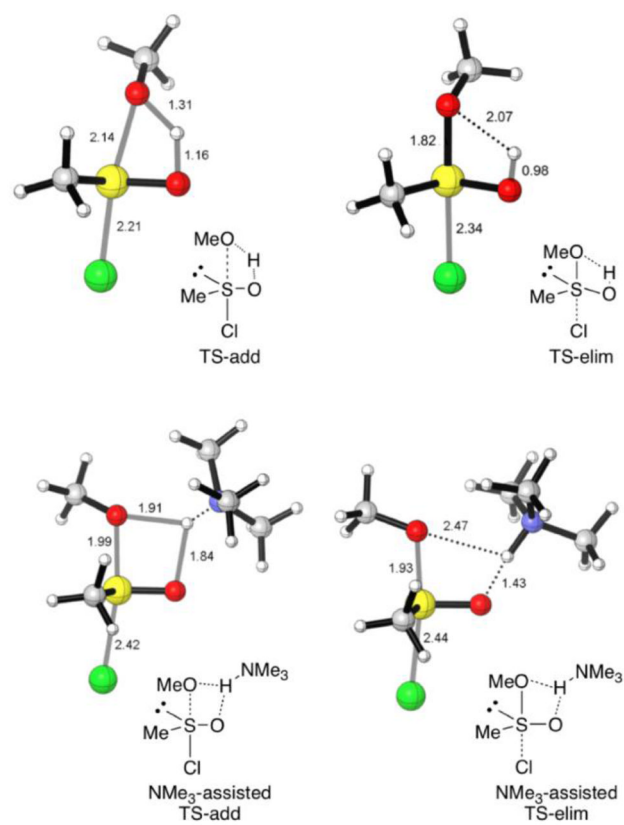


Figure 57.
Optimized addition and elimination TSs for the neutral mechanism.

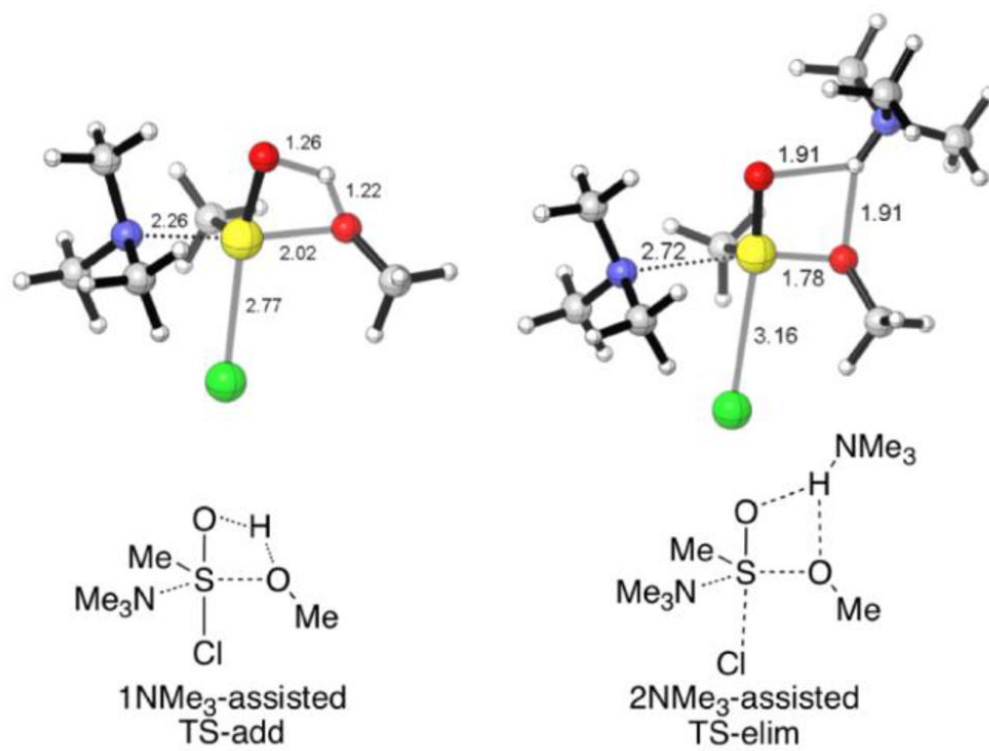


Figure 58.
Optimized TSs for the addition step of the ion-pair mechanism.

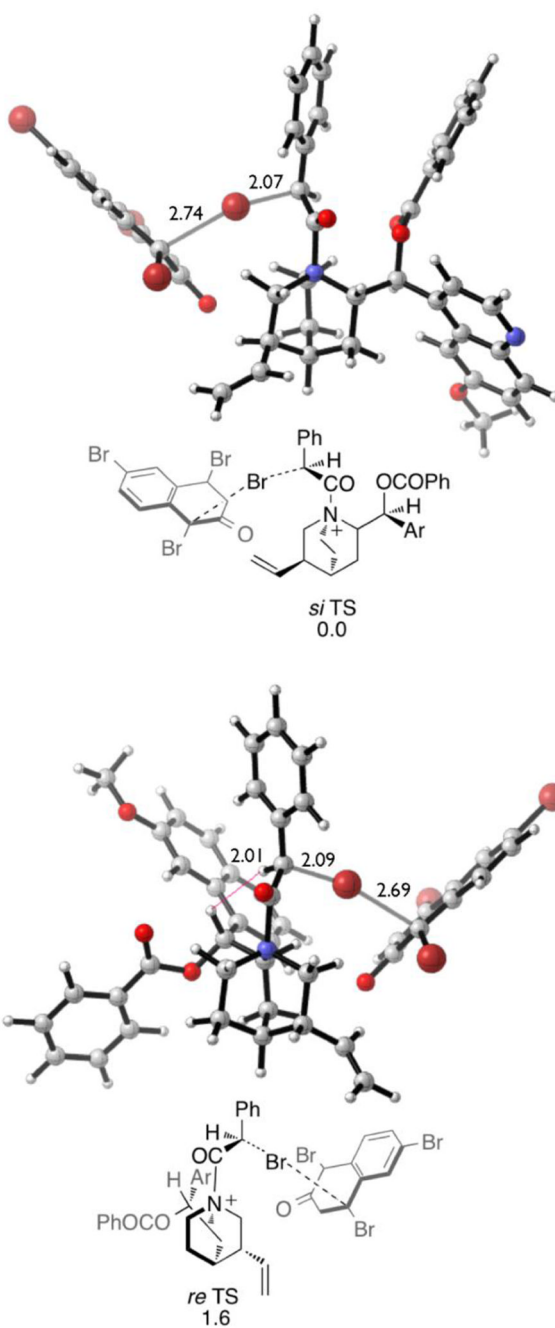


Figure 59.
re and *si* TSs for the bromination step with **29b**

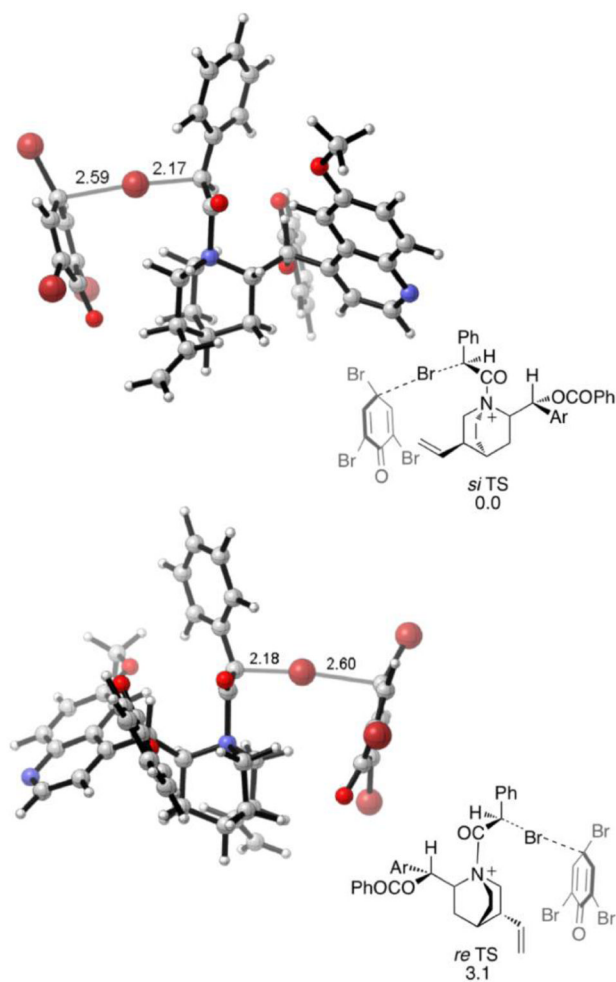


Figure 60.
re and *si* TSs for the bromination step with **29a**.

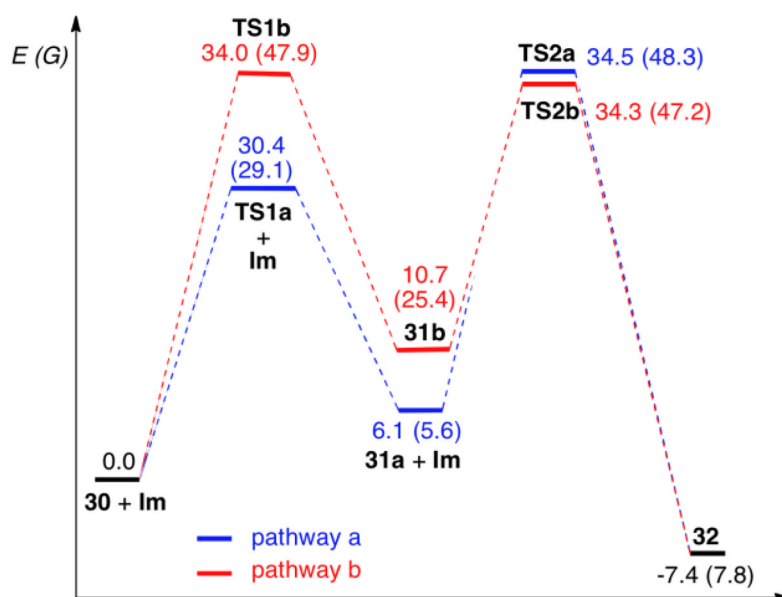


Figure 61. Relative electronic energy and free energy (in parentheses) profiles for the uncatalyzed Strecker reaction. Energy units are in kcal/mol.

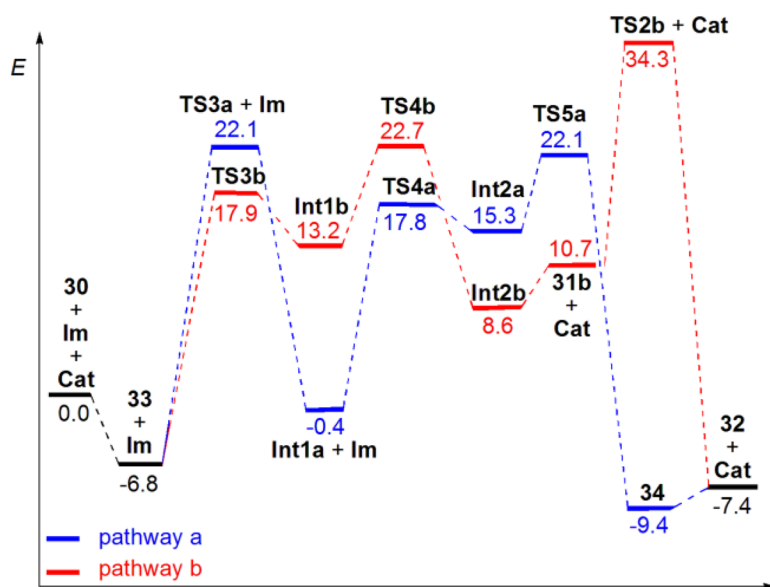


Figure 62. Relative electronic energy profiles for the uncatalyzed Strecker reaction. Energy units are in kcal/mol.

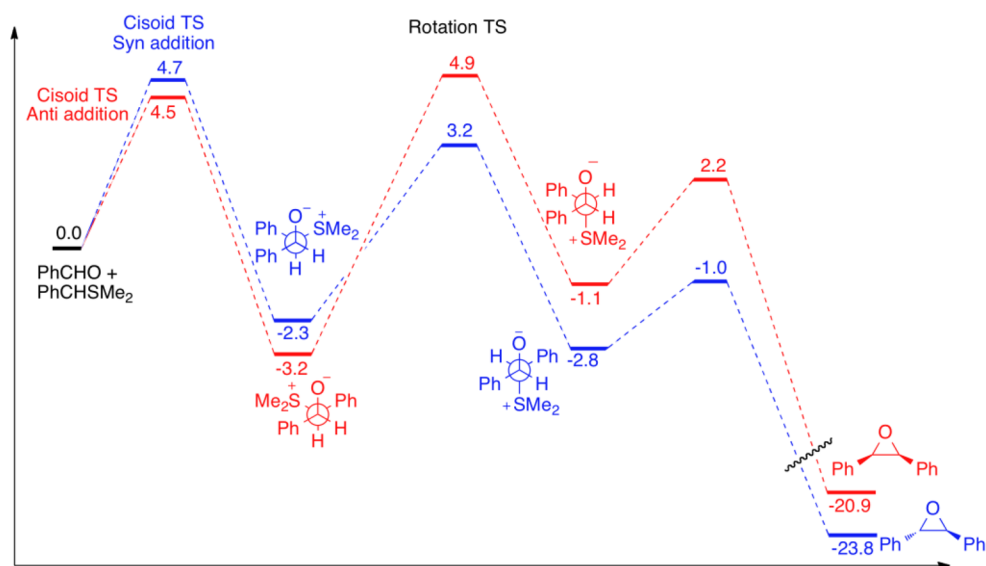


Figure 63.
Relative energy profiles (kcal/mol) for the epoxidation process.

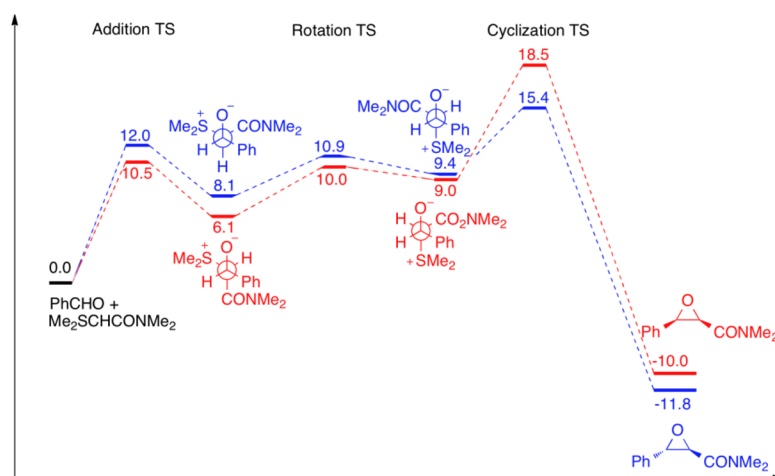


Figure 64.
Relative energy profiles (kcal/mol) for the epoxidation process.

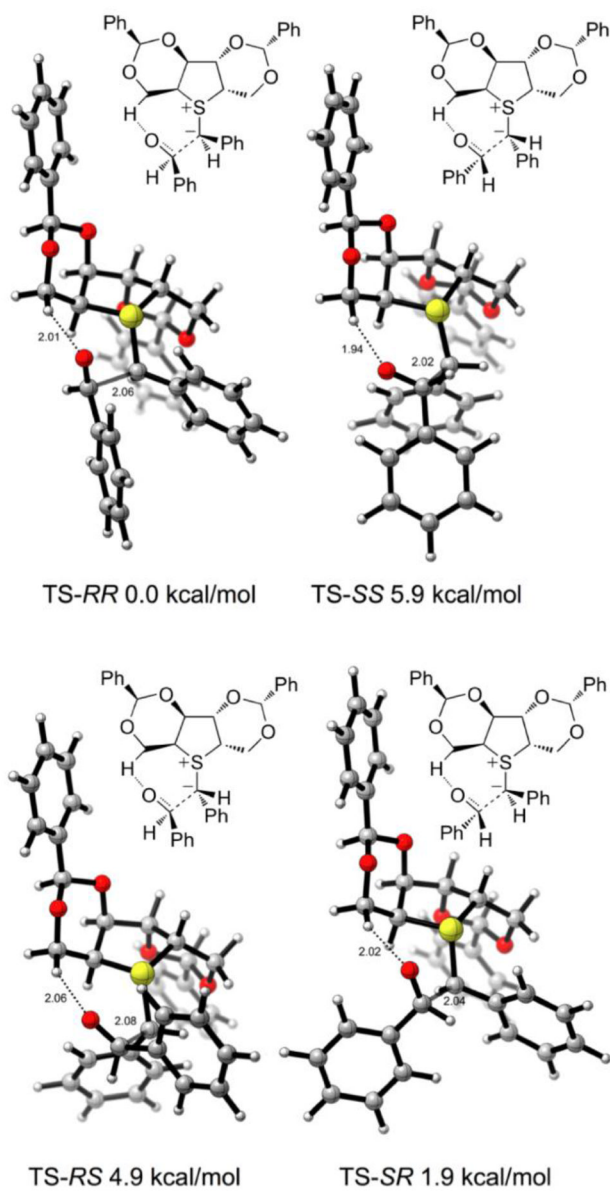


Figure 65. B3LYP/6-31G(d) geometries and relative energies (kcal/mol) for the addition of benzyl ylides derived from sulfide **36** to benzaldehyde.

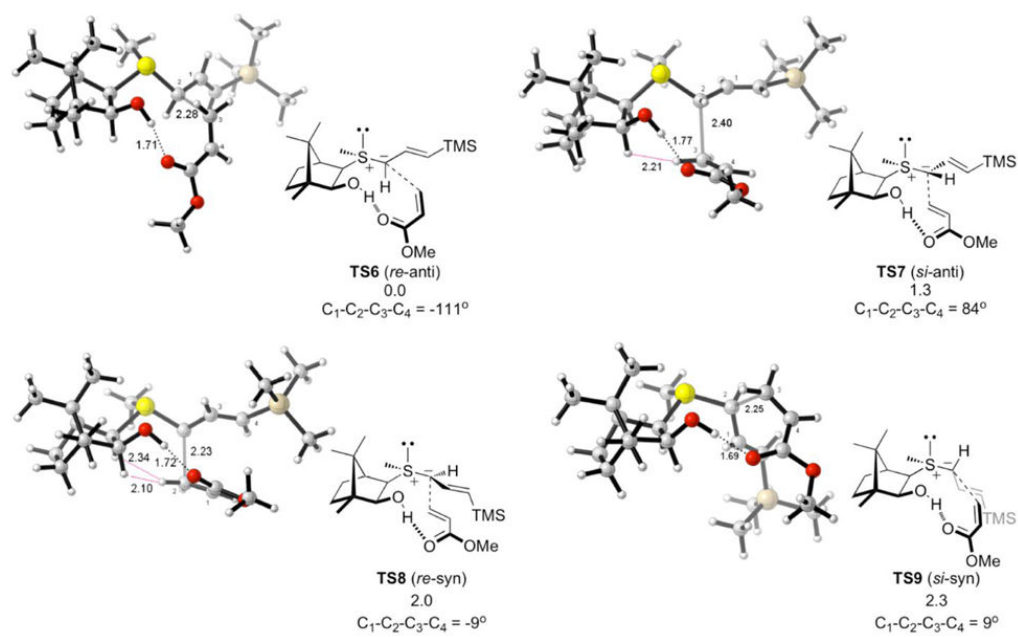


Figure 66.
Computed transition structures for the addition step between the *exo*-ylide and methyl acrylate.

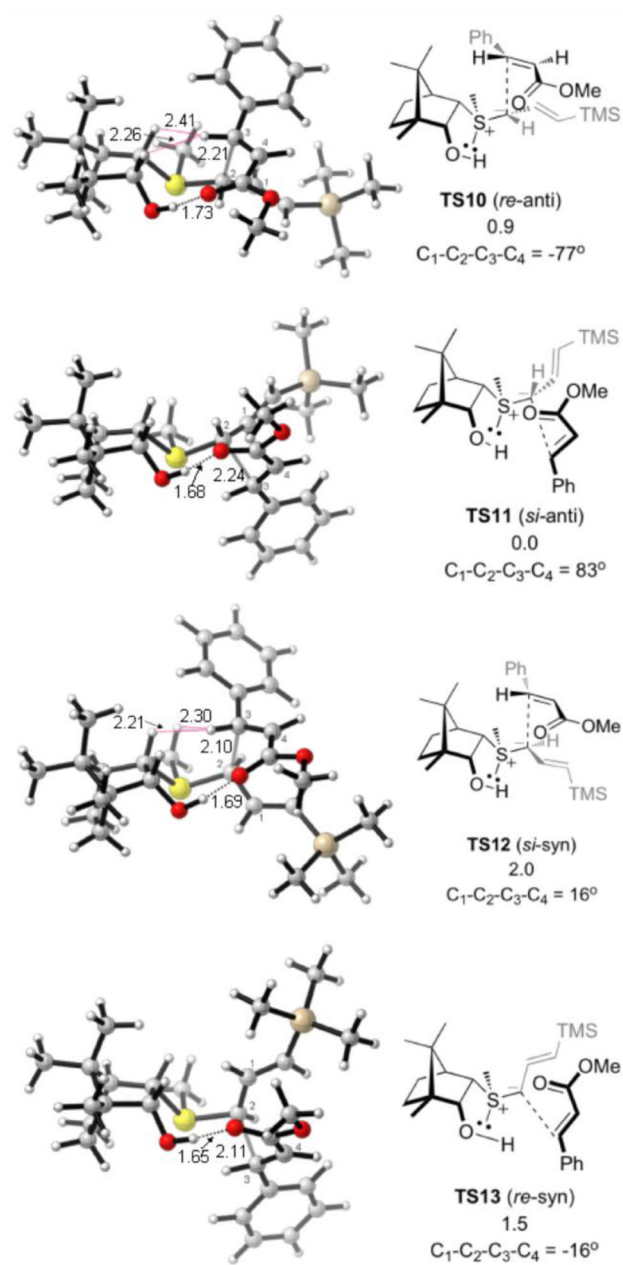


Figure 67.
Computed transition structures for the addition step between the *endo*-ylide and methyl cinnamate.

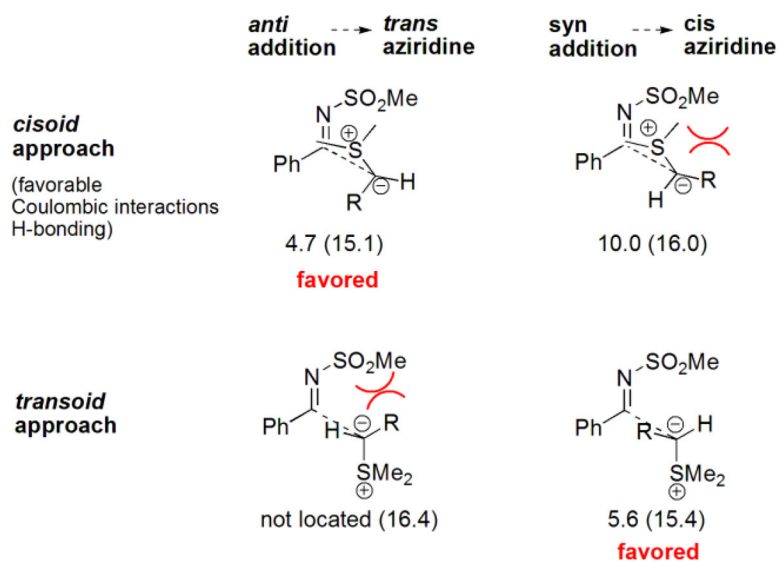


Figure 68. Activation energies (kcal/mol) for the addition of Me₂SCHR (R = Ph, and R = CO₂Me given in parenthesis) to PhCH=NSO₂Me.

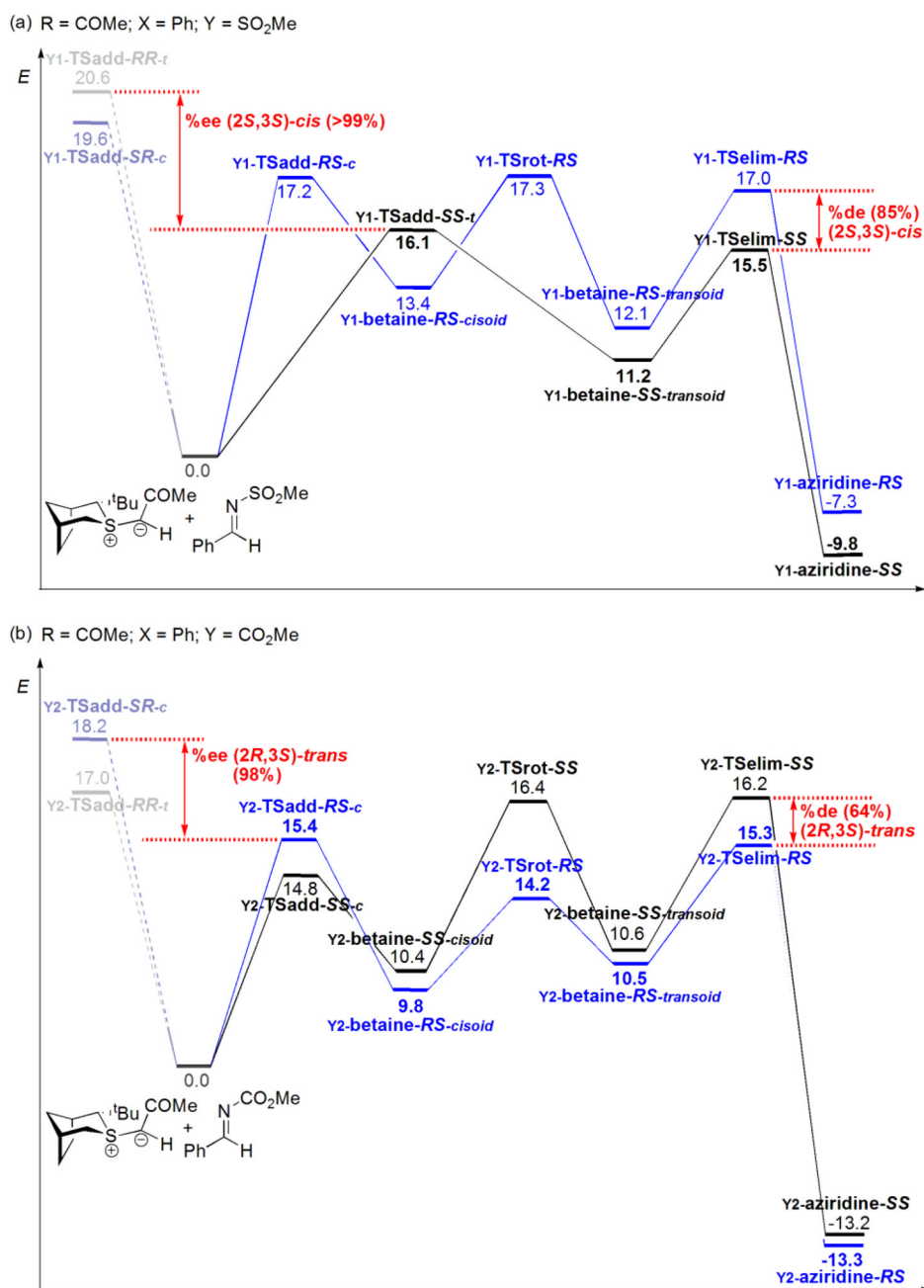


Figure 69. Energy profiles (kcal/mol) for chiral sulfur ylide promoted aziridinations involving (a) SO₂Me and (b) CO₂Me protected imines.

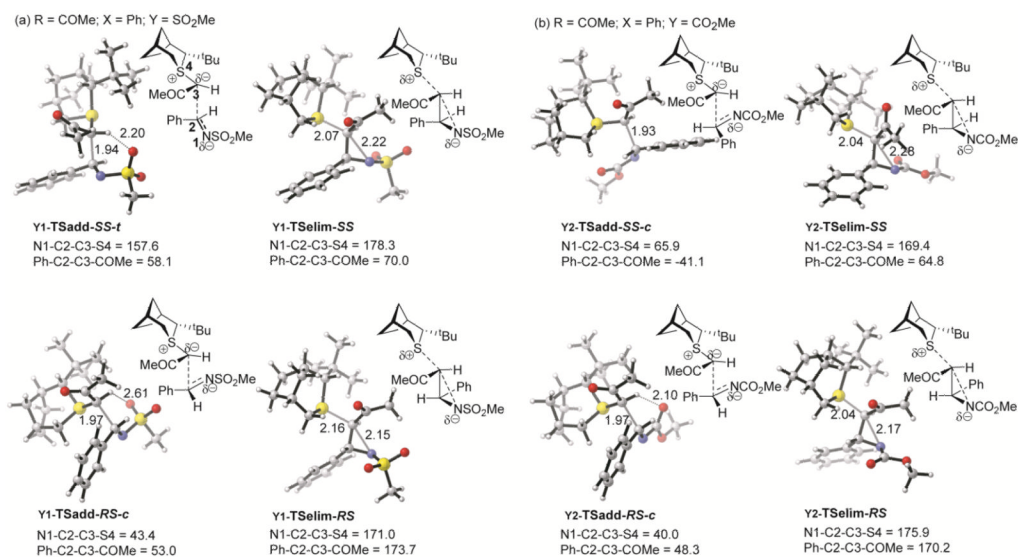


Figure 70. Transition structures (*cisoid* (-c) or *transoid* (-t) for chiral sulfur ylide promoted aziridinations involving (a) SO₂Me and (b) CO₂Me protected imines.

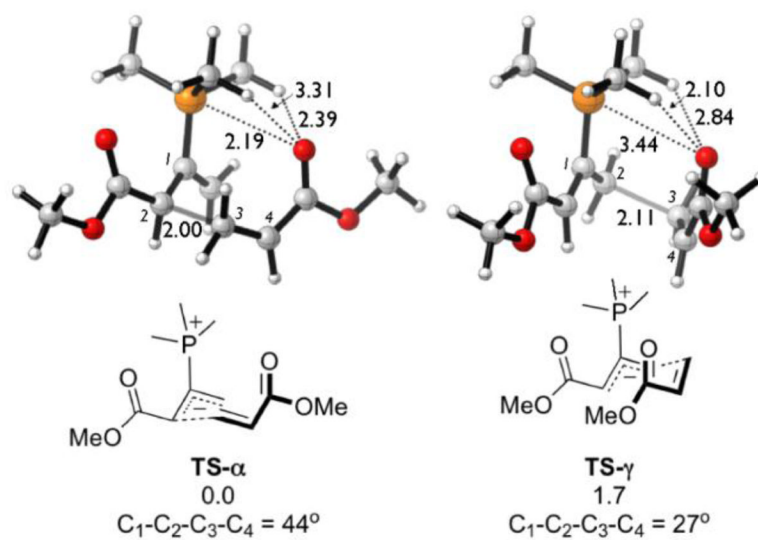


Figure 71.
Transition structures of the C-C bond formation with methyl acrylate.

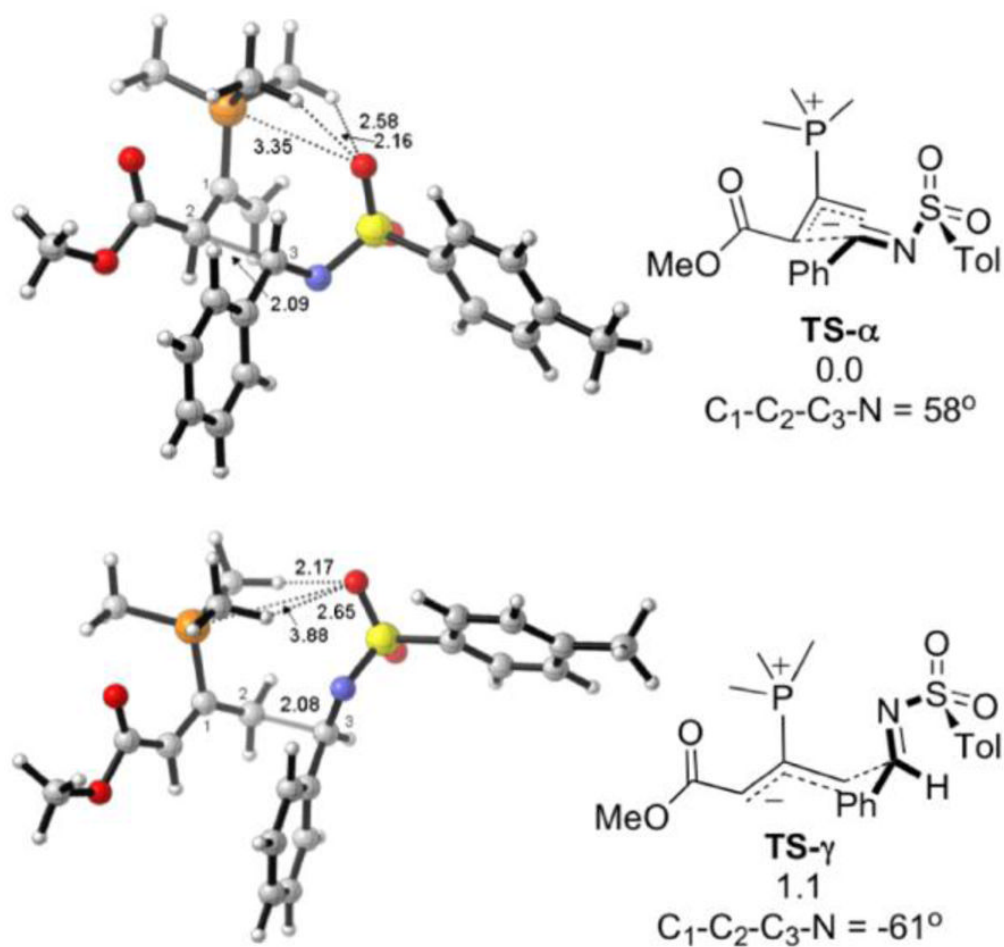


Figure 72.
 Transition structures of the C-C bond formation with *N*-Tosyl benzaldimine.

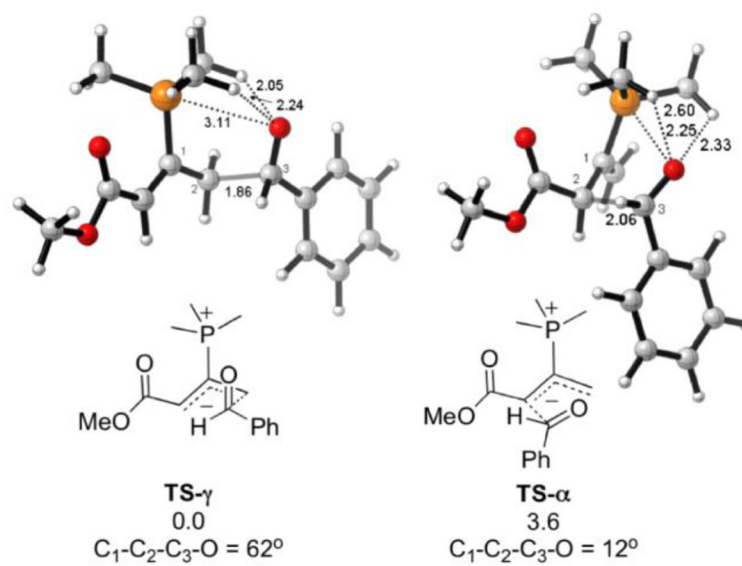


Figure 73.
 Transition structures of the C–C bond formation with benzaldehyde.

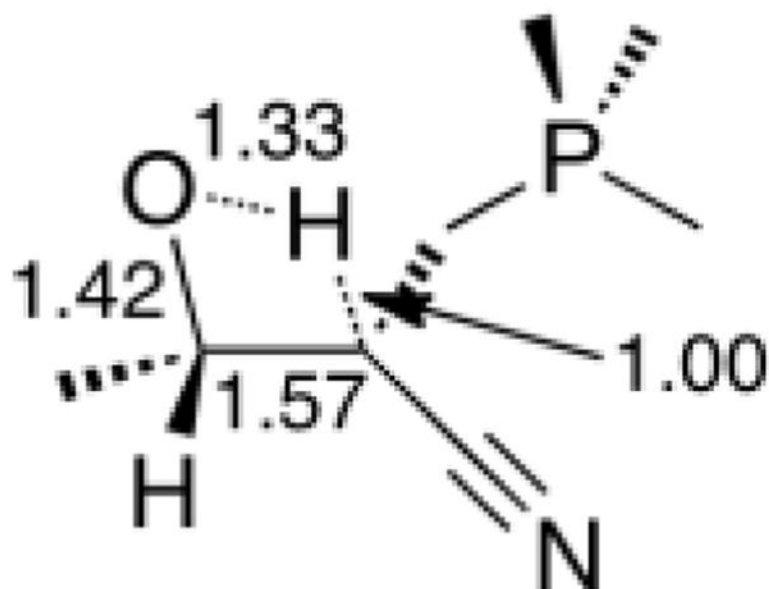


Figure 74.
B3LYP/6-311+G(d) rate-determining transition structure (**TS-H⁺**).

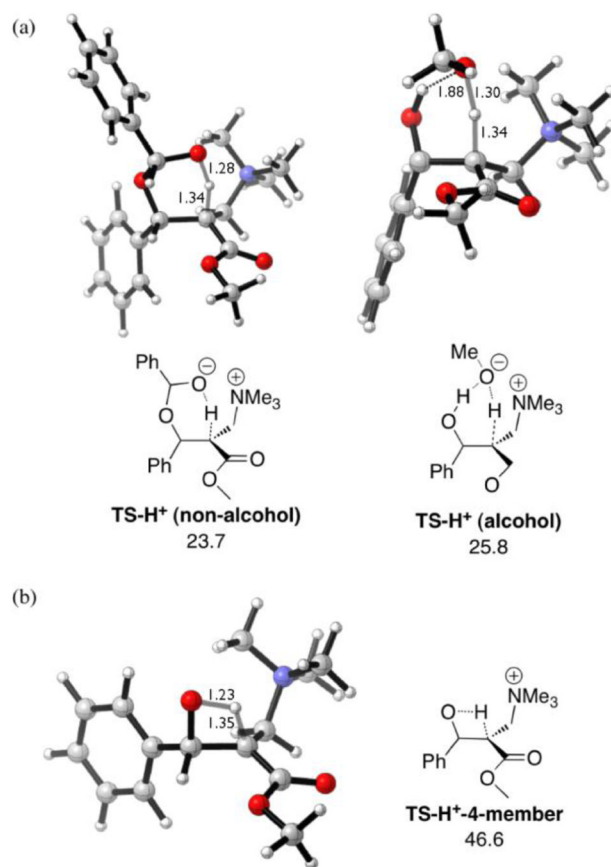


Figure 75.

(a) Rate-determining transition structures for proton transfer in the non-alcohol and alcohol-catalyzed MBH pathways. (b) Intramolecular proton transfer via four-membered transition state.

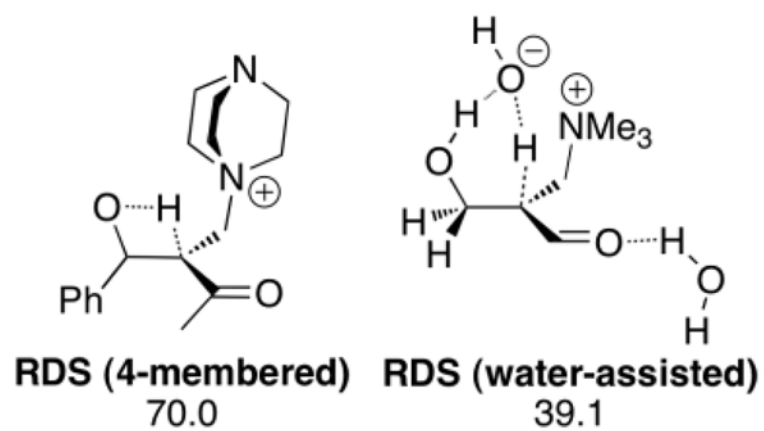


Figure 76.

(a) mPW1K/6-31+G(d) transition structure for intramolecular proton transfer. (b) mPW1K/6-31+G(d) transition structure of water-assisted pathway.

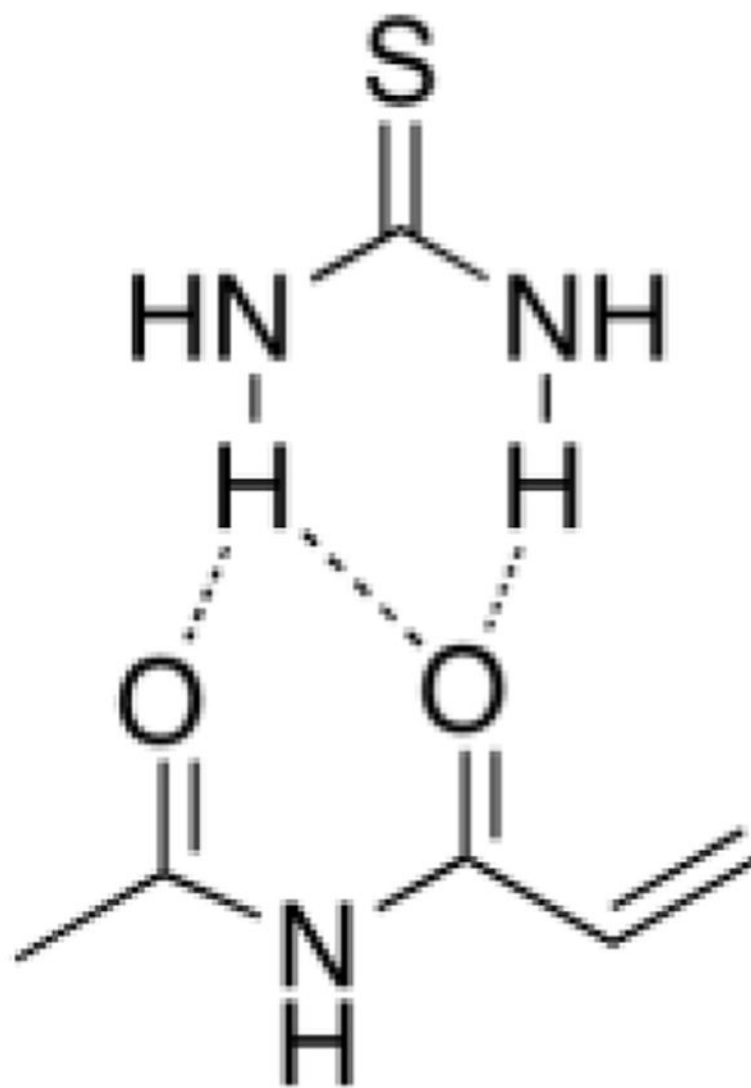


Figure 77.
Binding mode of the complexed model catalyst.

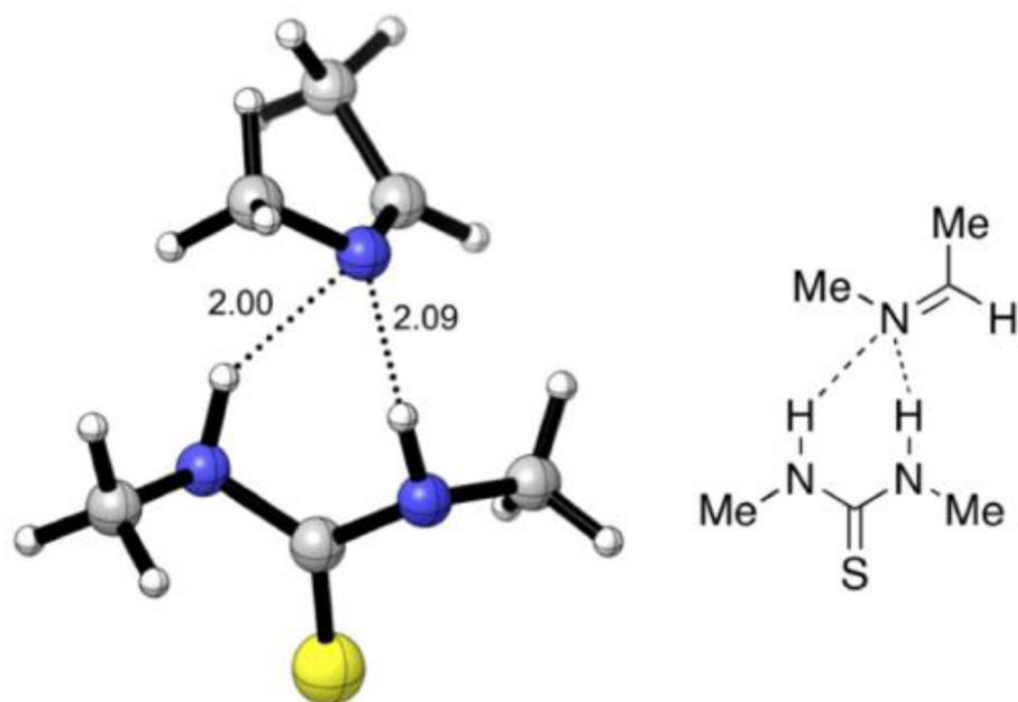


Figure 78. Minimum energy geometry of a catalyst-imine complex 13 at the B3LYP/6-31G(d, p) level.

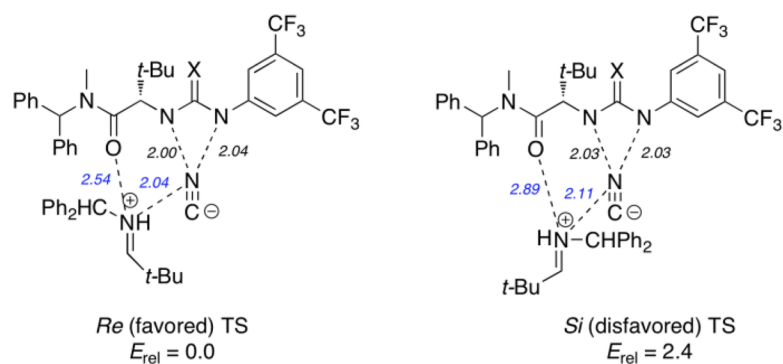


Figure 79. Lowest energy rate-determining transition structures for the major and minor enantiomer products of the Strecker reaction.

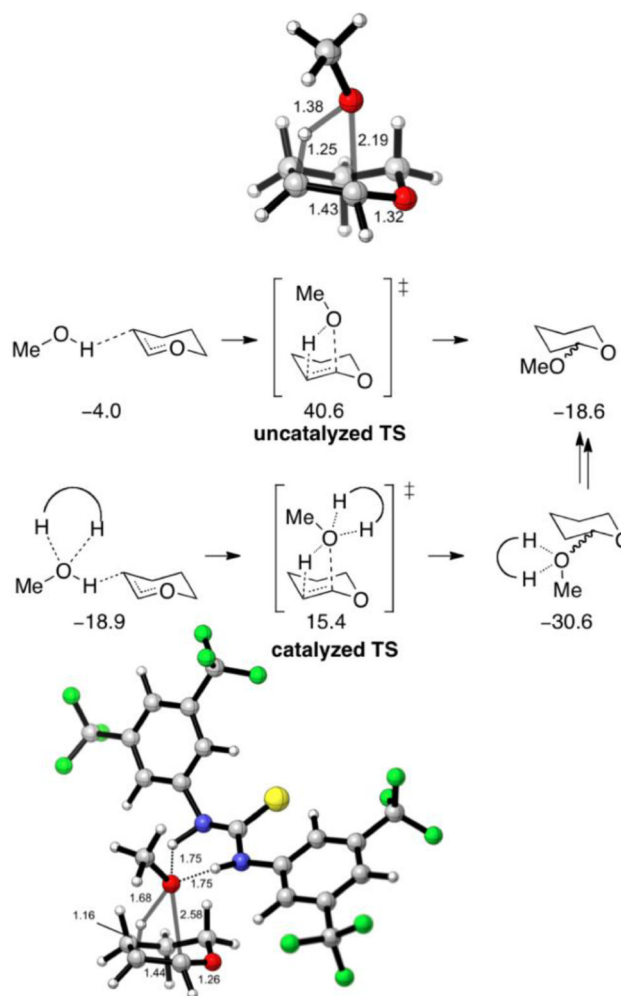


Figure 80. B3LYP/6-31G(d, p) optimized TSs for the addition of methanol to dihydropyran; uncatalyzed (top) and catalyzed (bottom). Energies are with respect to separated reactants.

1. catalyst-ionized lactam

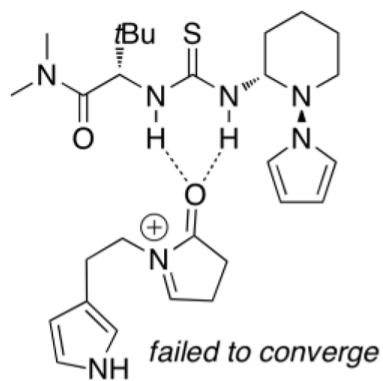
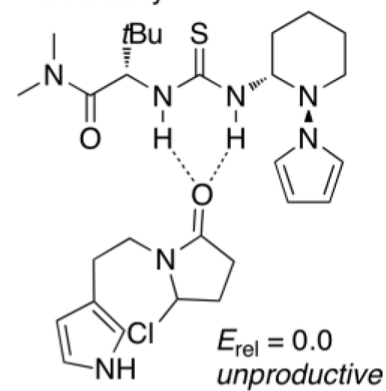
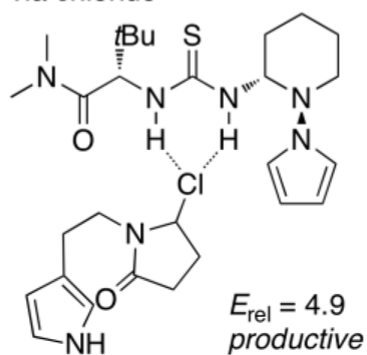
2. catalyst-chlorolactam
via carbonyl3. catalyst-chlorolactam
via chloride

Figure 81.
B3LYP ground state structures.

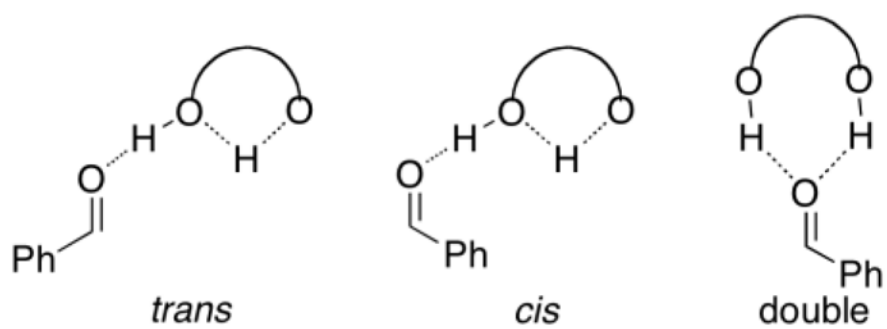


Figure 82.
TADDOL-dienophile H-bonding interactions.

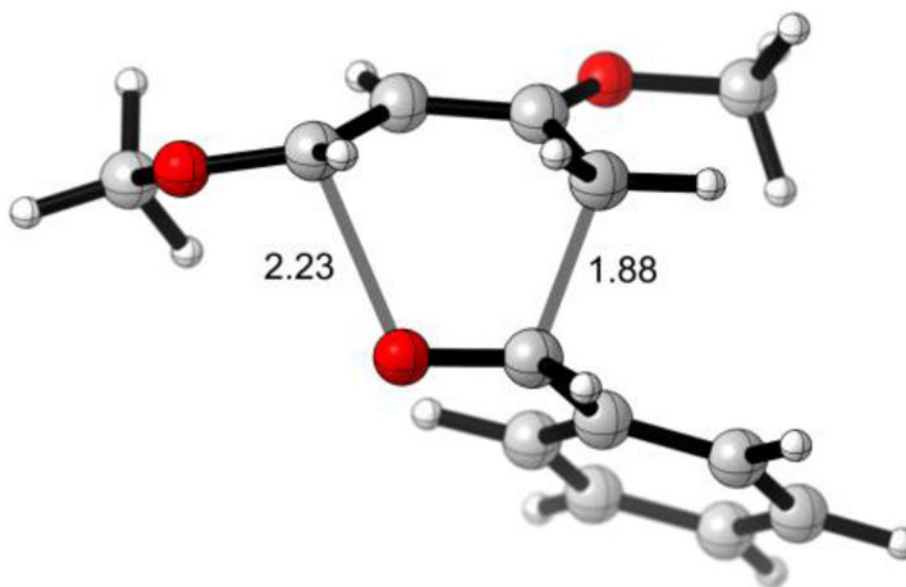


Figure 83.
B3LYP/6-31G(d)//B3LYP/6-31G(d):PM3 transition structure of the uncatalyzed hetero-Diels-Alder cycloaddition of benzaldehyde with 1,3-dimethoxy-1,3-butadiene.

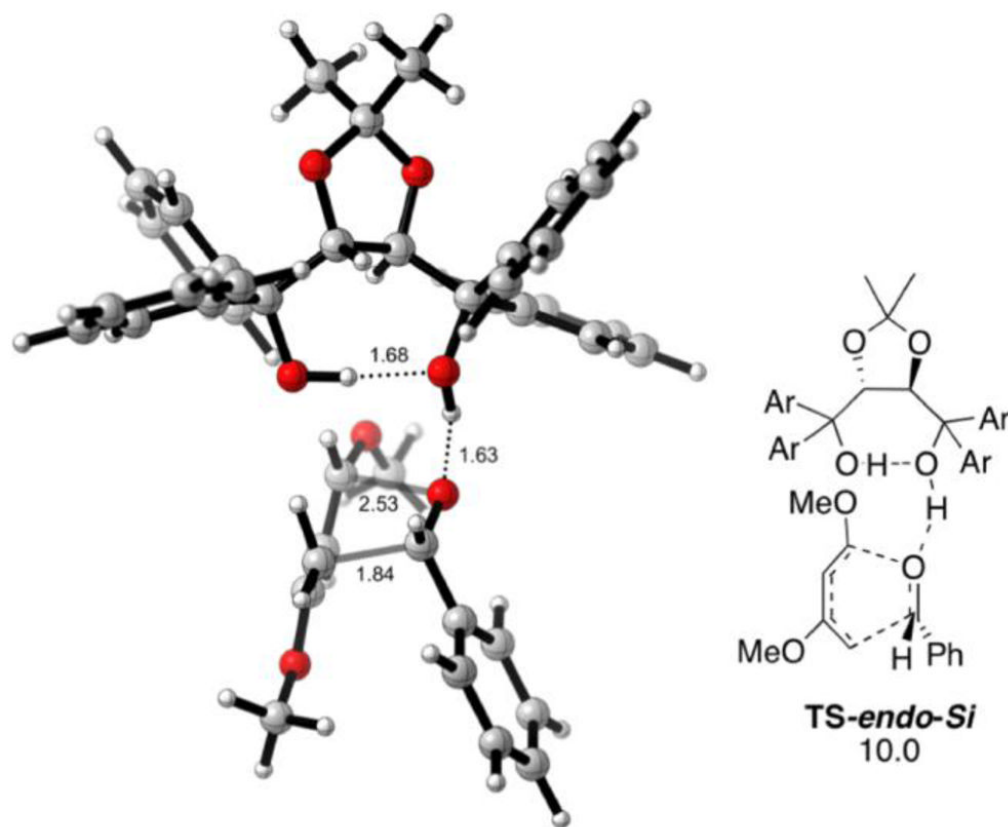
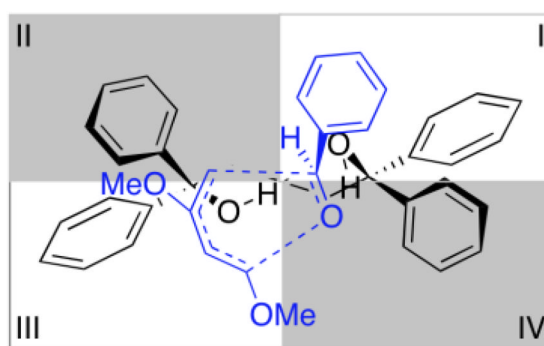
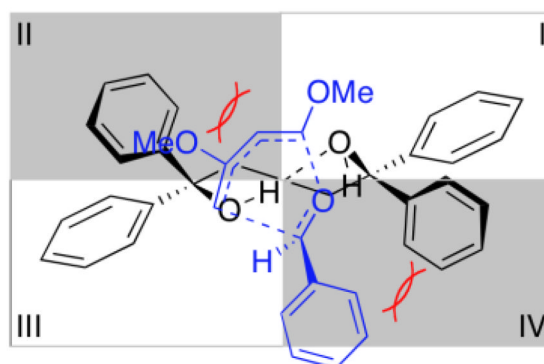


Figure 84.
B3LYP/6-31G(d)//B3LYP/6-31G(d):PM3 transition structure of the TADDOL-catalyzed hetero-Diels-Alder cycloaddition.



(a) *si*-approach, favored



(b) *re*-approach, disfavored

Figure 85. Quadrant diagrams of (a) *si*-face approach. (b) *re*-face approach. Adopted and modified from reference 164.

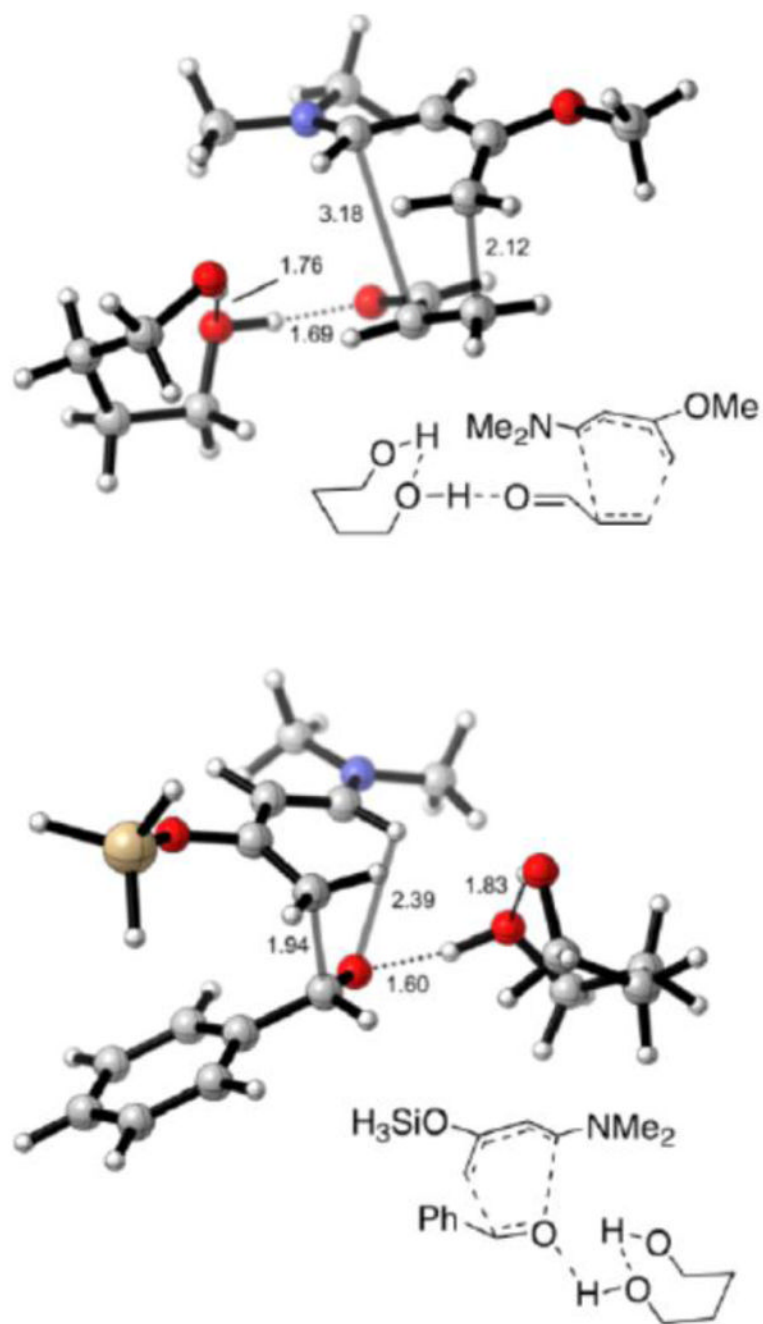


Figure 86.
B3LYP/6-31G(d) transition structures for the 1,4-butanediol Diels-Alder and hetero-Diels-Alder reactions.

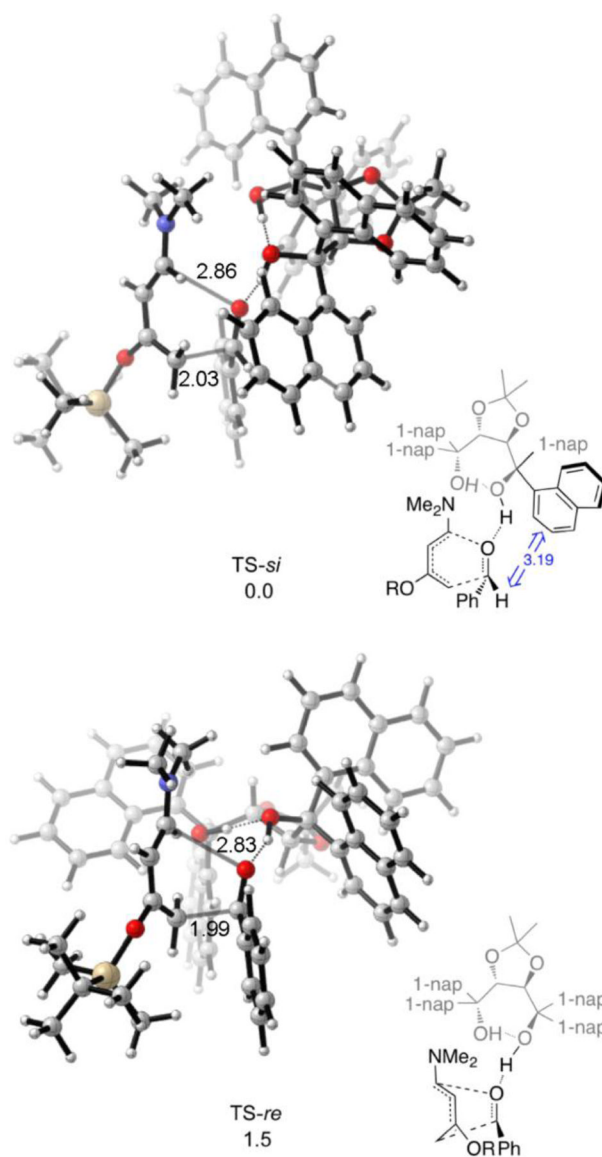


Figure 87. Enantiodetermining B3LYP/6-31G(d)//ONIOM(B3LYP/6-31G(d):AM1) transition structures for (*R,R*)-1-Np-TADDOL-catalyzed hetero-Diels-Alder reaction. R = TBDMS.

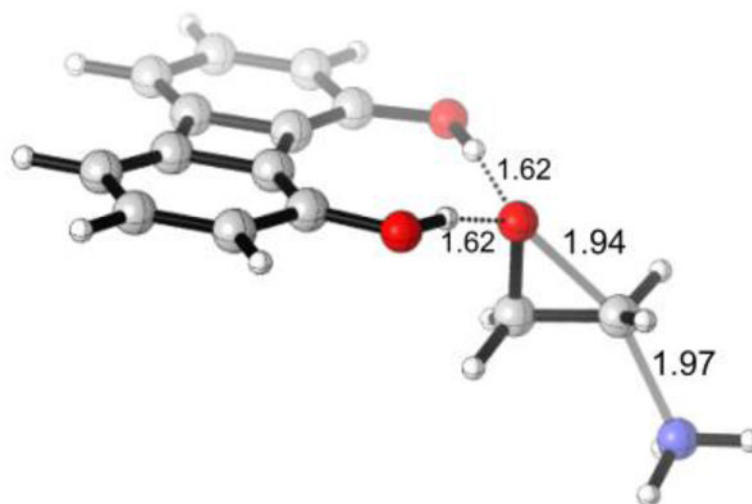


Figure 88.
B3LYP/6-31G(d) optimized transition state geometry of the 1,8-biphenylenediol catalyzed nucleophilic opening of oxirane by ammonia.

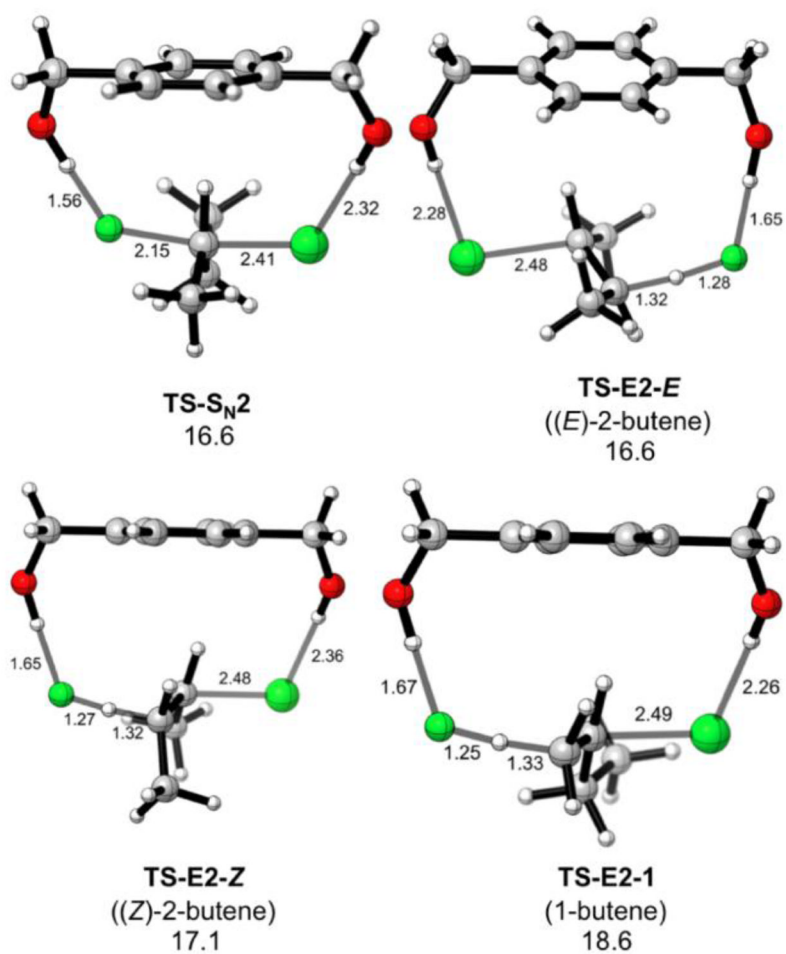


Figure 89. Lowest energy transition structures for the S_N2 and E2 reactions of 2-chlorobutane and F⁻, catalyzed by 1,4-benzenedimethanol.

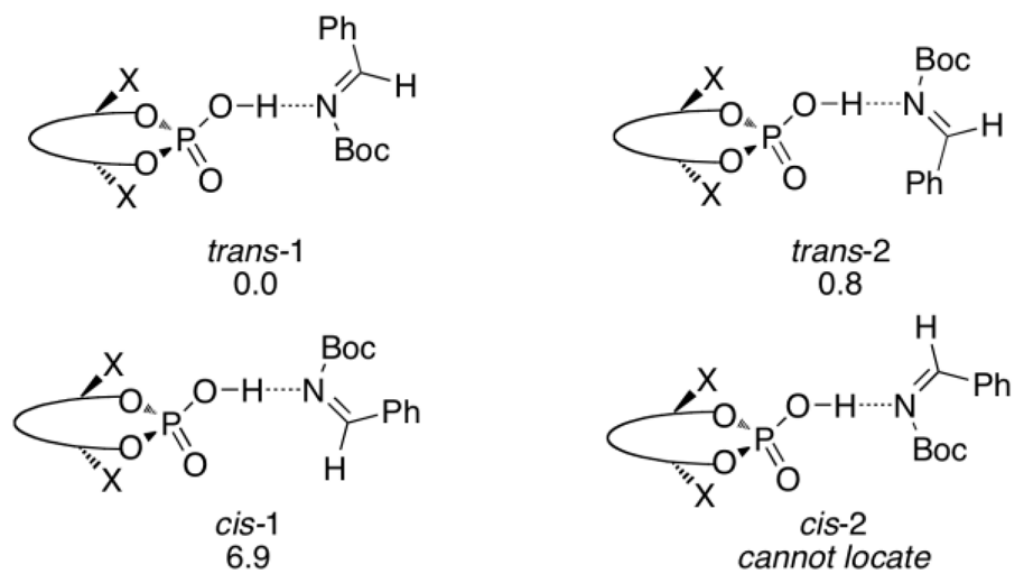


Figure 90. Relative energies of possible imine-phosphoric acid catalyst adducts in the asymmetric Mannich reaction.

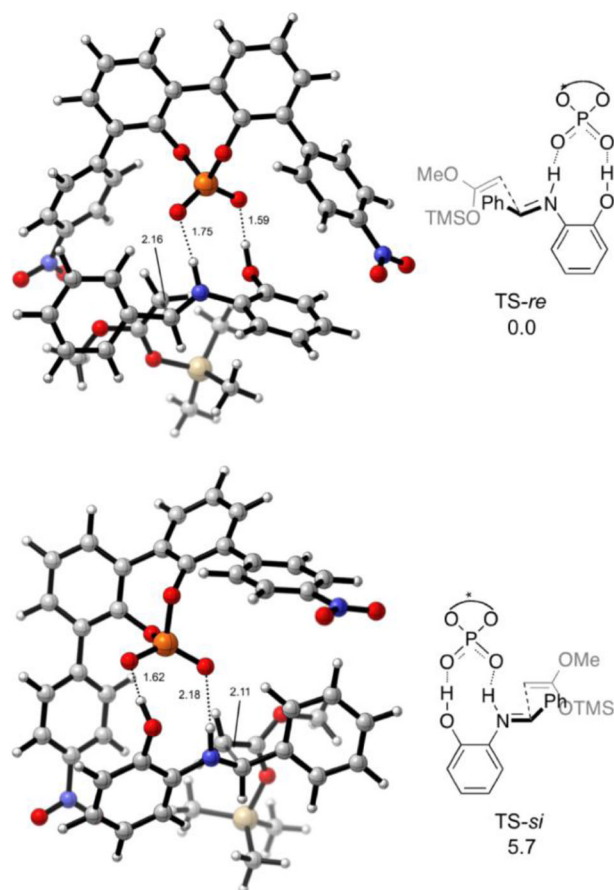


Figure 91. BHandHLYP/6-31G(d) transition structures for the *re*-face and *si*-face attack of enolate to aldimine.

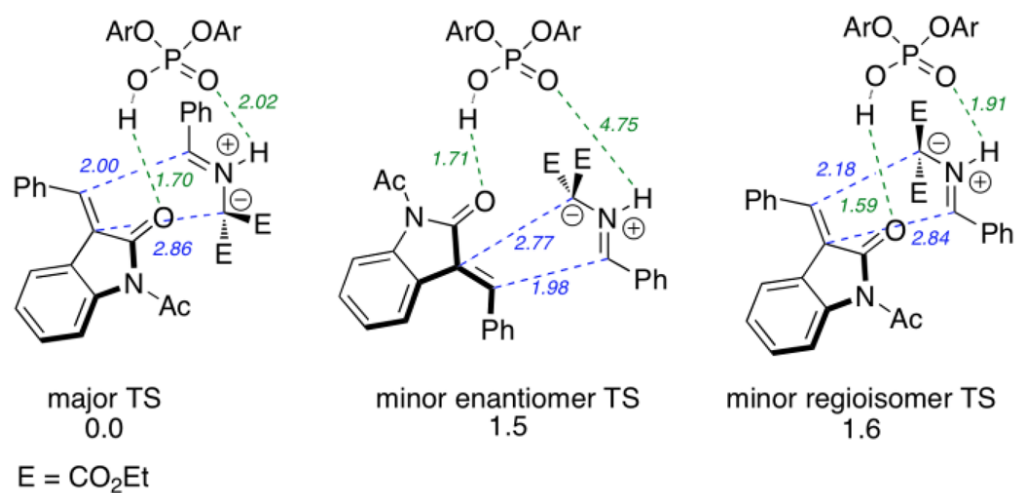


Figure 92. Major and minor transition structures for the chiral phosphoric acid catalyzed 1,3-dipolar cycloaddition.

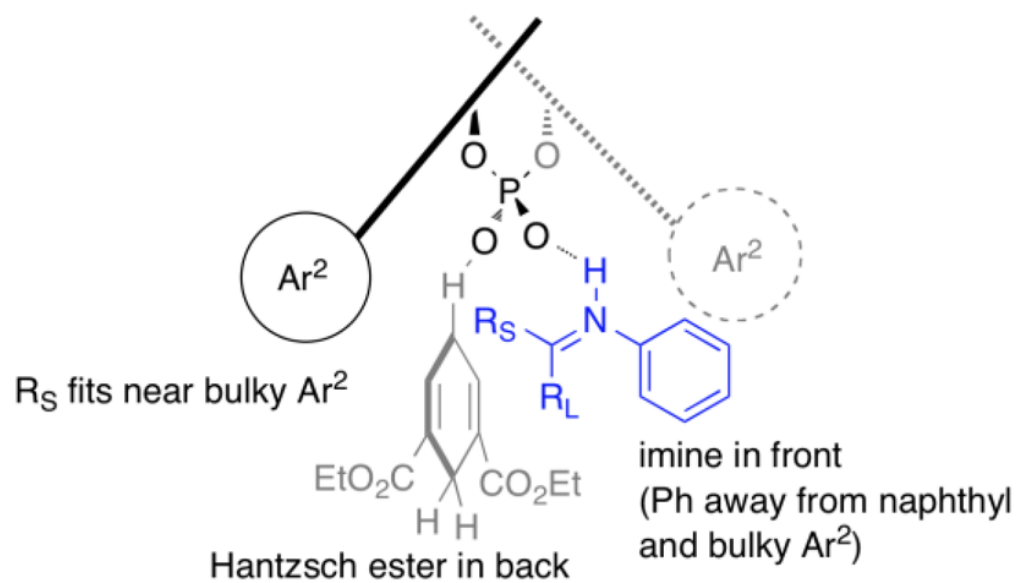


Figure 93.
 Enantioselectivity model for chiral phosphoric acid catalyzed imine hydrogenation.

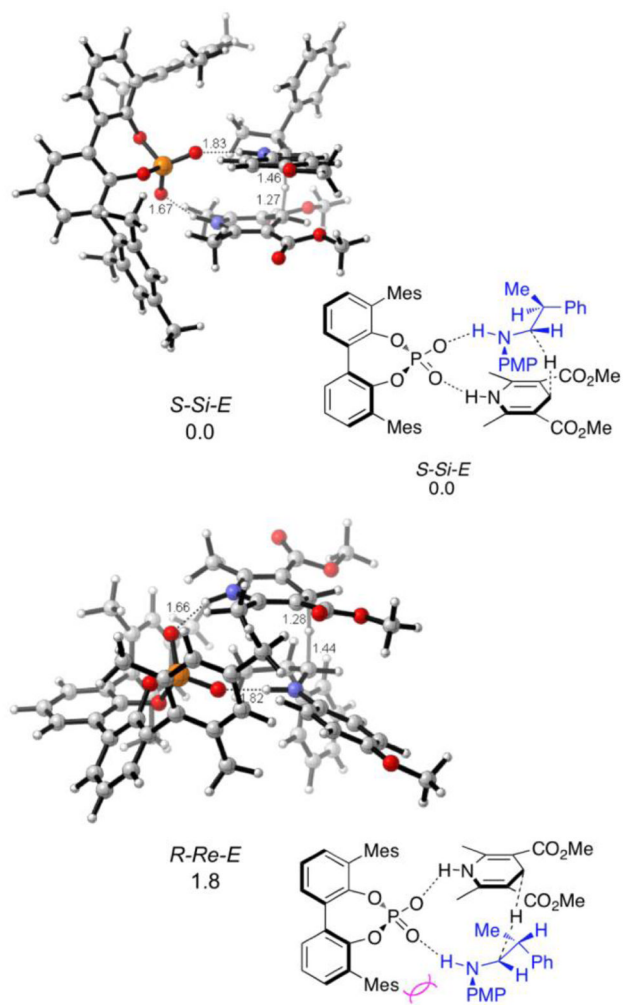


Figure 94.
Lowest energy major and minor transition structures.

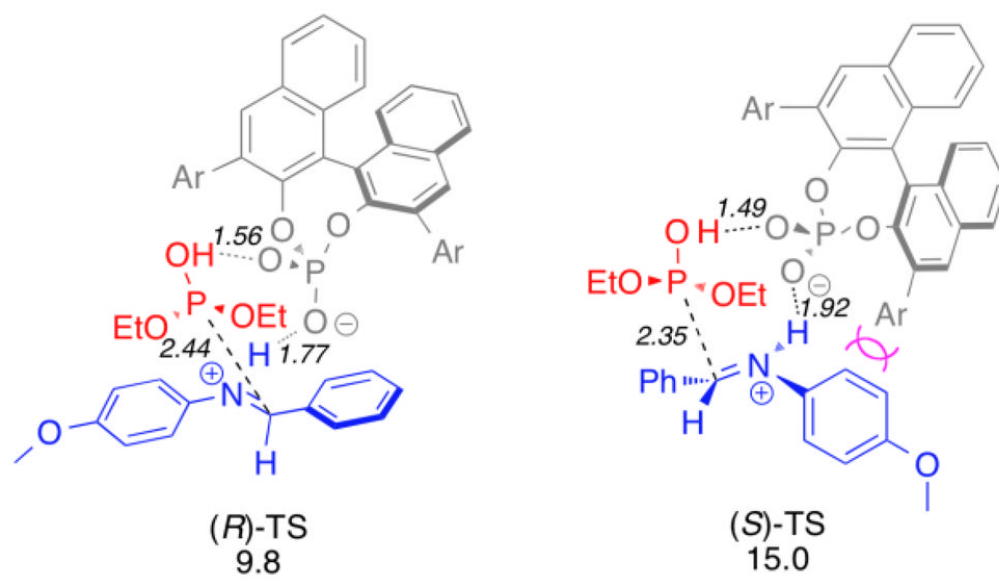


Figure 95.
Lowest energy enantiomeric transition structures for 4-methoxyphenyl protected imine.

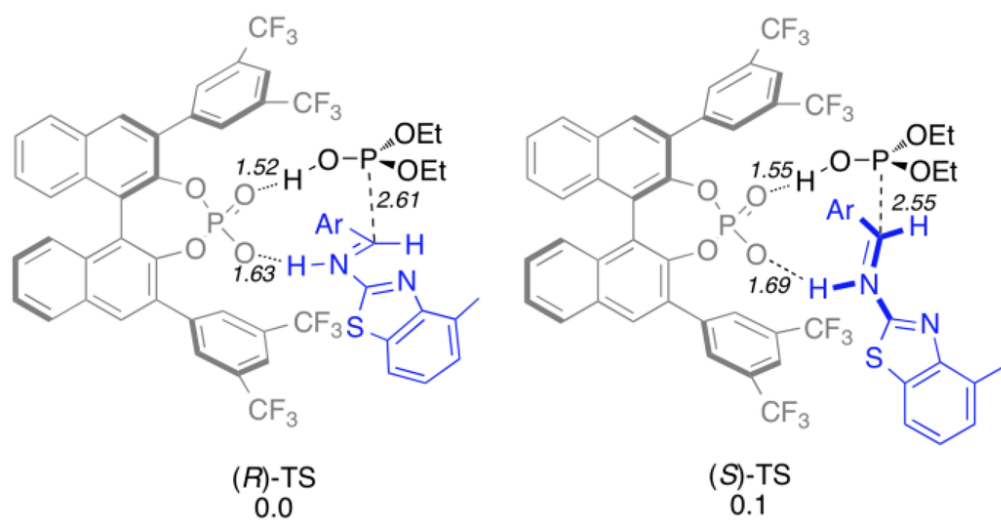


Figure 96.
Lowest energy enantiomeric transition structures for benzothiazole protected imine.

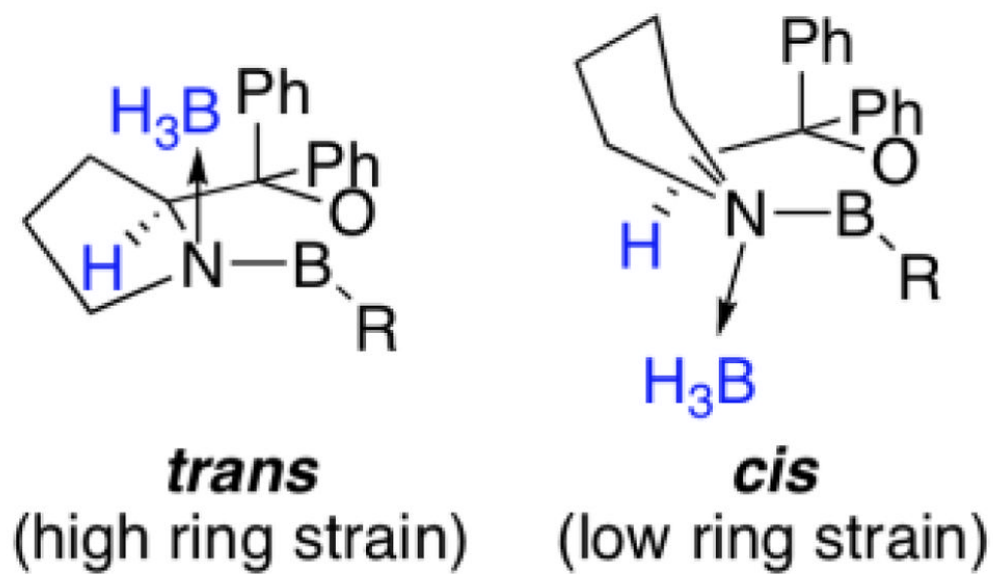


Figure 97.
cis and *trans* (BH₃ and C-4 hydrogen relationship) BH₃-oxazaborolidine complexes.

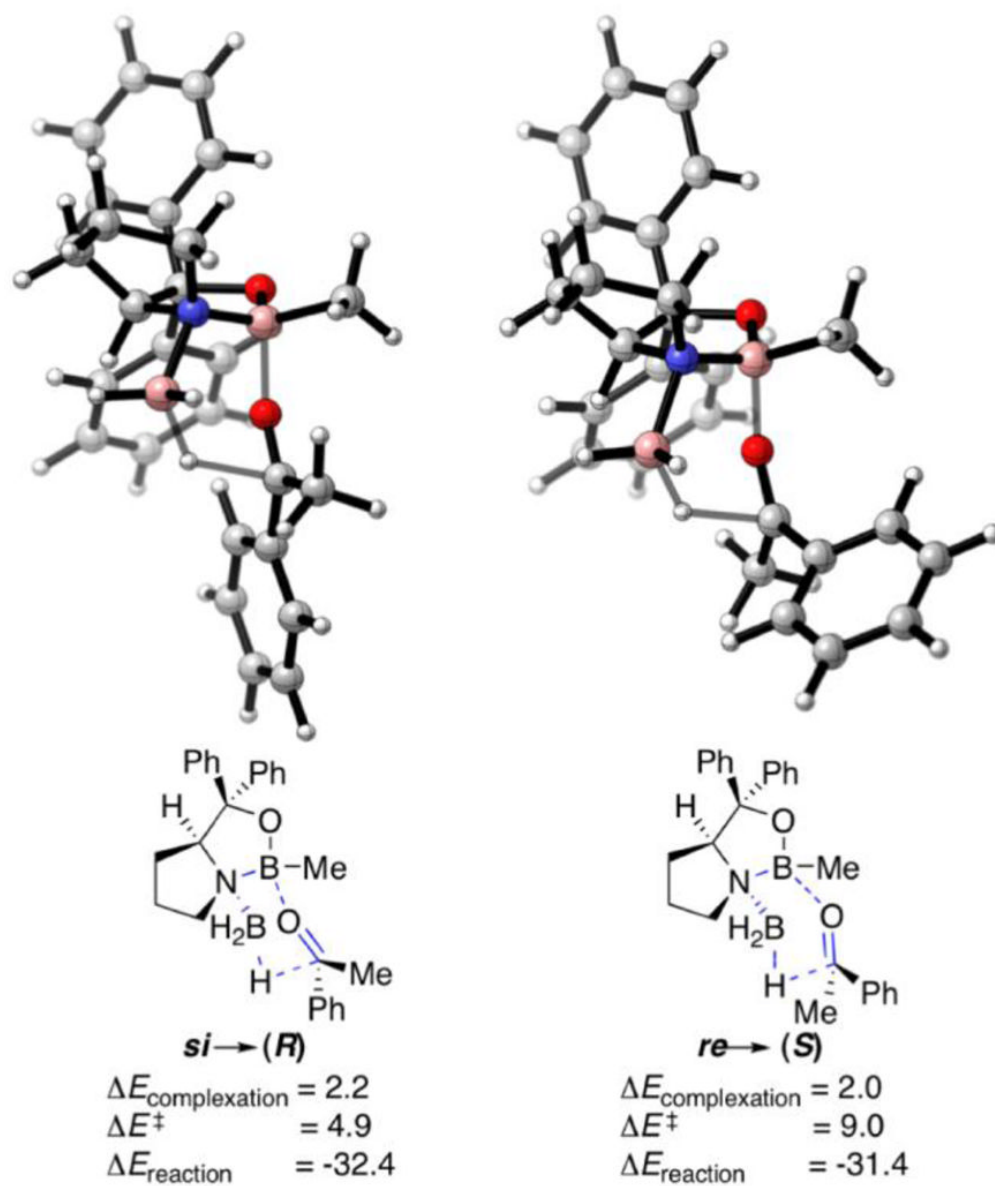


Figure 98. B3LYP/6-31G(d) transition structures for *si* and *re* face hydride transfers to phenyl methyl ketone.

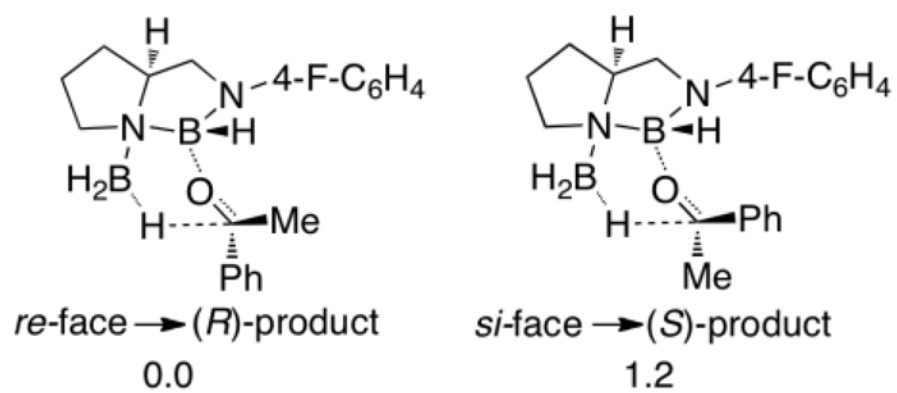


Figure 99.
B3LYP/6-31G(d, p) relative transition structure energies for the reduction of methylphenylketone.

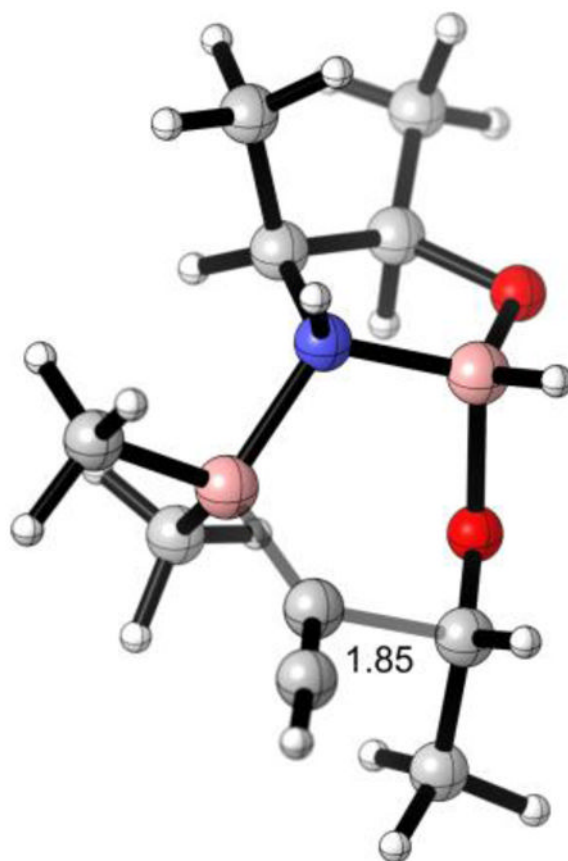


Figure 100. B3LYP/6-31G(d) optimized transition state of lowest energy alkyne transfer (*exo-anti*).

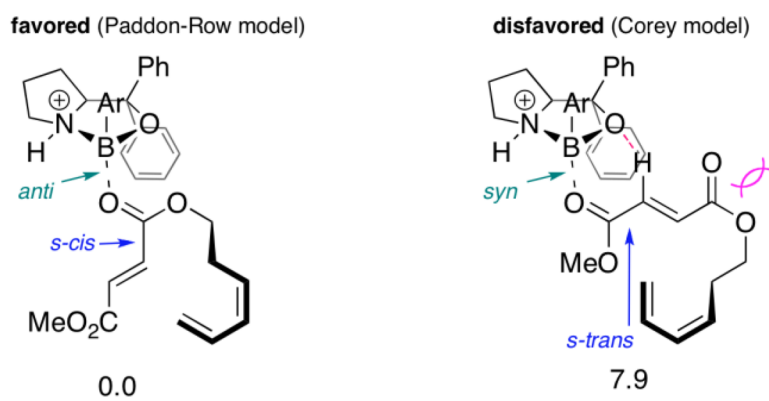


Figure 101. Relative free energies for *s-cis* C=C-C=O versus *s-trans* C=C-C=O ester-activated Diels-Alder cycloaddition.

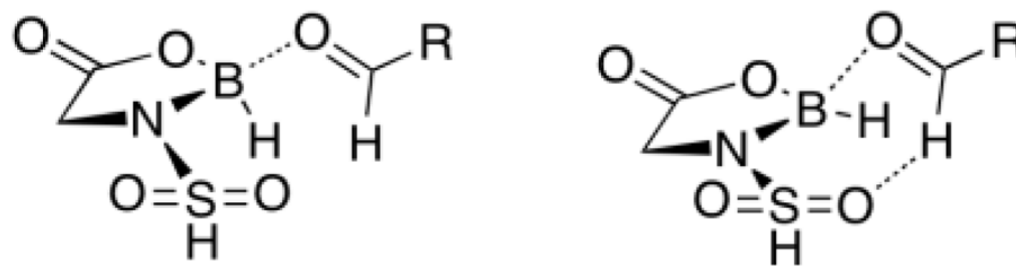


Figure 102.
Favored binding modes of aldehydes with *N*-sulfonylated oxazaborolidine catalysts.

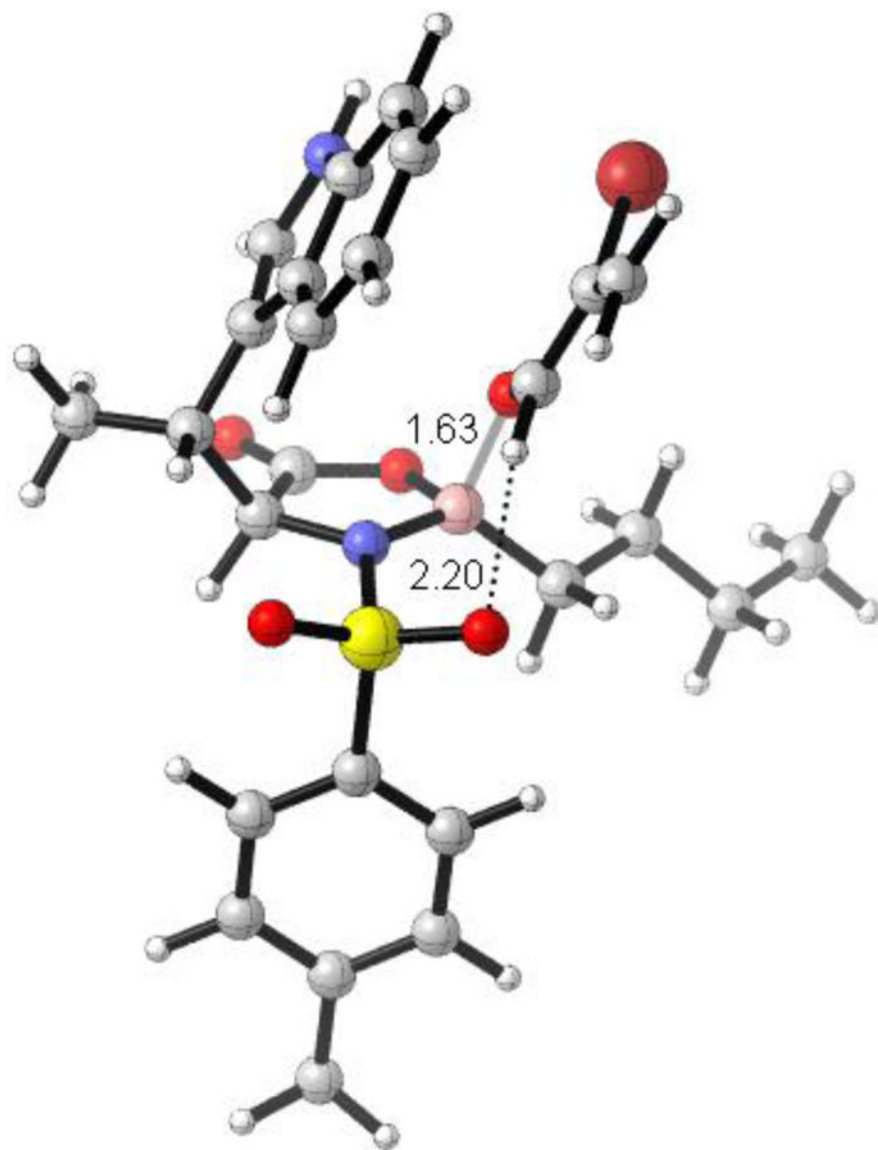


Figure 103.
PW91PW91/6-31G(d) optimized bromoacrolein-catalyst complex.

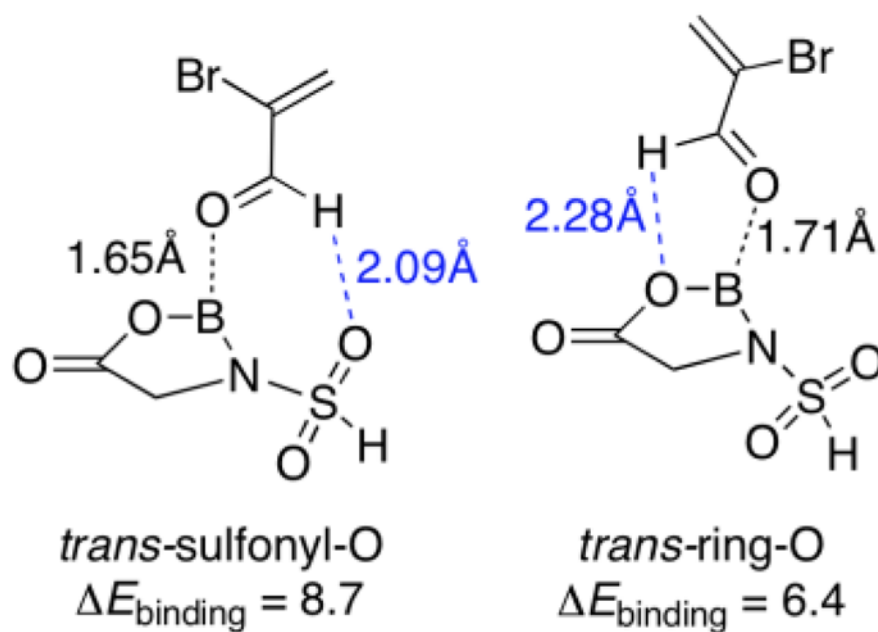


Figure 104. Binding energies (MP2/6-31+G(d)//PW91PW91/6-31G(d)+ZPE) of *s-trans*-2-bromoacrolein-*N*-sulfonylated 1,3,2-oxazaborolidine-5-one complexes.

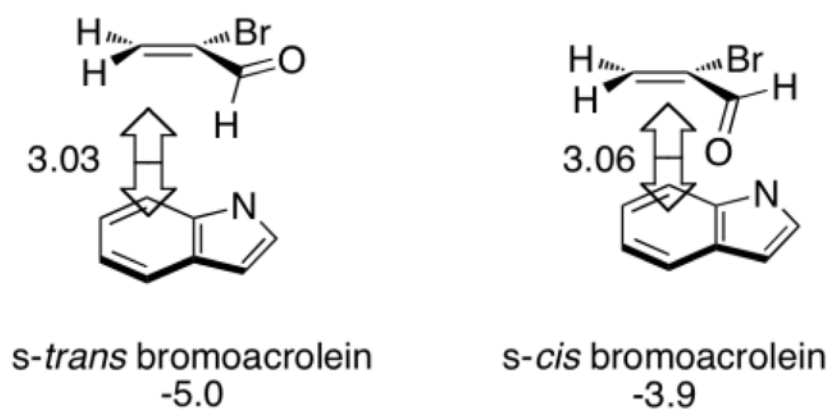


Figure 105. Binding energies (MP2/6-31+G(d)//PW91PW91/6-31G(d)+ZPE) of *s-trans*- and *s-cis*-2-bromoacrolein-*N*-sulfonylated 1,3,2-oxazaborolidine-5-one complexes.

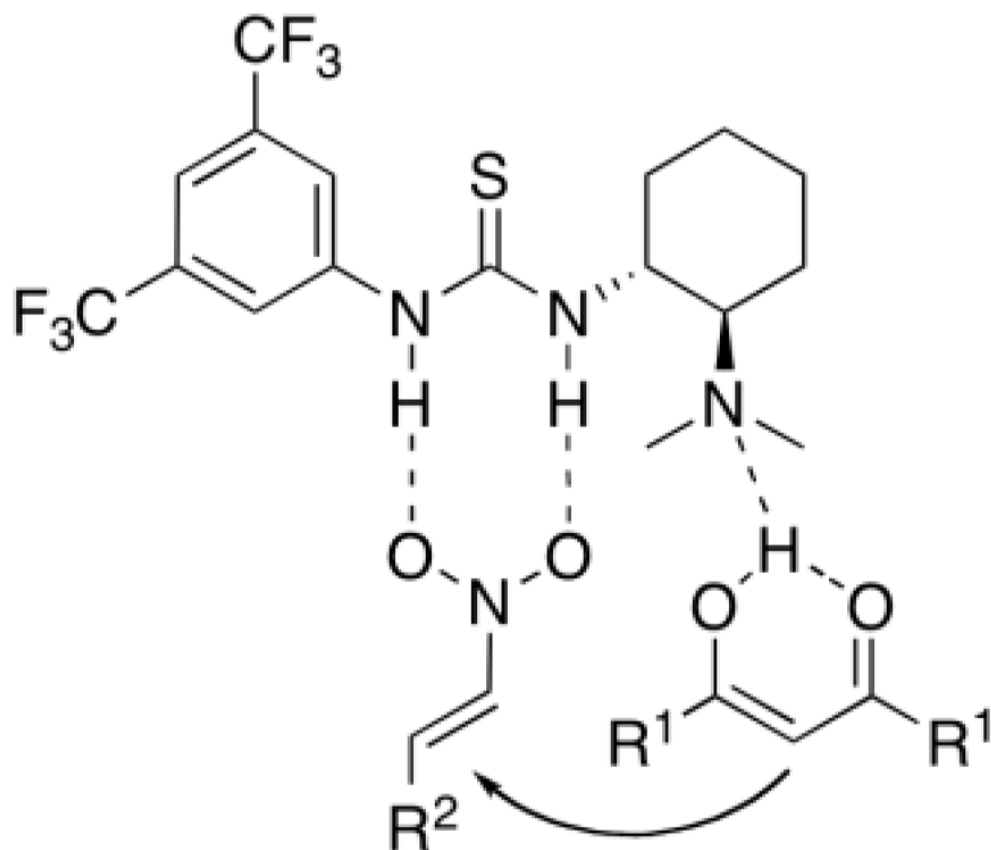
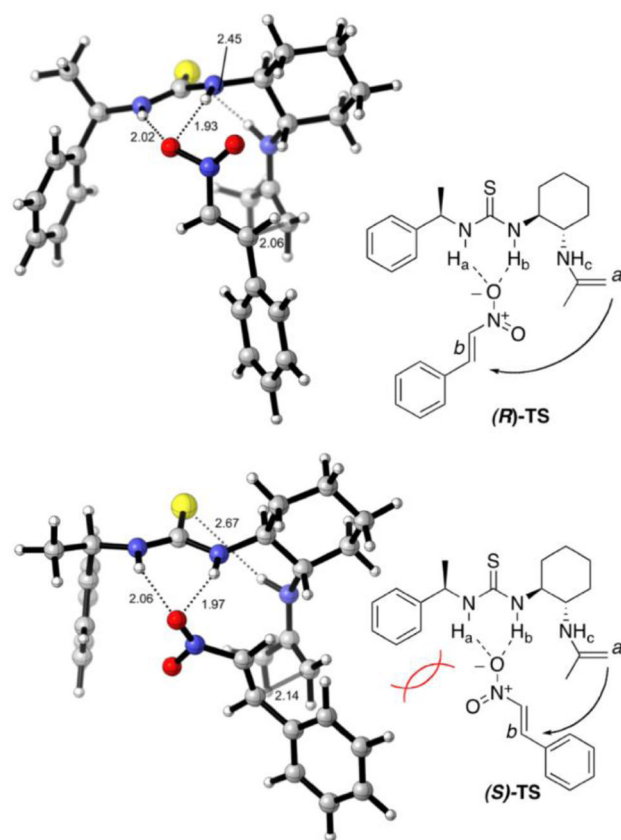


Figure 106.
Dual-activation proposed by Takemoto.



B3LYP/6-31G(d) $\Delta\Delta G = 1.0$
 B3LYP/6-31G(d,p)//B3LYP/6-31G(d) $\Delta\Delta G = 1.0$
 B3LYP/6-31+G(d)//B3LYP/6-31G(d) $\Delta\Delta G = 1.2$
 B3LYP/6-31+G(d,p)//B3LYP/6-31G(d) $\Delta\Delta G = 1.3$

Figure 107.
 Transition structures of the formation of the *R* and the *S* enantiomeric products.

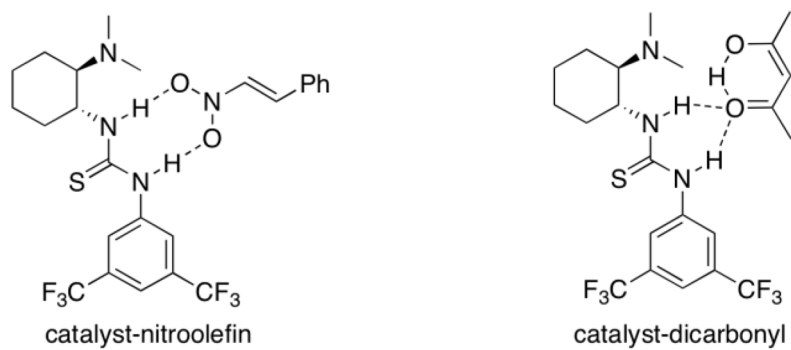


Figure 108.
Most stable catalyst-nitro-olefin complex and most stable catalyst-dicarbonyl complex.

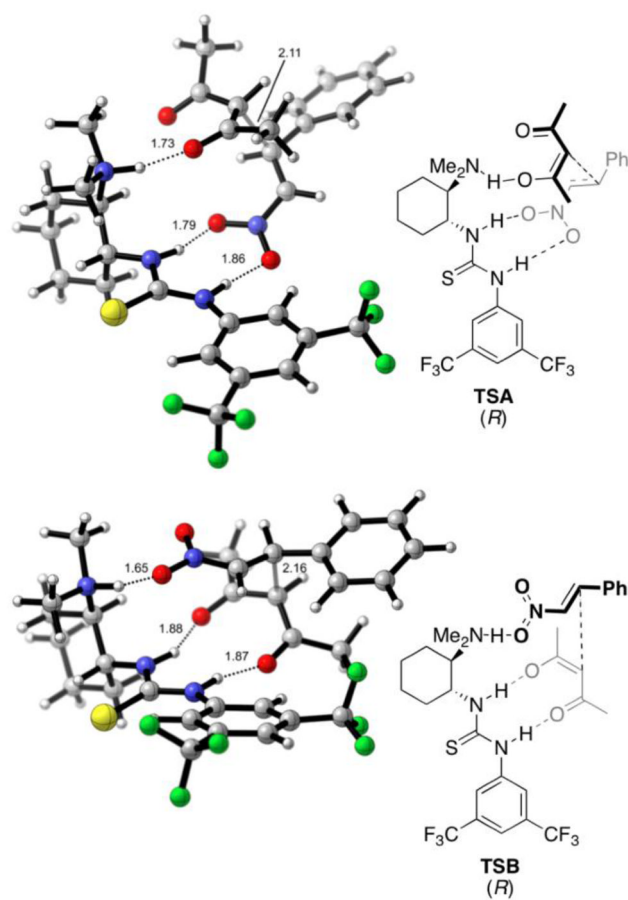


Figure 109.
Michael addition transition structures for major (*R*) pathways A and B.

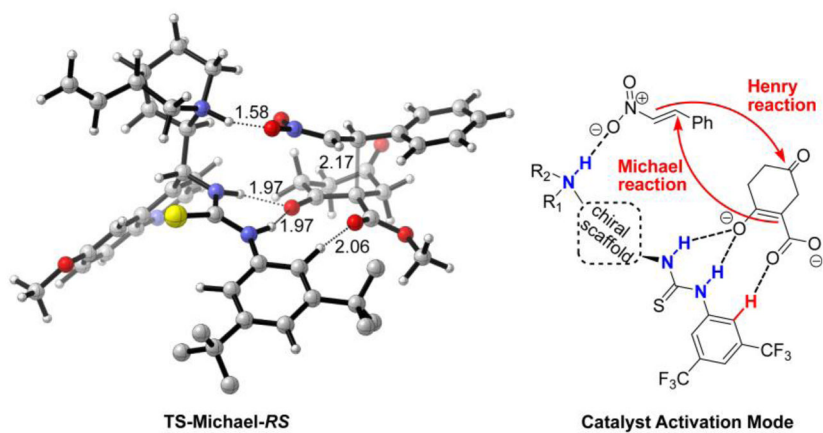


Figure 110. Lowest energy Michael addition transition structure and proposed activation mode of the catalyst and the substrate.

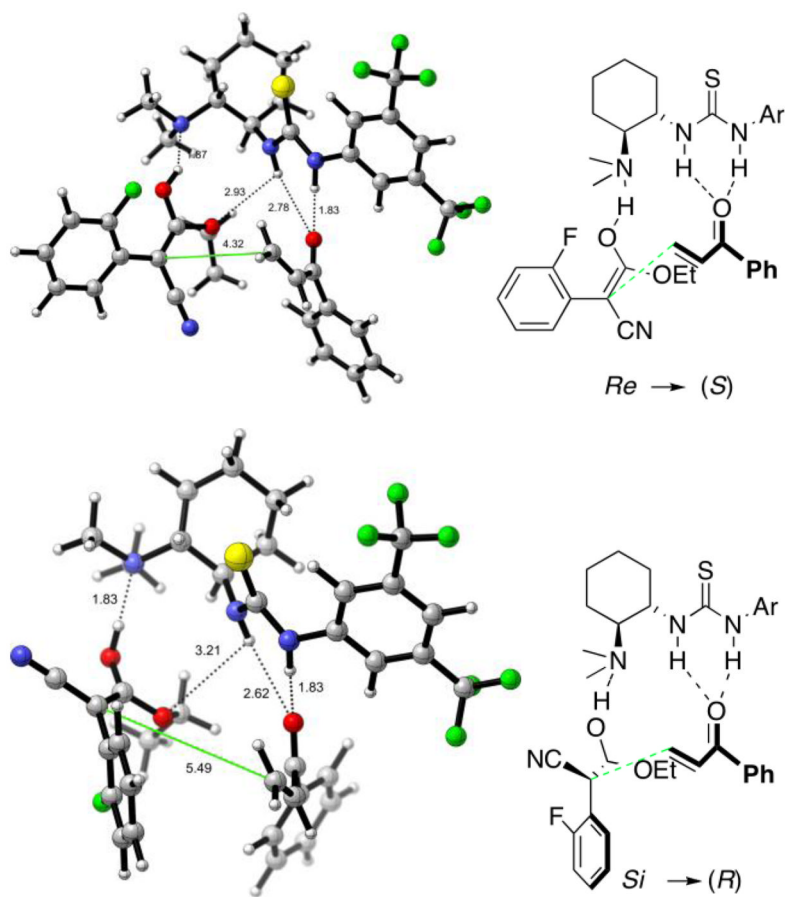


Figure 111. Possible intermediates in the Michael addition of α -2-fluorophenyl cyanoacetate to phenyl vinyl ketone. Top: *Re*-face attack, yielding the major (*S*)-enantiomer. Bottom: *Si*-face attack, yielding the minor (*R*)-enantiomer.

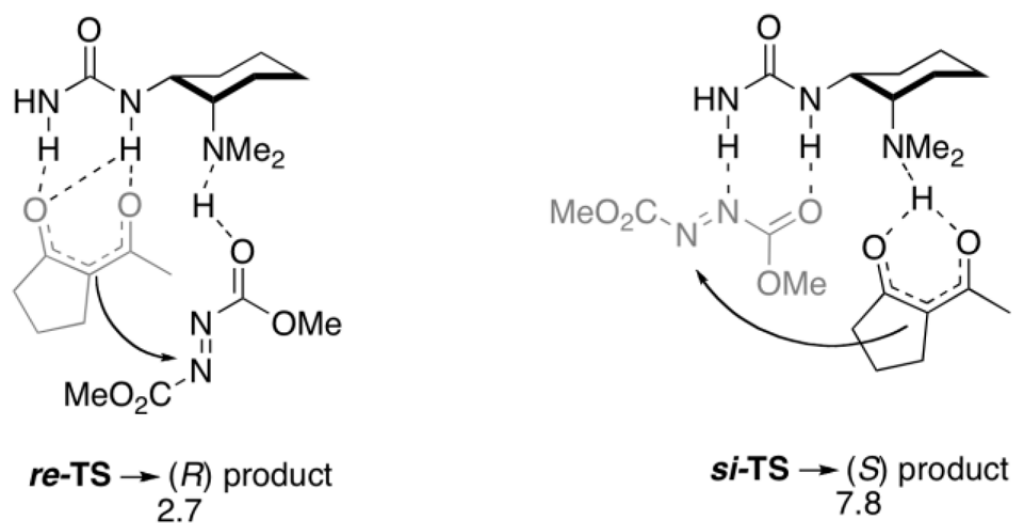


Figure 112.

Lowest energy B3LYP/6-311++G(d, p)/B3LYLP/6-31G(d) transition state energies for the enantiomeric products of the α -amination reaction.

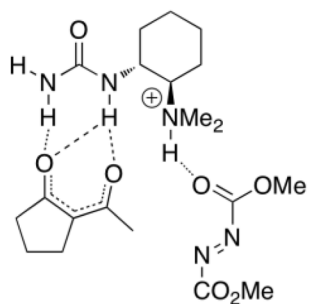
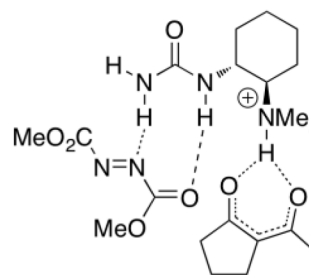
A: urea-dicarbonyl activation**B: azodicarboxylate activation**

Figure 113.
Activation modes for the α -amination reaction.

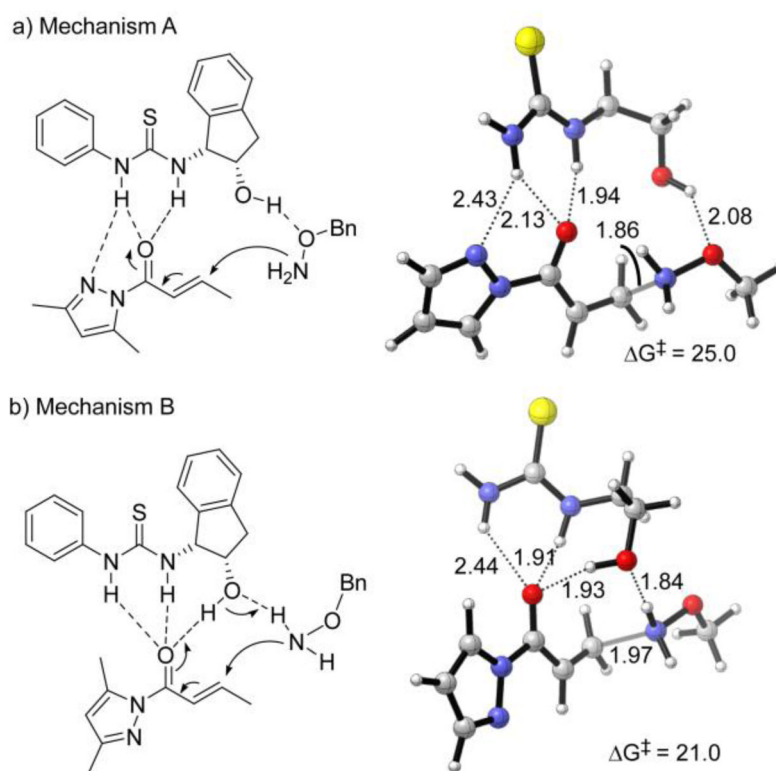


Figure 114. Proposed mechanisms for the conjugate addition of amines to pyrazole crotonates and corresponding transition structures calculated with a simplified model catalyst.

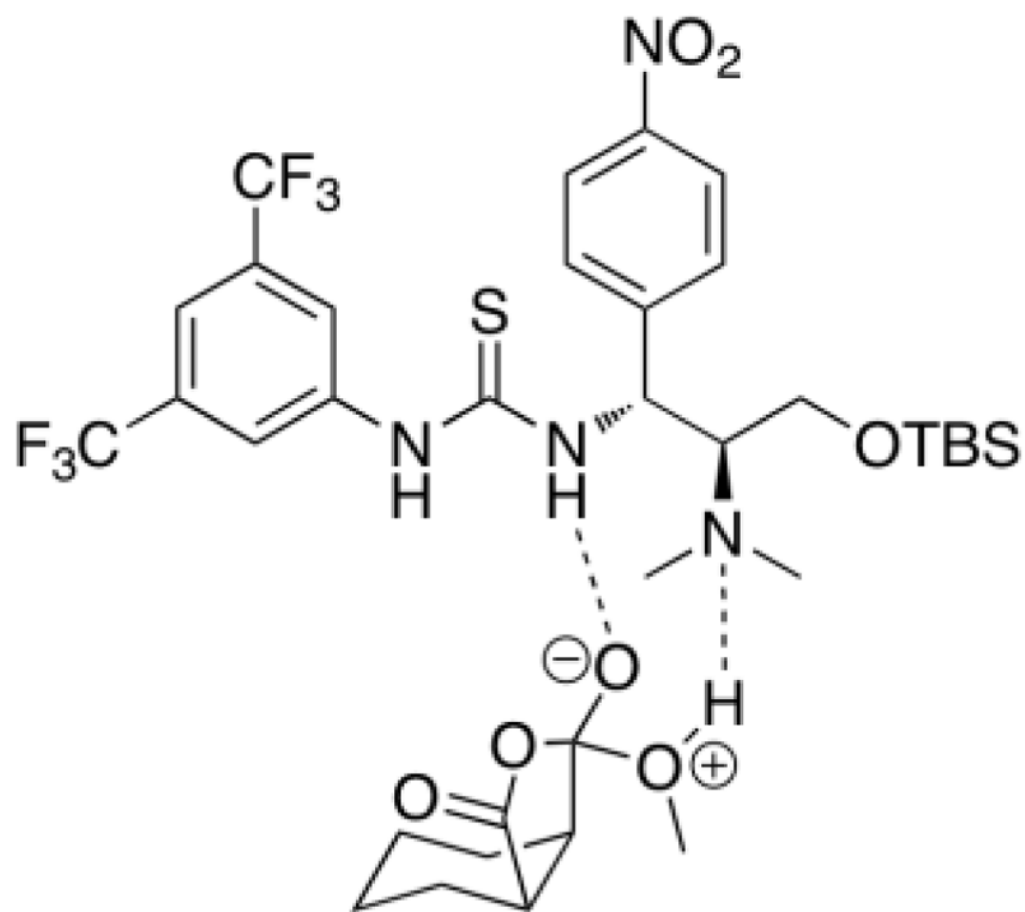


Figure 115. Transition state model for major enantiomer in the thiourea catalyzed alcoholysis of a *meso*-anhydride.

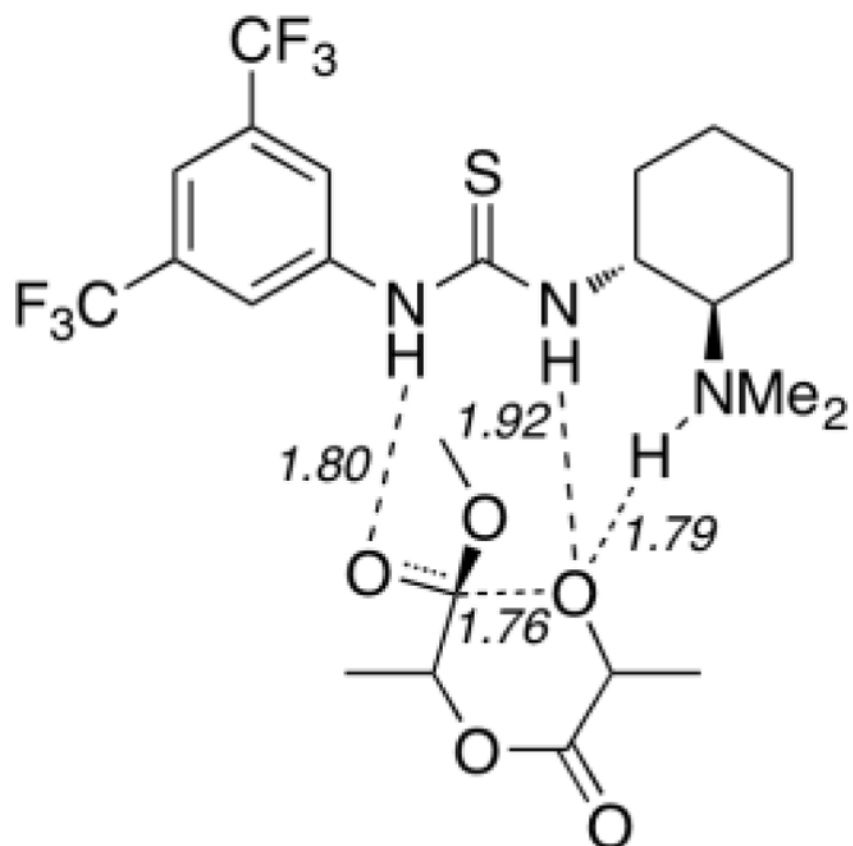


Figure 116.
Rate-determining transition structure for the stepwise ring-opening of D-lactide catalyzed by a bifunctional thiourea.

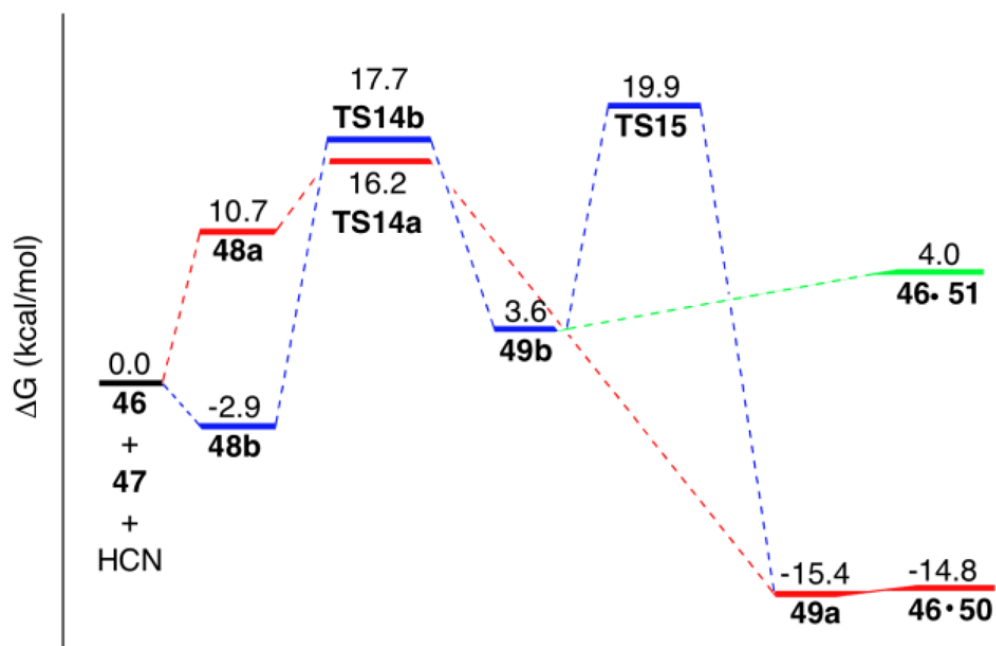


Figure 117. B3LYP/6-31G(d) free energy profile for the reaction of HCN or HNC with formylimine, catalyzed by **46**, in toluene at 298.15K. Red = Pathway A. Blue = Pathway B.

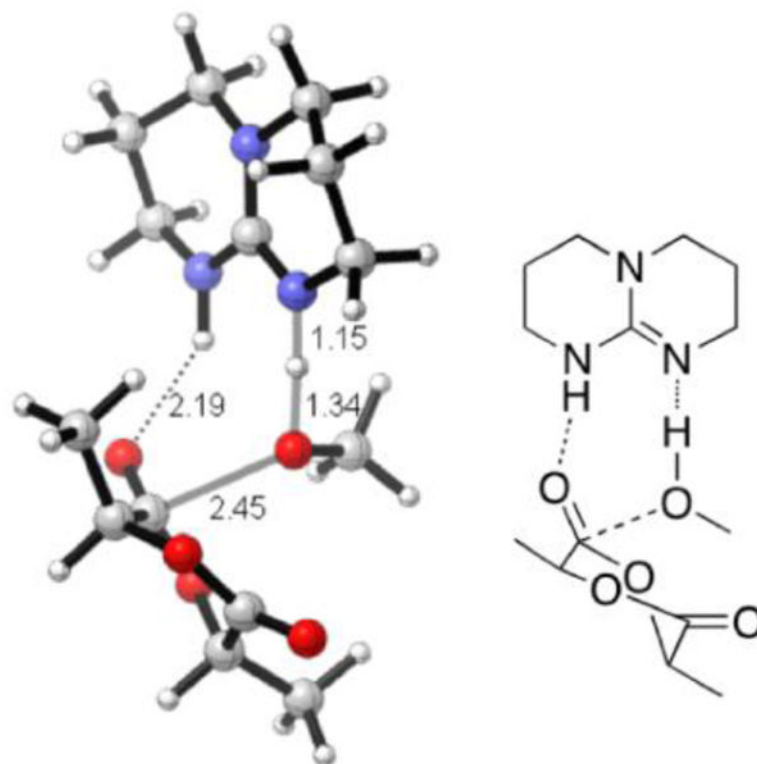
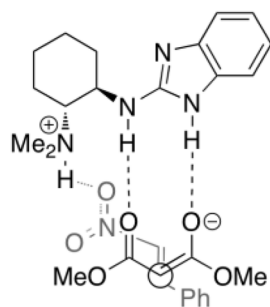
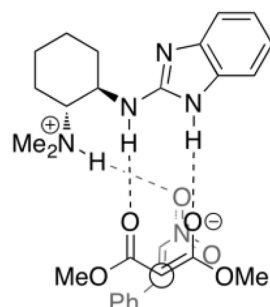


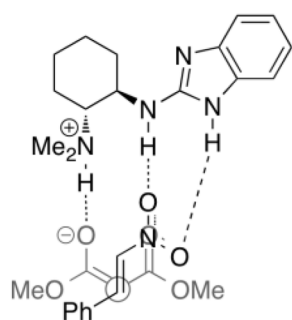
Figure 118.
Rate-determining transition structure for TBD-catalyzed ring-opening polymerization of L-lactide.

Di-coordinated 1,3-dicarbonyl

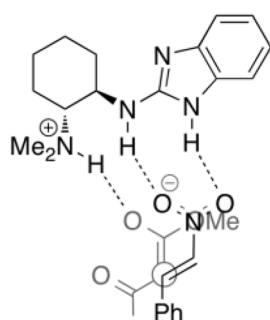
R-TS
0.0 (0.0)



S-TS
2.6 (3.2)

Di-coordinated nitroalkene

R-TS
1.9 (3.0)



S-TS
2.4 (3.7)

Figure 119. B3LYP/6-311++G(d, p)//B3LYP/6-31G(d). Single-point values in a toluene model (IEF-PCM) in parentheses.

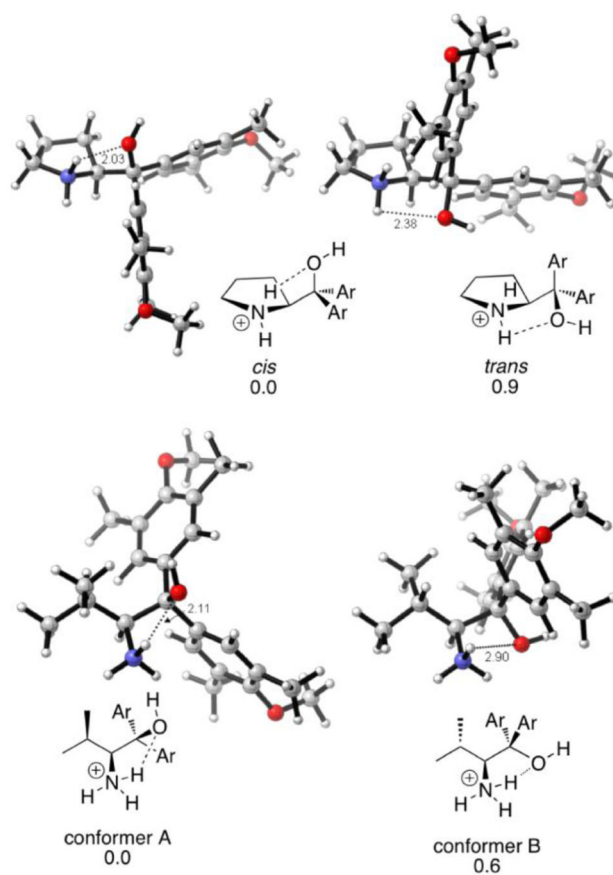


Figure 120.
B3LYP/6-31G(d) conformers and relative energies of protonated catalysts.

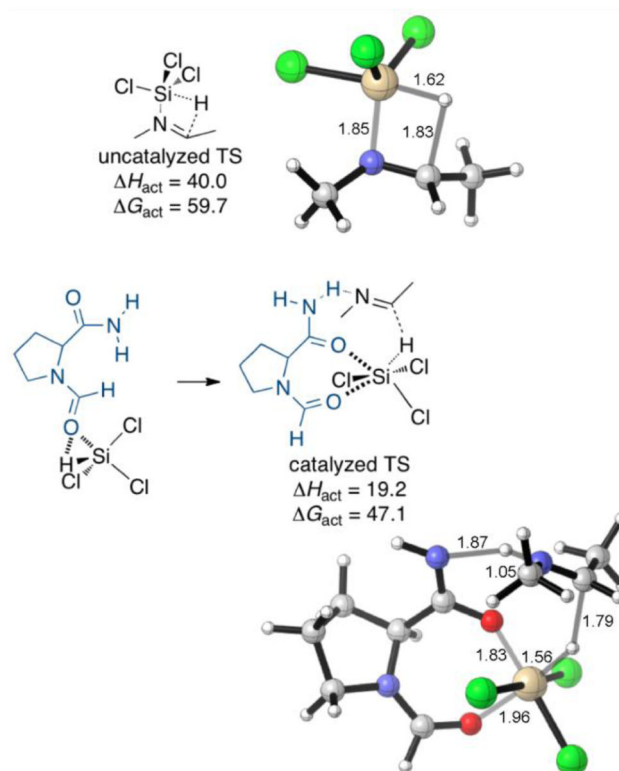


Figure 121. Uncatalyzed (left) and catalyzed (right) rate-determining transition structures for hydride transfer from trichlorosilane to *N*-methyl-methylaldimine.

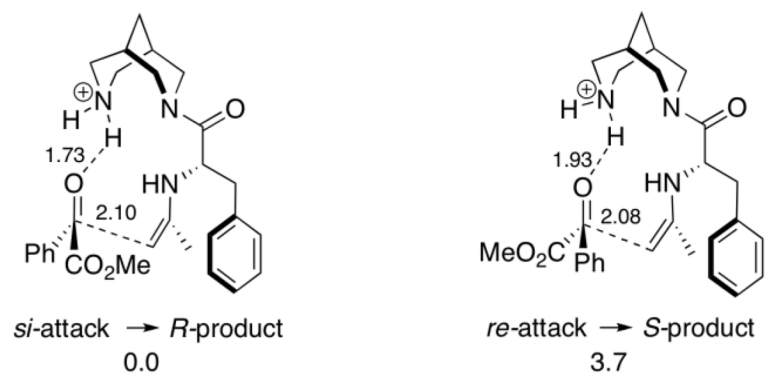


Figure 122. B3LYP/6-311G(d, p)//HF/6-31G(d) (IEFPCM, acetone) relative energies and distances for the calculated transition structures of the aldol reaction.

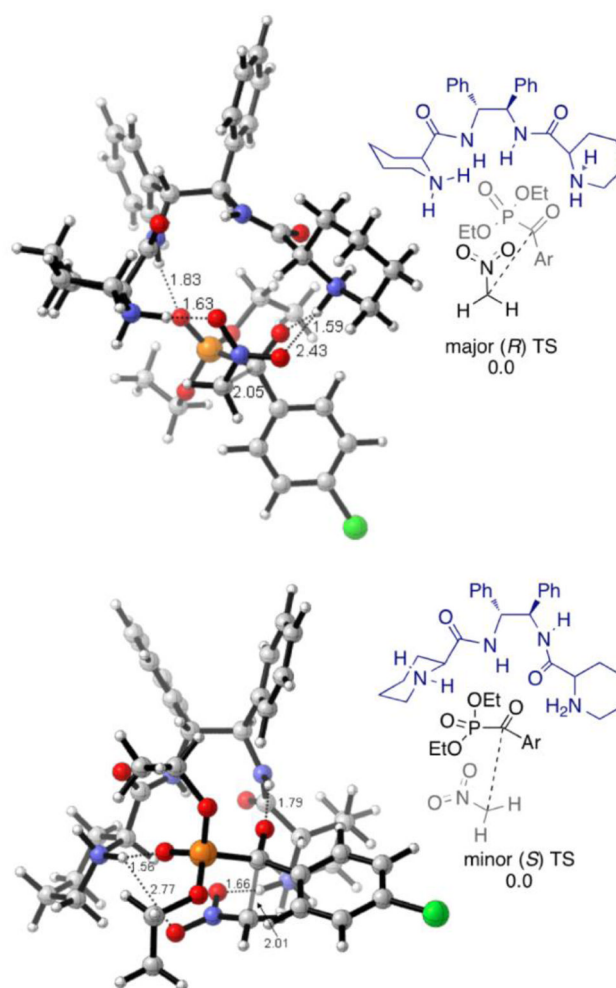


Figure 123. Major (*R*) and minor (*S*) transition structures for the nitroaldol reaction. (H-bonds were omitted from ChemDraw diagrams for clarity).

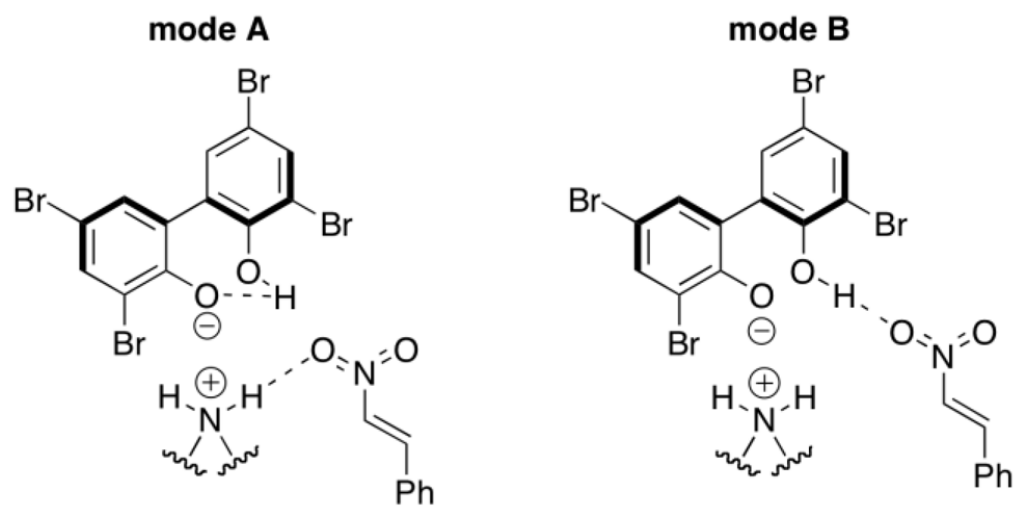


Figure 124.
Activation modes of the bispidine catalyzed Michael addition reaction.

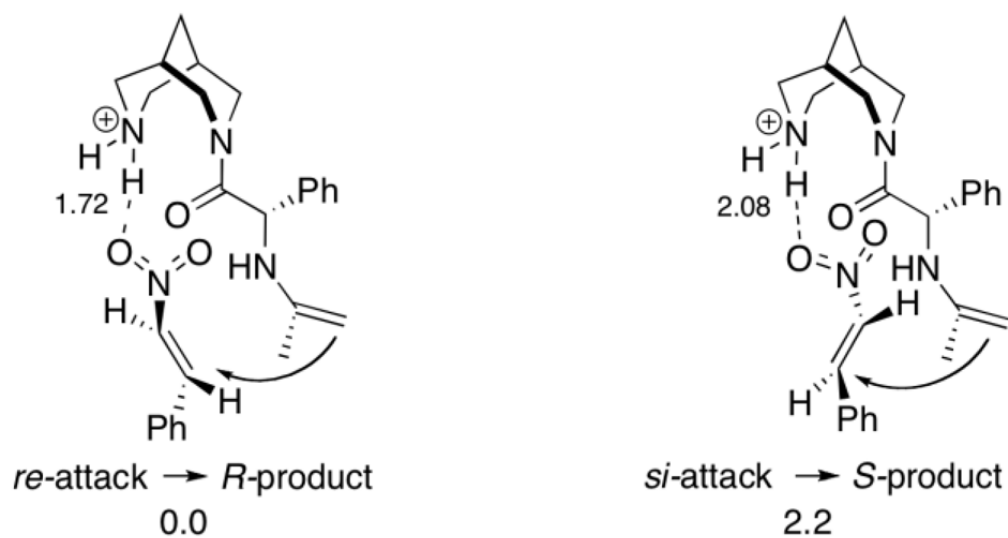


Figure 125. B3LYP/6-311G(d, p)//HF/6-31G(d) (IEFPCM, acetone) relative energies and distances for the lowest-energy transition structures of the bispidine-catalyzed Michael addition of acetone to phenylstyrene.

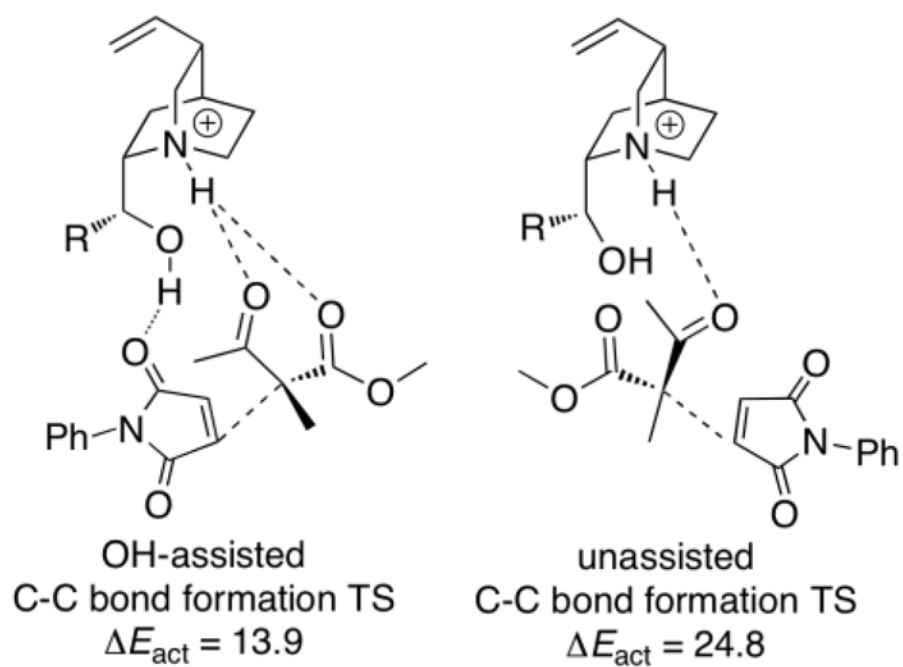


Figure 126. QM/MM transition structures for C-C bond formation, with (left) and without (right) OH assistance.

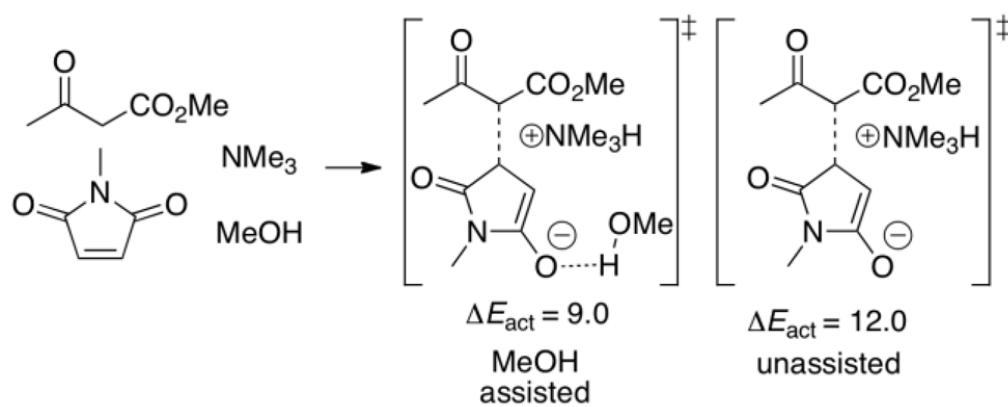


Figure 127. B3LYP/6-311+G(d, p) activation energies for Michael addition, with and without methanol assistance.

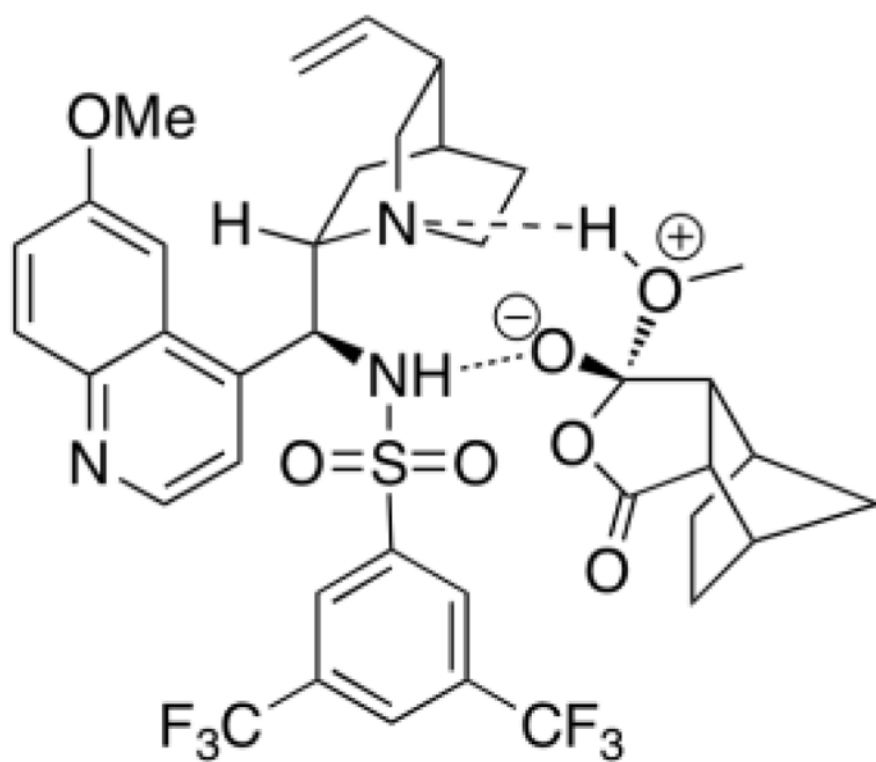


Figure 128.
Transition state model for bifunctional cinchona alkaloid catalyzed desymmetrization of cyclic *meso*-anhydride.

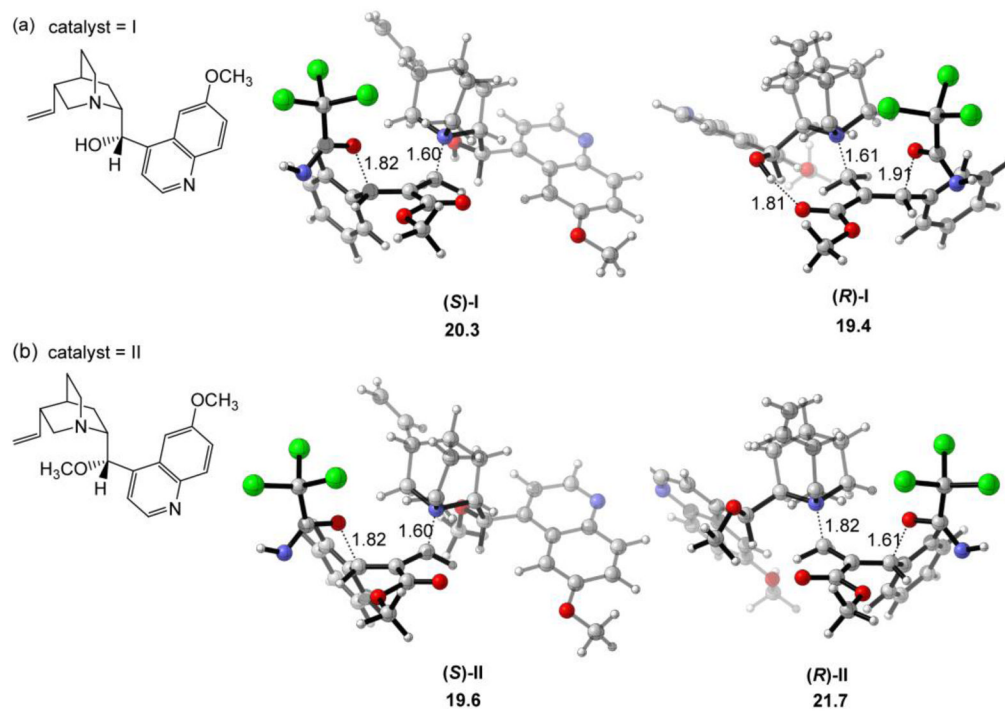


Figure 129. Enantiomeric transition structures and their activation free energies (ΔG , kcal/mol) for the addition of the catalyst to trichloroacetimidate.

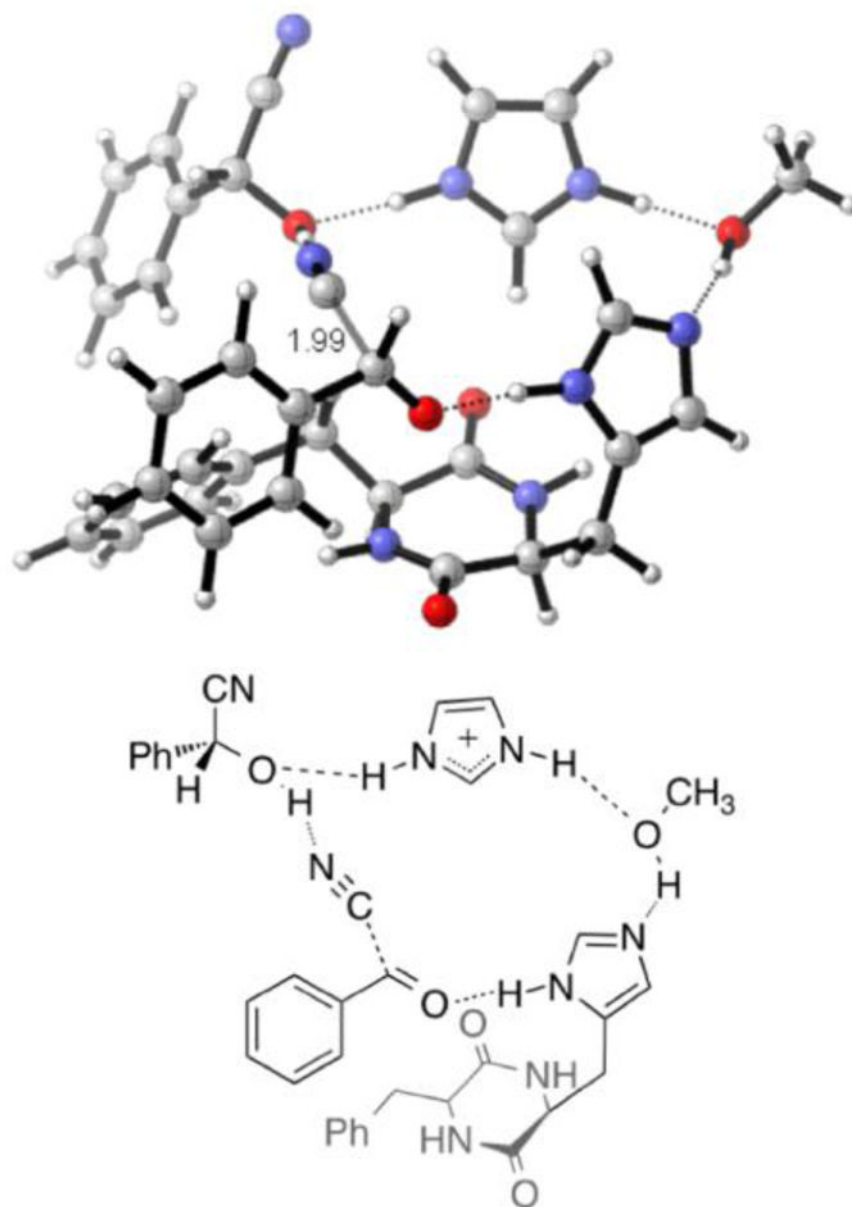


Figure 130.
Model transition state for enantioselective autoinduction.

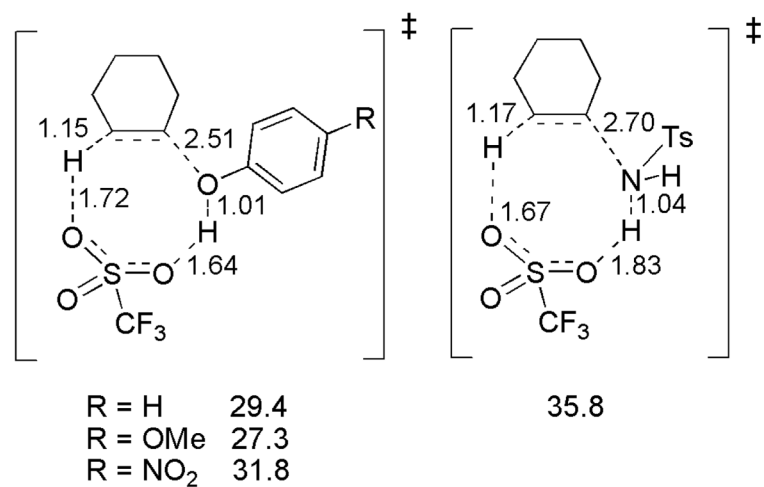


Figure 131. Transition states and activation free energies (ΔG , kcal/mol) relative to the separated reactants for the TfOH-catalyzed addition of phenols and tosylamide to cyclohexene.

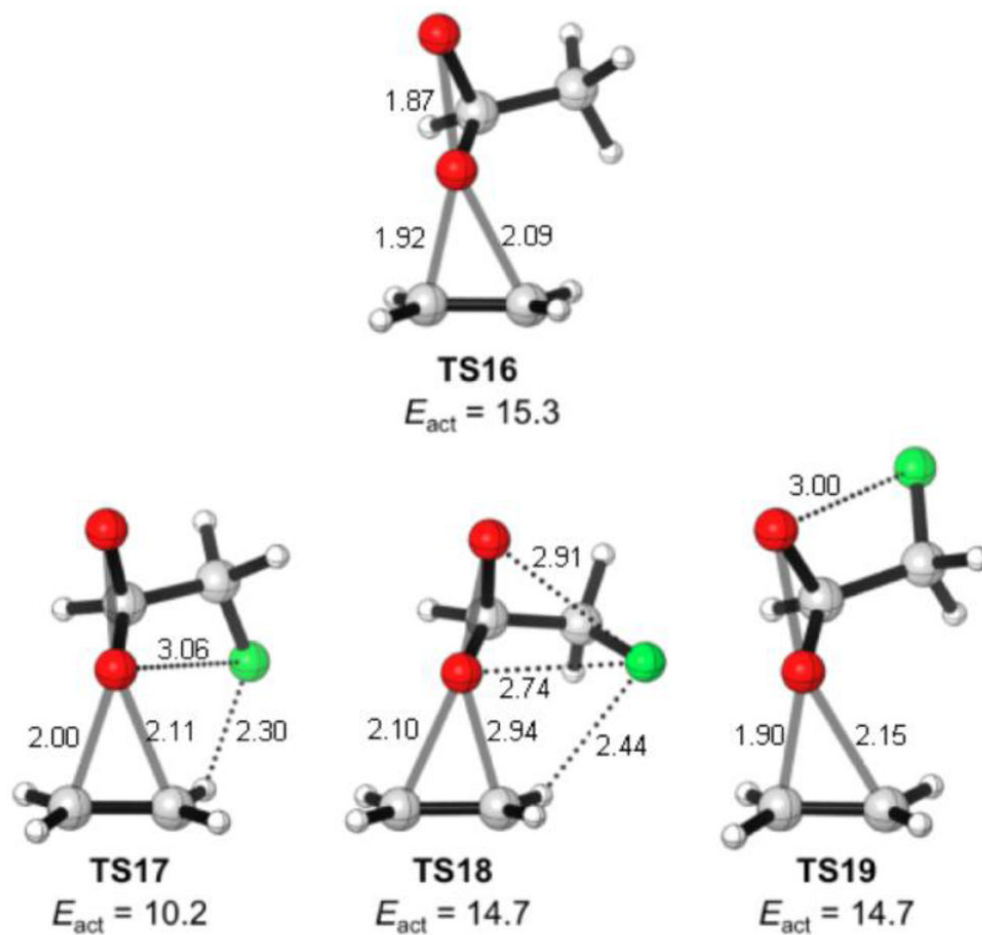


Figure 132. TSs for the epoxidation of ethane by methyl- and fluoromethyldioxirane (B3LYP/6-31G(d)).

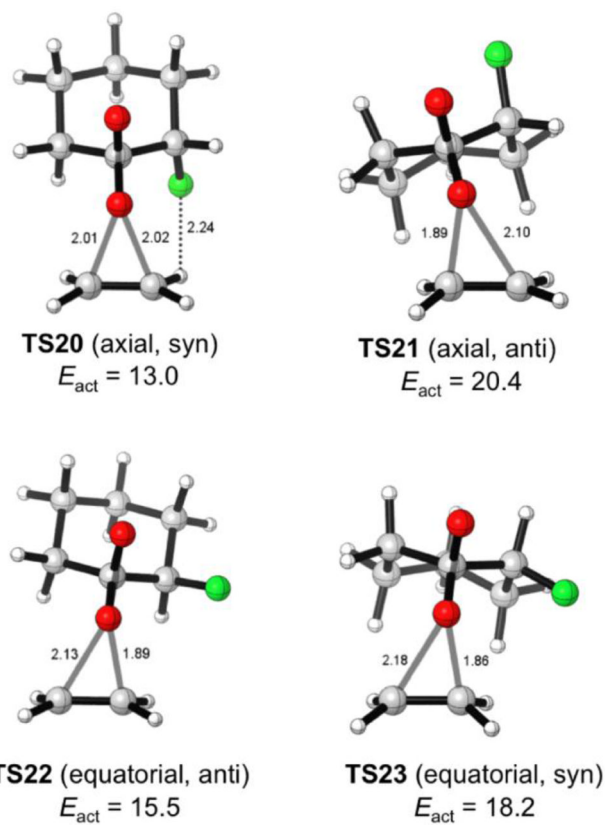


Figure 133. TSs for the epoxidation of ethane by 2-fluorocyclohexanone dioxirane (B3LYP/6-31G(d)).

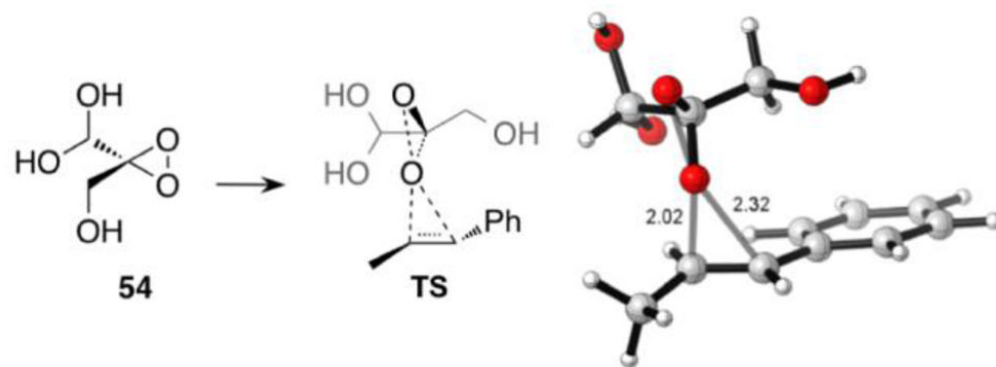


Figure 134.
TS for the epoxidation of *trans*- β -methylstyrene using dioxirane **54**.

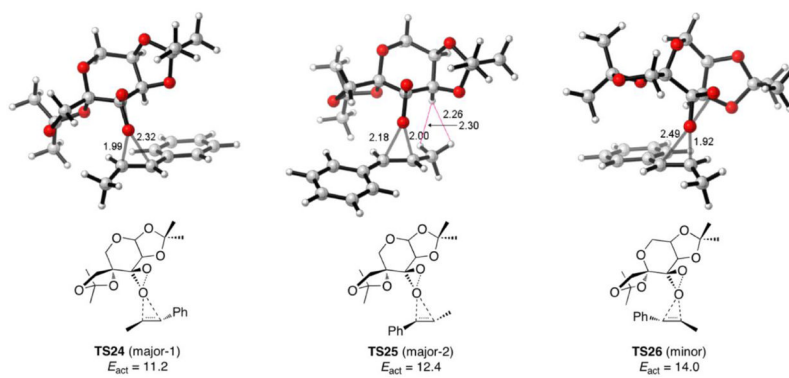


Figure 135. TSs for the epoxidation of *trans*- β -methylstyrene using dioxirane derived from catalyst **52**.

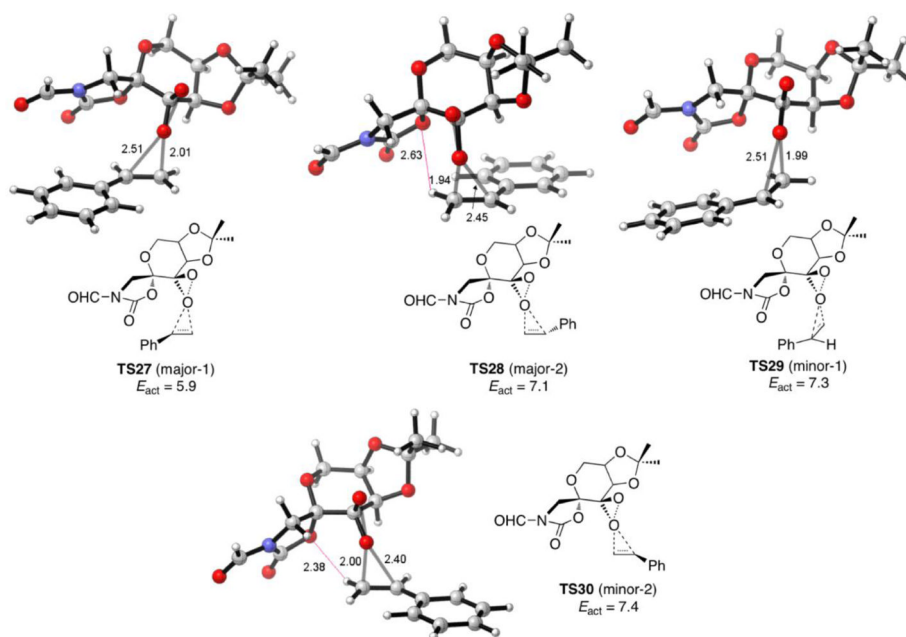


Figure 136. TSs for the epoxidation of styrene using dioxirane derived from catalyst **53b**.

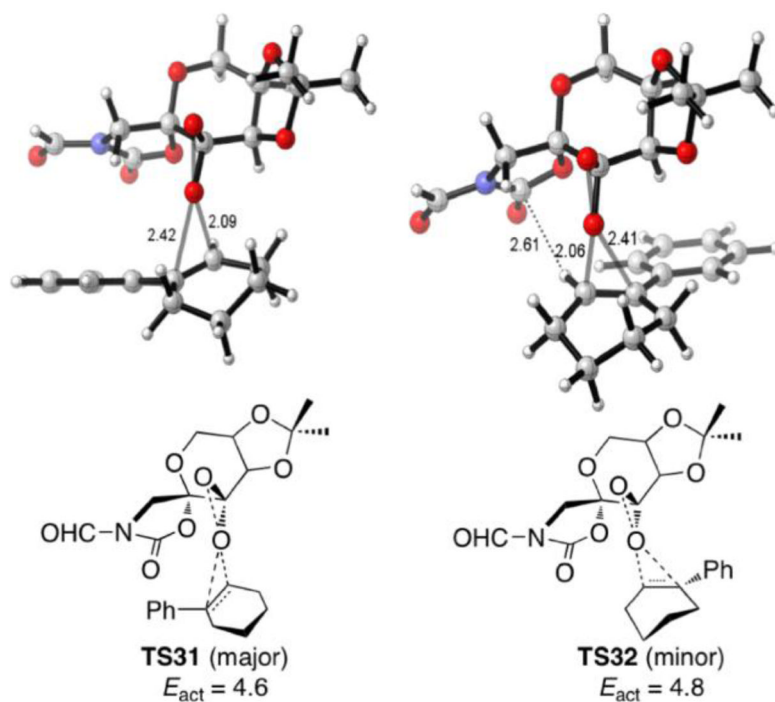
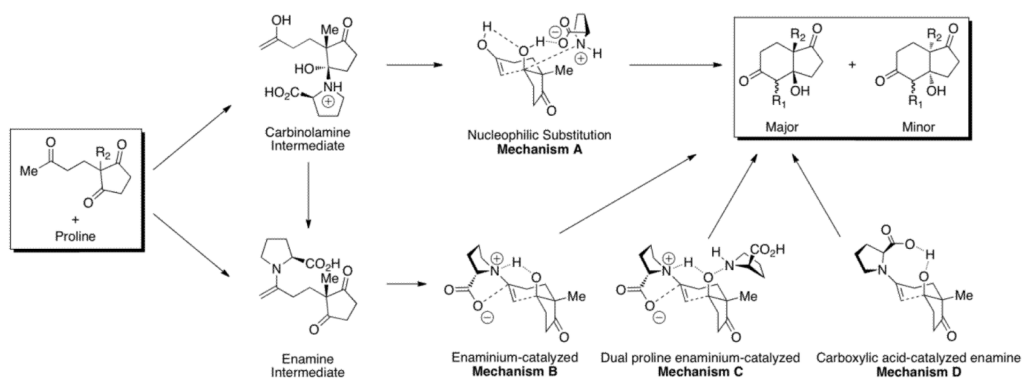
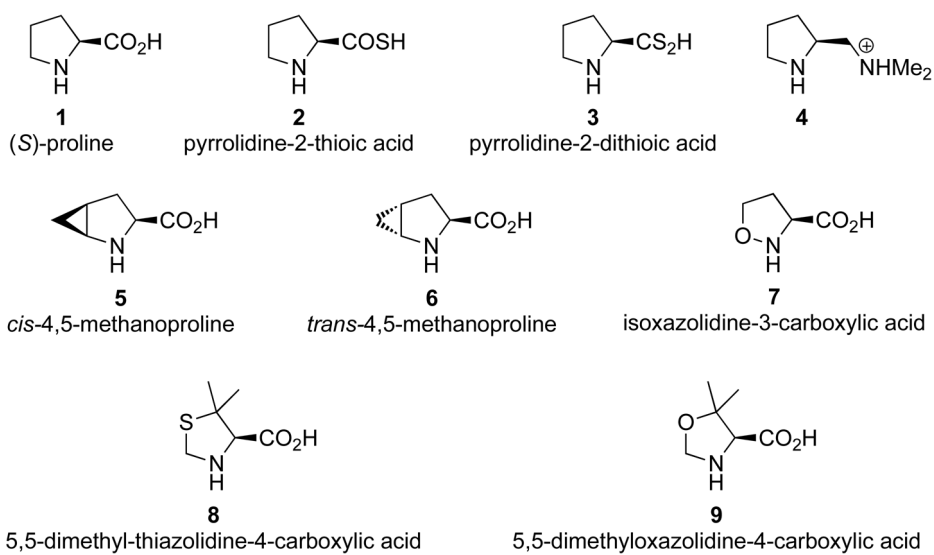


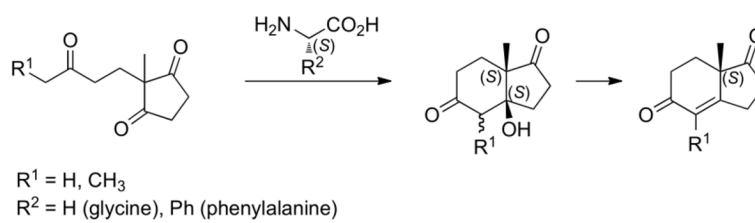
Figure 137. TSs for the epoxidation of 1-phenyl-cyclohexene using dioxirane derived from catalyst **53b**.

**Scheme 1.**

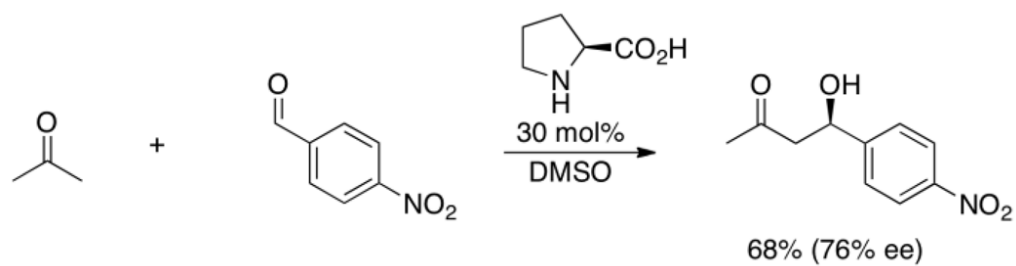
Four proposed mechanisms of the Hajos-Parrish reaction

**Scheme 2.**

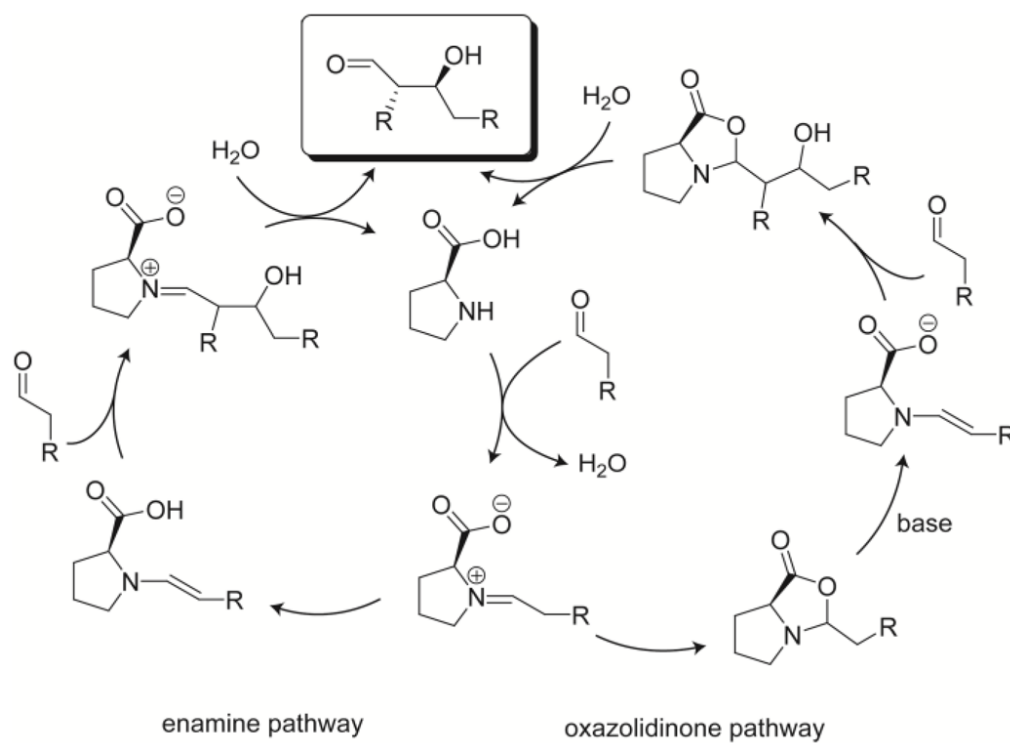
Various proline derivative catalysts for the Hajos-Parrish reaction studied by Houk

**Scheme 3.**

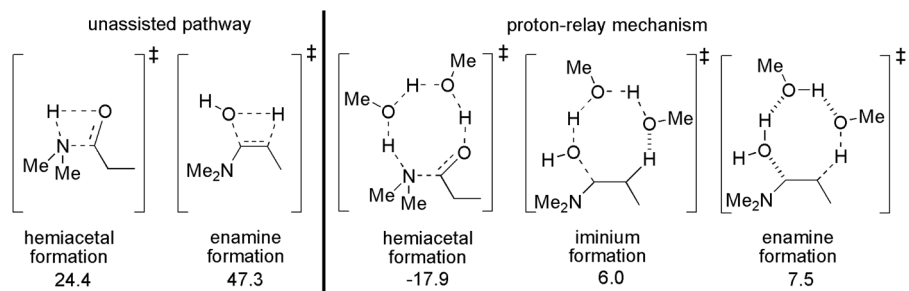
Various primary amino acids and the intramolecular aldol cyclizations studied

**Scheme 4.**

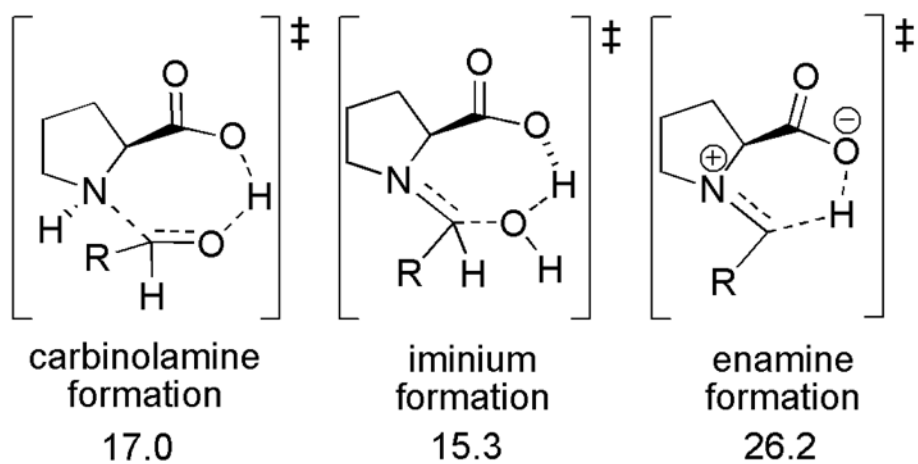
The intermolecular aldol reaction catalyzed by proline



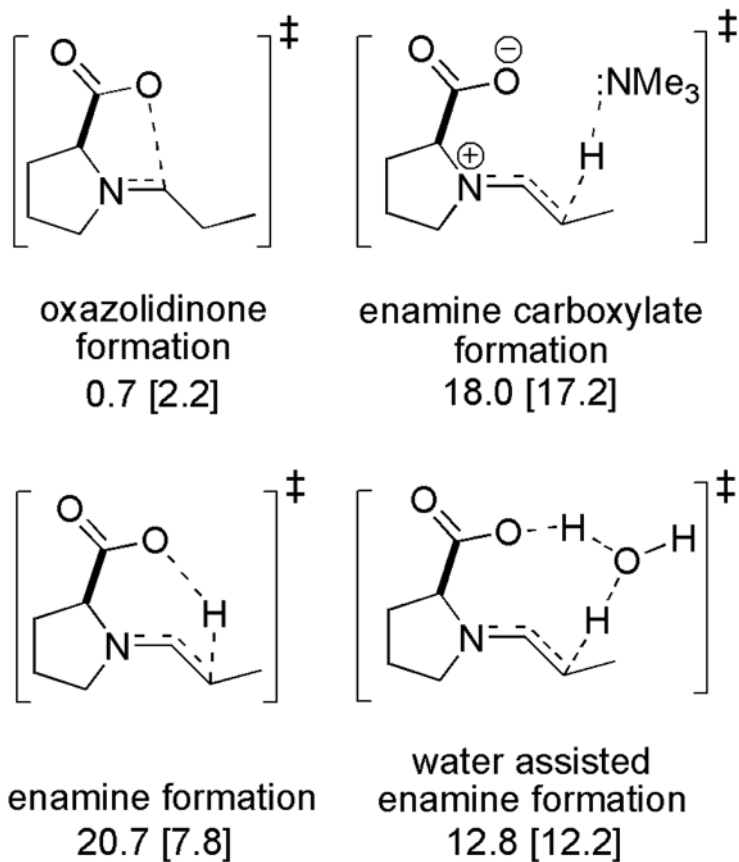
Scheme 5.
Mechanistic possibilities involving the enamine and oxazolidinone pathways

**Scheme 6.**

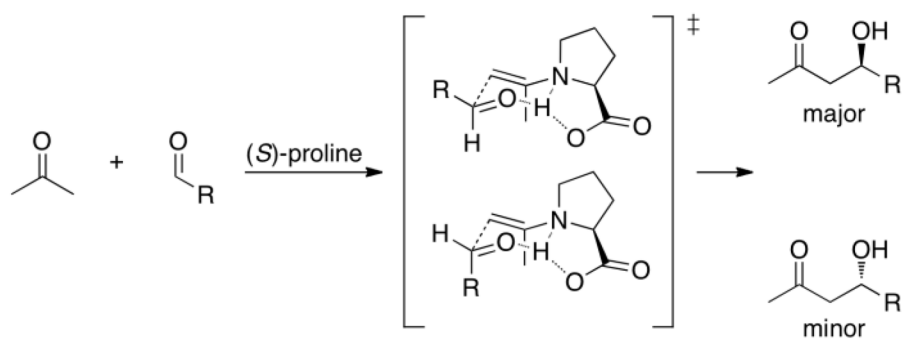
Activation free energies (ΔG^\ddagger , kcal/mol) for hemiacetal, iminium and enamine formation with respect to separated reactants. mPW1PW91/6-31G(d), using PCM and UAKS radii

**Scheme 7.**

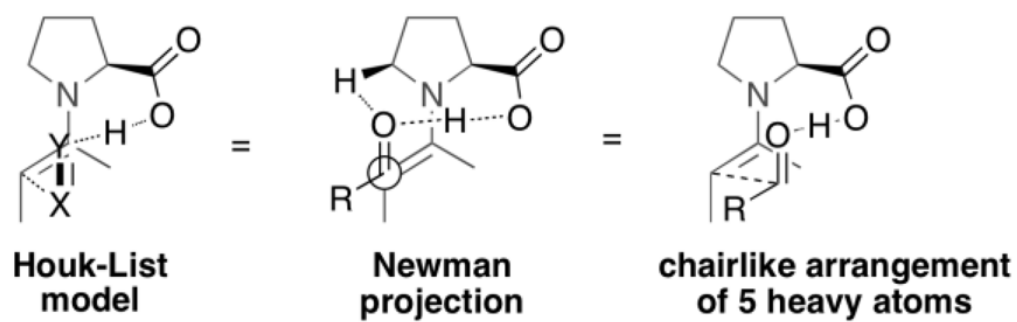
Activation energies (ΔE^\ddagger , kcal/mol) for carbinolamine, iminium and enamine formation with respect to separated reactants (B3LYP-6-31+G(d, p)//B3LYP/6-31G(d))

**Scheme 8.**

Gibbs free energies of activation (ΔG^\ddagger , kcal/mol) for the conversion of iminium carboxylate to various key intermediates calculated with B3LYP/6-31+G(d, p) (Energies for the formation of *anti* intermediates are given along with that for *syn* intermediates in square brackets)

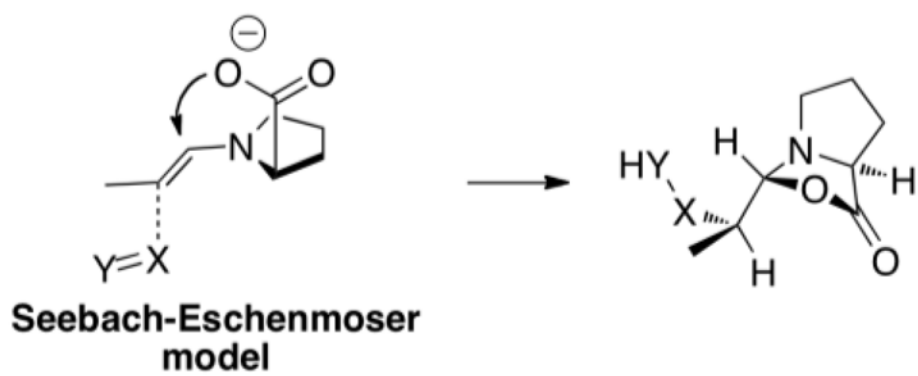
**Scheme 9.**

The Zimmerman-Traxler transition states proposed by List and co-workers to rationalize the stereoselectivities of proline-catalyzed intermolecular aldol reactions

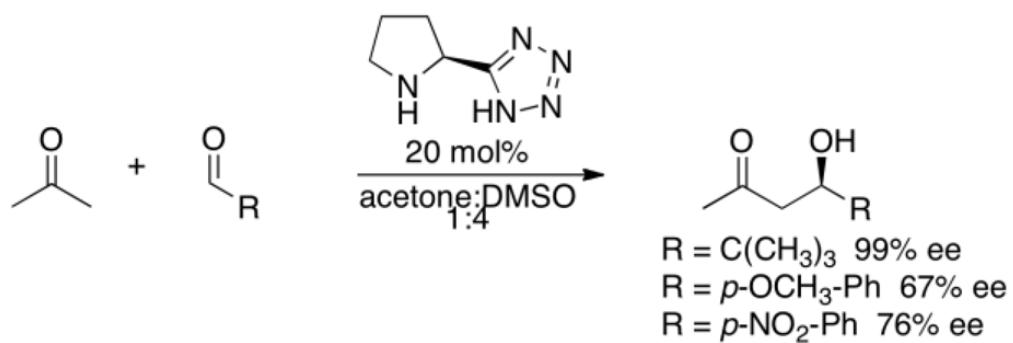


Scheme 10.

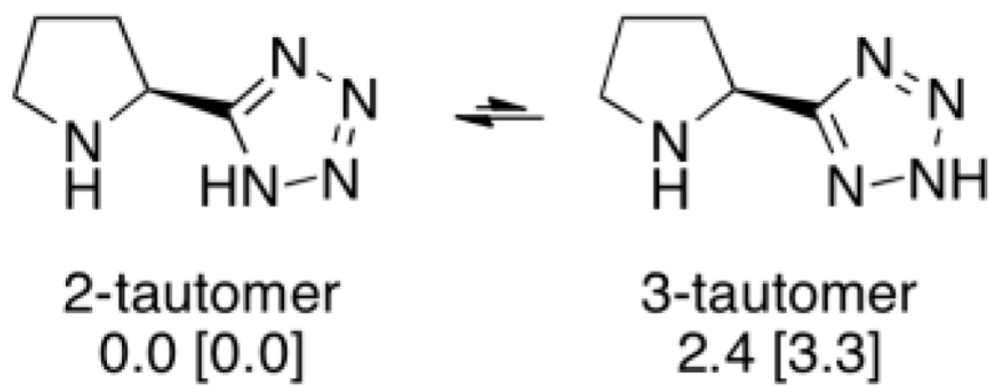
The Houk-List model for predicting the stereoselectivity of the intermolecular aldol reaction catalyzed by proline

**Scheme 11.**

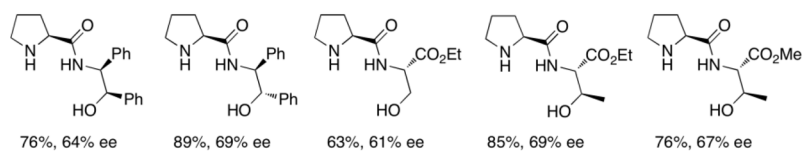
The Seebach-Eschenmoser model for predicting the stereoselectivity of the intermolecular aldol reaction catalyzed by proline

**Scheme 12.**

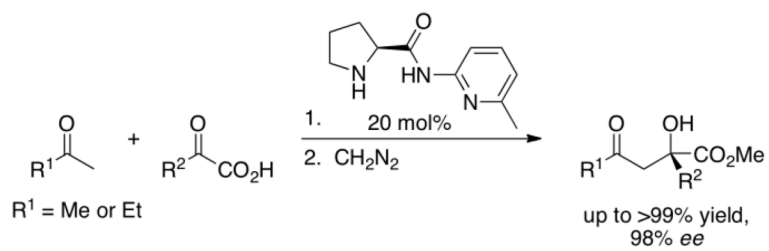
The 5-pyrrolidin-2-yltetrazole catalyzed intermolecular aldol reactions

**Scheme 13.**

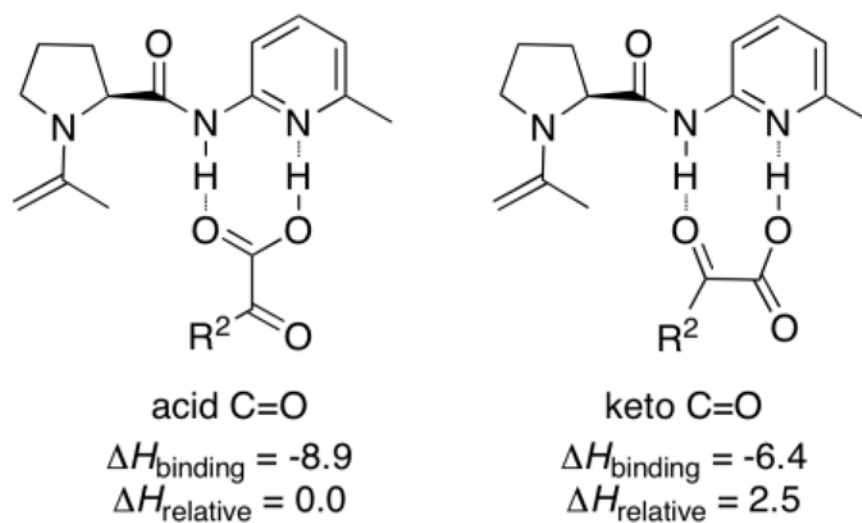
The two tautomeric forms of 5-pyrrolidin-2-yltetrazole catalyst. DMSO energies are in brackets

**Scheme 14.**

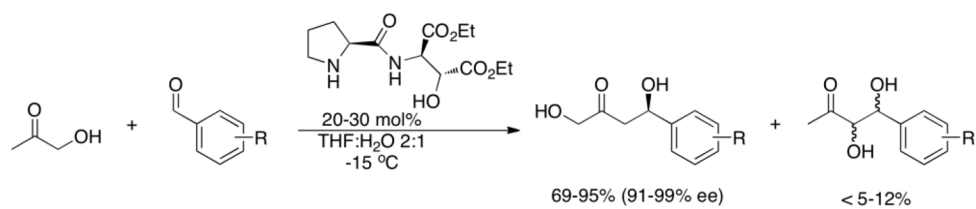
Proline amide derivatives as catalysts for the intermolecular aldol reaction



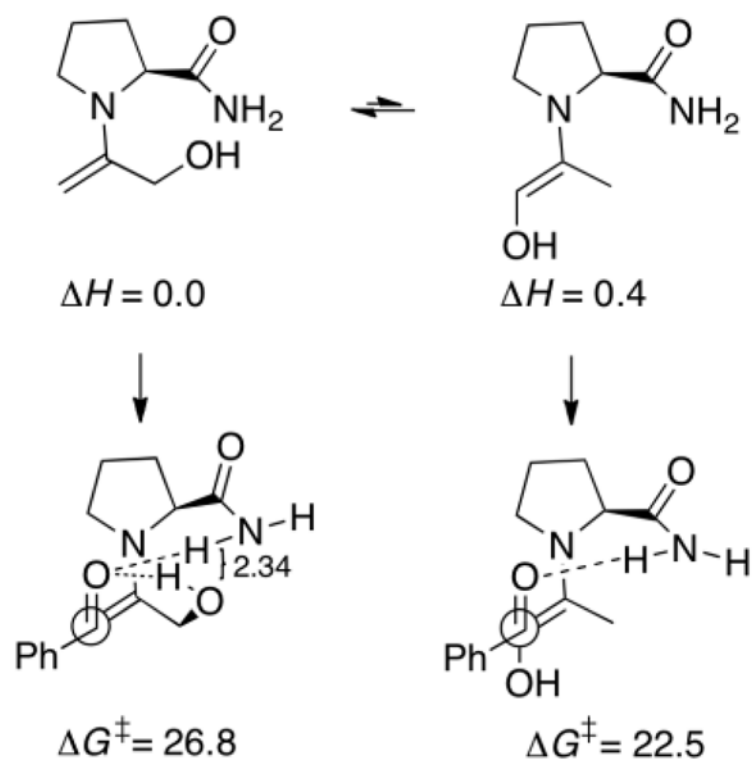
Scheme 15.
Organocatalyzed aldol reaction of ketones with α -keto acids



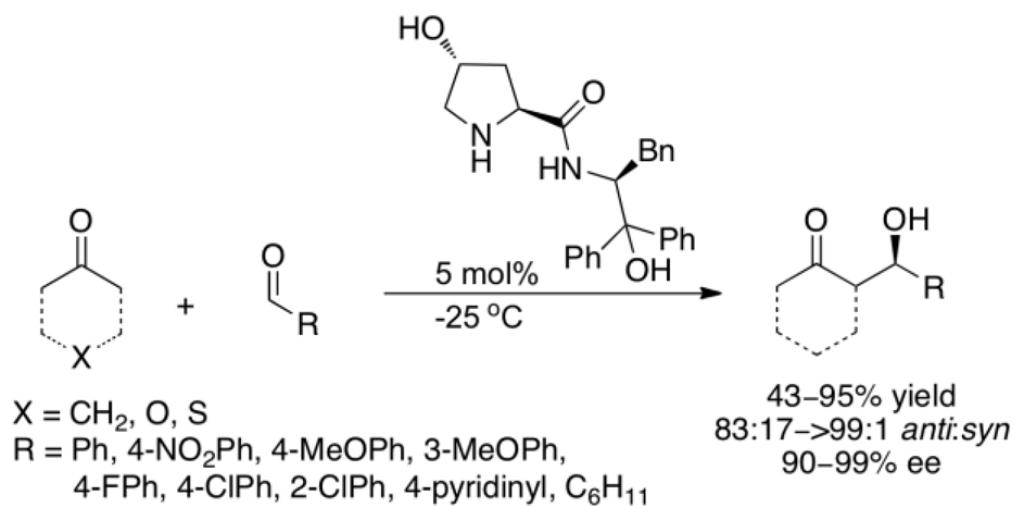
Scheme 16.
Possible binding modes of catalyst with α -keto acid



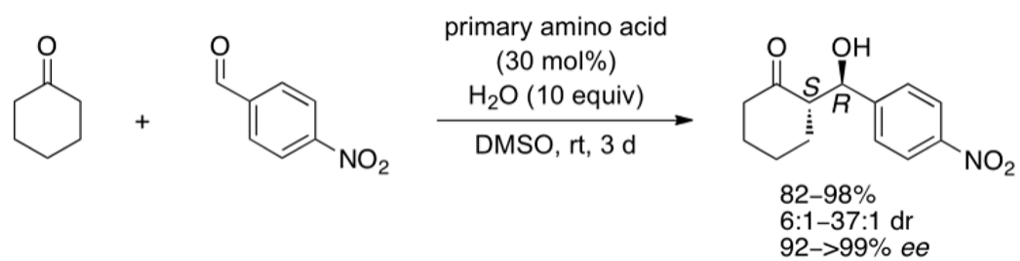
Scheme 17.
Intermolecular aldol reaction of hydroxyacetone with benzaldehyde, catalyzed by a proline amide

**Scheme 18.**

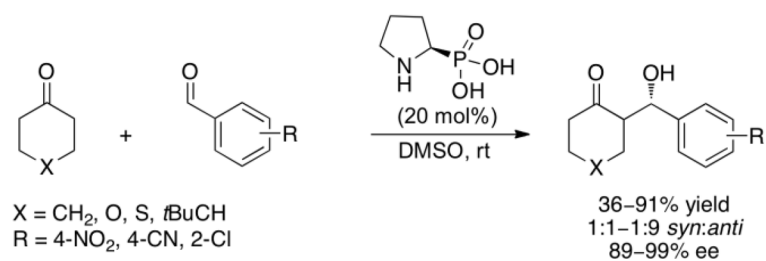
Top: Relative stabilities of *anti* enamine and *anti* enol enamine. Bottom: Activation free energies for 1,2-diol and 1,4-diol formation

**Scheme 19.**

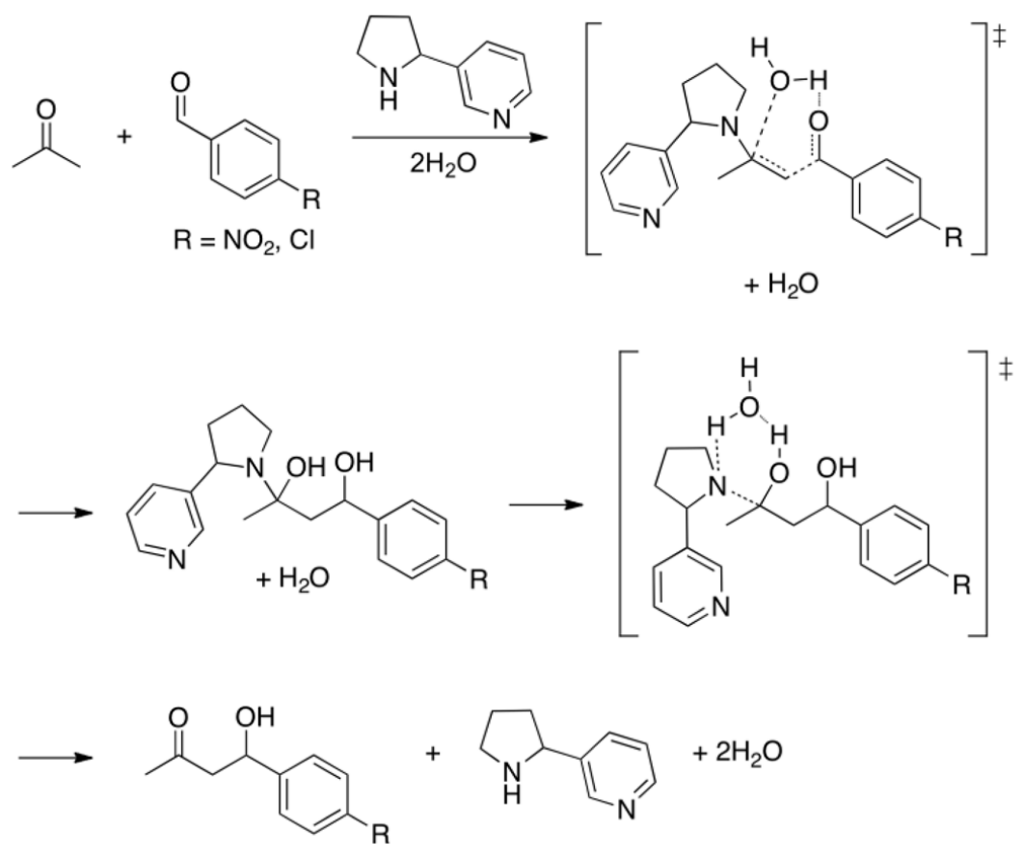
Aldol reaction of acetone and cyclohexanones catalyzed by a 4-hydroxyprolineamide alcohol

**Scheme 20.**

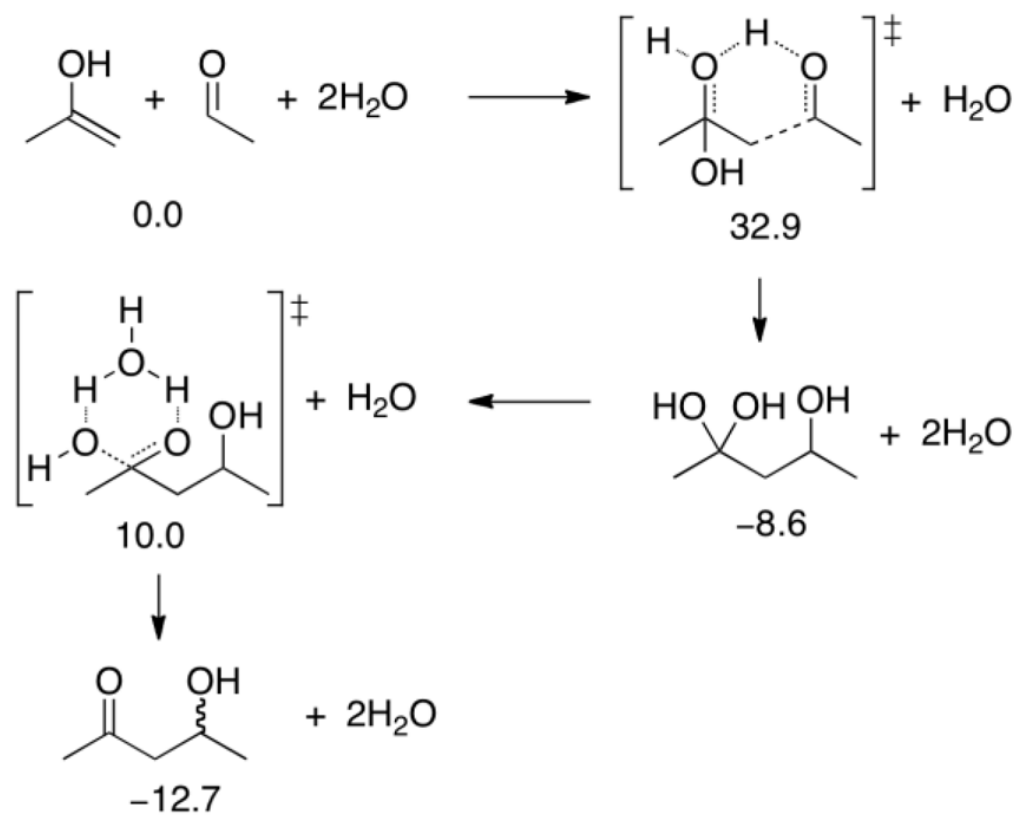
Primary amino acid catalyzed intermolecular aldol reaction between cyclohexanone and *para*-nitrobenzaldehyde



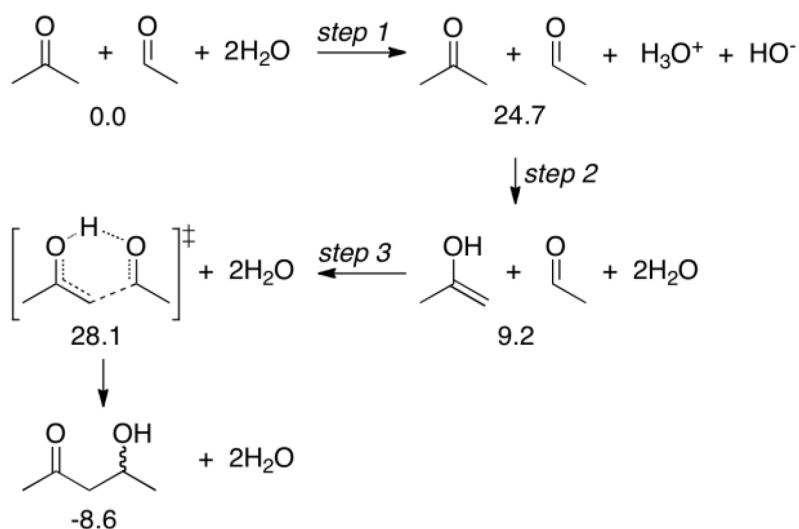
Scheme 21.
Pyridin-2-ylphosphonic acid catalyzed intermolecular aldol reactions



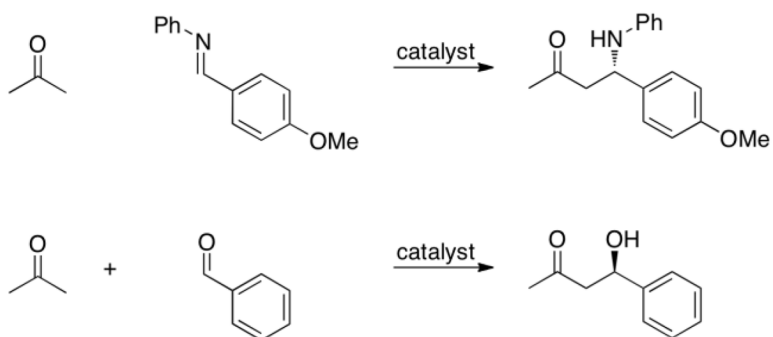
Scheme 22.
Nornicotine catalyzed intermolecular aldol reaction mechanism

**Scheme 23.**

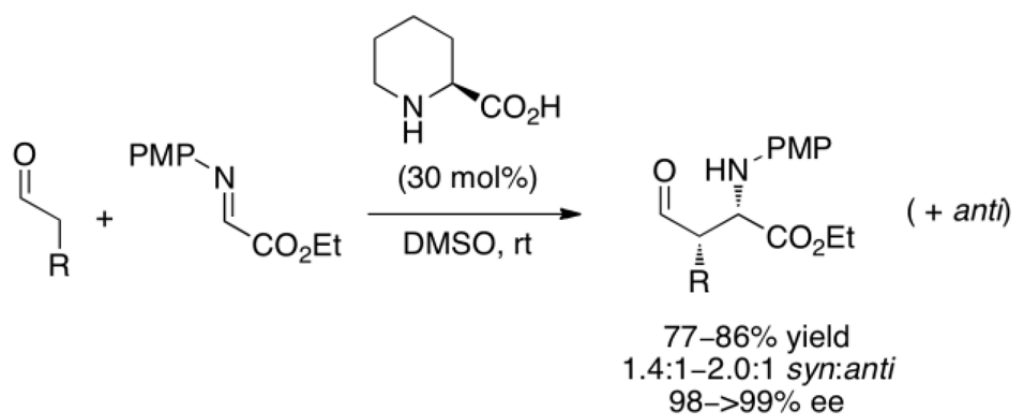
Intermolecular aldol reaction mechanism computed by Janda and co-workers⁴³ (B3LYP/6-311+G(2d,2p)//B3LYP/6-311G(d, p); COSMO model for solvation energies (water))

**Scheme 24.**

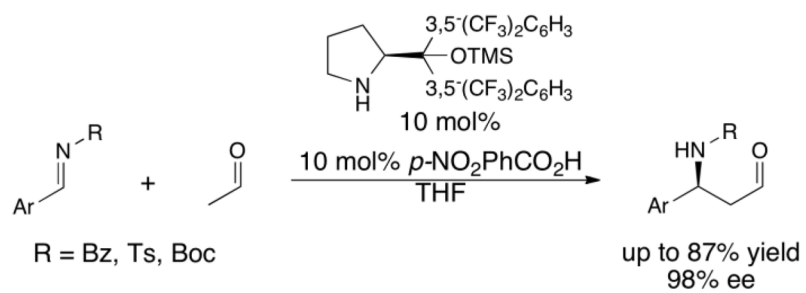
Intermolecular aldol reaction mechanism computed by Janda and co-workers⁴³ (B3LYP/6-311+G(2d,2p)//B3LYP/6-311G(d, p); COSMO model for solvation energies (water))



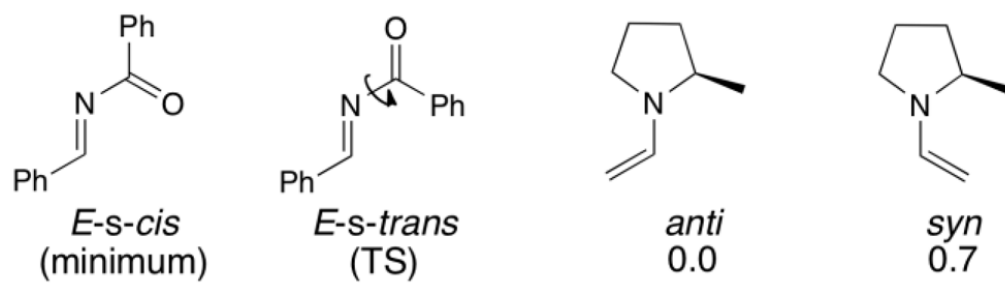
Scheme 25.
Typical intermolecular Mannich and aldol reactions catalyzed by proline



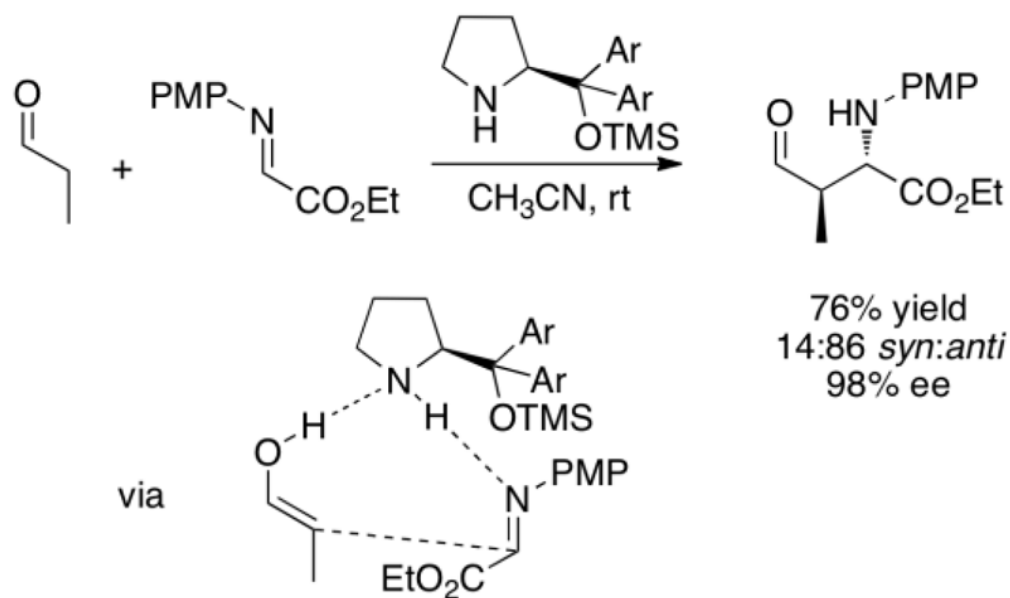
Scheme 26.
Intermolecular Mannich reaction of aldehydes catalyzed by pipecolic acid



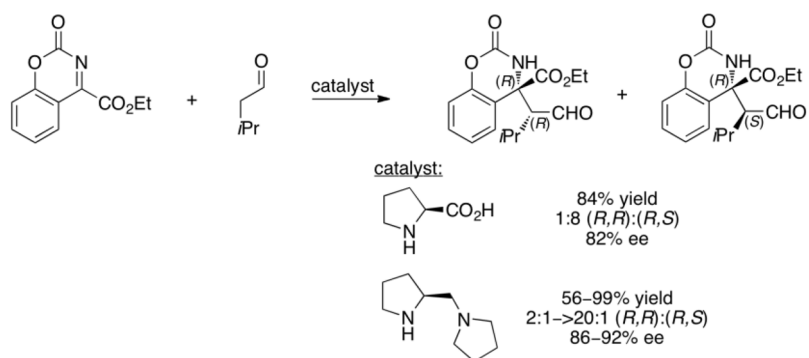
Scheme 27.
Diarylprolinol silyl ether catalyzed Mannich reaction



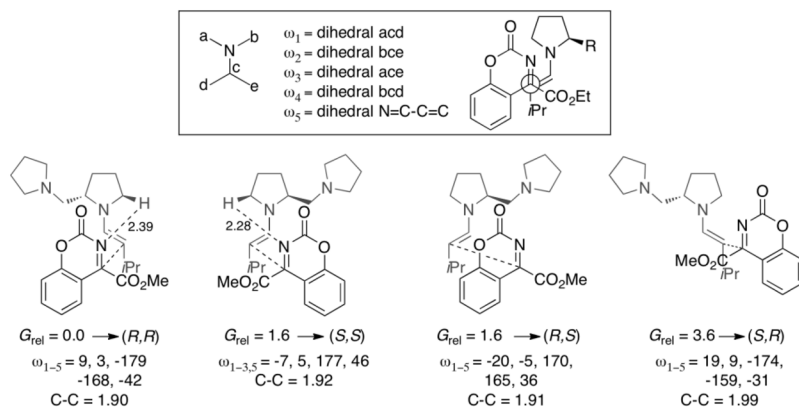
Scheme 28.
Imine and enamine conformers



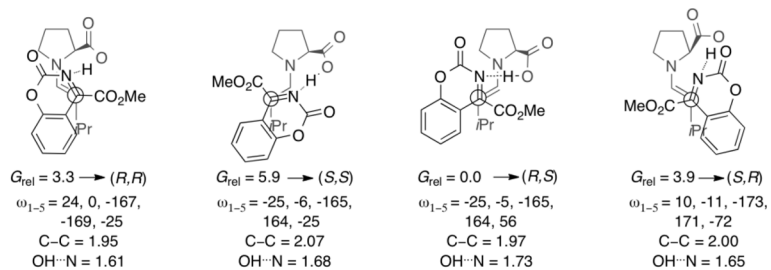
Scheme 29.
Mannich reaction via an enol mechanism



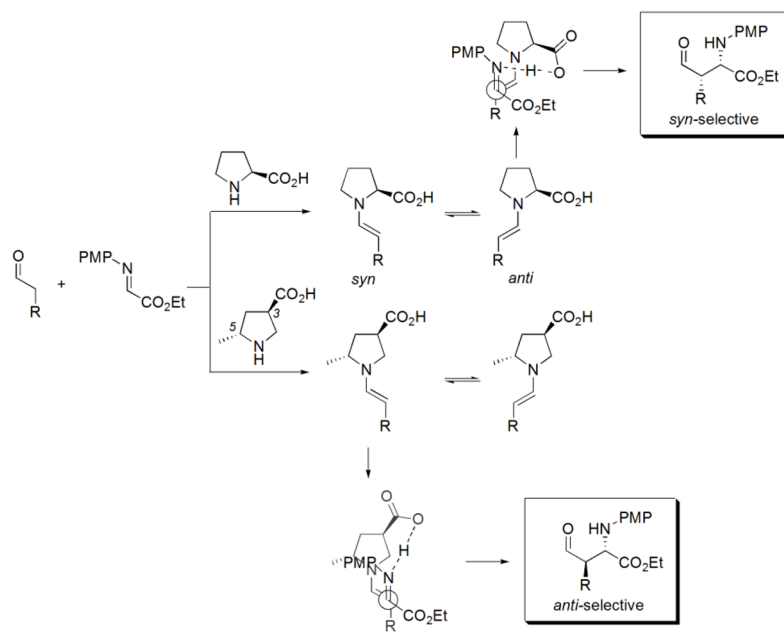
Scheme 30.
Opposite diastereoselectivities observed in the Mannich reaction with proline and pyrrolidinylmethylpyrrolidine catalysts

**Scheme 31.**

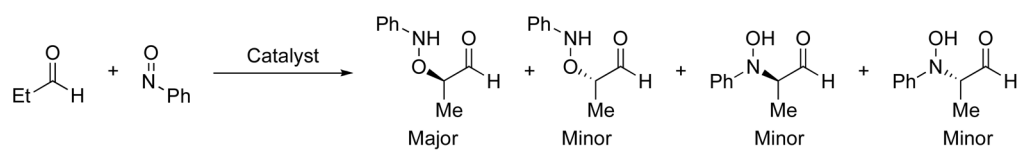
Lowest energy transition structures leading to each diastereomer of the Mannich reaction (BH&HLYP/6-31G(d, p), including solvation energies—CH₂Cl₂, CPCM/UAKS model)

**Scheme 32.**

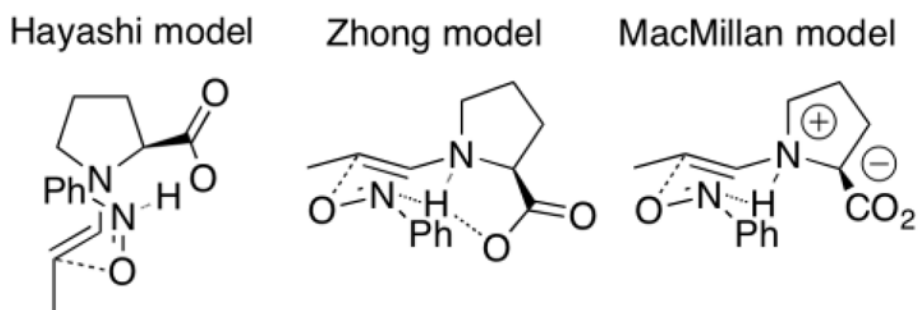
Lowest energy transition structures leading to each diastereomer of the Mannich reaction (BH& HLYP/6-31G(d, p), including solvation energies—CH₂Cl₂, CPCM/UAKS model)



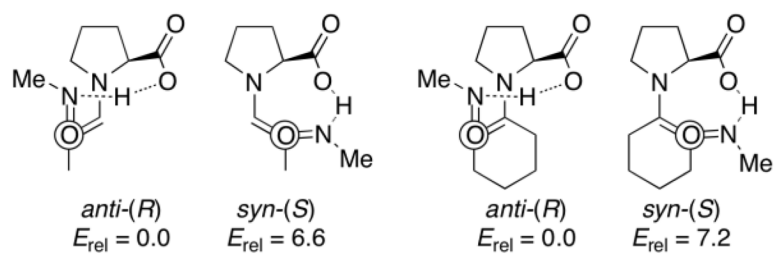
Scheme 33.
Development of *anti*-selective Mannich reaction organocatalyst



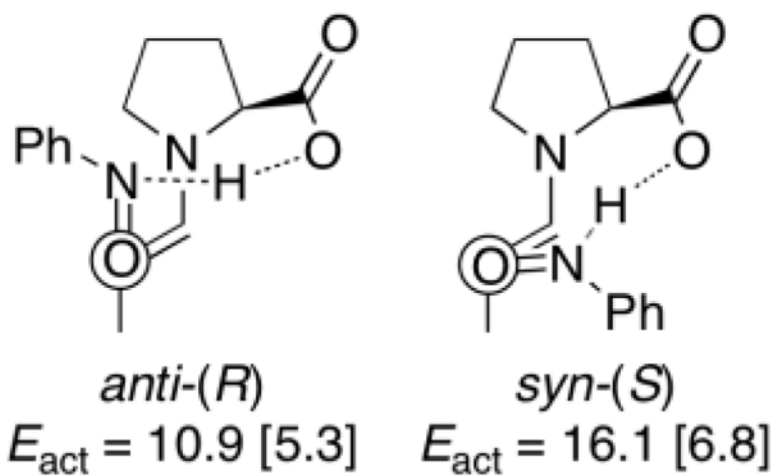
Scheme 34.
Oxyamination reaction



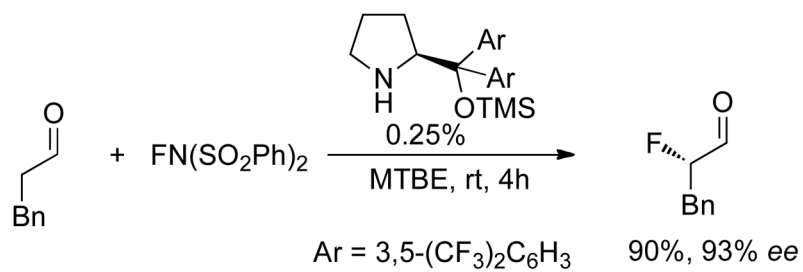
Scheme 35.
Proposed transition states of proline-catalyzed α -aminoxylation reaction

**Scheme 36.**

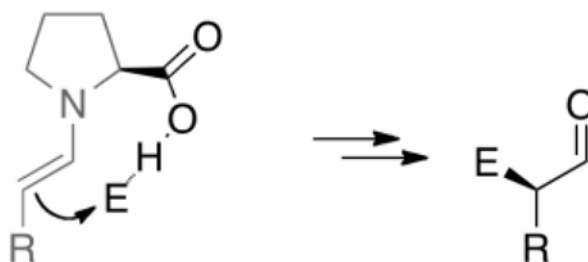
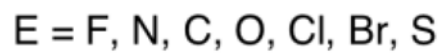
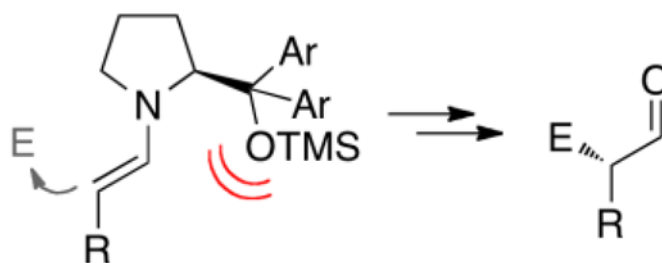
B3LYP/6-311+G(2d,2p)//B3LYP/6-31G(d, p) relative gas phase transition structure energies for the aminoxylation reaction

**Scheme 37.**

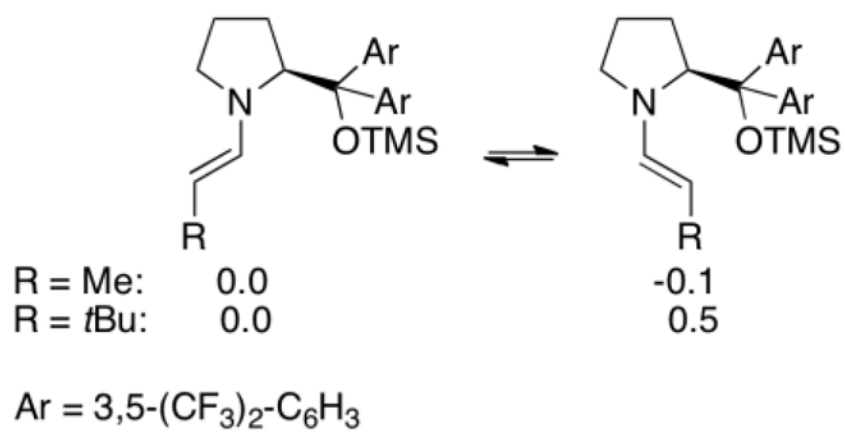
B3LYP/6-31G(d, p) activation energies for the α -aminoxylation reaction (Solvation energy corrections (B3LYP/6-311+G(2d,2p) PCM, DMSO) are in brackets)



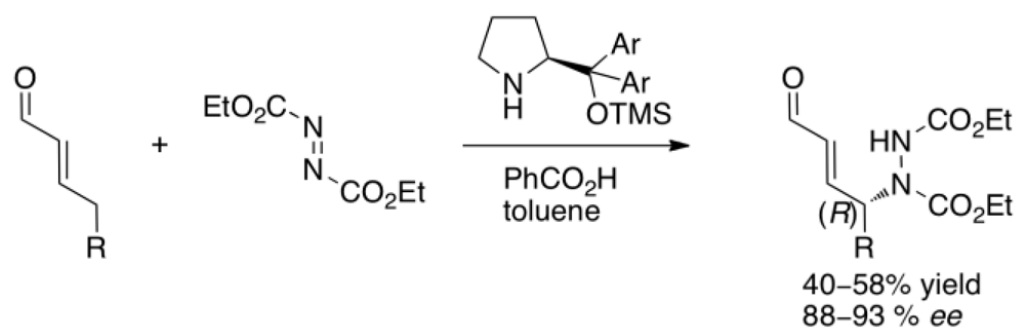
Scheme 38.
Organocatalyzed α -fluorination reaction

hydrogen-bond stereocontrol**steric face stereocontrol**

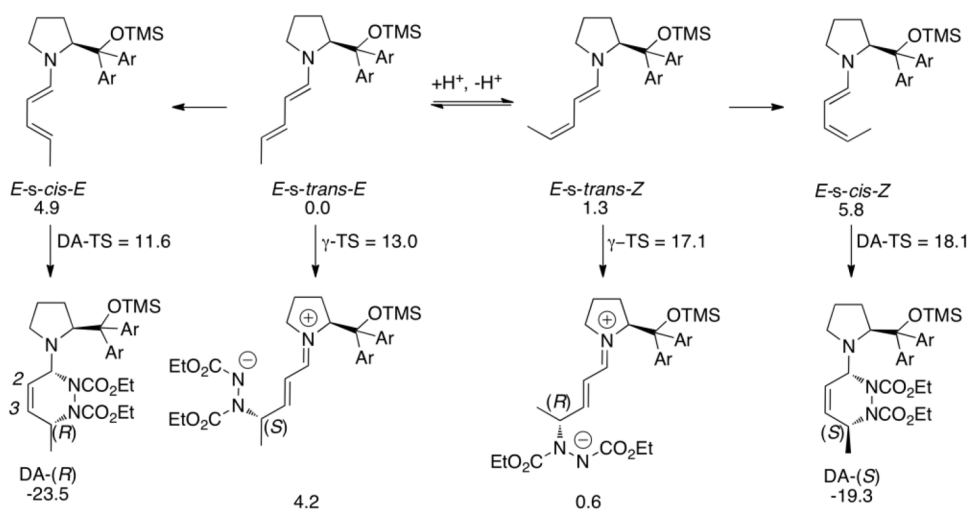
Scheme 39.
Hydrogen bond and steric stereocontrol

**Scheme 40.**

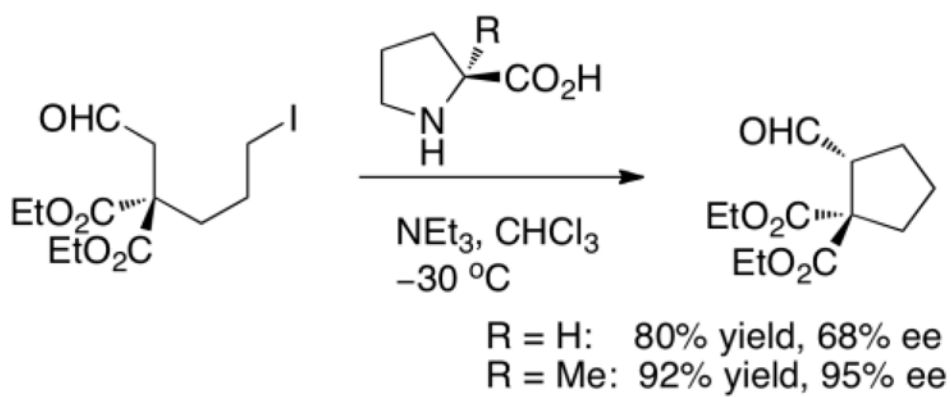
B3LYP/6-31G(d) relative free energies of *anti* versus *syn* enamines



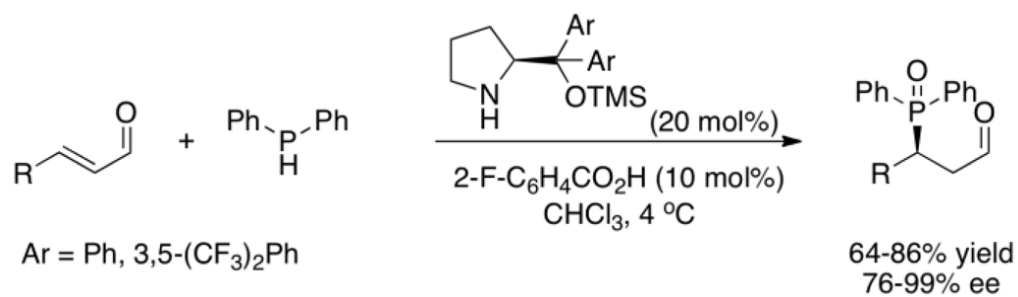
Scheme 41.
 γ -amination of α,β -unsaturated aldehydes

**Scheme 42.**

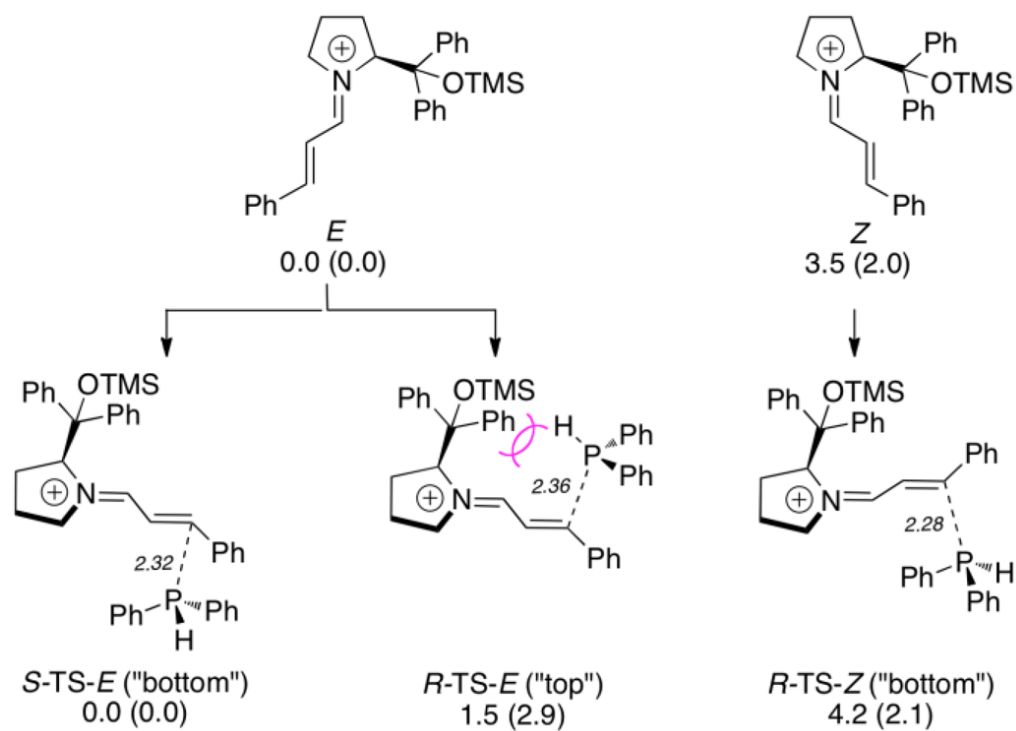
Mechanism for the γ -amination of 2-pentalen. B3LYP/6-31G(d) energies (with CPCM solvent corrections)

**Scheme 43.**

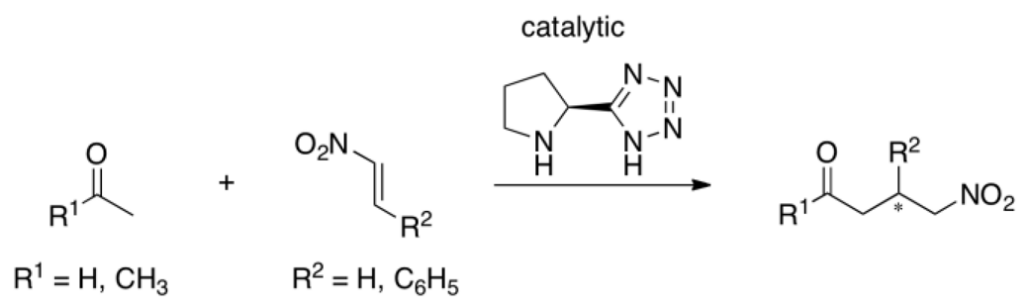
The prototypical proline and 2-methylproline catalyzed alkylation reaction



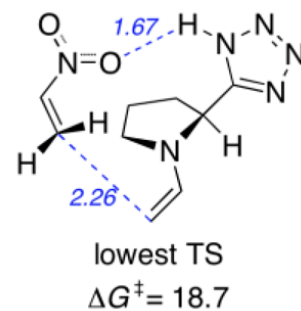
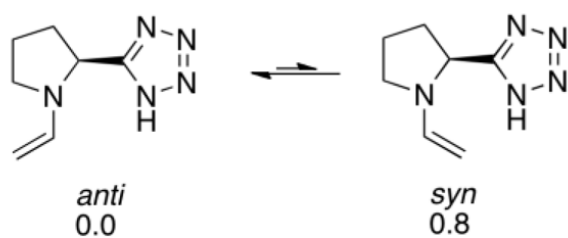
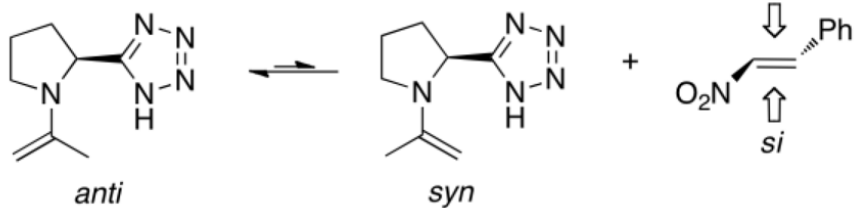
Scheme 44.
Asymmetric hydrophosphination reaction

**Scheme 45.**

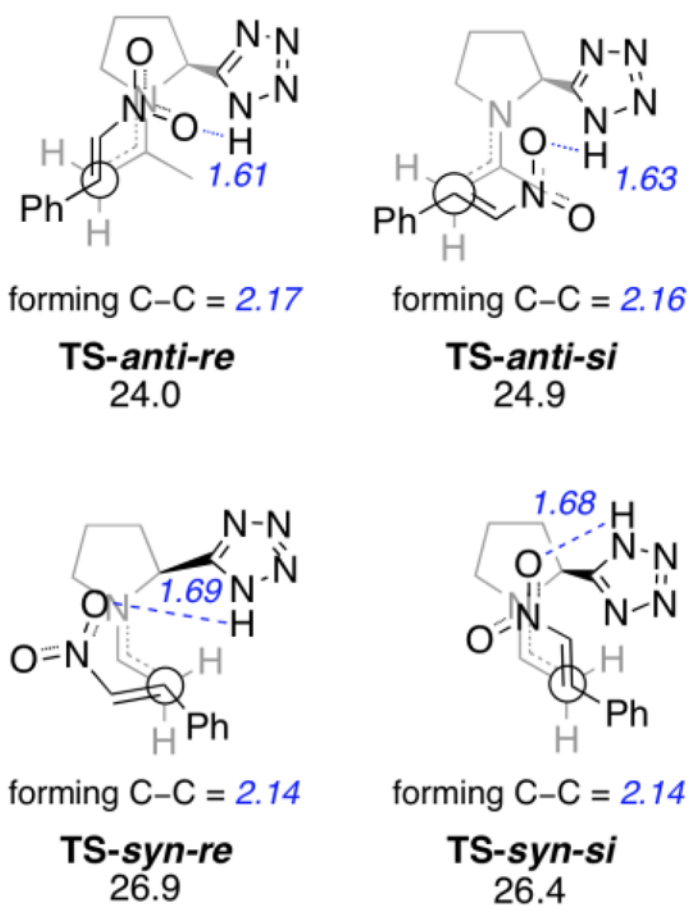
B3LYP/6-31G(d, p) iminium ion and transition structure energies. Solvent-corrected values (B3LYP/6-311+G(2d,2p) single point, CPCM, CHCl₃) are in parentheses



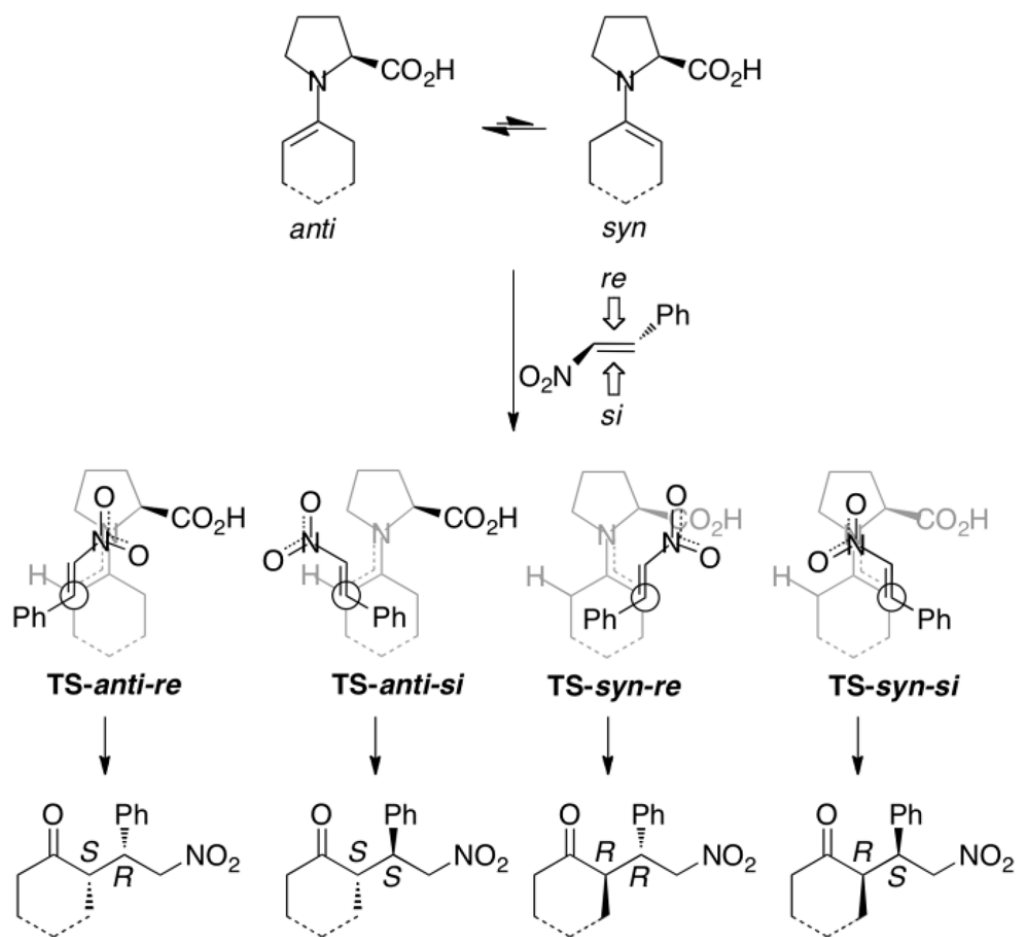
Scheme 46.
Michael addition of nitroalkenes to acetaldehyde and acetone

Model A: R¹ = H, R² = H**Model B: R¹ = CH₃, R² = C₆H₅**

Scheme 47.
Relative energies of Michael addition



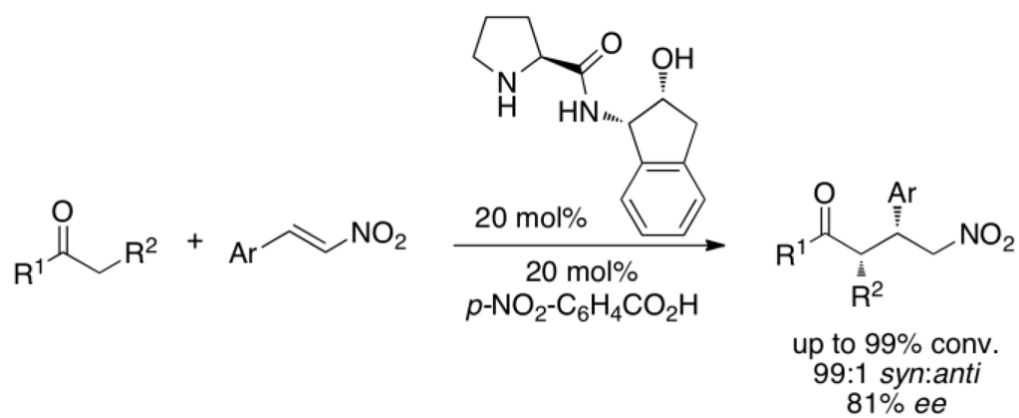
Scheme 48.
Transition structures and activation energies for addition of acetaldehyde-enamine to nitrostyrene

**Experimental:**

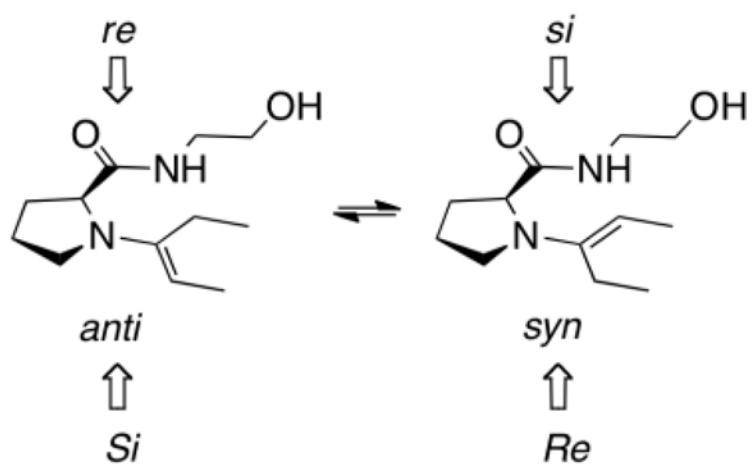
3-pentanone: 88% de *syn*, 76% ee (*S*, *R*)
 cyclohexanone: 94% de *syn*, 57% ee (*S*, *R*)

Scheme 49.

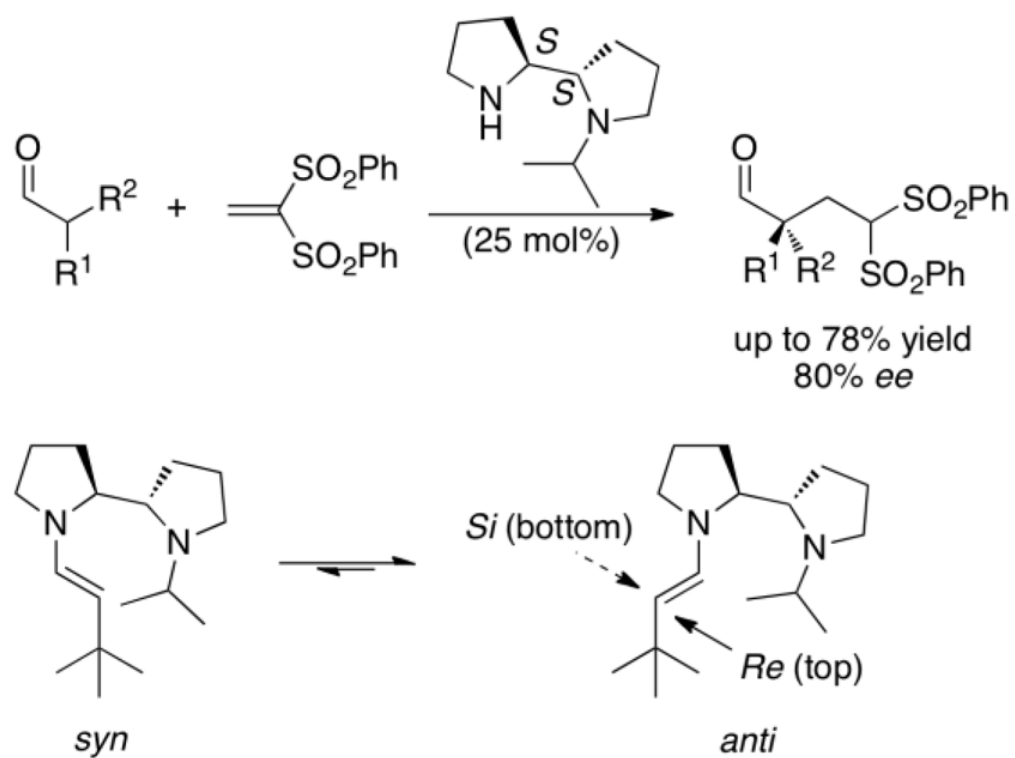
Proline-catalyzed addition of 3-pentanone and cyclohexanone to nitrostyrene



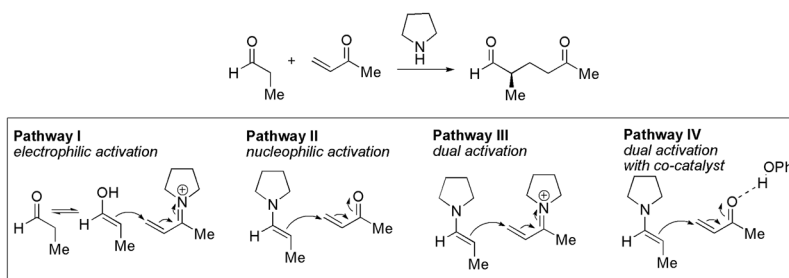
Scheme 50.
Michael addition catalyzed by prolinamide catalysts



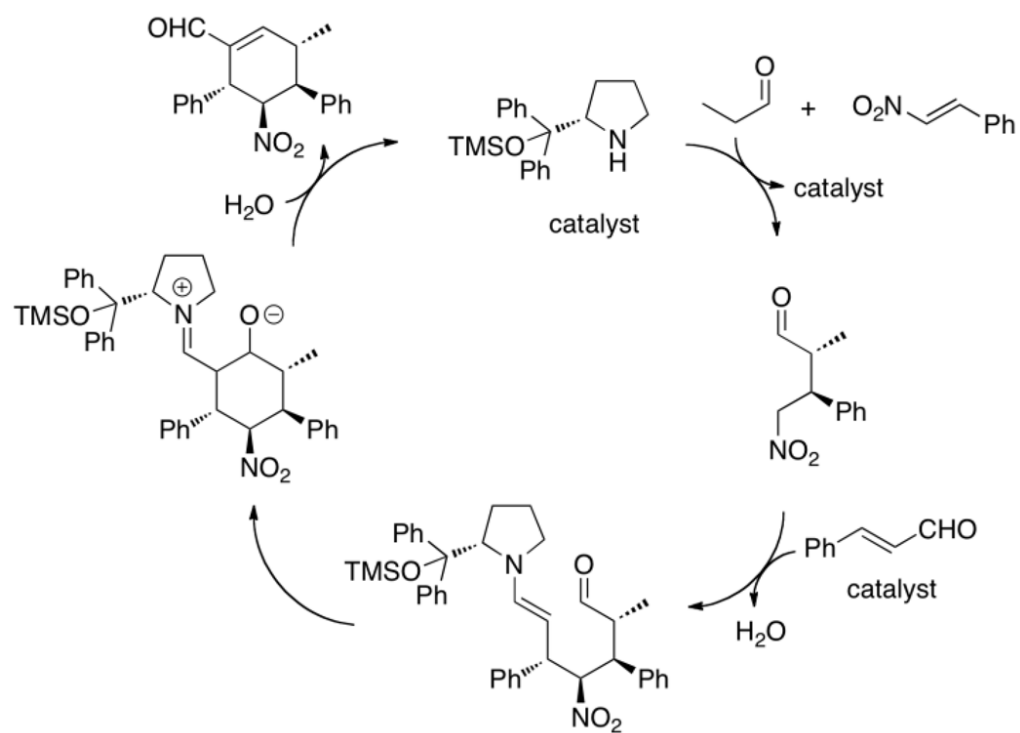
Scheme 51.
Possible modes of attack for the Michael addition reaction



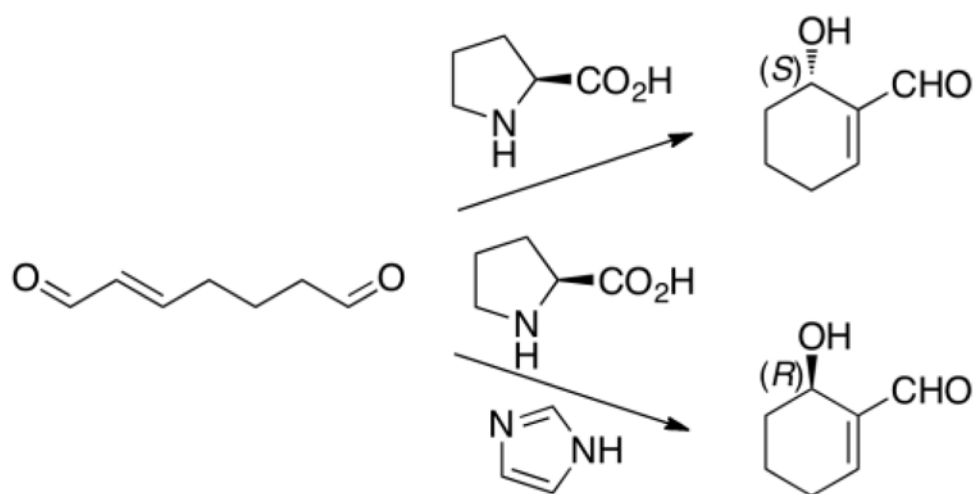
Scheme 52.
Michael addition reaction of vinyl sulfones



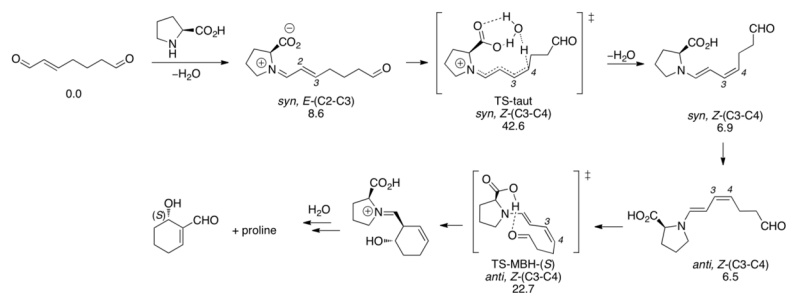
Scheme 53.
Competing pathways for pyrrolidine catalyzed Michael addition of propanal with methyl vinyl ketone (MVK)



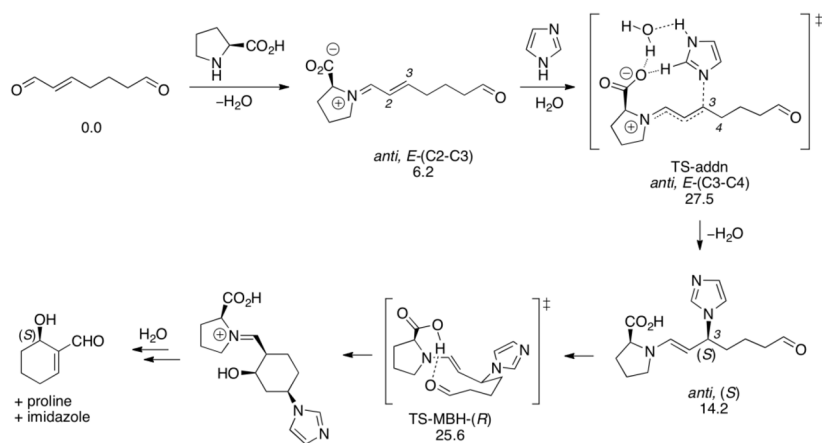
Scheme 54.
Organocatalyzed Michael addition-aldol reaction cascade



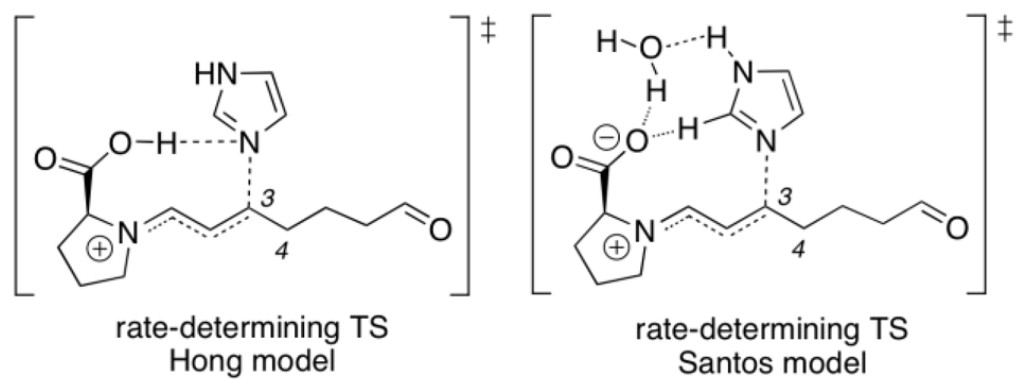
Scheme 55.
Proline-catalyzed intramolecular Morita-Baylis-Hillman reaction



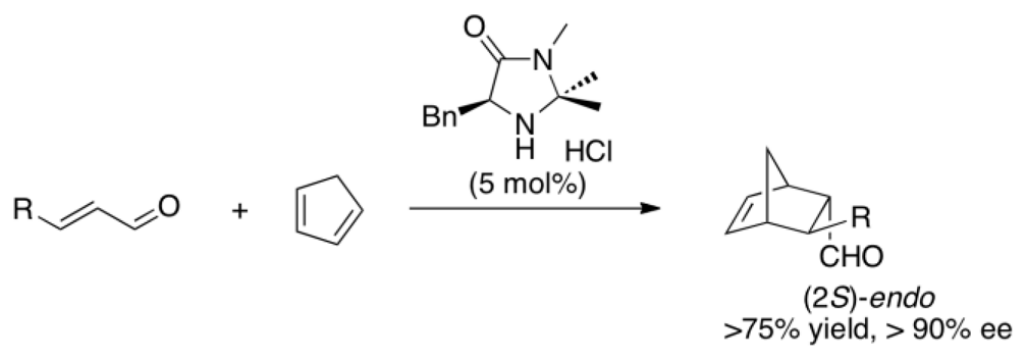
Scheme 56.
B3LYP/6-31G(d, p) mechanism for proline-catalyzed intramolecular Morita-Baylis-Hillman reaction (Relative energies include B3LYP/6-31++G(d, p) (PCM, CH₃CN) corrections.)

**Scheme 57.**

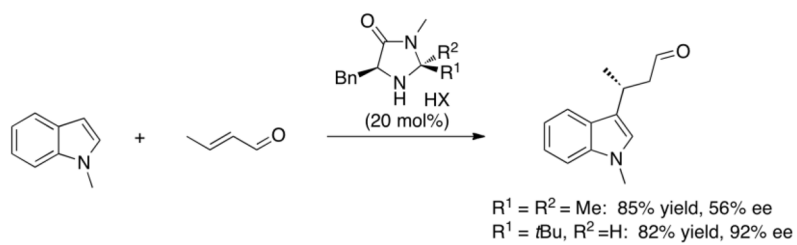
B3LYP/6-31G(d, p) mechanism for proline-catalyzed intramolecular Morita-Baylis-Hillman reaction with imidazole co-catalyst (Relative energies include B3LYP/6-31++G(d, p) (PCM, CH₃CN) corrections at 0 °C)

**Scheme 58.**

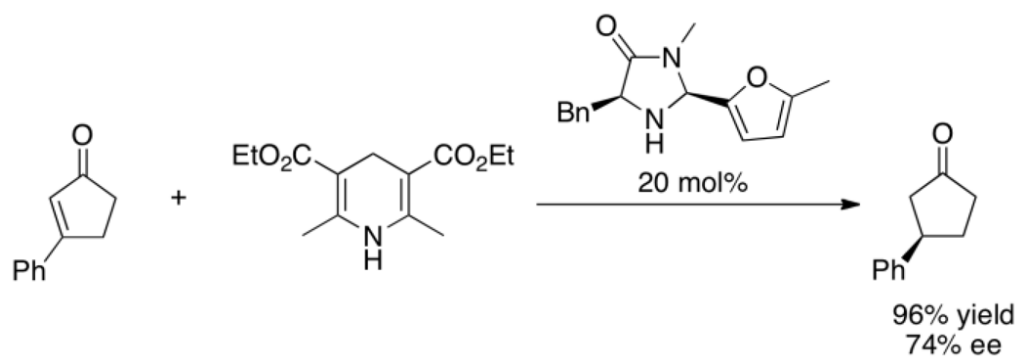
Rate-determining transition structures proposed by Hong and Santos



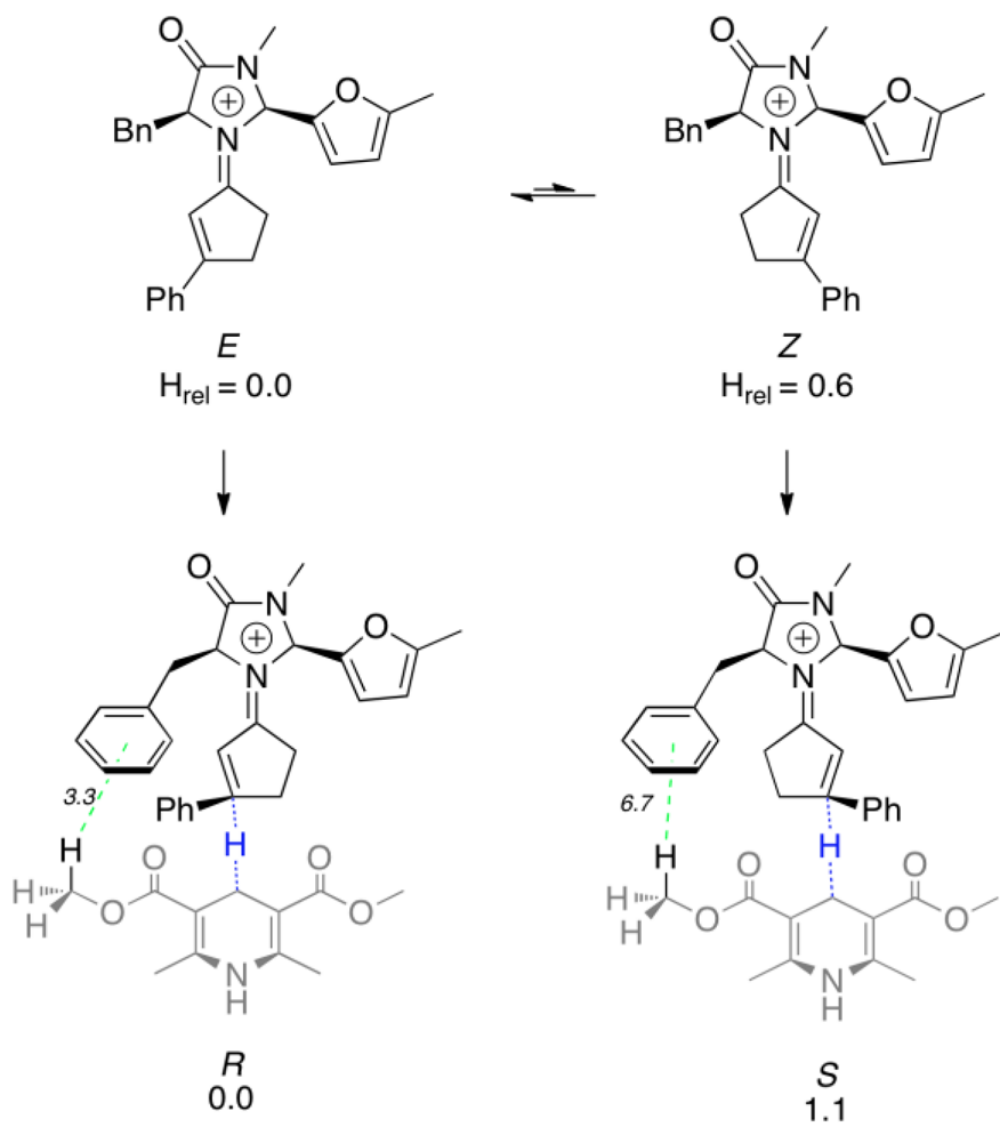
Scheme 59.
Imidazolidinone-catalyzed Diels-Alder cycloaddition

**Scheme 60.**

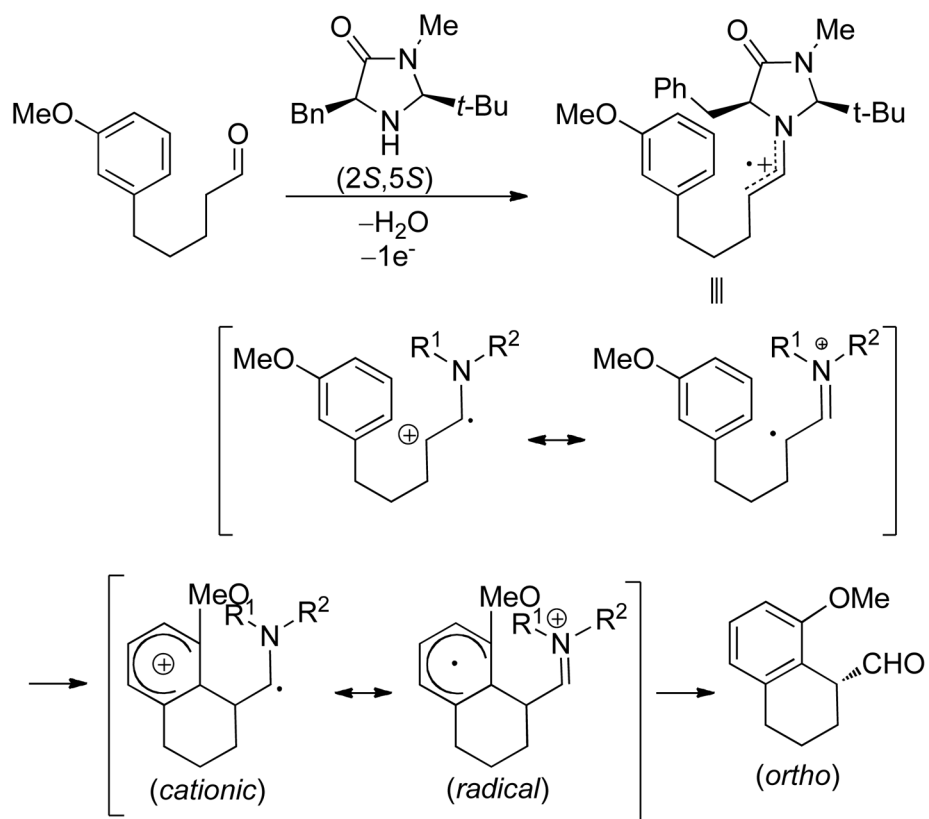
Imidazolidinone-catalyzed indole alkylation reactions



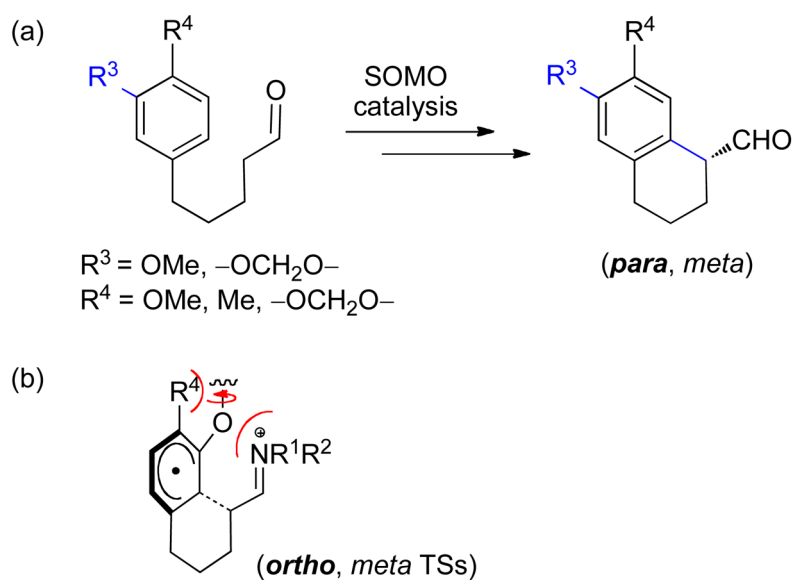
Scheme 61.
Imidazolidinone-catalyzed transfer hydrogenation



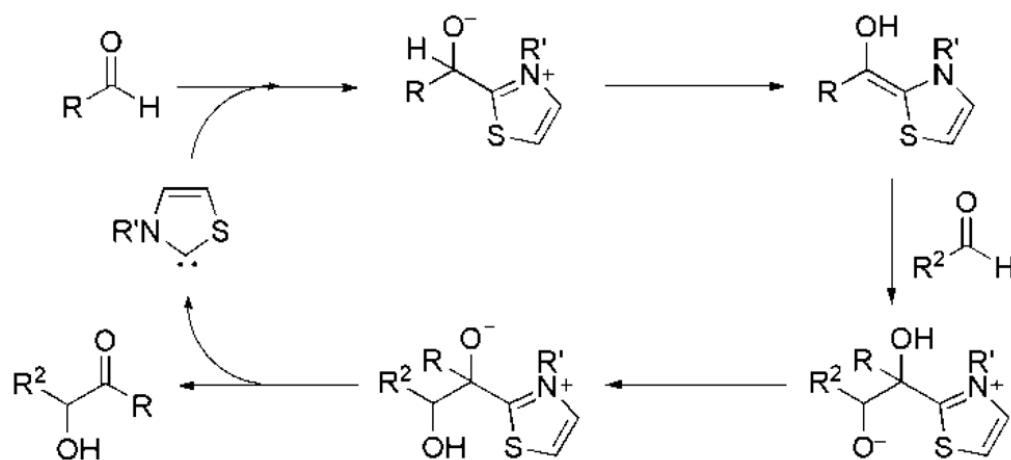
Scheme 62. Reduction leading to major (*R*) and minor (*S*) enantiomers (Relative B3LYP/6-31G(d) enthalpies (kcal/mol))



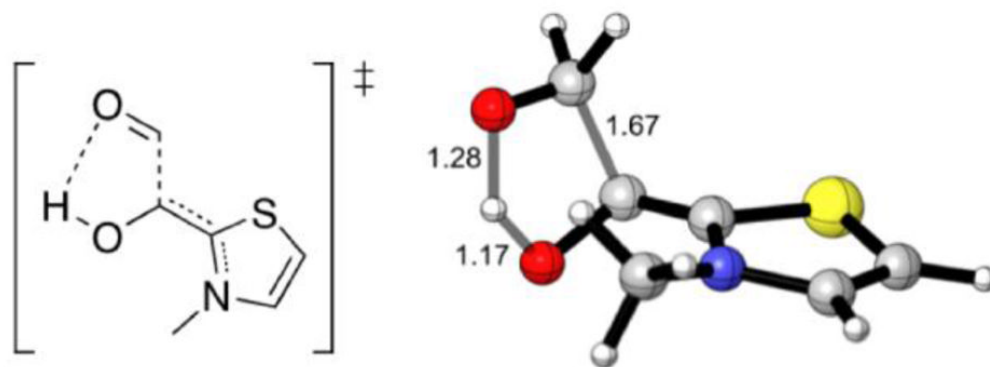
Scheme 63.
Intramolecular α -arylation reaction via SOMO activation

**Scheme 64.**

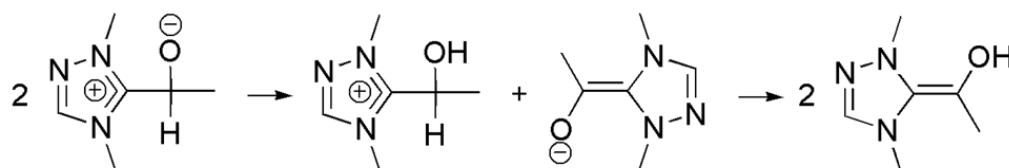
(a) *Para, meta* α -arylation selectivity of 1,3,4-trisubstituted aromatics (b) Destabilization of *ortho, meta* transition states



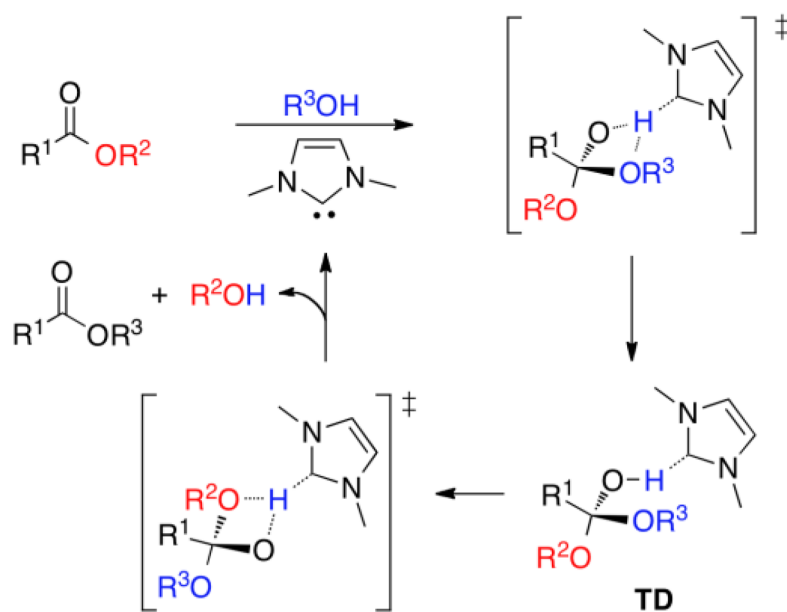
Scheme 65.
Mechanism for the benzoin condensation as proposed by Breslow



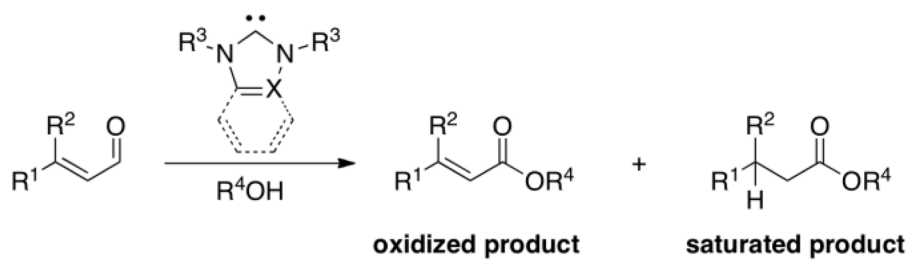
Scheme 66.
Transition structure for the C-C bond formation in the benzoin condensation of formaldehyde

**Scheme 67.**

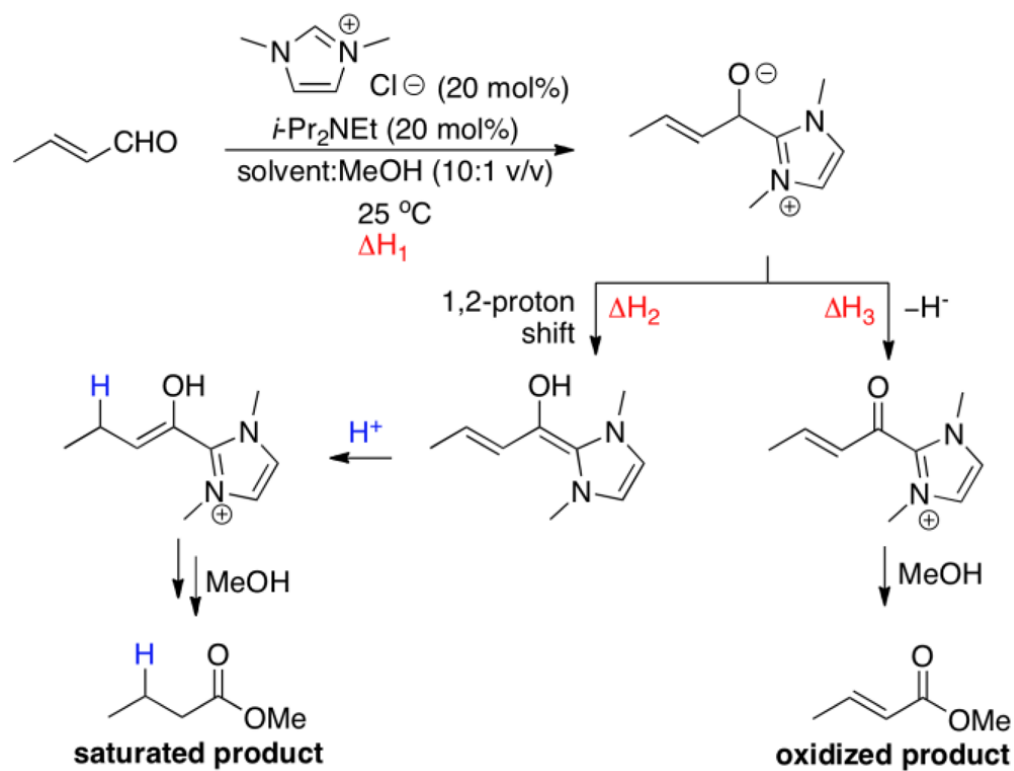
Intermolecular proton transfer pathway to the Breslow intermediate



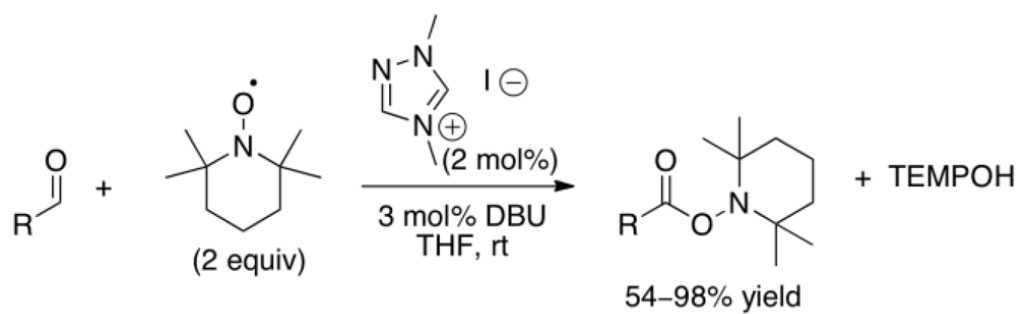
Scheme 68.
Reaction pathway for the NHC catalyzed transesterification involving a neutral tetrahedral intermediate



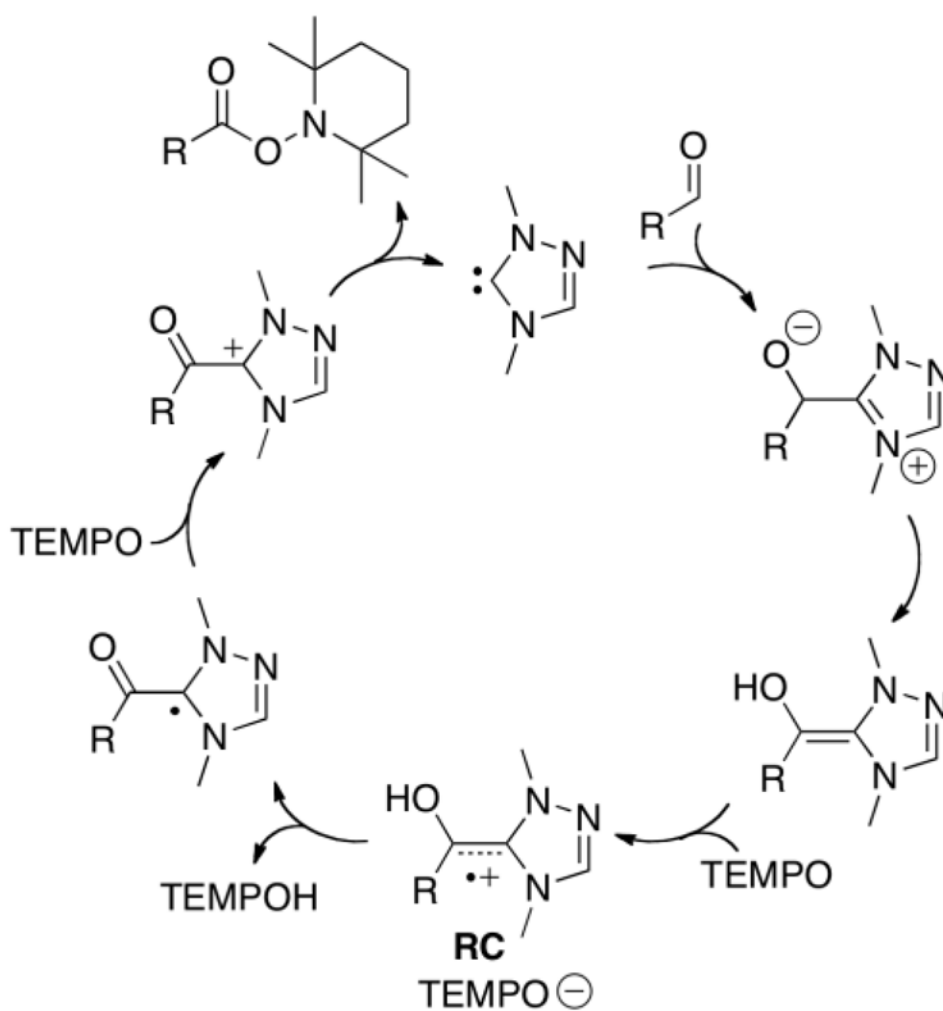
Scheme 69.
Esterification of α,β -unsaturated aldehydes



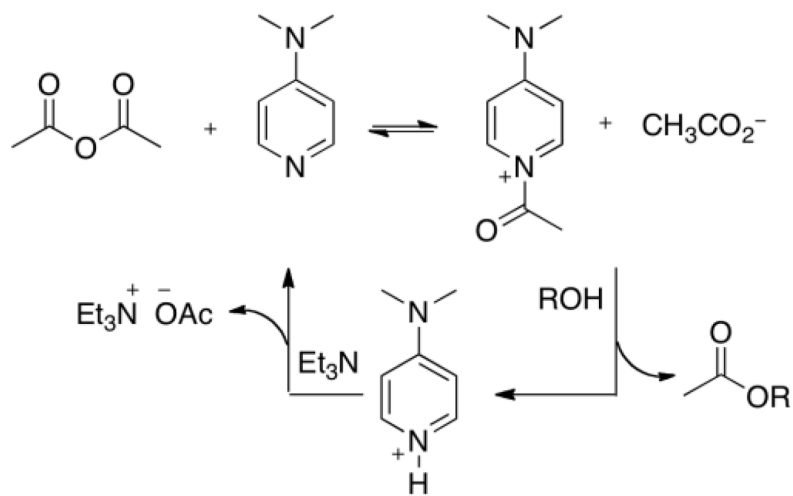
Scheme 70.
Transesterification mechanism



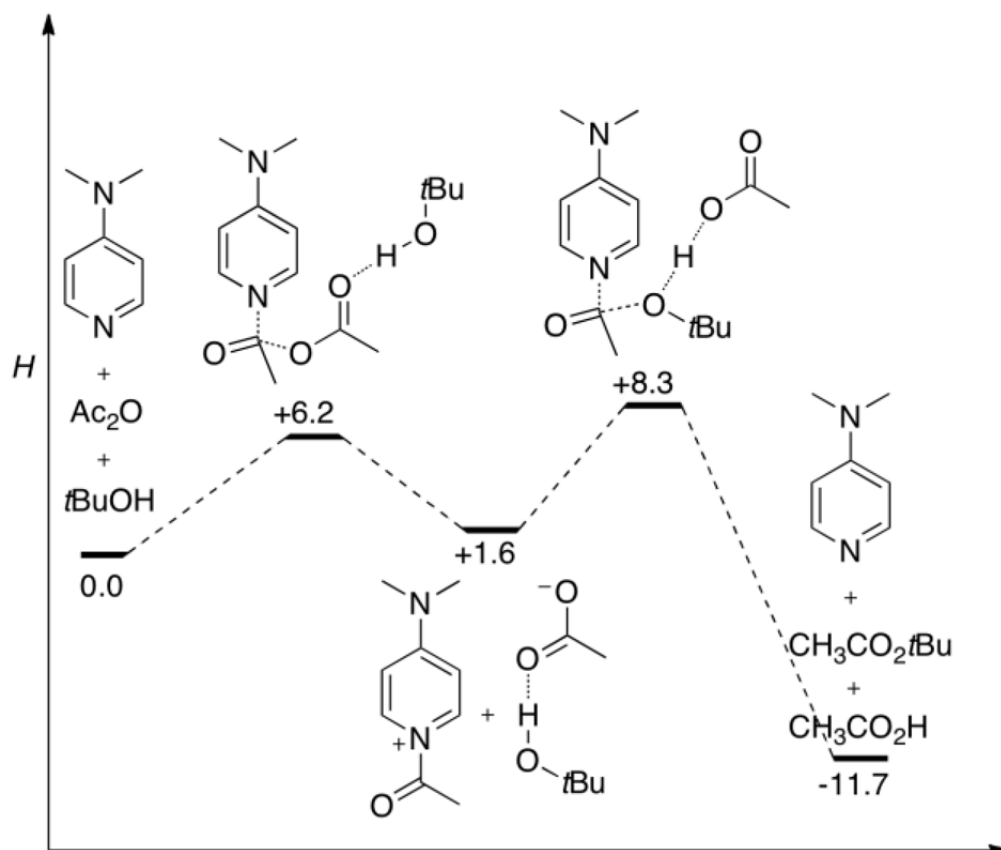
Scheme 71.
Organocatalyzed oxidation of aldehydes by TEMPO



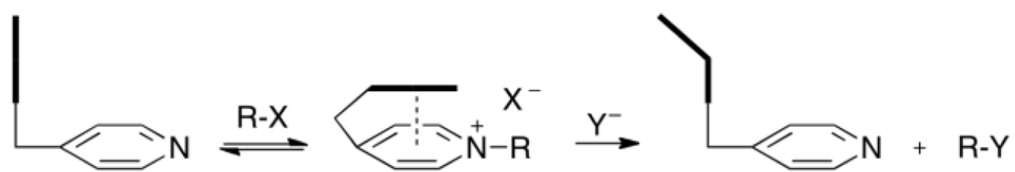
Scheme 72.
Proposed mechanism for carbene-catalyzed oxidation of aldehydes

**Scheme 73.**

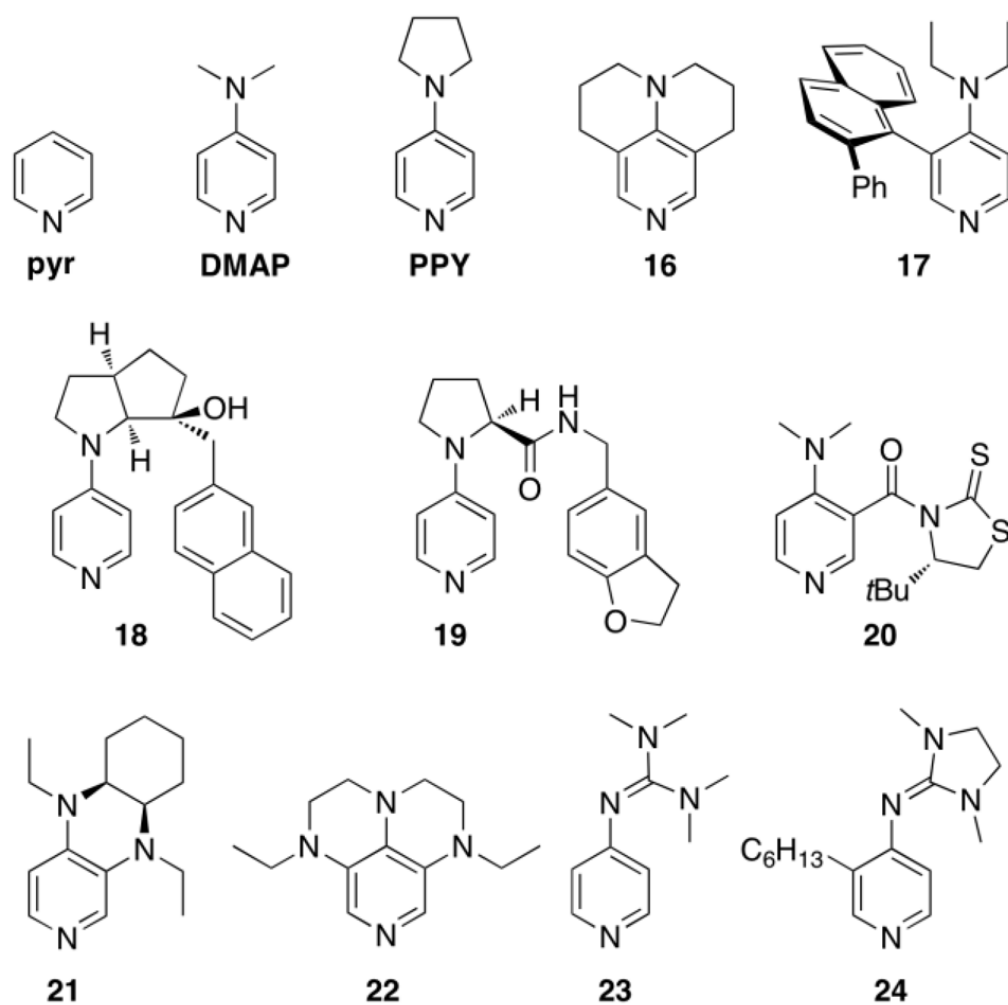
Accepted mechanism for the acylation of alcohols catalyzed by DMAP



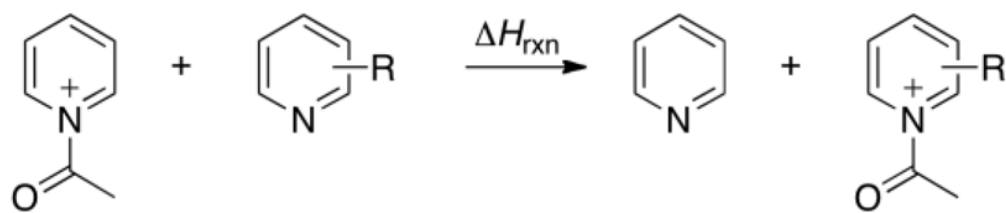
Scheme 74.
Gas phase enthalpy diagram of the DMAP catalyzed acylation process

**Scheme 75.**

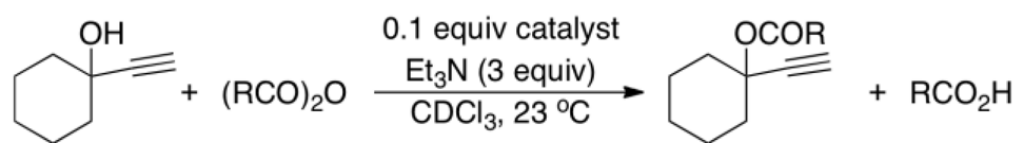
The use of π - π interactions to shield a face of DMAP derivatives



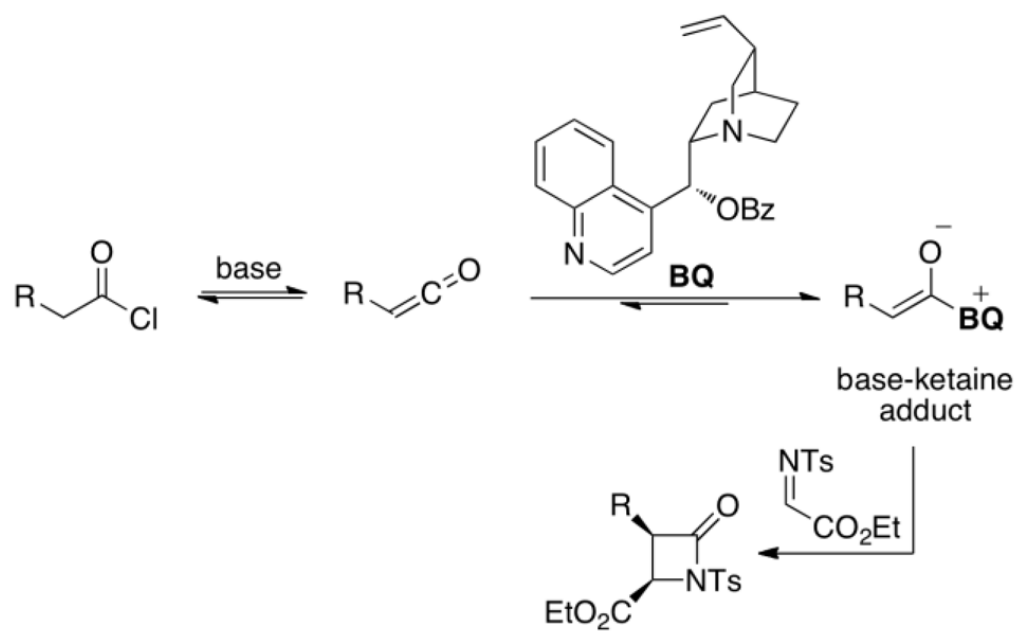
Scheme 76.
Various studied DMAP derivatives



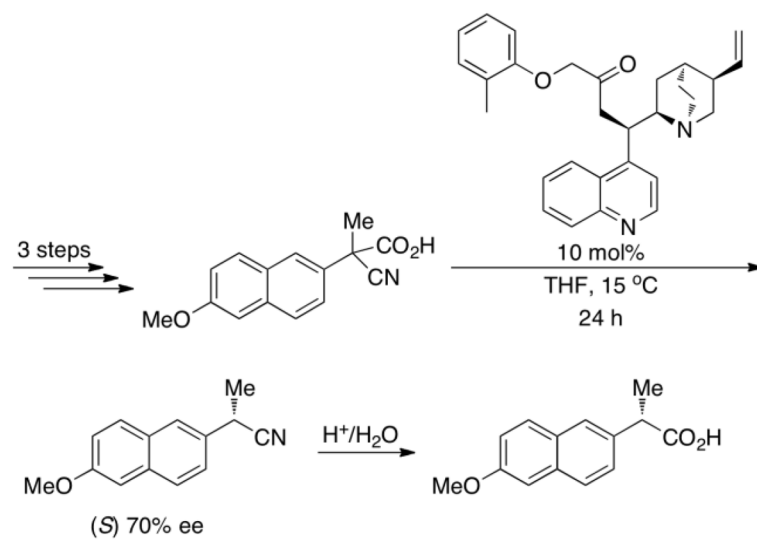
Scheme 77.
Isodesmic reaction for measuring relative stabilities of acyl pyridinium intermediates



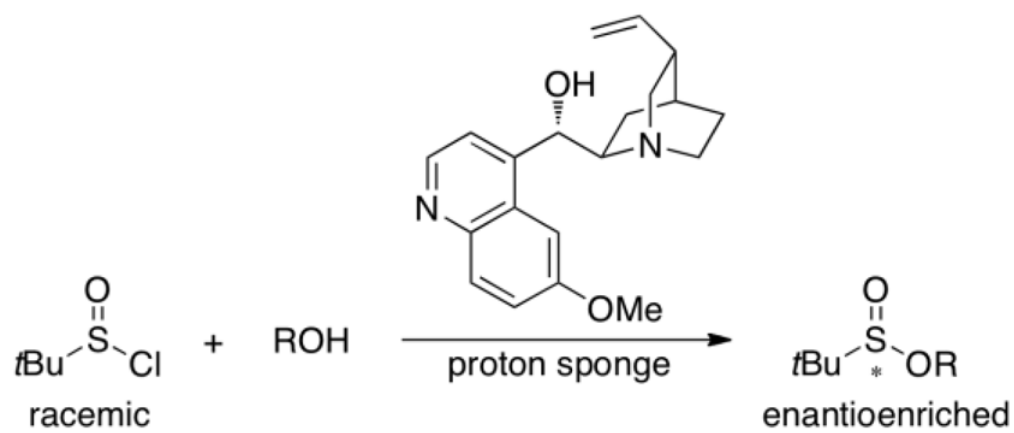
Scheme 78.
Acyl transfer reaction catalyzed by pyridines



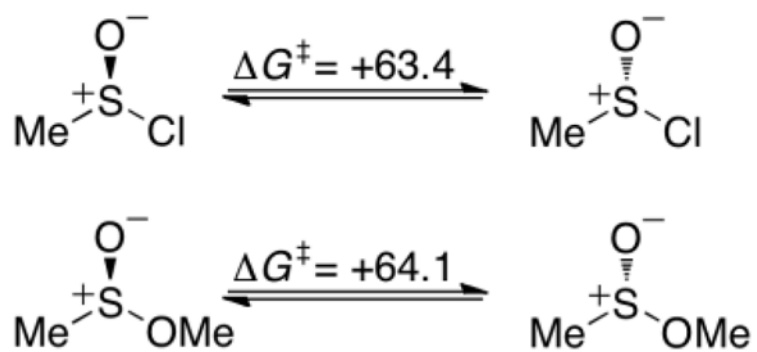
Scheme 79.
Proposed mechanism for the **BQ** catalyzed β -lactam synthesis



Scheme 80.
Enantioselective decarboxylation step

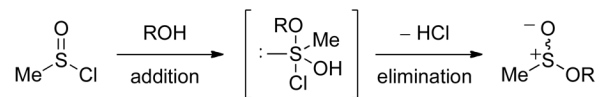


Scheme 81.
Cinchona catalyzed dynamic kinetic resolution of sulfinyl chlorides

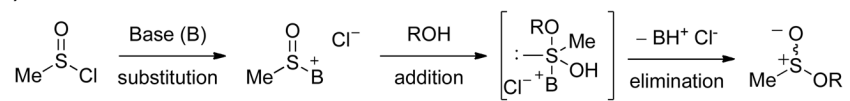


Scheme 82.
Barriers of the base-free inversion of sulfinyl chloride and methyl sulfinate

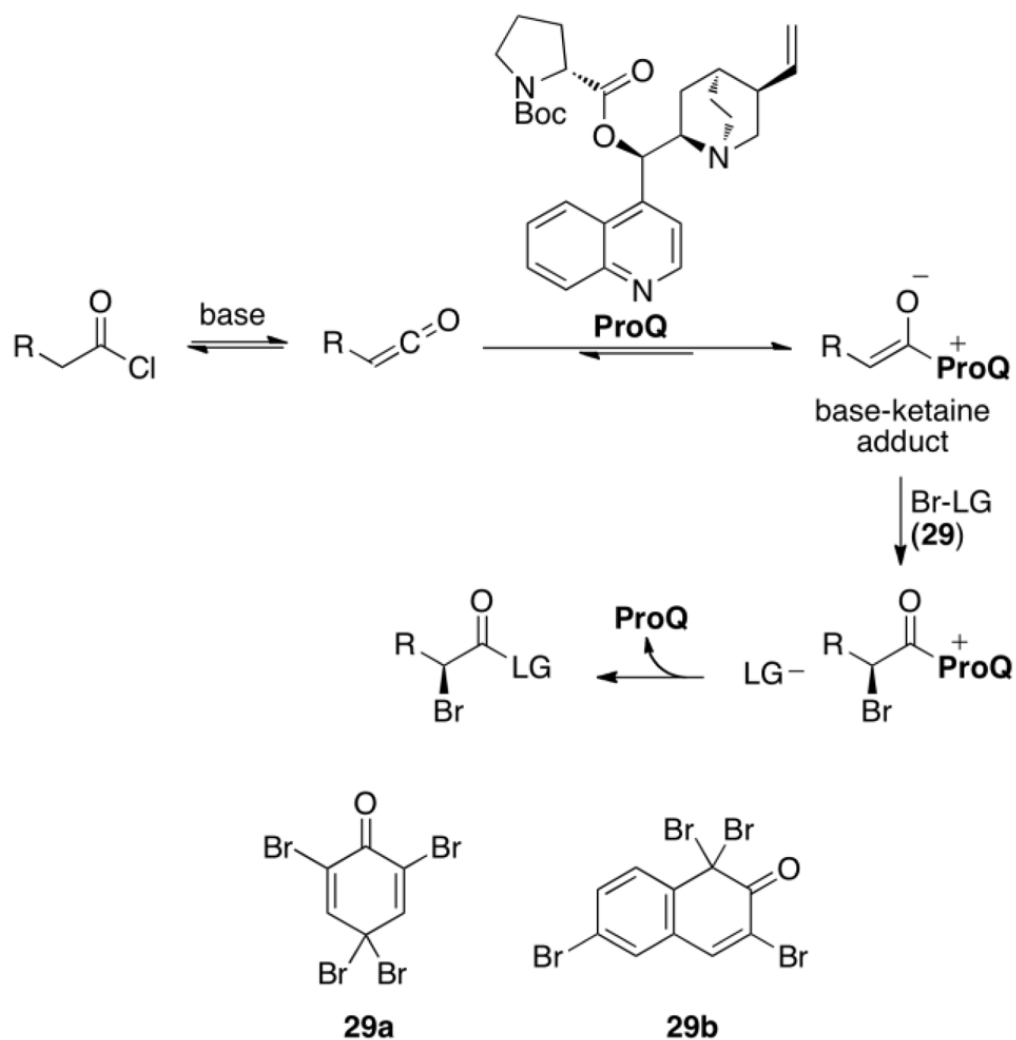
a) Neutral mechanism



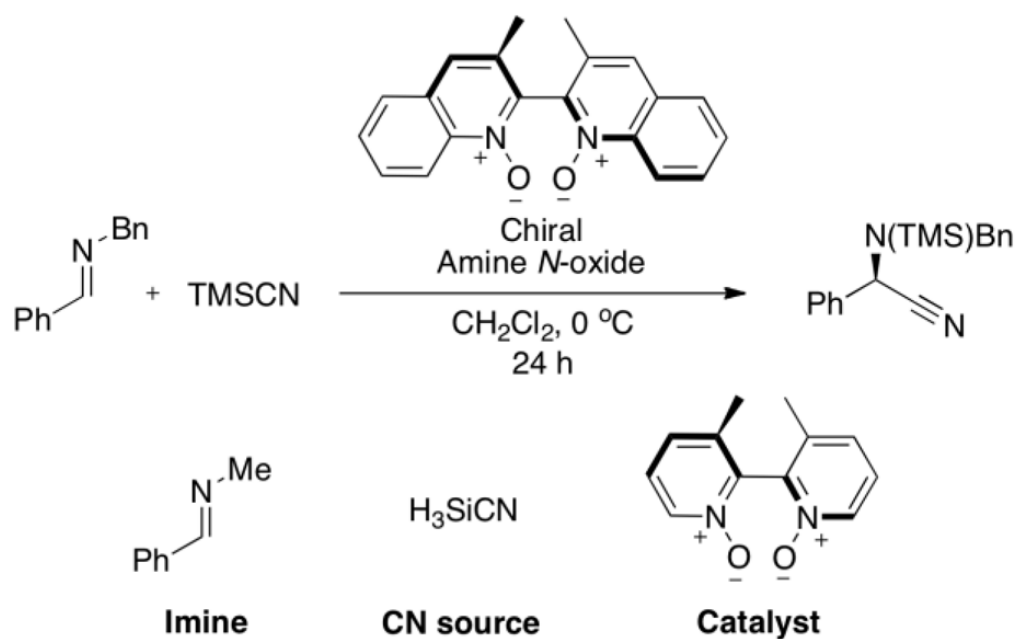
b) Ion-Pair mechanism

**Scheme 83.**

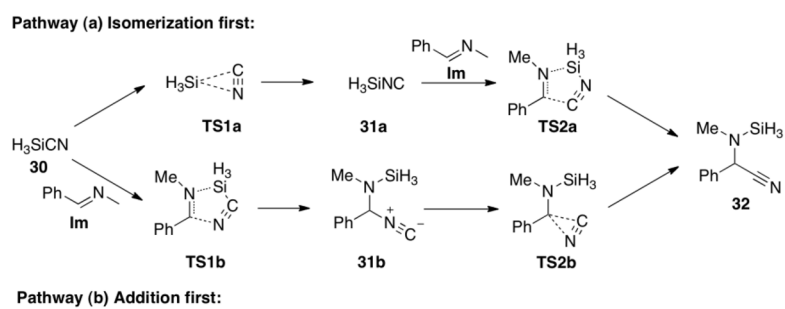
Possible pathways for the sulfonylation reaction



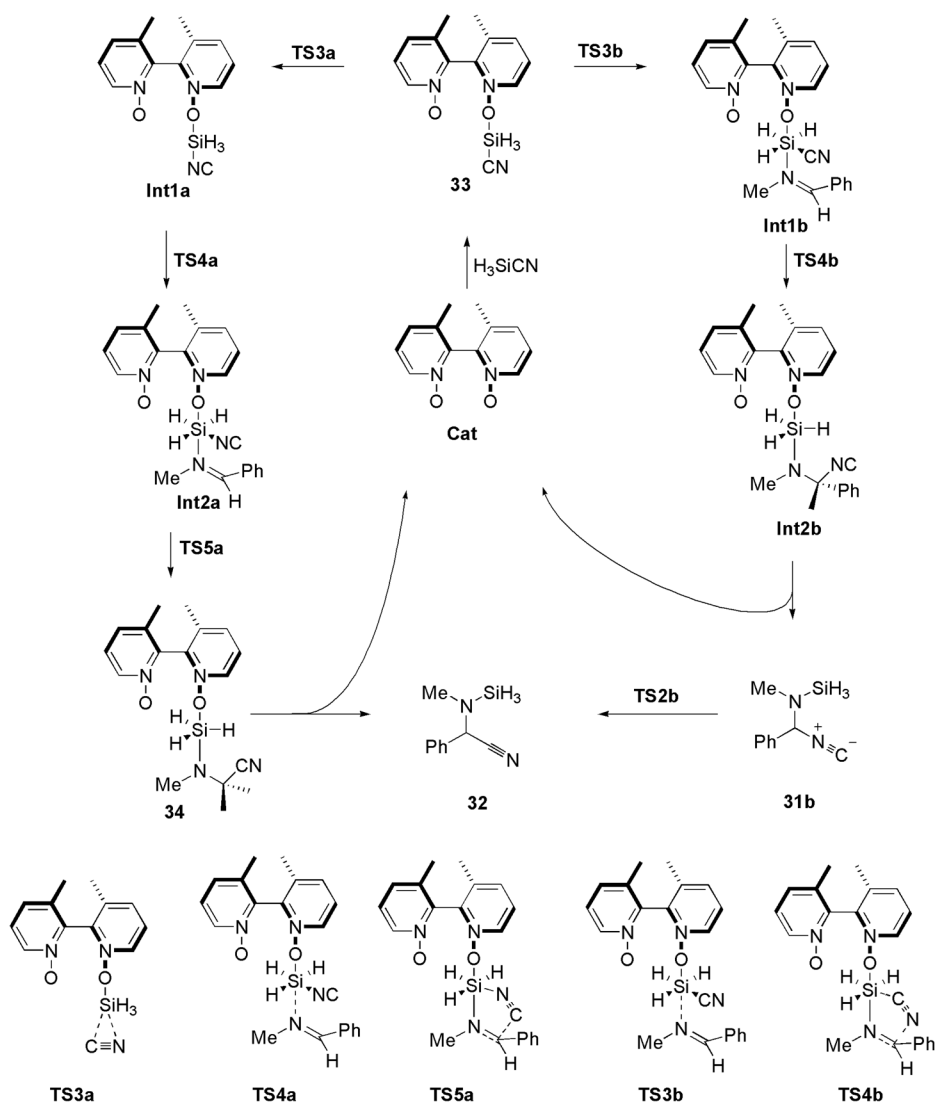
Scheme 84.
Catalytic, asymmetric α -bromination methodology developed by Letcka and coworkers

**Scheme 85.**

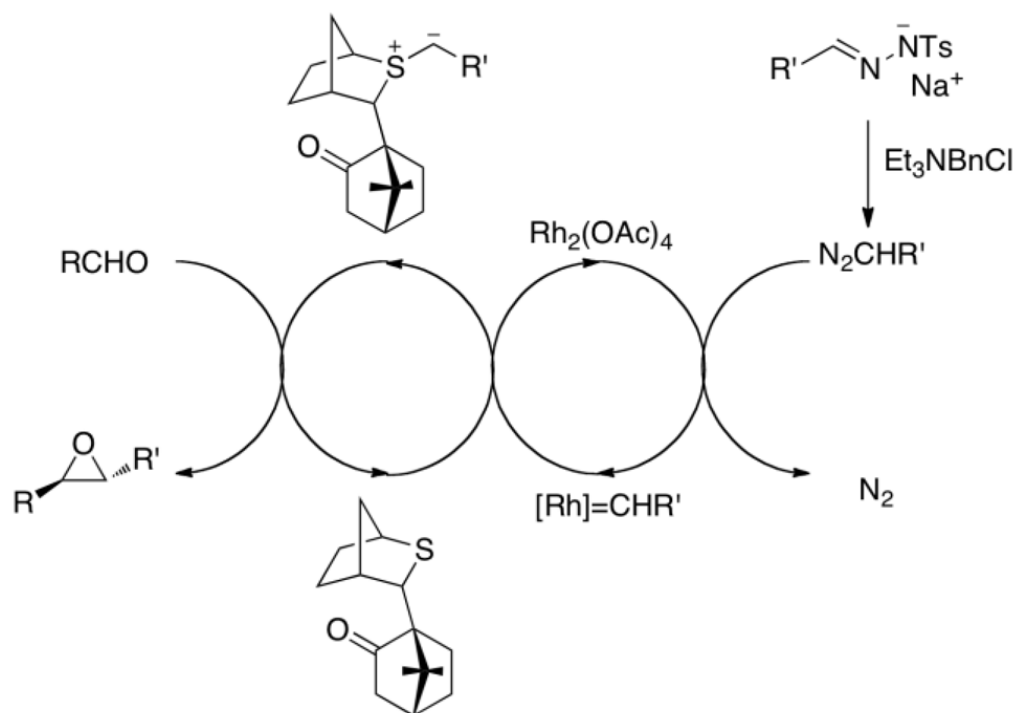
Methodology studied by Hu and co-workers; model molecules used in the study

**Scheme 86.**

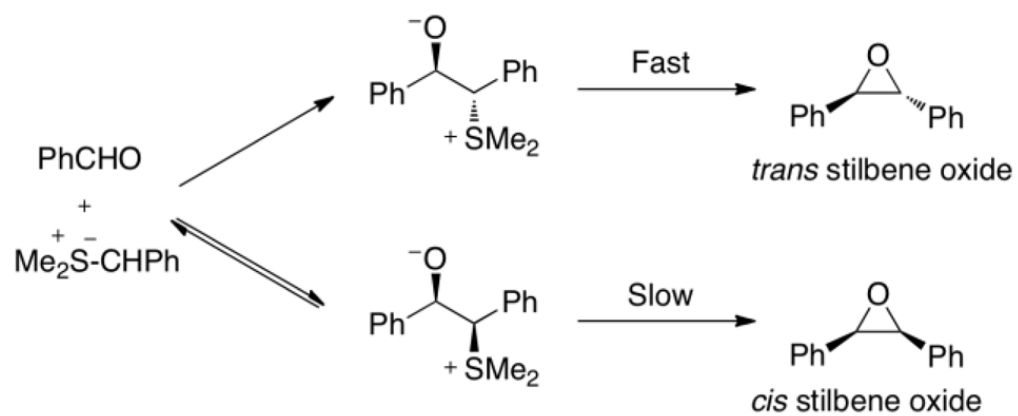
Possible pathways for the uncatalyzed Strecker reaction



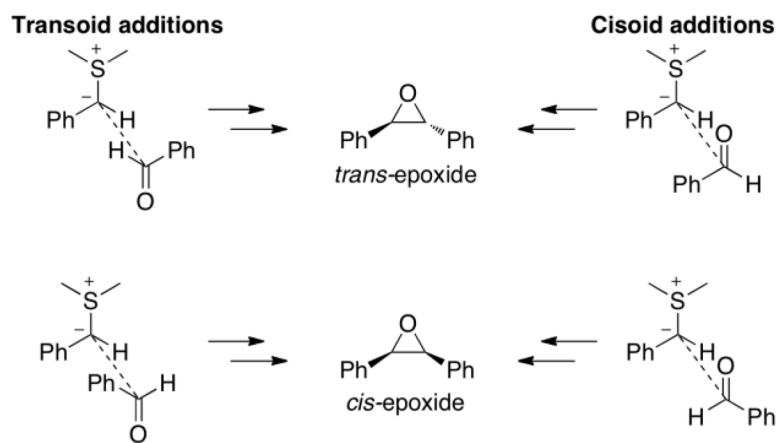
Scheme 87.
Different pathways for the *N*-oxide catalyzed Strecker reaction

**Scheme 88.**

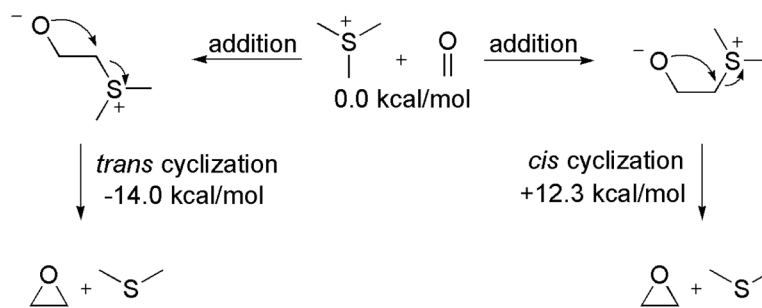
Catalytic process for the sulfur ylide mediated epoxidation developed by Aggarwal and co-workers



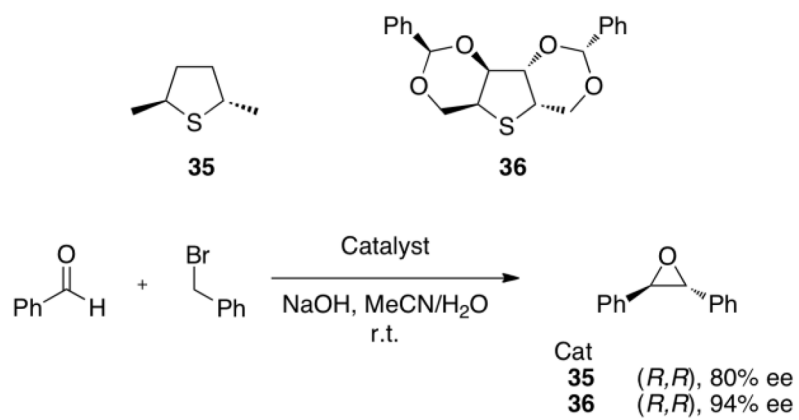
Scheme 89.
Rational for the *trans* selectivity observed in the epoxidation process



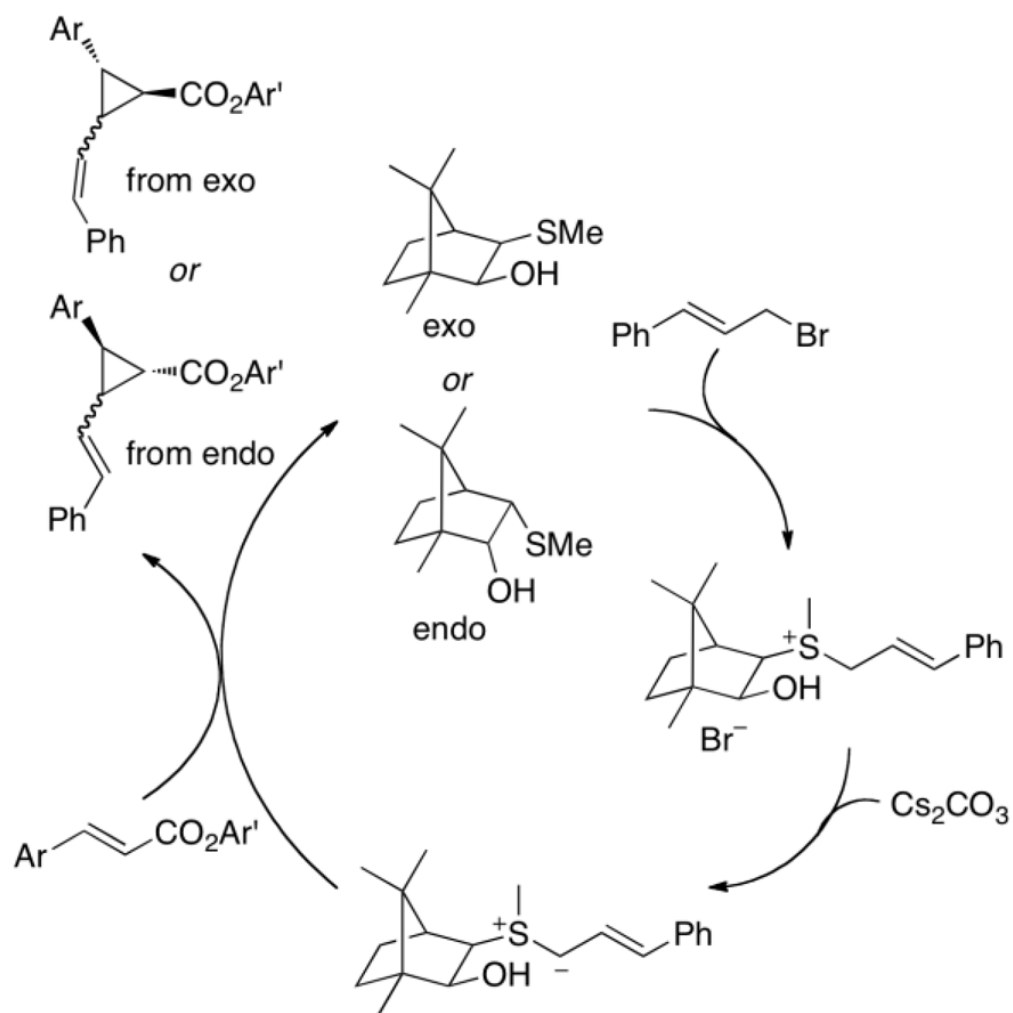
Scheme 90.
Different approaches of the ylide to the aldehyde



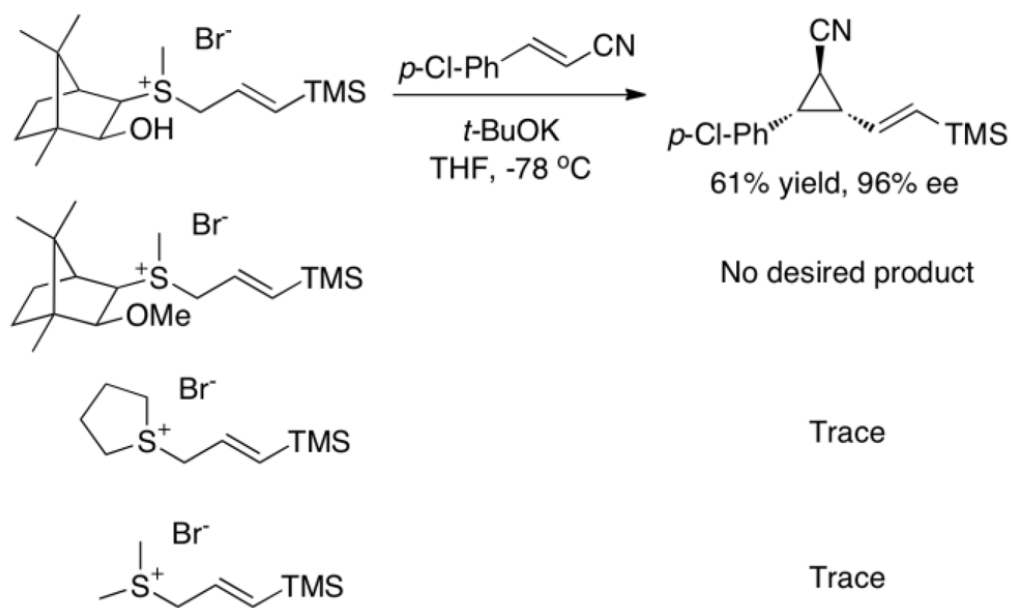
Scheme 91.
Cyclization step on a small model system



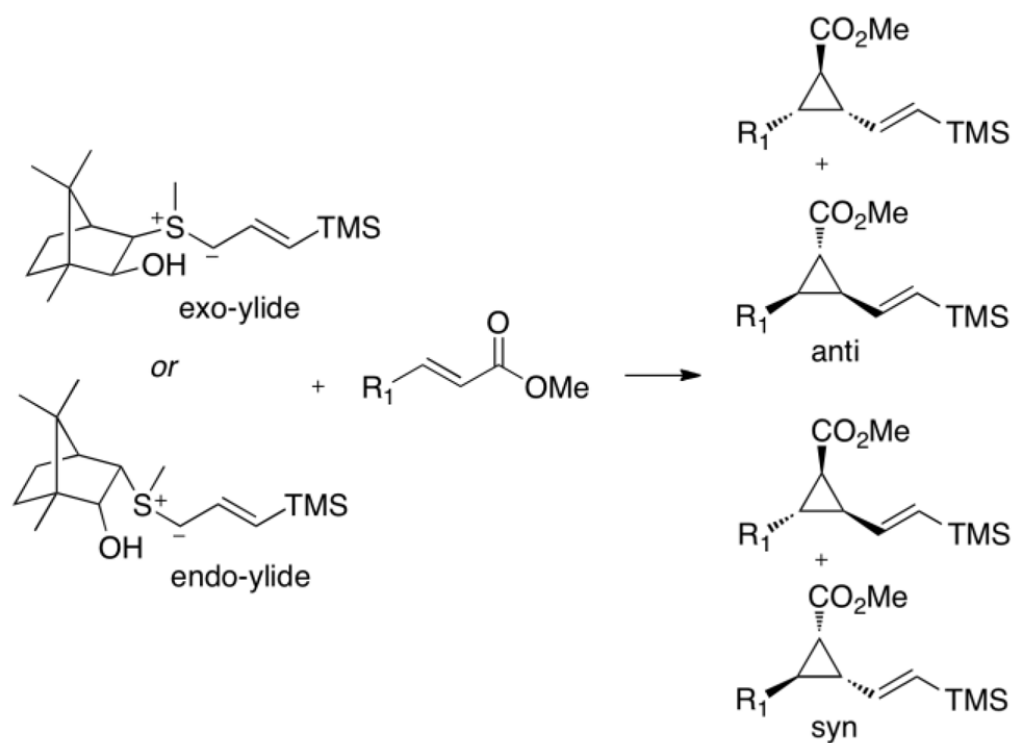
Scheme 92.
Enantioselective epoxidation mediated by chiral sulfides **35** or **36**



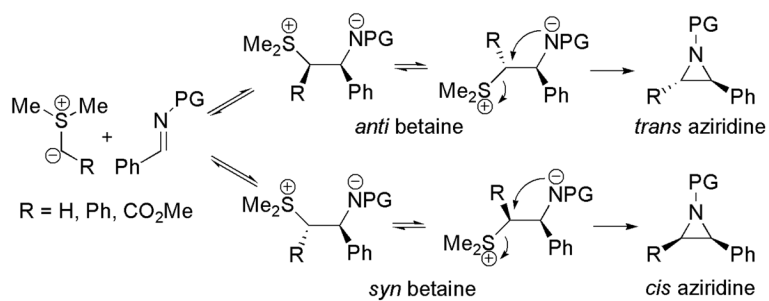
Scheme 93.
Mechanism for the sulfide catalyzed cyclopropanation



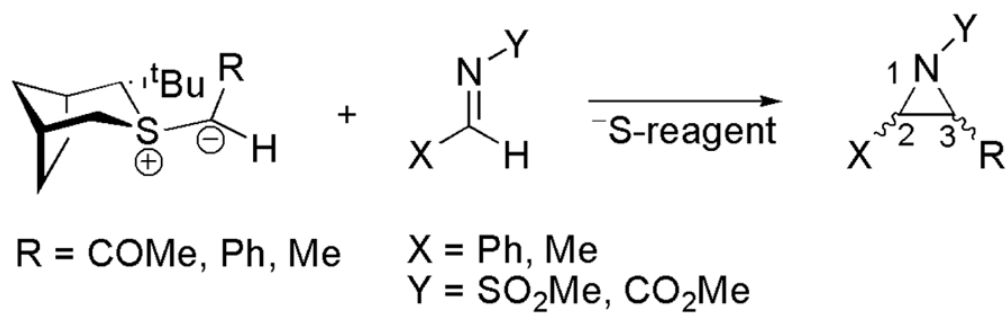
Scheme 94.
Relative reactivities for different sulfides



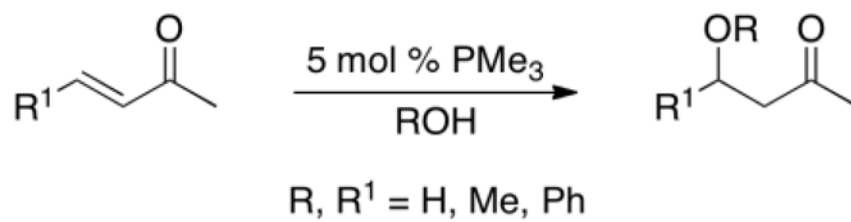
Scheme 95.
Model reactions studied by Wu and co-workers



Scheme 96.
Aziridine formation from sulfur ylides and imines

**Scheme 97.**

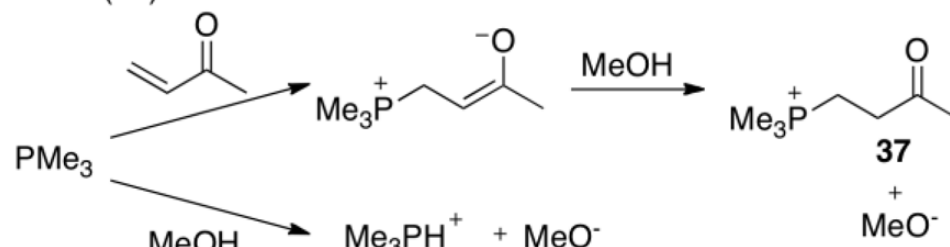
Chiral sulfur ylide promoted asymmetric aziridination



Scheme 98.
Phosphine catalyzed hydroalkoxylation of enones

Step 1 : Base formation

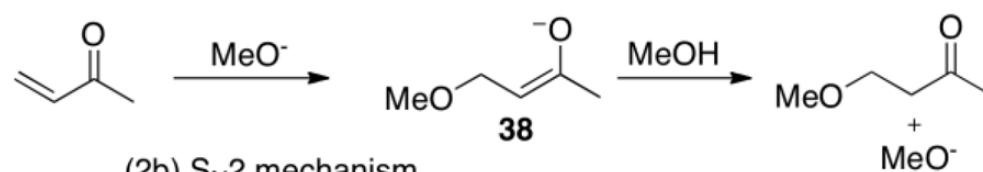
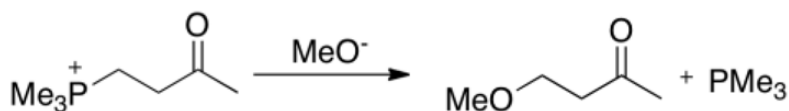
(1a) MVK induced base formation



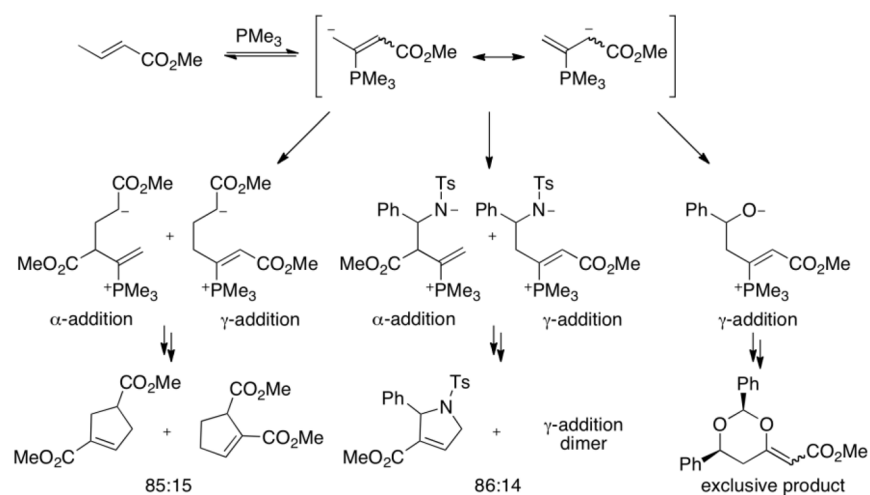
(1b) Direct base formation

Step 2: Hydroalkoxylation

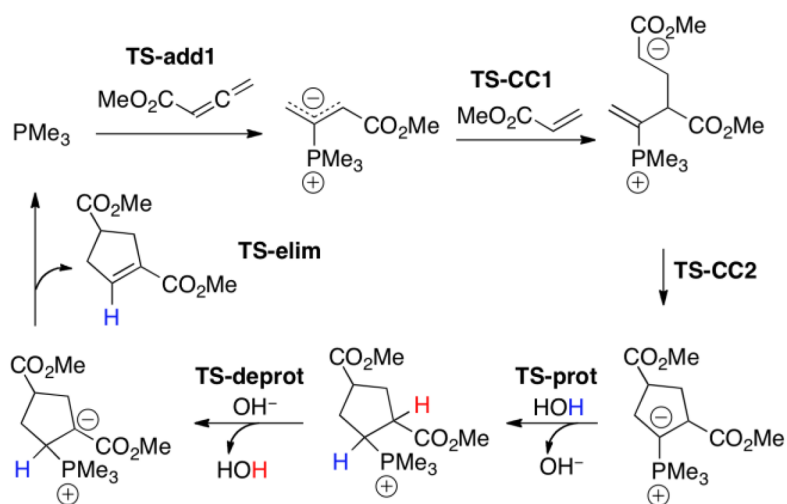
(2a) Base catalyzed mechanism

(2b) S_N2 mechanism**Scheme 99.**

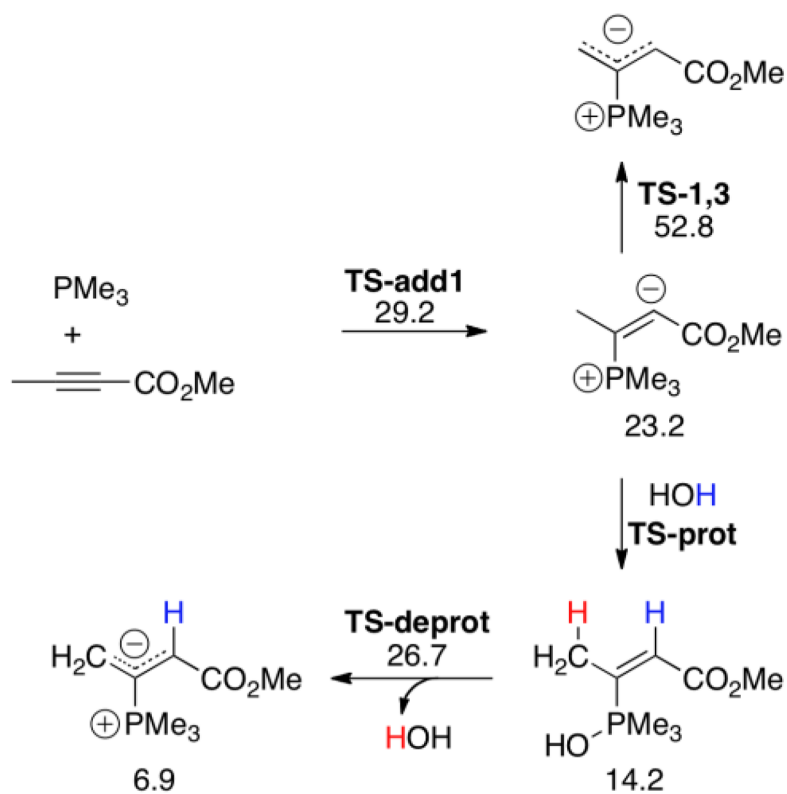
Possible pathways for the phosphine catalyzed hydroalkoxylation reaction

**Scheme 100.**

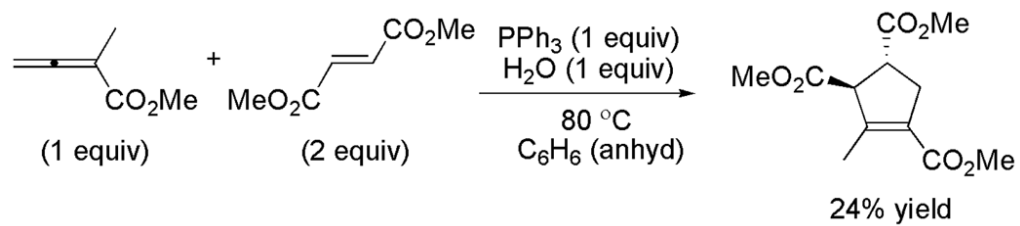
Proposed mechanism for the annulation of allenates with various electrophiles



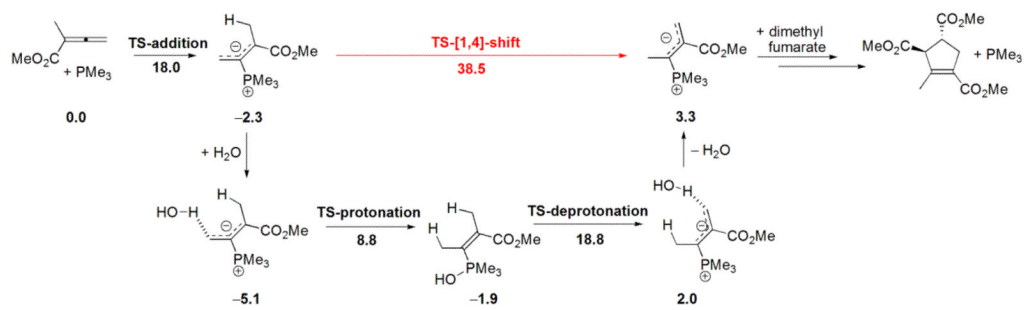
Scheme 101.
 PMe_3 catalyzed [3+2] cycloaddition mechanism of allenolate and acrylate

**Scheme 102.**

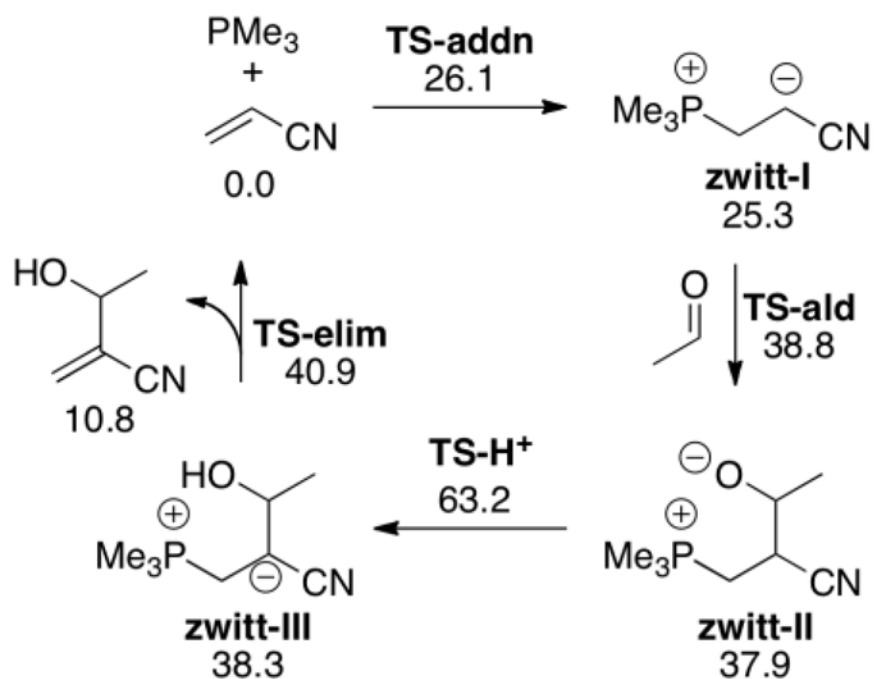
B3LYP/6-31+G(d) free energies for dipole formation from alkynoate. CPCM single point corrections (benzene) are included

**Scheme 103.**

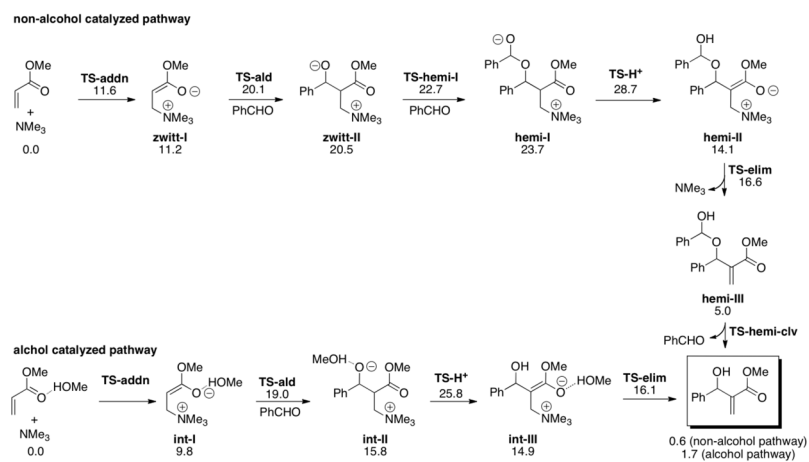
Phosphine and water co-catalyzed reaction of 2-methyl-2,3-butadienoate and dimethyl fumarate

**Scheme 104.**

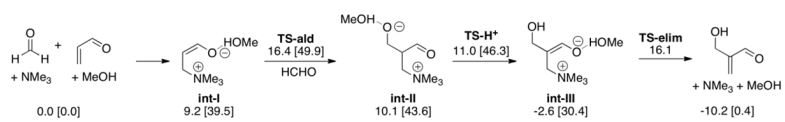
Possible pathways for the [1,4]-proton-shift in the PMe_3 -catalyzed reaction of 2-methyl-2,3-butadienoate with dimethyl fumarate (ΔH , kcal/mol)



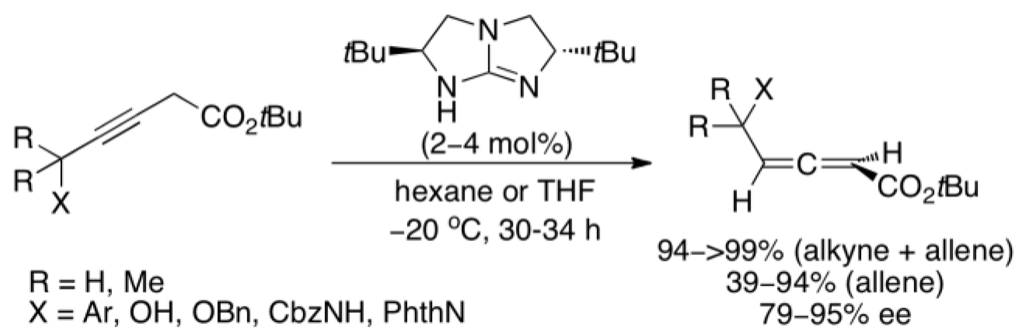
Scheme 105.
 PMe_3 -catalyzed MBH reaction

**Scheme 106.**

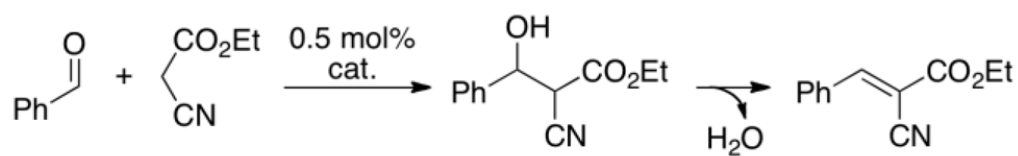
Calculated mechanism of the MBH reaction in the absence and presence of alcohol



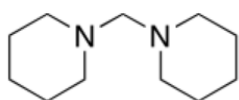
Scheme 107.
 B3LYP/6-311++G(d, p) energies (free energies in brackets) for the MBH reaction of formaldehyde and acrolein catalyzed by NMe₃ with MeOH

**Scheme 108.**

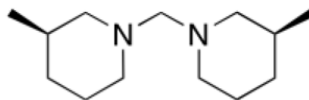
Guanidine-catalyzed isomerization of 3-alkynoates to chiral allenates



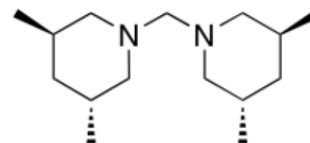
catalysts:



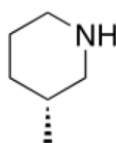
39



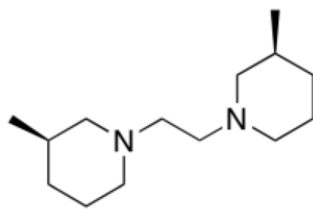
40



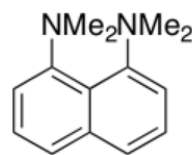
41



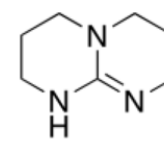
42



43

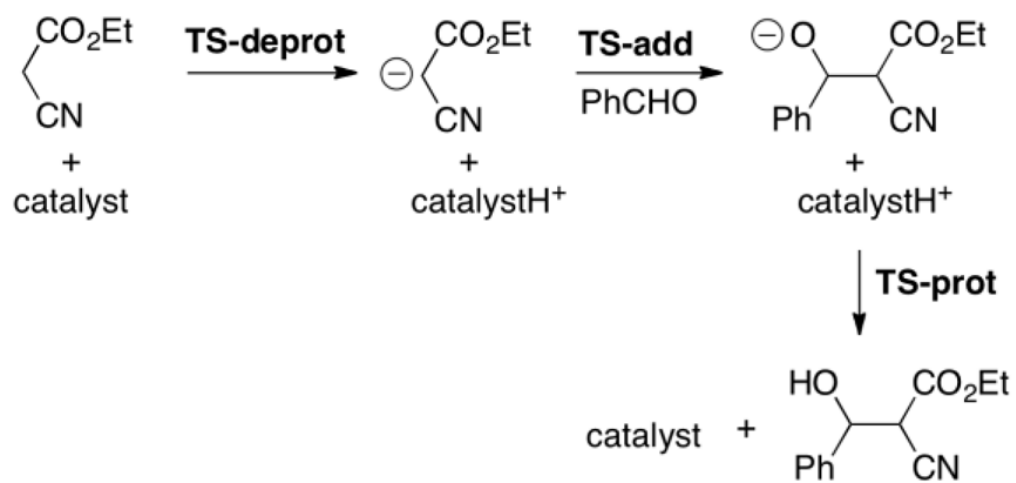


44

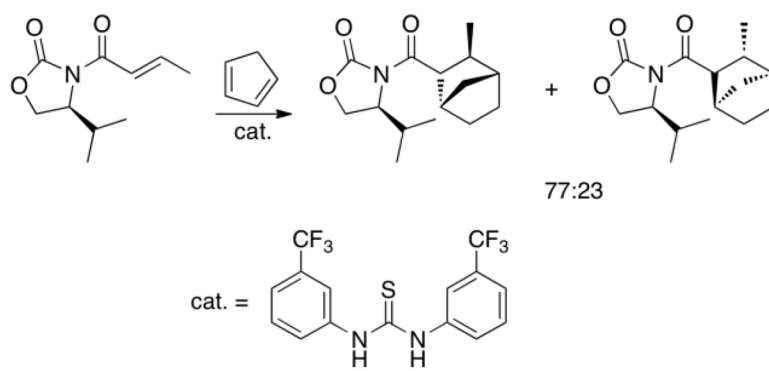


45

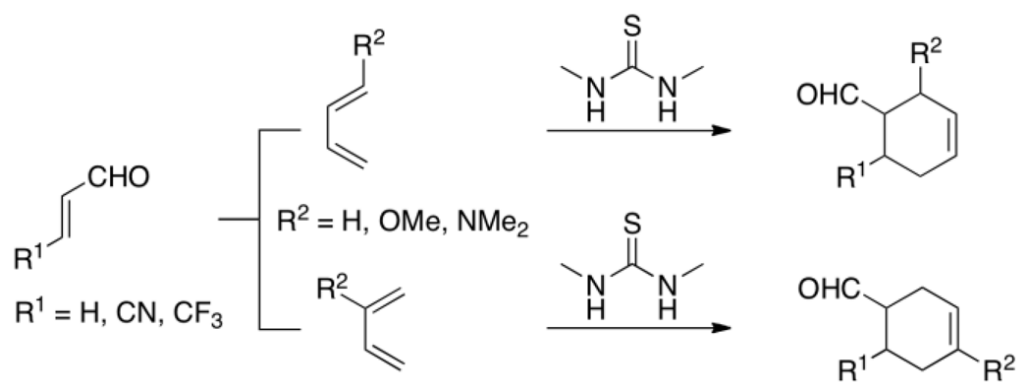
Scheme 109.
Knoevenagel condensation catalyzed by amines



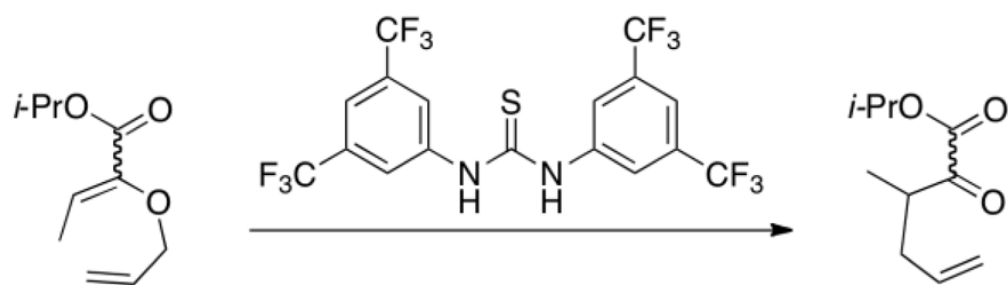
Scheme 110.
Knoevenagel condensation mechanism



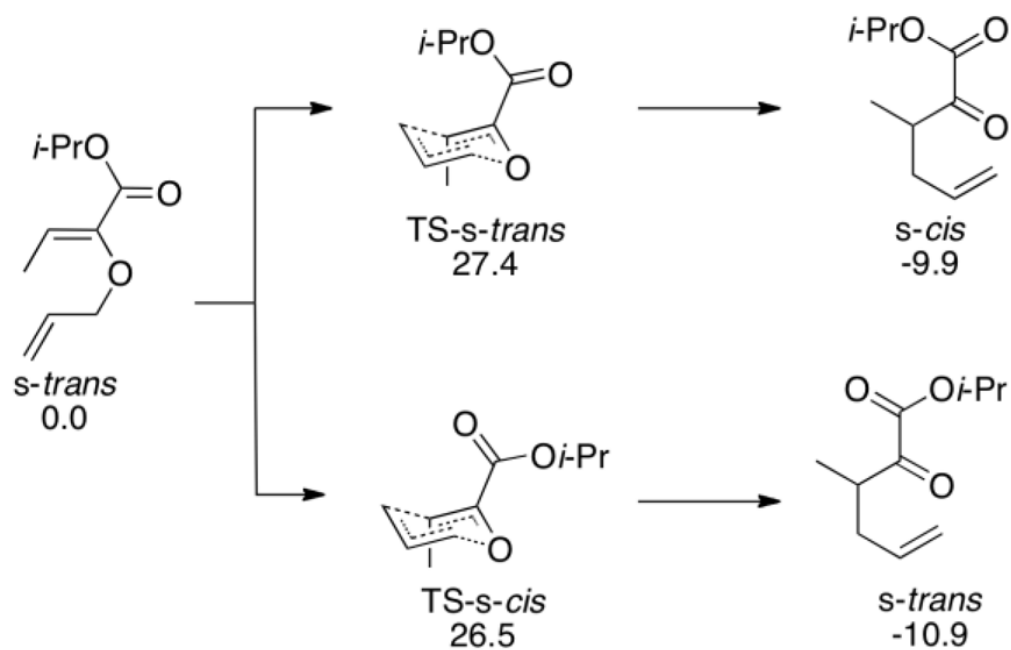
Scheme 111.
Thiourea-catalyzed Diels-Alder cycloaddition



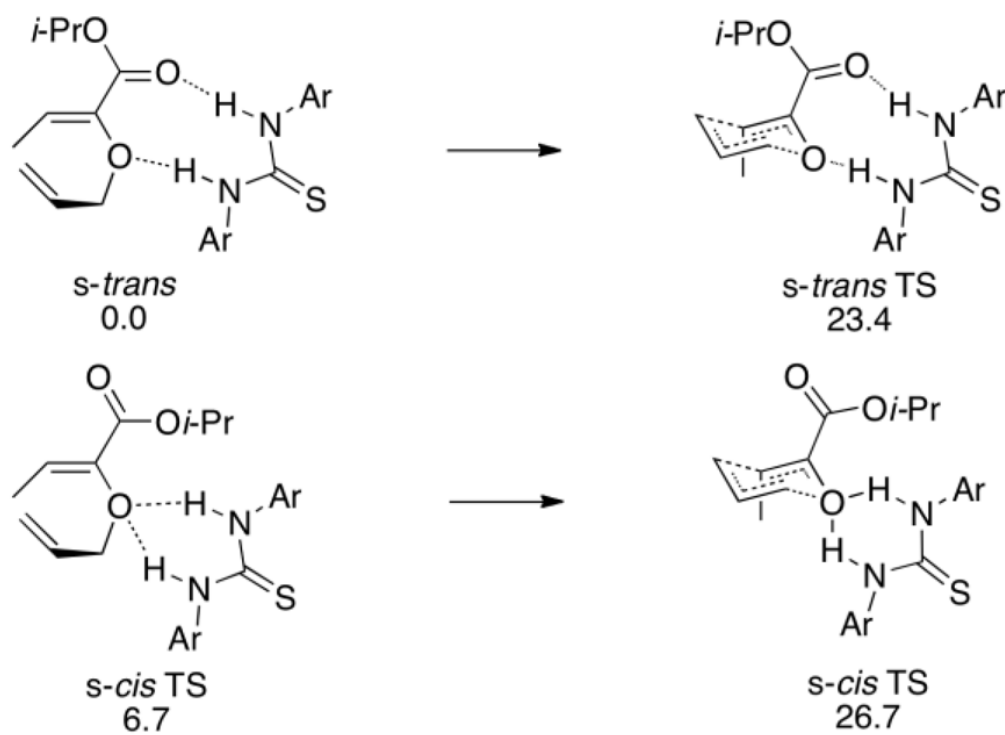
Scheme 112.
Thiourea catalyzed Diels-Alder cycloaddition



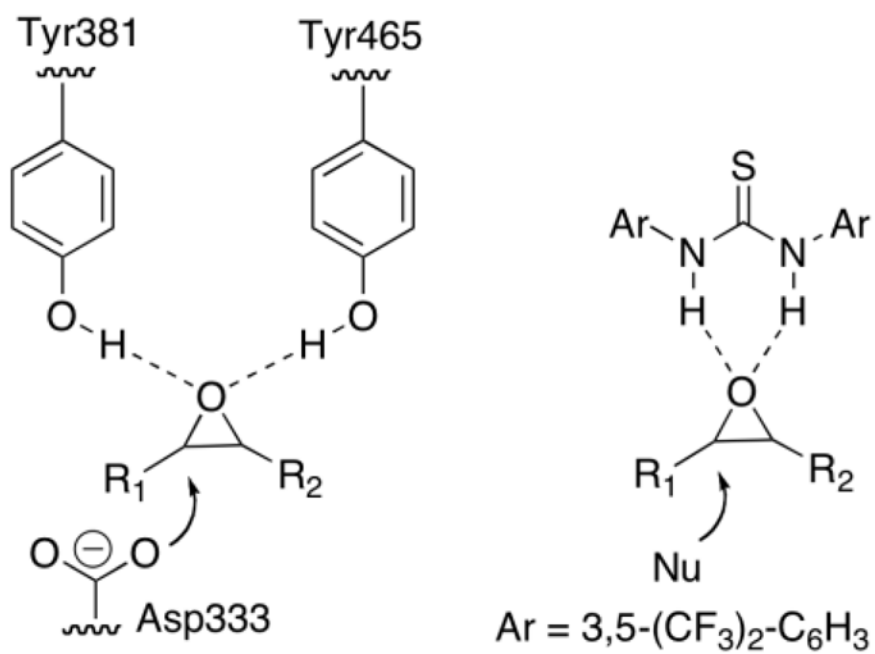
Scheme 113.
Thiourea-catalyzed Claisen rearrangement of allyl vinyl ether



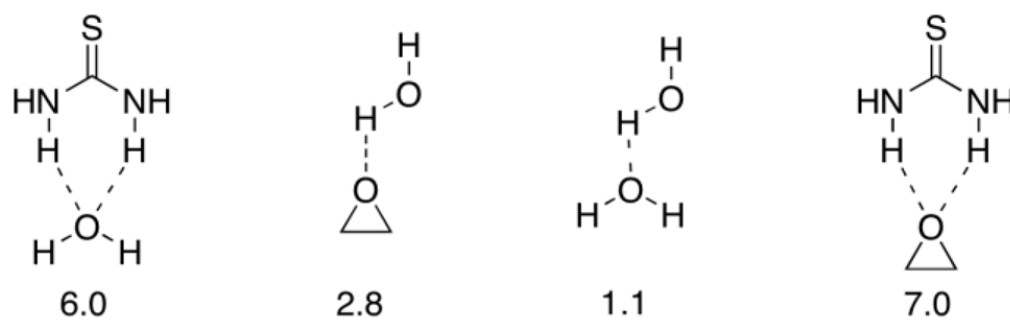
Scheme 114.
B3LYP/6-31++G(d, p) gas phase free energies for the uncatalyzed Claisen rearrangement

**Scheme 115.**

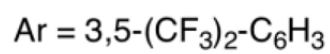
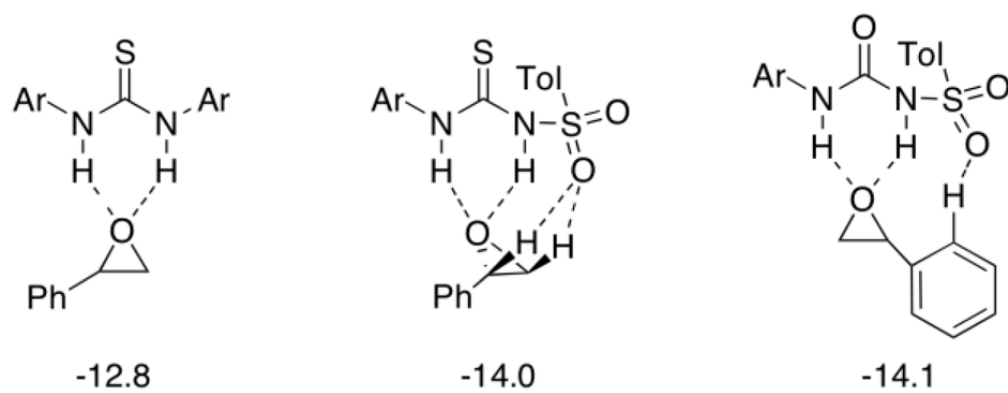
B3LYP/6-31++G(d, p) gas phase free energies for the thiourea-catalyzed Claisen rearrangement



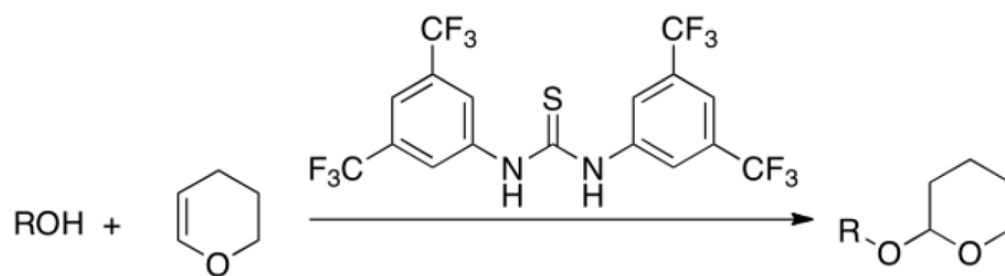
Scheme 116.
Epoxide recognition of epoxide hydrolase and diarylthiourea



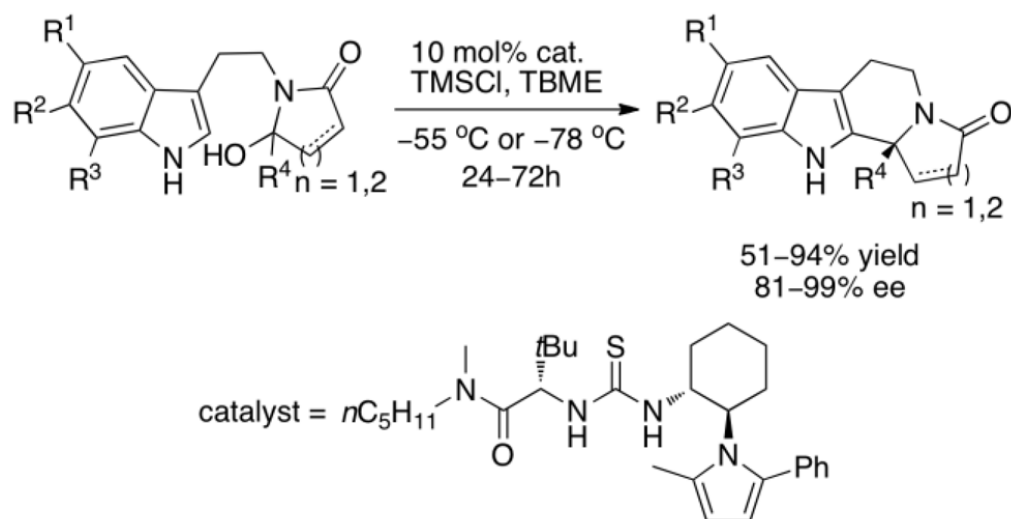
Scheme 117.
Binding energies of possible hydrogen bond complexes

**Scheme 118.**

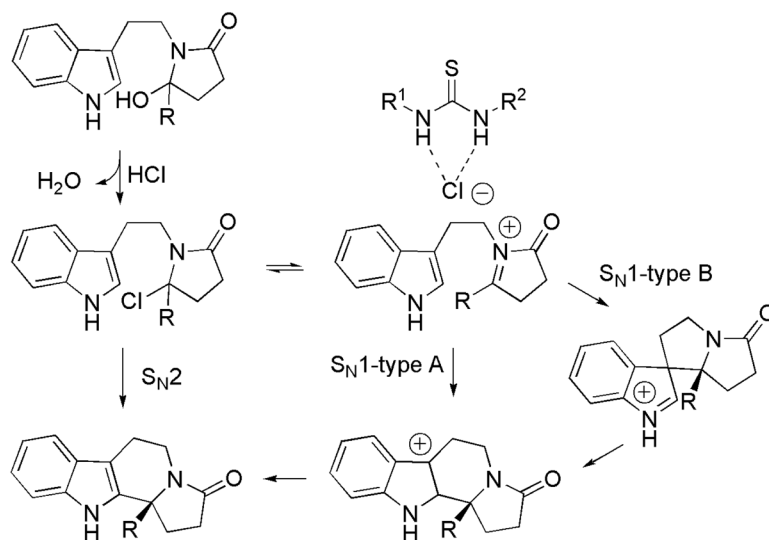
B3LYP/6-31+G(d) interaction energies of lowest-energy catalyst phenyloxirane complexes



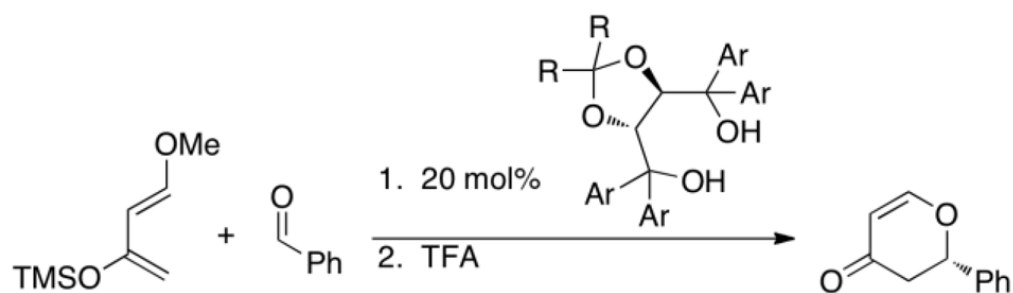
Scheme 119.
Tetrahydropyran (THP) protection of alcohols catalyzed by diarylthiourea

**Scheme 120.**

Asymmetric cyclization of hydroxylactams catalyzed by thiourea



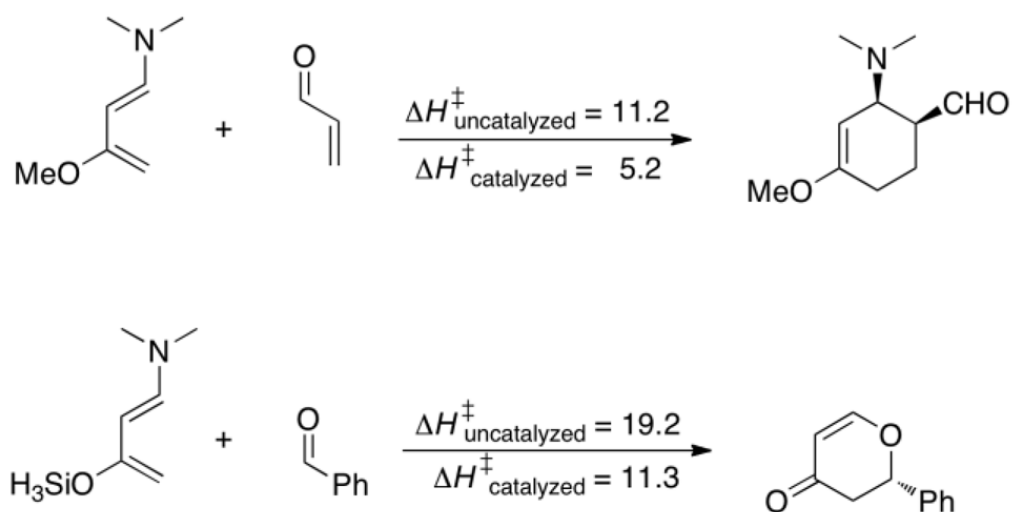
Scheme 121.
Proposed reaction mechanism



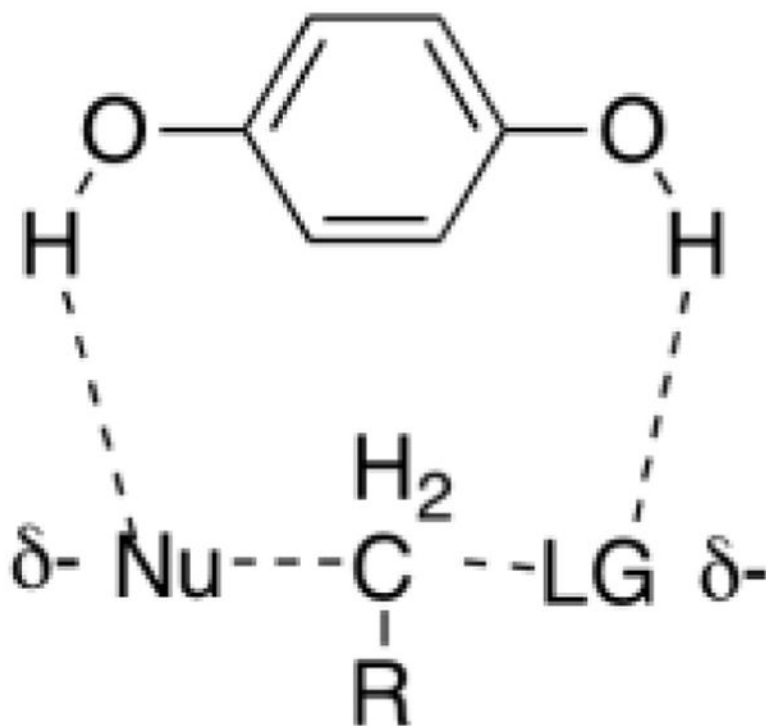
	<u>% Yield</u>	<u>%ee</u>
Ar = 1-naphthyl, R = CH ₃	77	76.3
Ar = Ph, R = CH ₃	18	12.1
Ar = 2-naphthyl, R = CH ₃	36	18.7

Scheme 122.

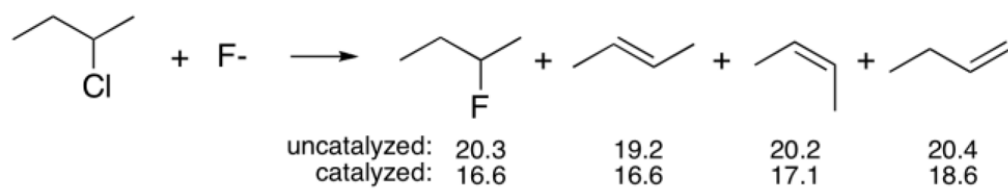
Diels-Alder reaction of benzaldehyde with Danishefsky's diene catalyzed by TADDOL catalysts.

**Scheme 123.**

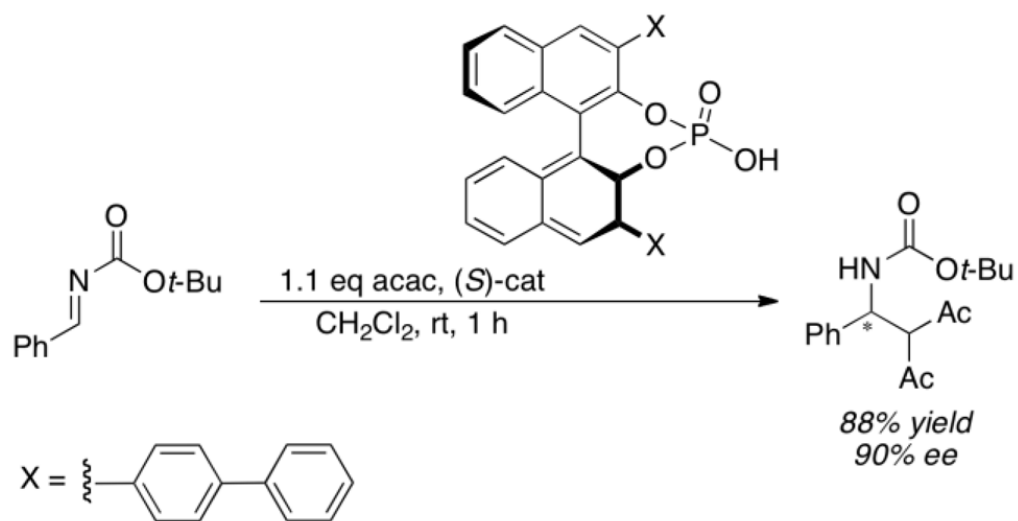
B3LYP/6-31G(d) ΔH^\ddagger for the uncatalyzed and alcohol-catalyzed Diels-Alder reaction with Rawal-type dienes



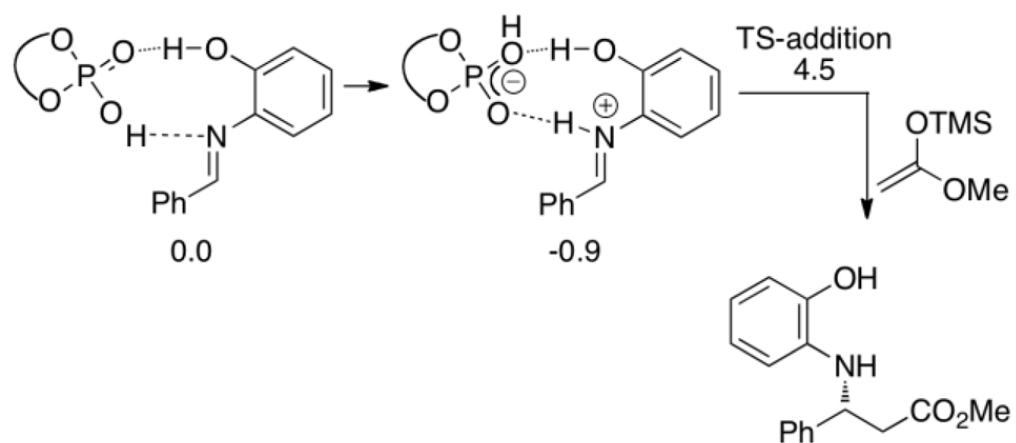
Scheme 124.
Catalysis of the S_N2 reaction by 1,4-benzenedimethanol

**Scheme 125.**

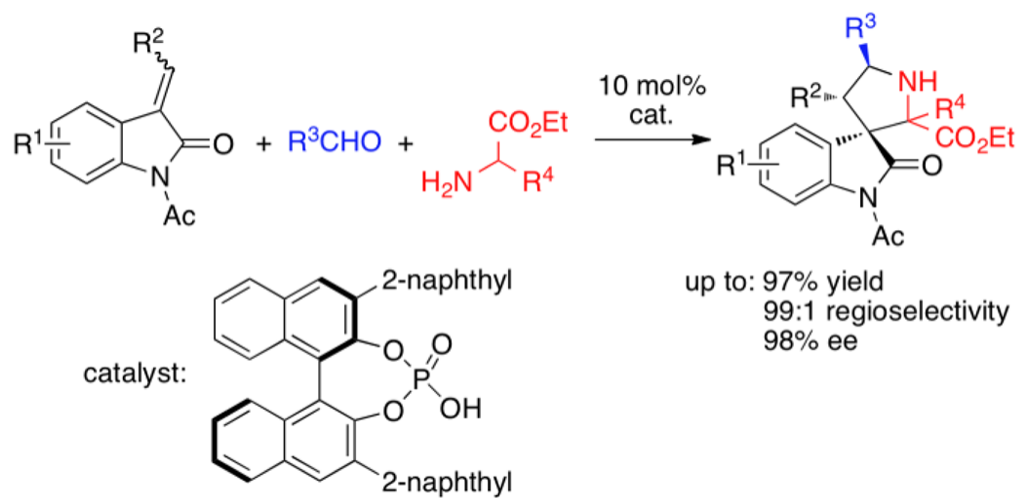
ONIOM[CCSD(T)/6-311+G(2df,2p):MP2/6-31+G(d)] free energy activation barriers for reaction of F^- with 3-chlorobutane. DMSO solvation by HF(PCM)/6-31+G(d)



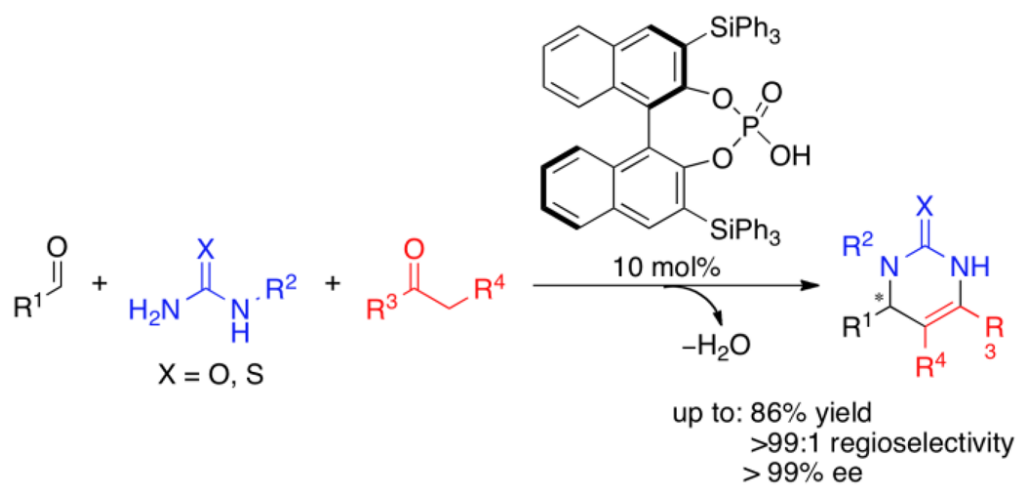
Scheme 126.
Phosphoric acid catalyzed Mannich reaction²¹²

**Scheme 127.**

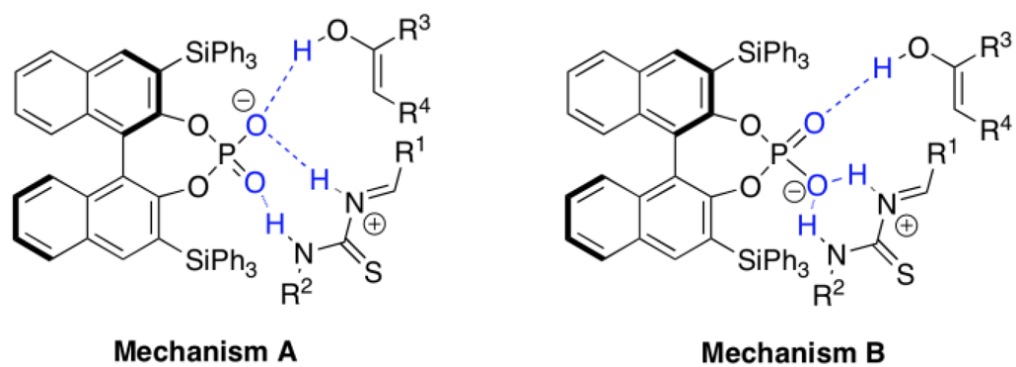
Chiral phosphoric acid catalyzed addition of silyl enolate to aldimine.

**Scheme 128.**

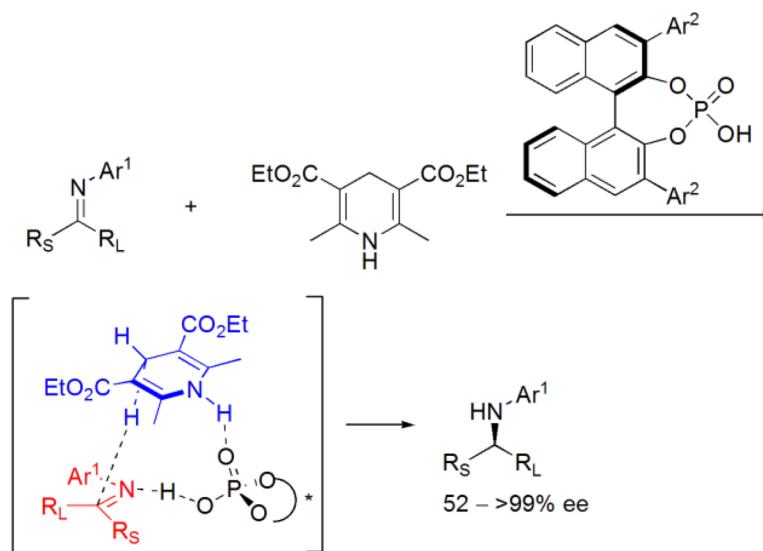
Chiral phosphoric acid catalyzed 1,3-dipolar cycloaddition



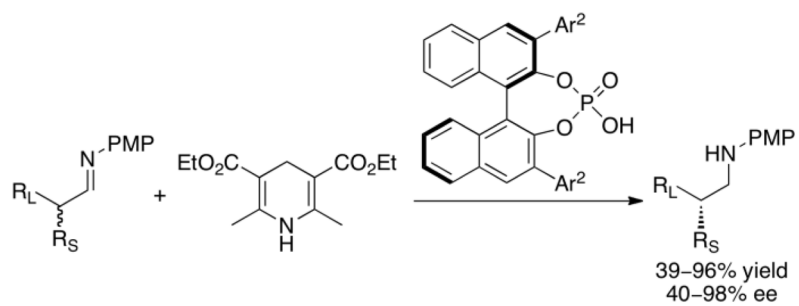
Scheme 129.
Chiral phosphoric acid catalyzed Biginelli reaction

**Scheme 130.**

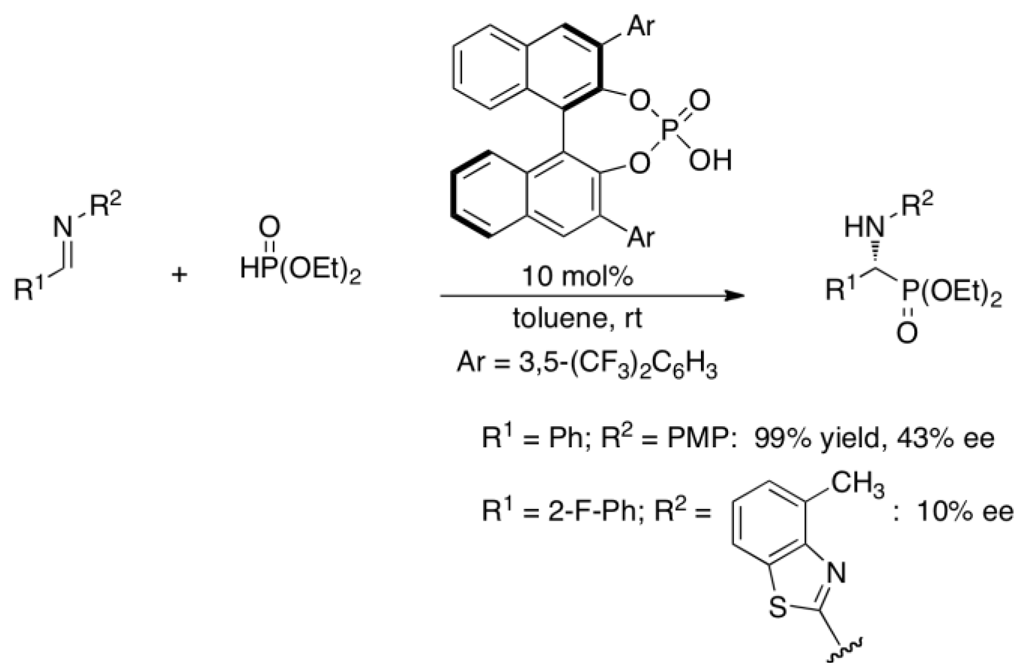
Proposed activation mechanisms for organocatalyzed Biginelli reaction



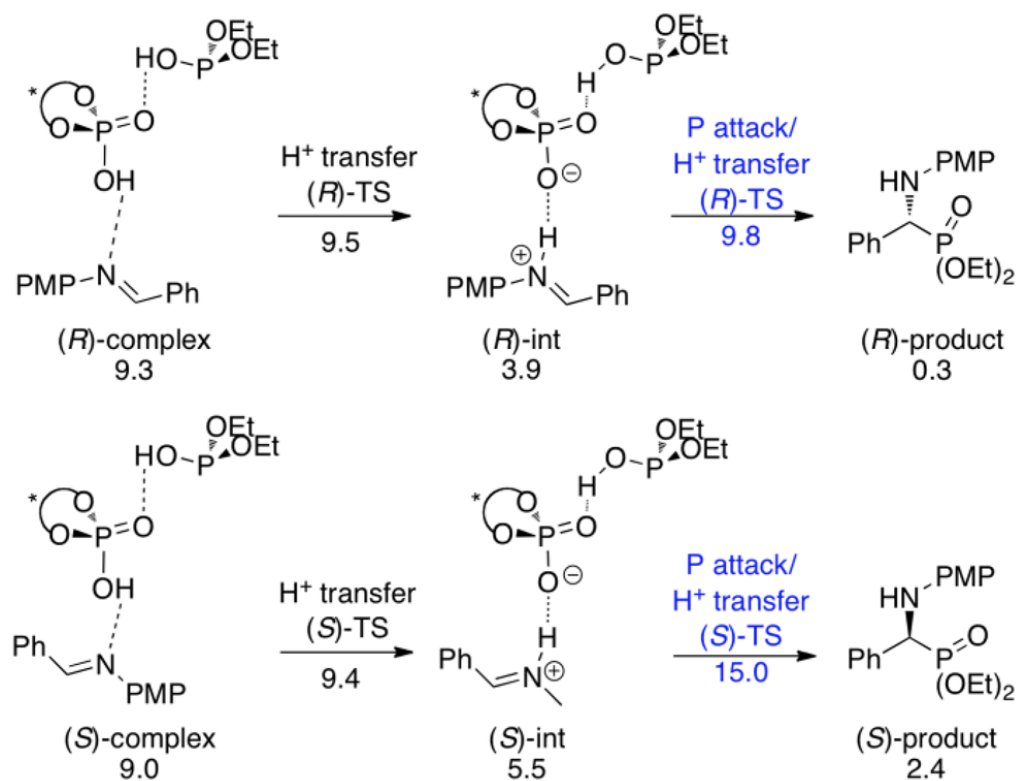
Scheme 131.
Chiral phosphoric acid catalyzed imine hydrogenation by Hantzsch ester



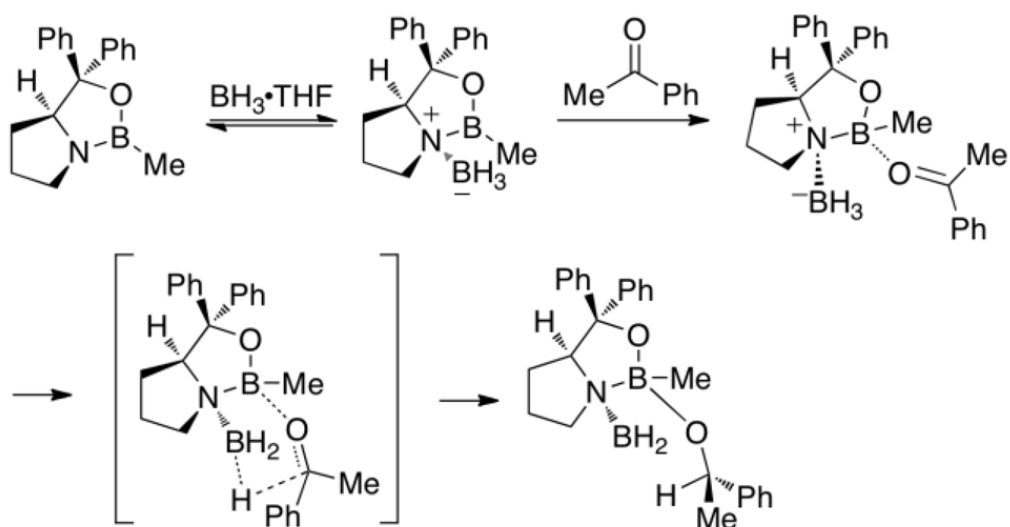
Scheme 132.
Organocatalyzed kinetic resolution of α -branched imines

**Scheme 133.**

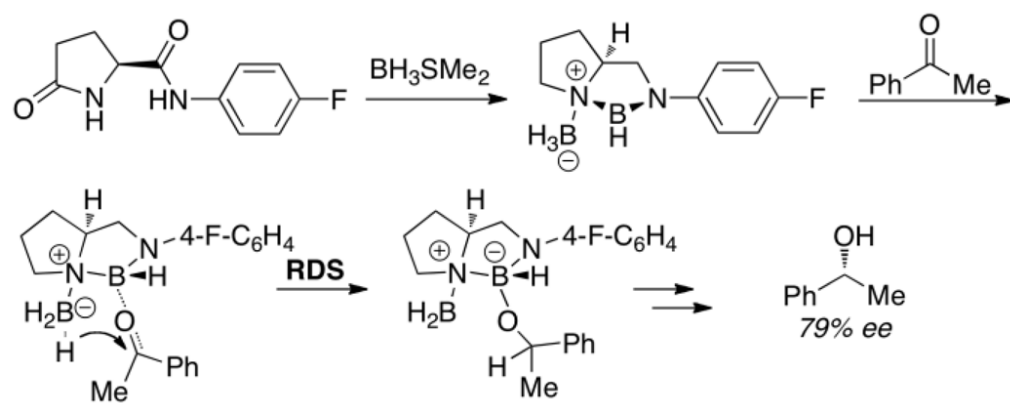
Imine hydrophosphonylation catalyzed by chiral phosphoric acid

**Scheme 134.**

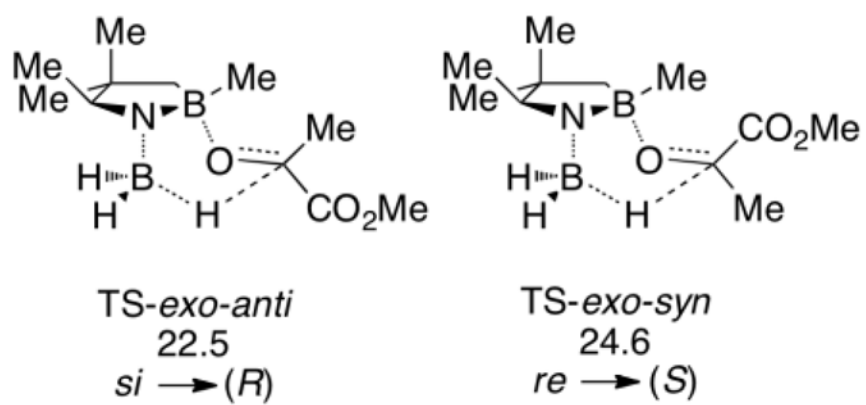
Mechanism of chiral phosphoric acid catalyzed hydrophosphinylation mechanism

**Scheme 135.**

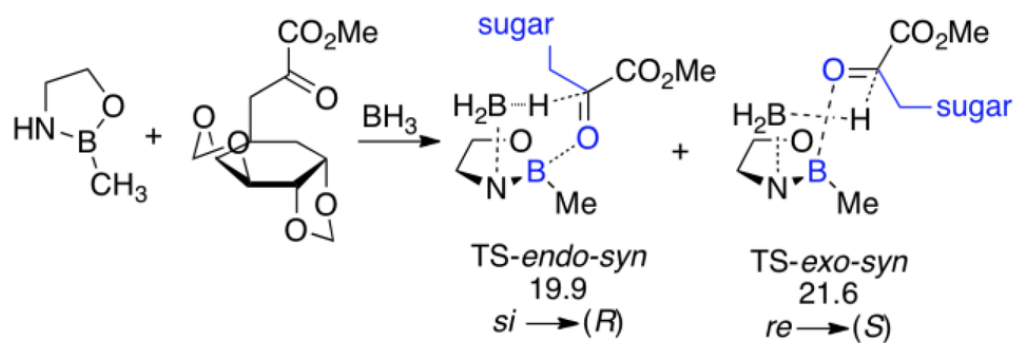
Mechanism of oxazaborolidine-catalyzed reduction of acetophenone proposed by Corey

**Scheme 136.**

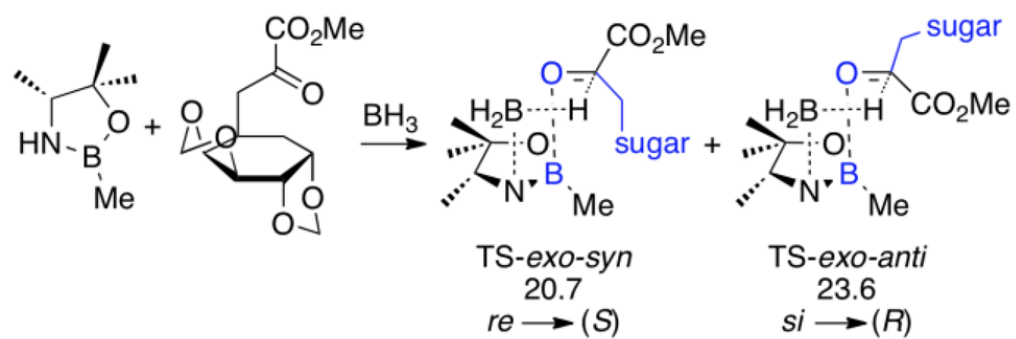
Oxazaborolidine catalyzed reduction of acetophenone



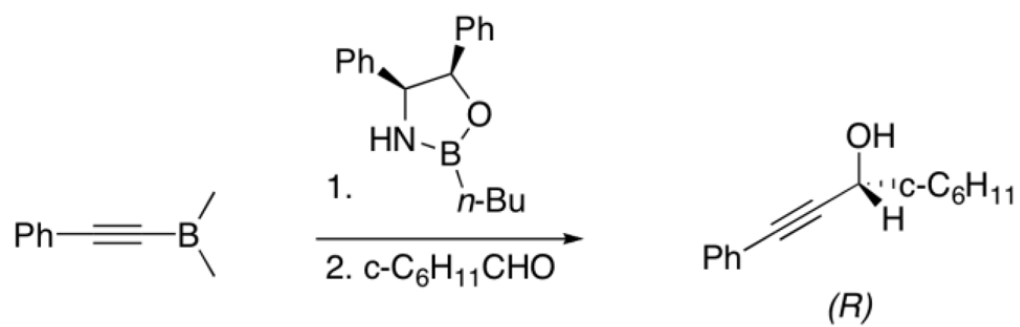
Scheme 137.
B3LYP/6-31G(d) ΔG^\ddagger for hydride transfer

**Scheme 138.**

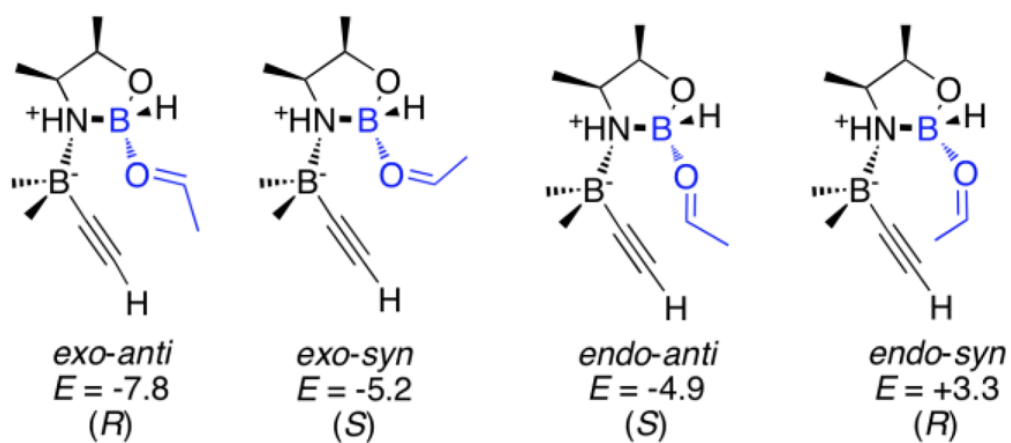
B3LYP/6-31G(d) ΔG^\ddagger for hydride transfer to chiral sugar by achiral catalyst

**Scheme 139.**

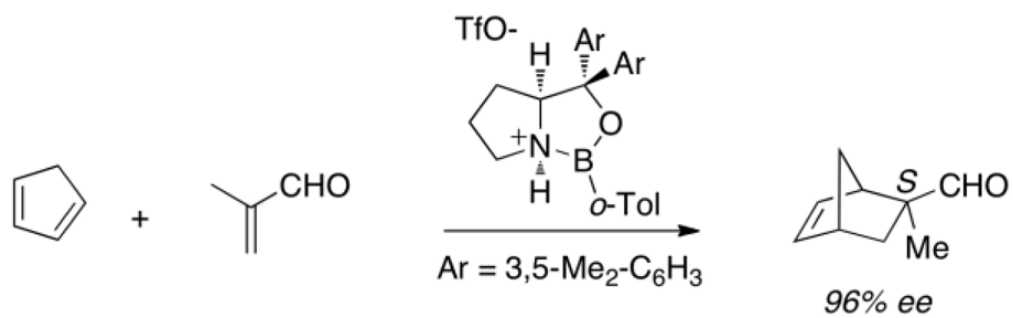
B3LYP/6-31G(d) ΔG^\ddagger for hydride transfer from mismatched catalyst to α -ketoester



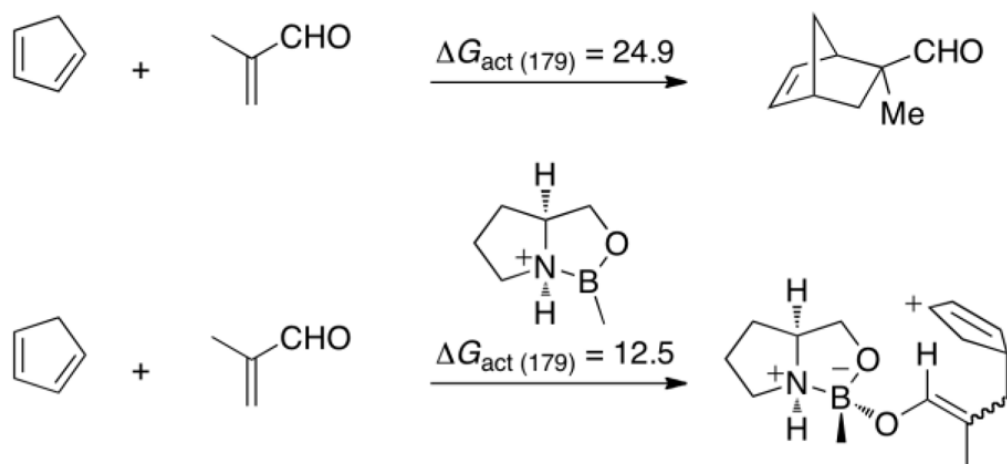
Scheme 140.
Oxazaborolidine-catalyzed alkyne-aldol reaction developed by Corey

**Scheme 141.**

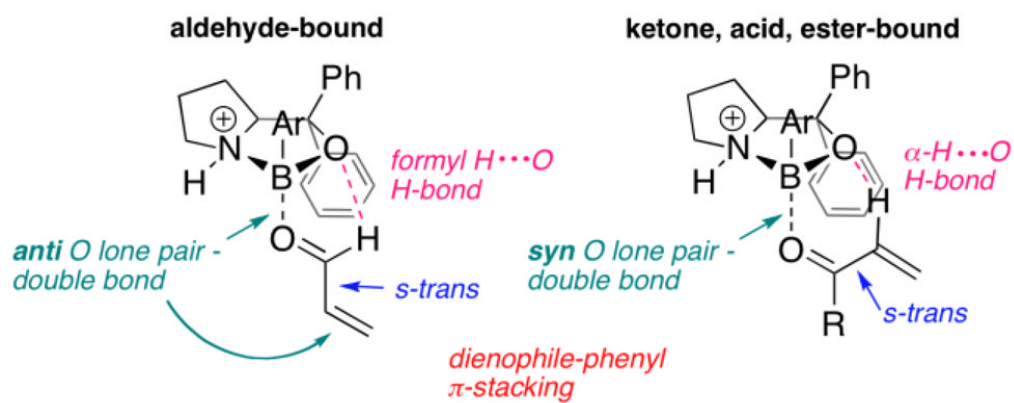
Binding energies of ethanal with catalyst-borane complexes

**Scheme 142.**

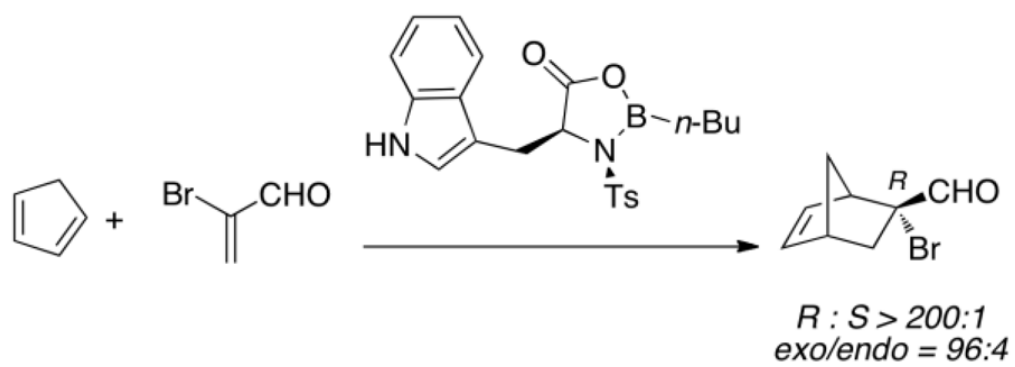
Oxazaborolidine catalyzed Diels-Alder cycloaddition between cyclopentadiene and 2-methylacrolein

**Scheme 143.**

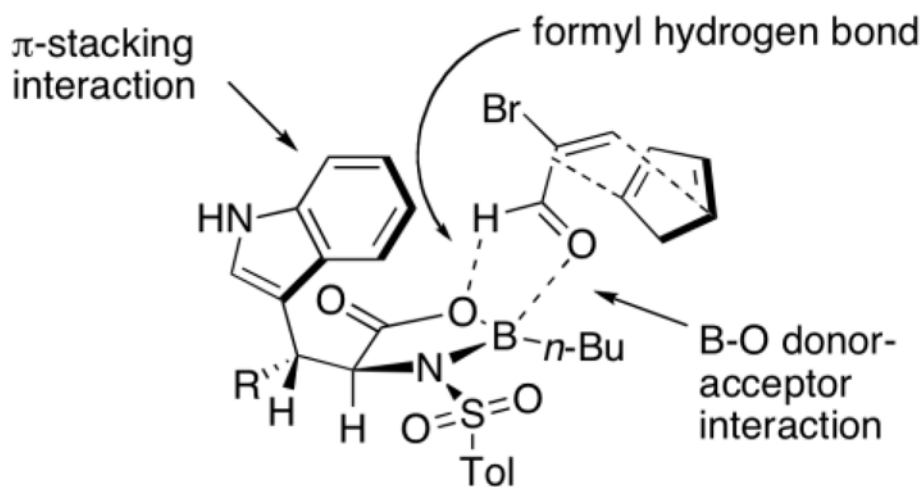
Uncatalyzed and catalyzed Diels-Alder cycloaddition between cyclopentadiene and 2-methylacrolein

**Scheme 144.**

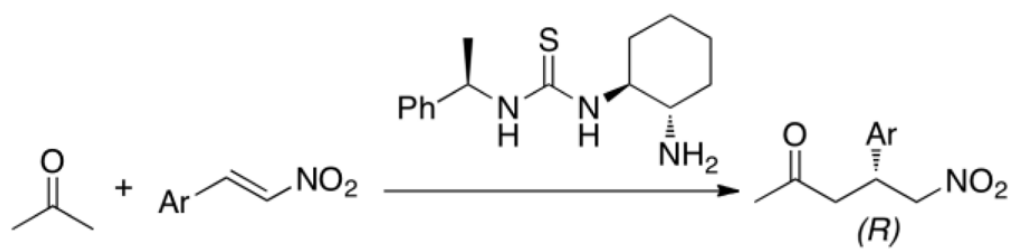
Corey's pre-transition state models for the oxazaborolidine-catalyzed Diels-Alder cycloaddition reaction

**Scheme 145.**

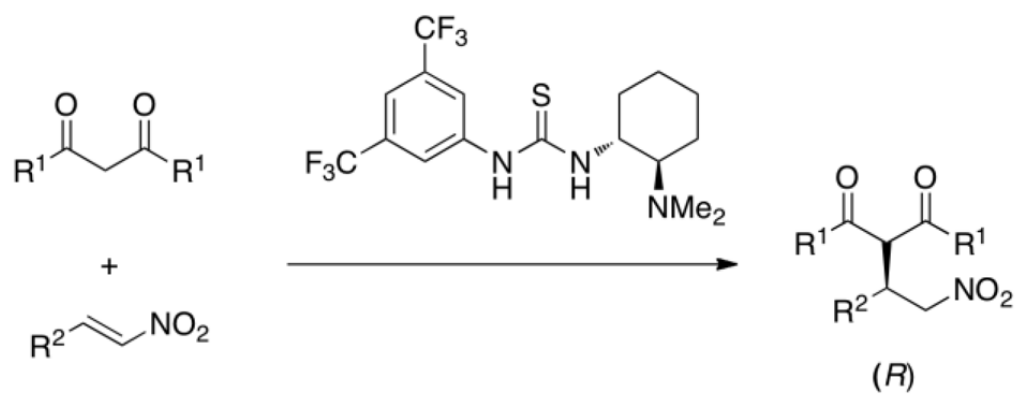
Diels-Alder cycloaddition of cyclopentadiene with bromoacrolein, catalyzed by oxazaborolidine

**Scheme 146.**

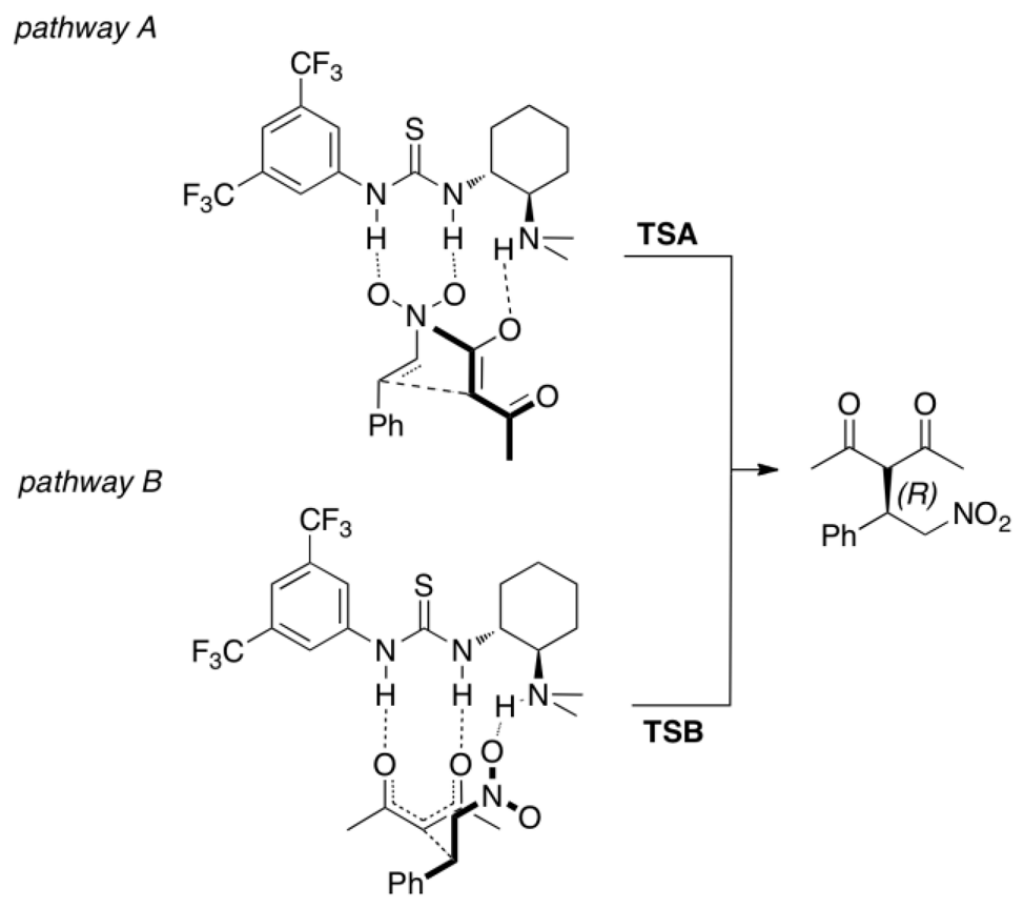
Corey's proposed model of transition state assembly involving *s-cis* bromoacrolein



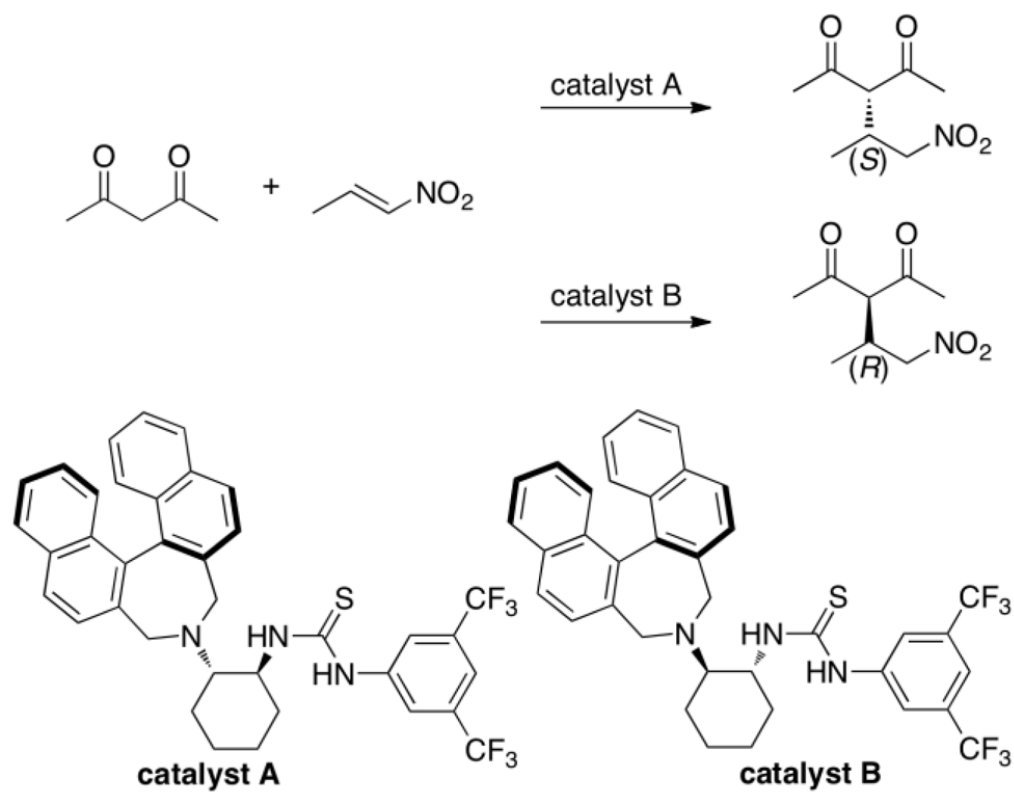
Scheme 147.
Conjugate addition of acetone to nitro-olefins

**Scheme 148.**

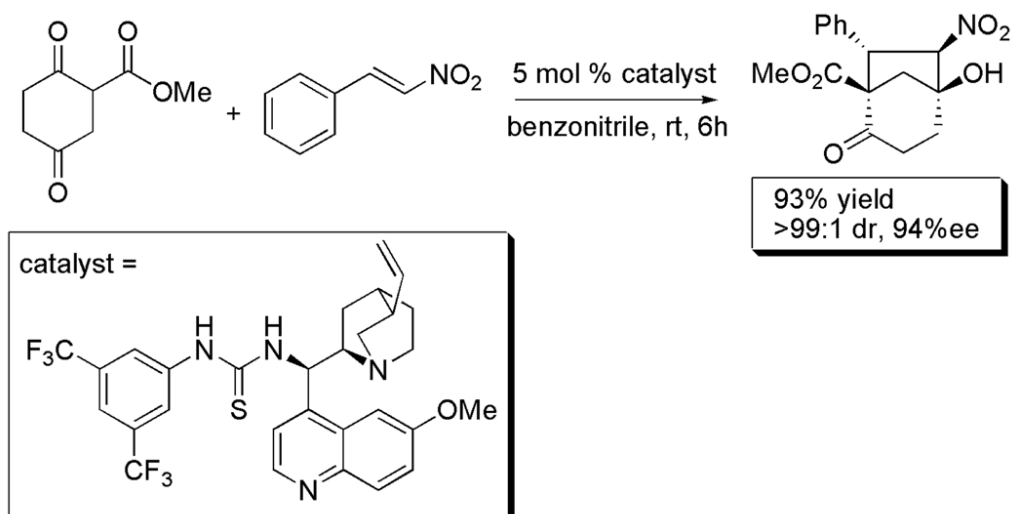
Enantioselective Michael addition of 1,3-dicarbonyls to nitro-olefins



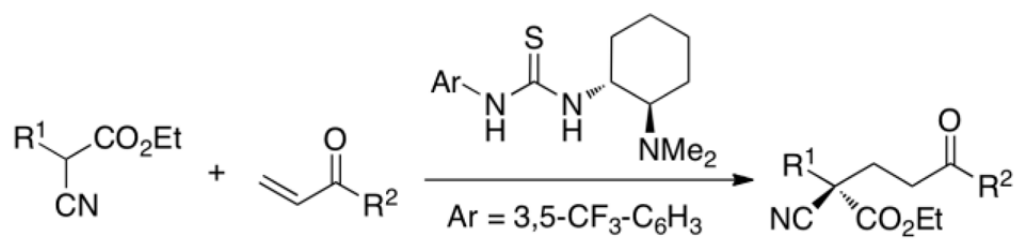
Scheme 149.
Two reaction routes envisioned for the catalyzed Michael addition of acetylacetone to nitrostyrene



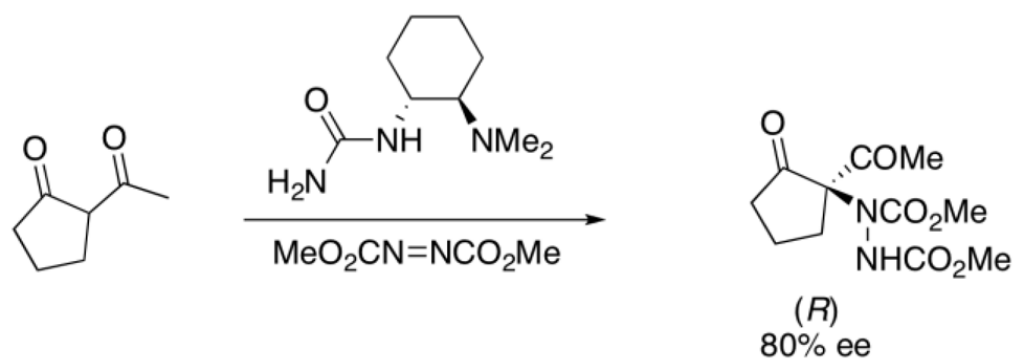
Scheme 150. Bifunctional thiourea-based organocatalyst in the Michael addition of 2,4-pentanedione to 1-nitropropene

**Scheme 151.**

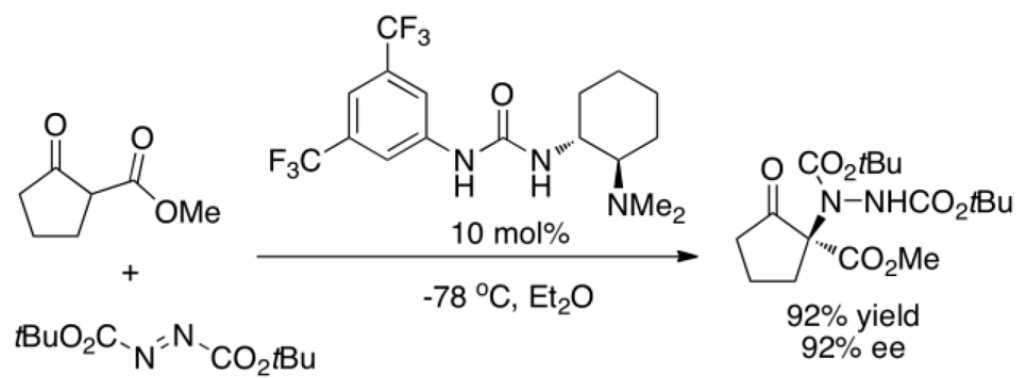
Organocatalytic domino Michael-Henry reactions of trisubstituted carbon nucleophiles and *trans*- β -nitrosostyrene

**Scheme 152.**

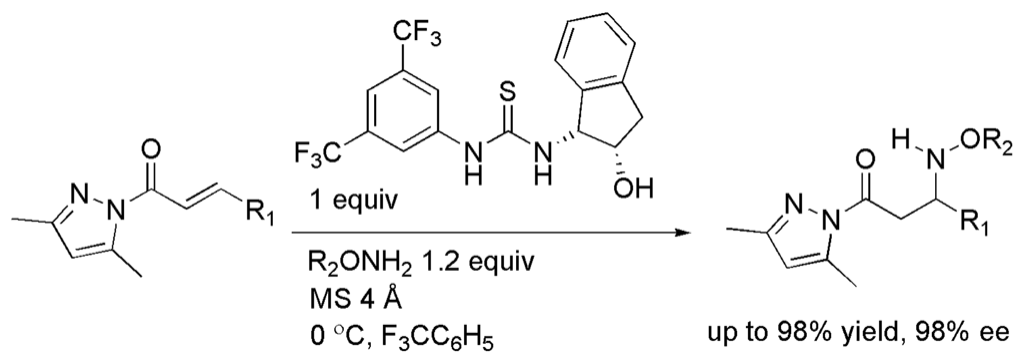
Asymmetric Michael addition of α -aryl and α -alkyl cyanoacetates to vinyl ketone.



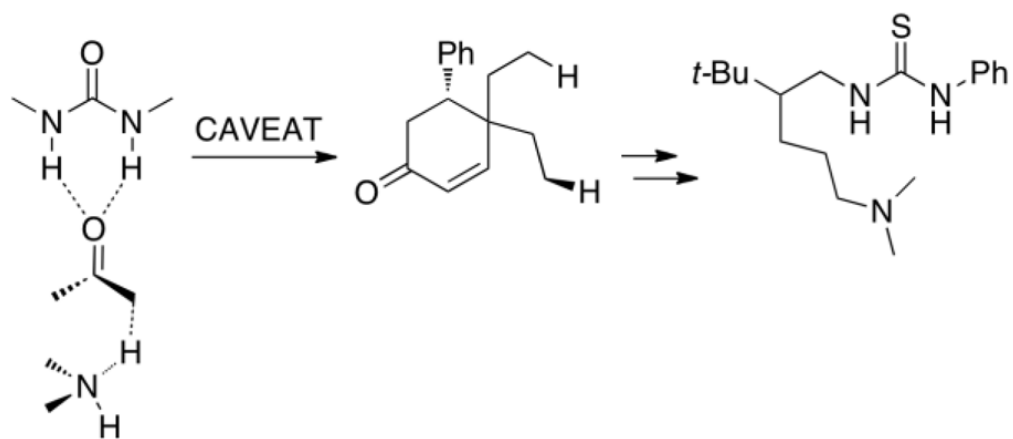
Scheme 153.
Bifunctional urea catalyzed α -amination



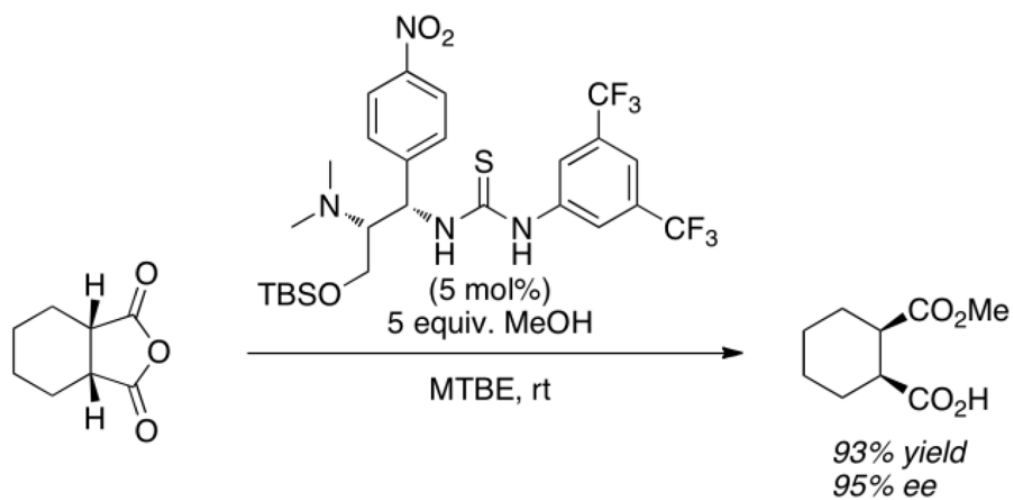
Scheme 154.
 α -amination reaction reported by Takemoto



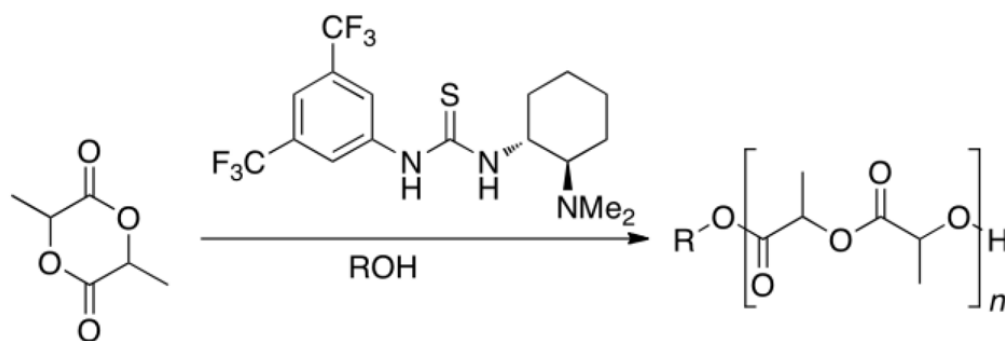
Scheme 155.
Conjugate amine additions to pyrazole crotonate derivatives



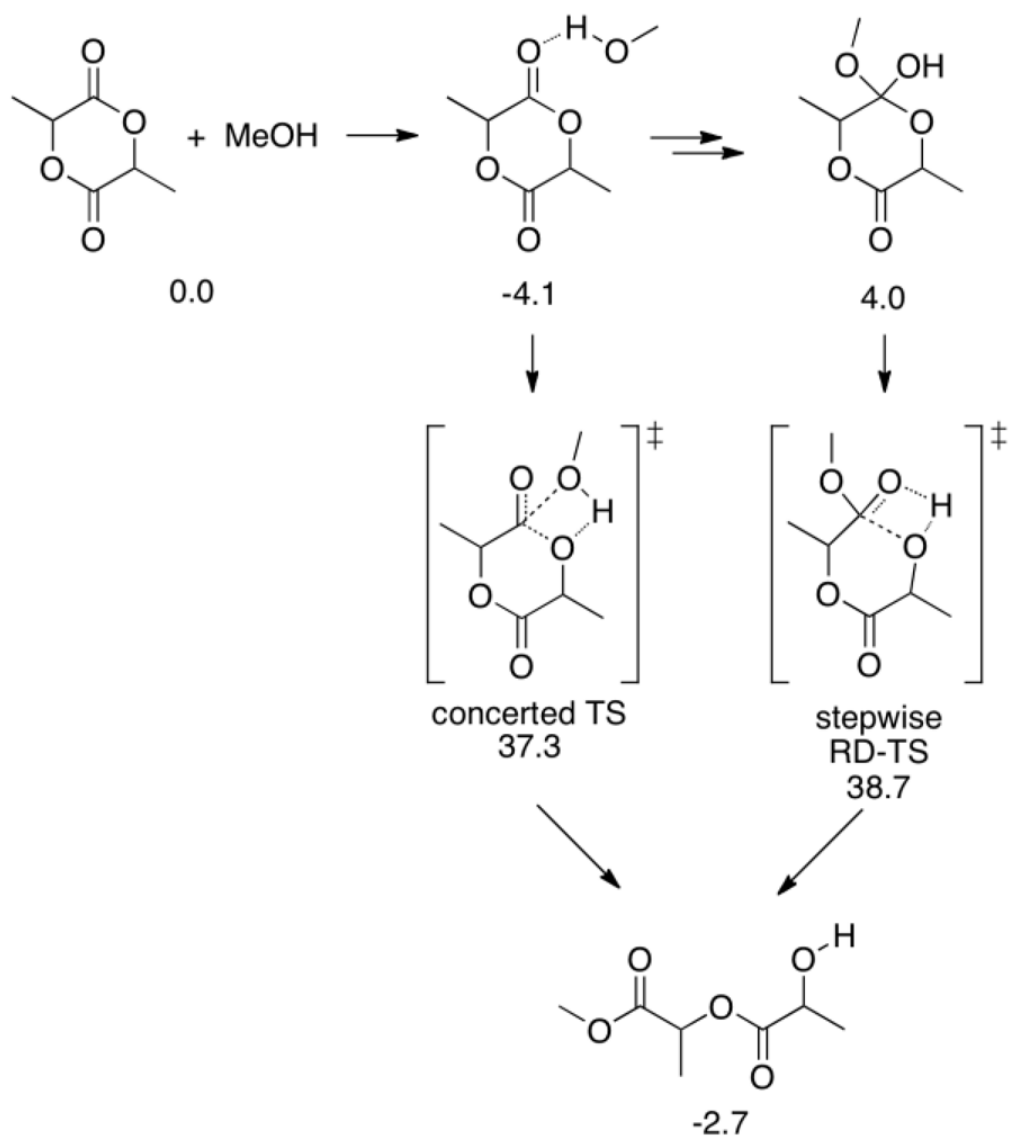
Scheme 156.
Design of bifunctional catalyst



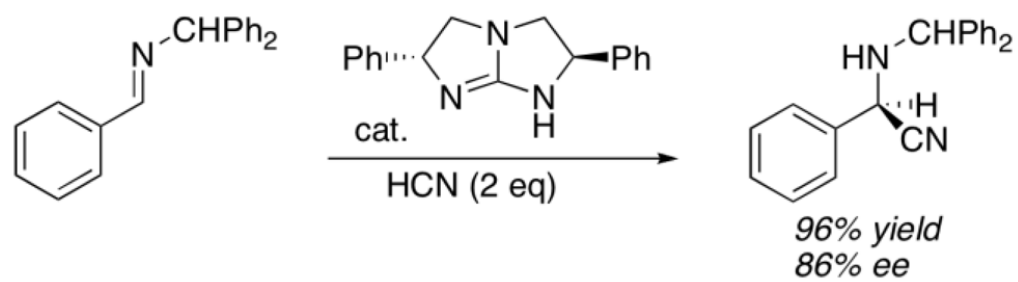
Scheme 157.
Bifunctional thiourea catalyzed *meso*-anhydride alcoholysis

**Scheme 158.**

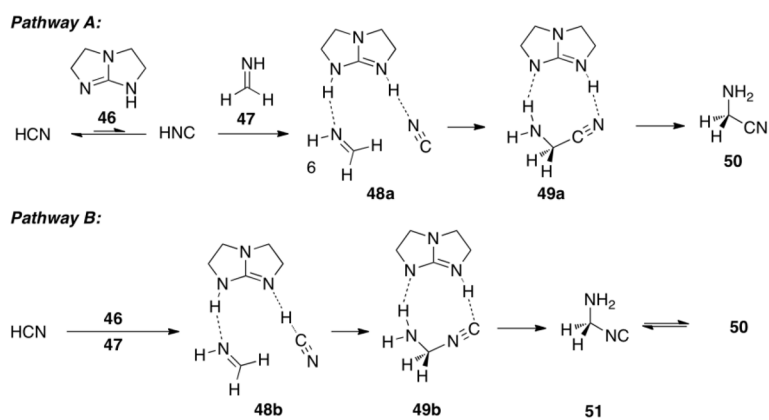
Bifunctional thiourea organocatalyzed ring-opening polymerization of D-lactide



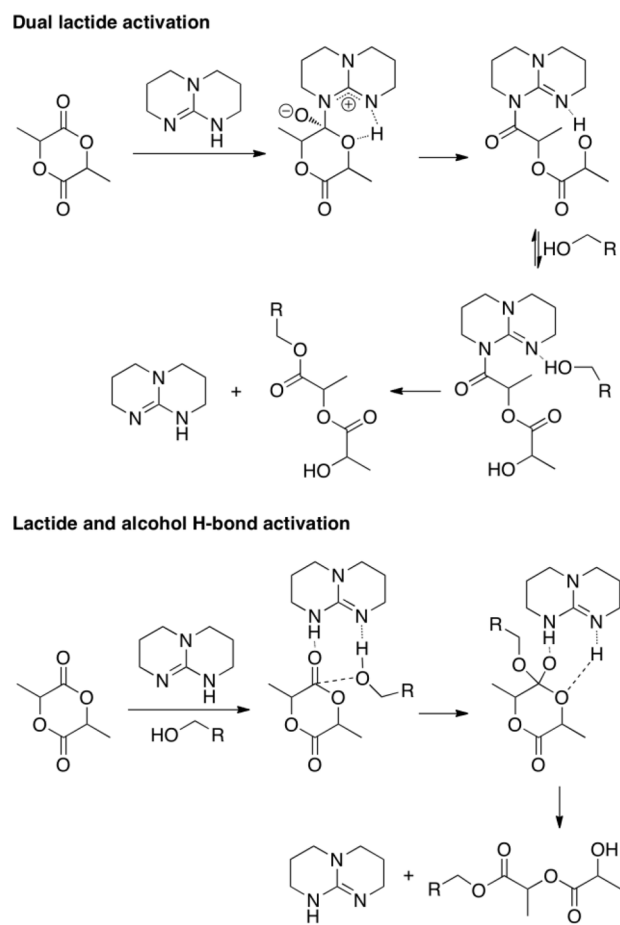
Scheme 159.
Relative energies for the uncatalyzed reaction



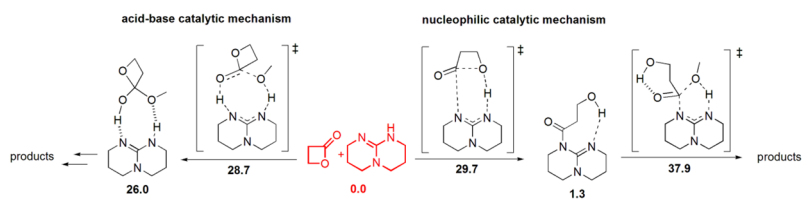
Scheme 160.
Guanidine catalyzed Strecker reaction



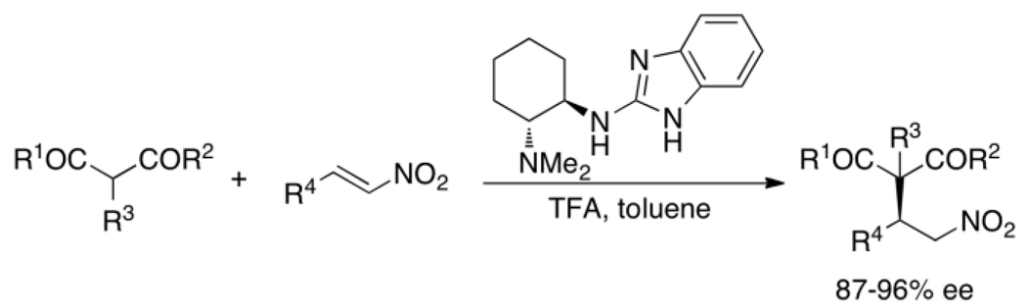
Scheme 161.
Possible pathways for the guanidine-catalyzed Strecker reaction

**Scheme 162.**

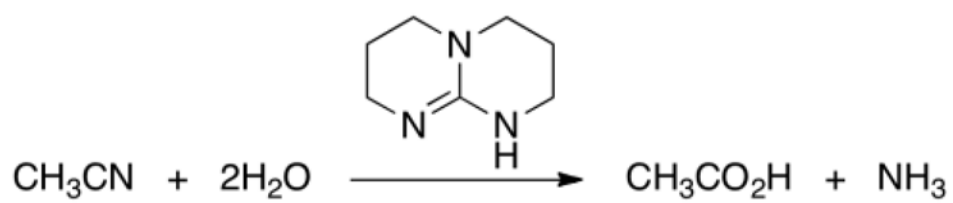
Two proposed mechanisms for the organocatalyzed ring-opening polymerization of L-lactide

**Scheme 163.**

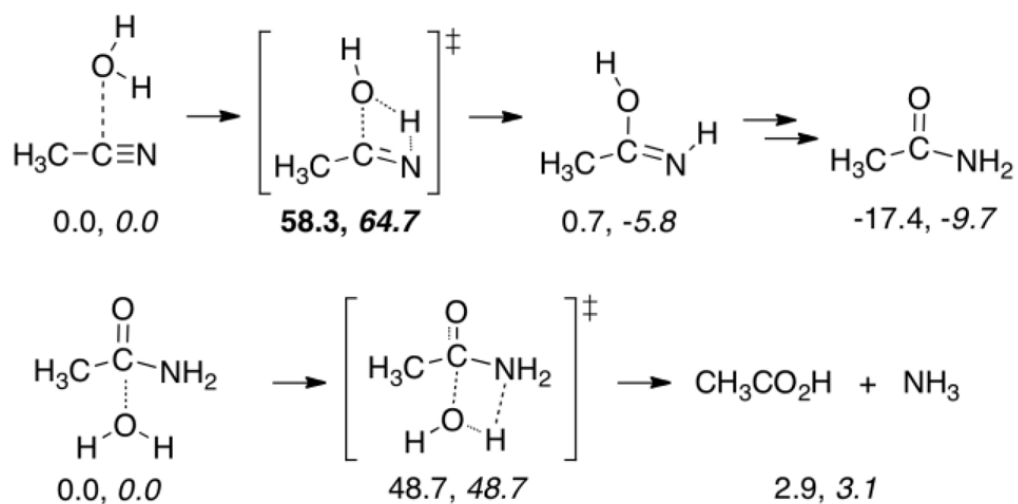
Competing reaction pathways in the ring-opening polymerization of butyrolactone catalyzed by TBD. B3LYP/6-311++G(d, p)//B3LYP/6-31+G(d) computed relative free energies are given in kcal/mol

**Scheme 164.**

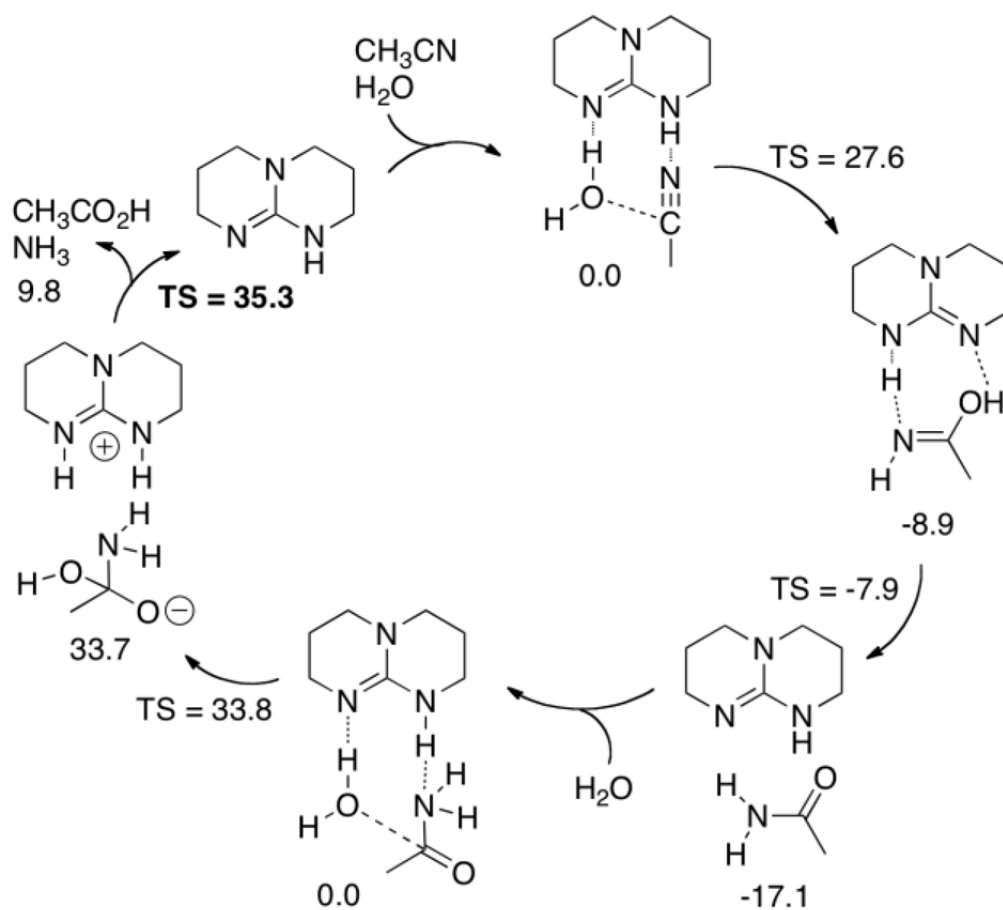
Trans-cyclohexanediamine-benzimidazole catalyzed conjugated addition reaction



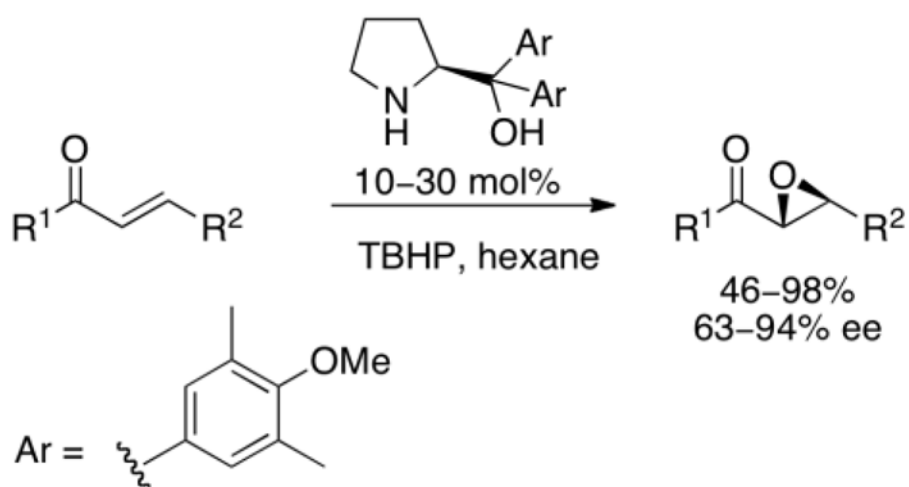
Scheme 165.
Organocatalyzed hydrolysis of acetonitrile

**Scheme 166.**

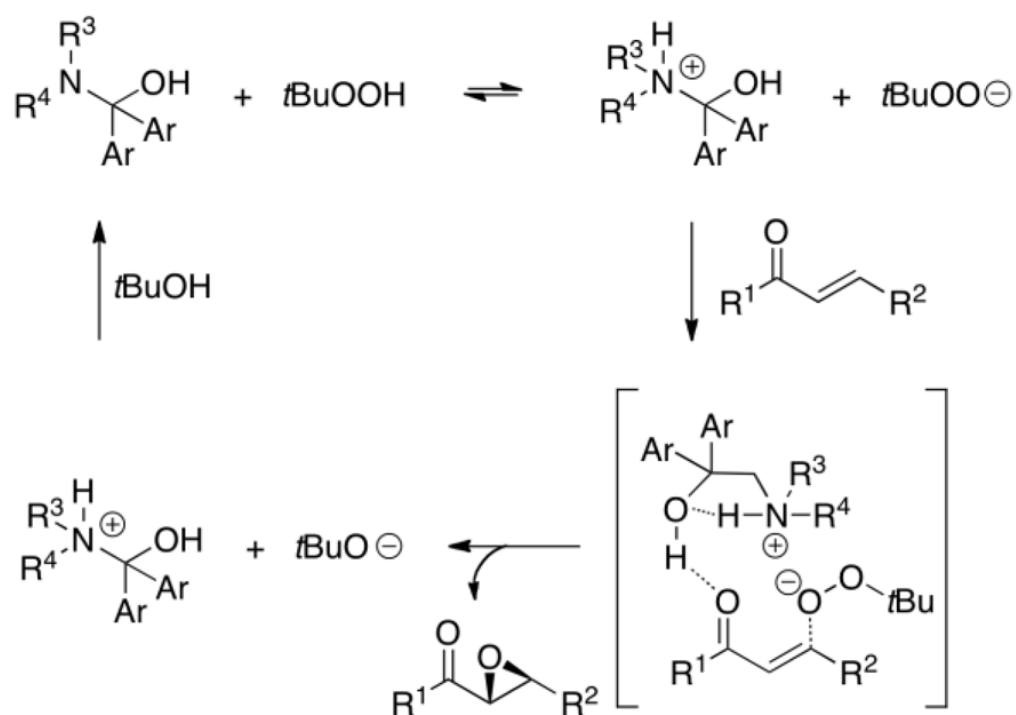
Uncatalyzed acetonitrile hydrolysis; B3LYP/6-311++G(d, p) energies, MP2/6-311++G(d, p) values in italics; rate-determining step in bold



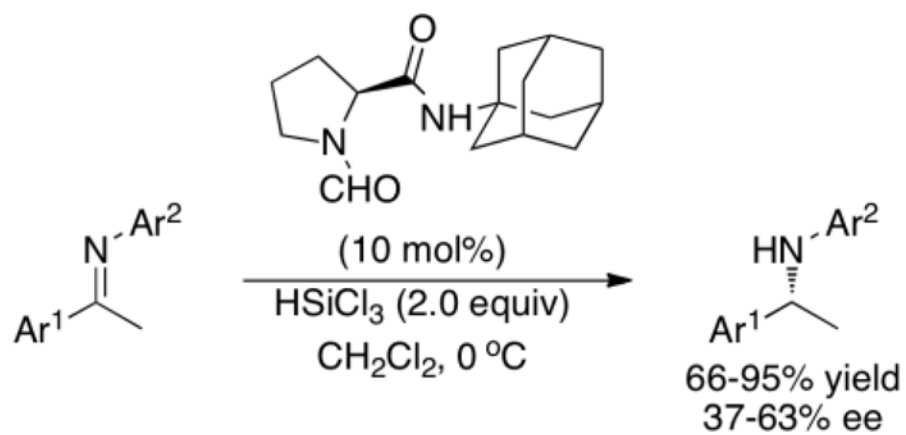
Scheme 167.
 B3LYP/6-311++G(d, p) energy profile for catalyzed reaction; rate-determining step in bold



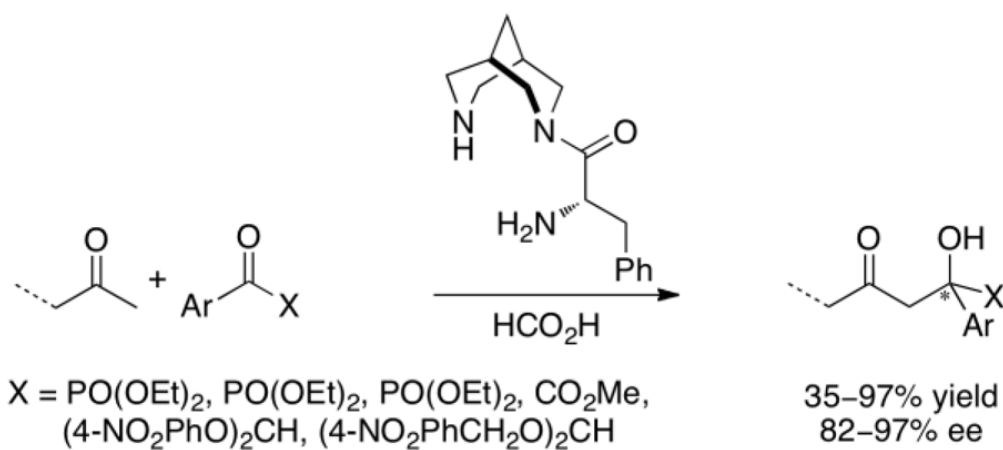
Scheme 168.
Diarylprolinol catalyzed asymmetric epoxidation



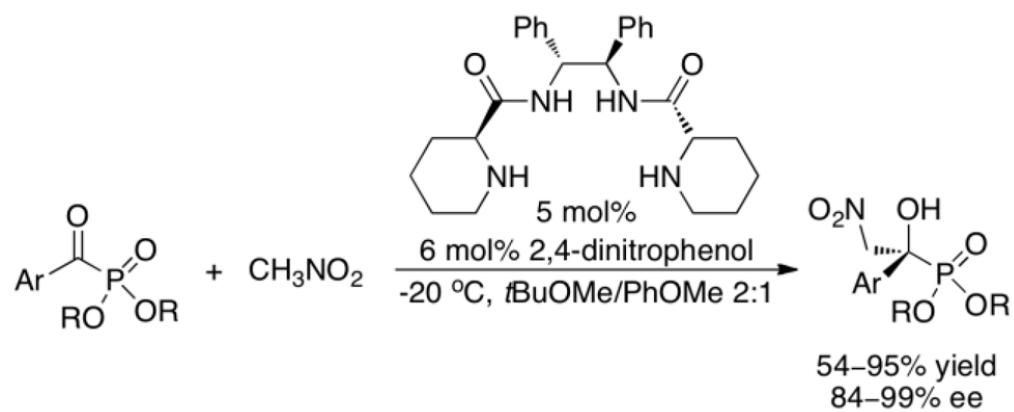
Scheme 169.
Mechanism for organocatalyzed epoxidation of α,β -unsaturated ketones by *tert*-butyl hydroperoxide

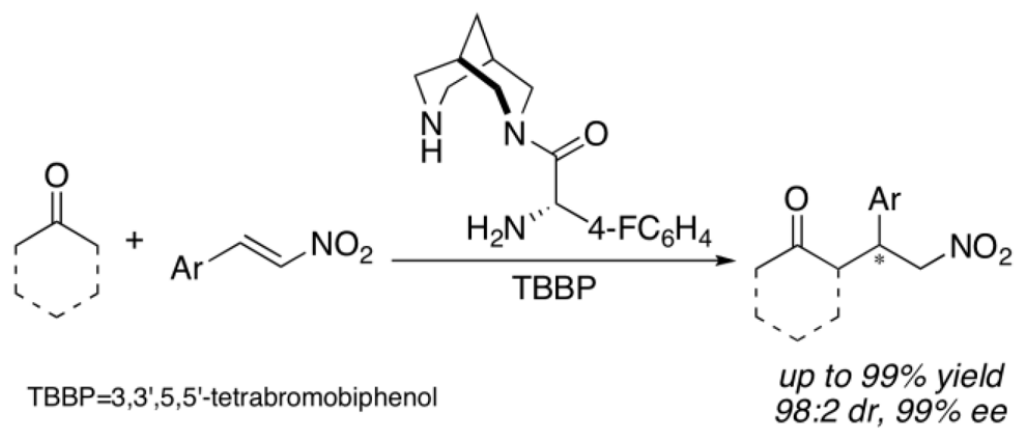
**Scheme 170.**

Organocatalyzed asymmetric transfer hydrogenation with trichlorosilane

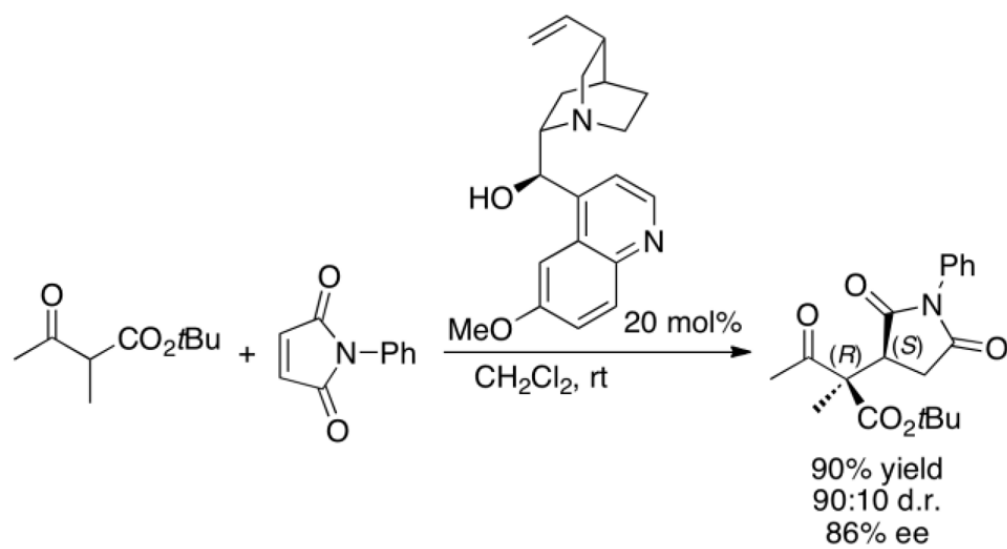


Scheme 171.
Bispidine catalyzed aldol reaction

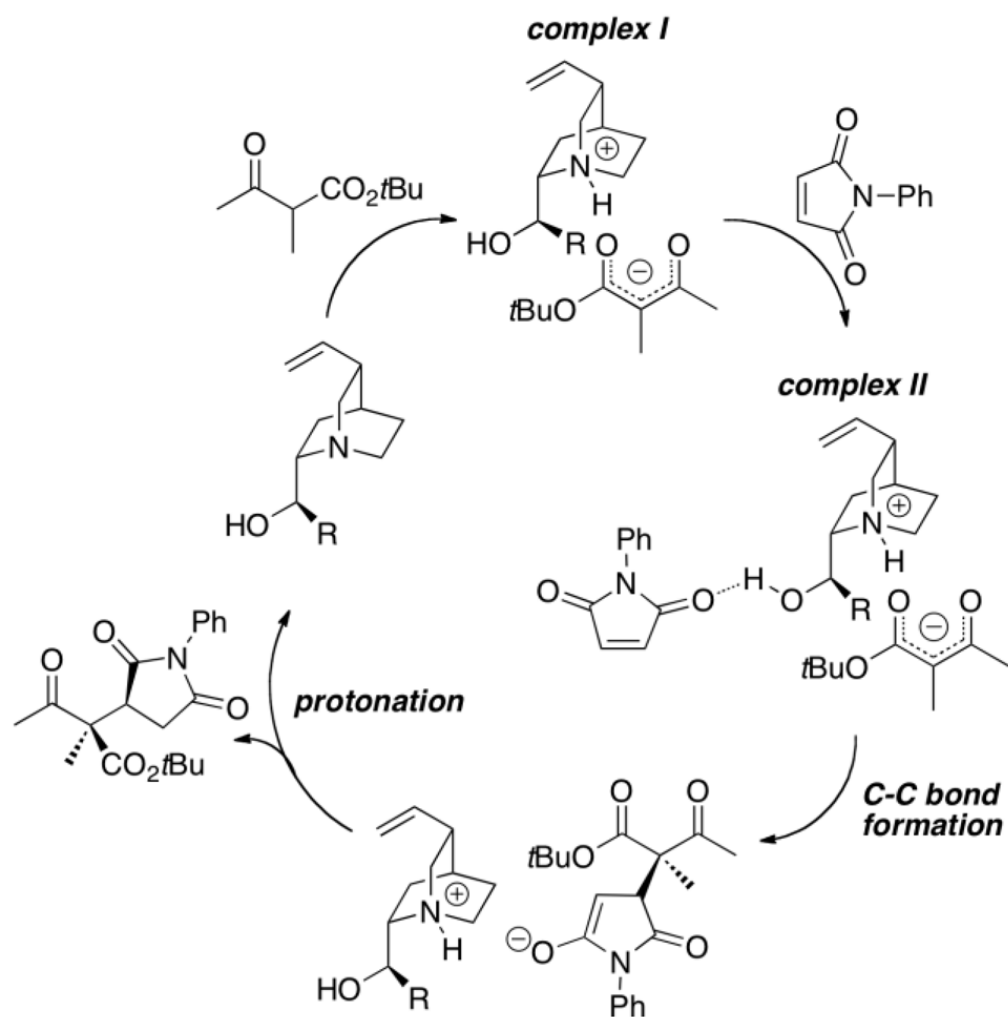
**Scheme 172.**Asymmetric nitroaldol reaction of α -ketophosphonates



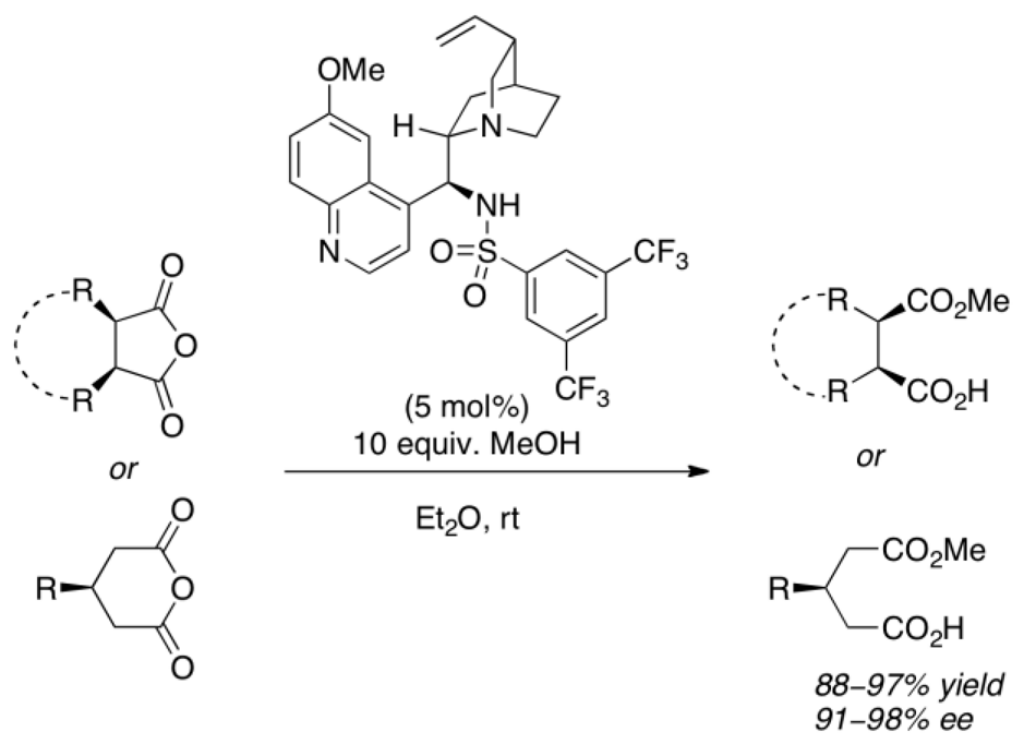
Scheme 173.
Bispidine-catalyzed Michael addition reaction



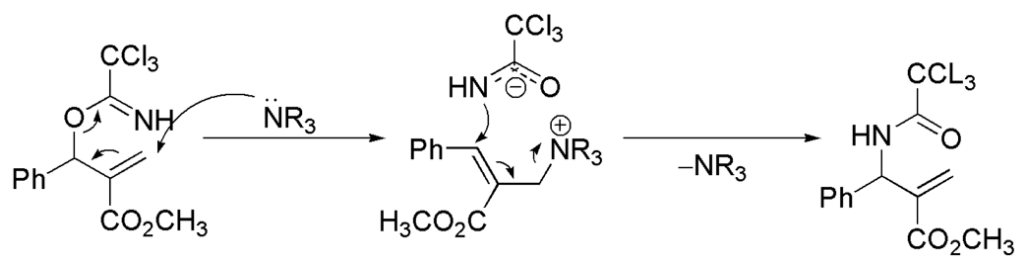
Scheme 174.
Bifunctional cinchona catalyzed Michael addition



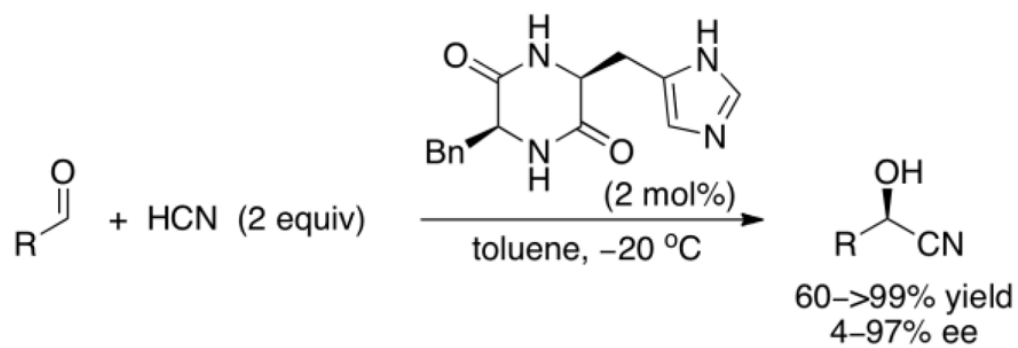
Scheme 175.
Catalytic cycle for Michael addition



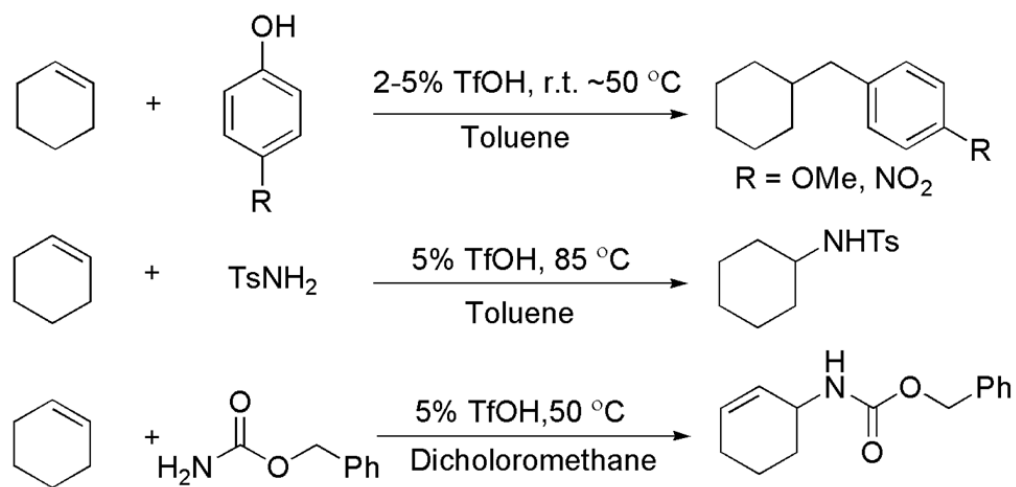
Scheme 176.
Bifunctional catalysis of *meso*-cyclic anhydride desymmetrization



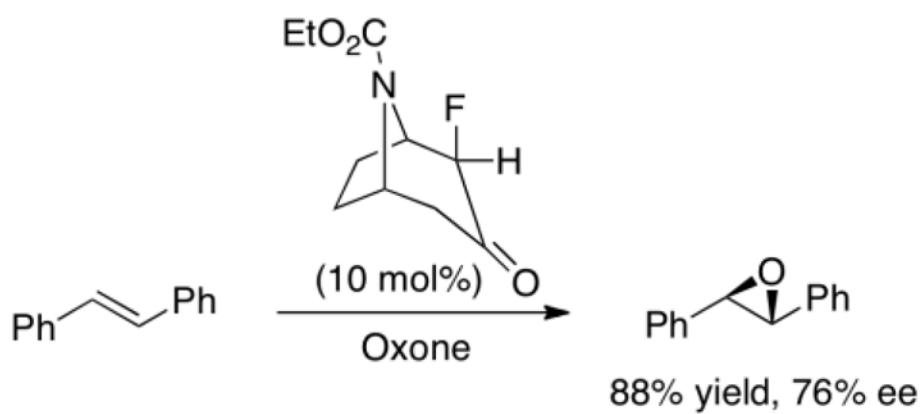
Scheme 177.
Mechanism of cinchona catalyzed [1,3]-shifts of allylic trichloroacetimidates



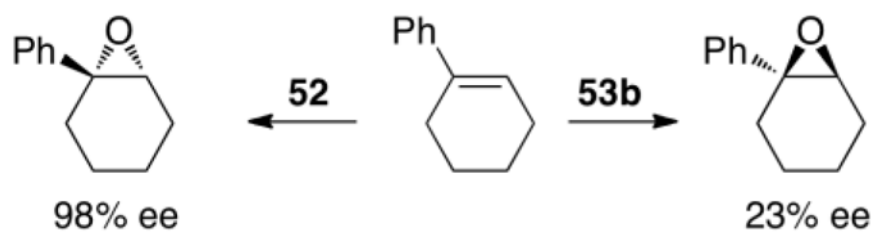
Scheme 178.
Dipeptide-catalyzed aldehyde hydrocyanation

**Scheme 179.**

TfOH-catalyzed addition of phenols and amides to alkenes



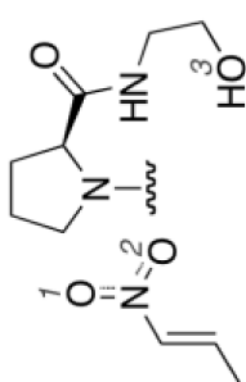
Scheme 180.
Epoxidation of (*E*)-stilbene



Scheme 181.
Selectivity of epoxidation of 1-phenyl-cyclohexene

Table 1

B3LYP/6-31G(d) activation energies (kcal/mol)



TS	E_{act}	Forming C ^{...} C	NH ^{...} O1	O3H ^{...} O1	NH ^{...} O2	O3H ^{...} O2
TS <i>anti, re</i>	15.0	2.13	2.03	1.89	2.59	2.72
TS <i>anti, si</i>	16.4	2.10	2.11	2.85	2.56	2.09
TS <i>syn, re</i>	18.2	2.01	-	-	-	-
TS <i>syn, si</i>	27.6	1.95	-	-	-	-

Table 2

Activation free energies^a (ΔG , kcal/mol) for the formation of enamine intermediate by the reaction of pyrrolidine and propanal, formation of the iminium ion by the reaction of pyrrolidine and MVK and for the C-C bond formation through various plausible pathways

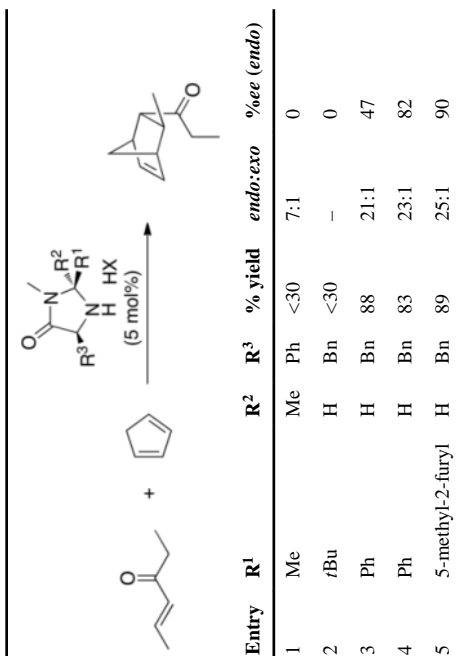
Enamine Formation		Iminium Ion Formation		C-C bond formation			
Addition	Dehydration	Addition	Dehydration	Pathway1	Pathway2	Pathway3	Pathway4
36.5 (17.0) ^b	49.0 (24.6) ^b	42.8 (24.2) ^b	--- (30.9) ^b	88.9	26.1	69.9	25.5

^a With respect to the separated reactants, computed with PCM(THF)/mPW1P91/6-311G(d, p)//6-31G(d) level of theory.

^b Activation free energies for phenol assisted enamine and iminium ion formation are given in parenthesis.

Table 3

Results of imidazolidinone-catalyzed Diels-Alder cycloaddition reactions



Entry	R ¹	R ²	R ³	% yield	endo:exo	%ee (endo)
1	Me	Me	Ph	<30	7:1	0
2	<i>t</i> Bu	H	Bn	<30	–	0
3	Ph	H	Bn	88	21:1	47
4	Ph	H	Bn	83	23:1	82
5	5-methyl-2-furyl	H	Bn	89	25:1	90

Table 4

Reaction enthalpies (kcal/mol) of the competing steps in the esterification of α,β unsaturated aldehydes catalyzed by *N*-heterocyclic carbenes

entry	solvent	ΔH_1	ΔH_2	ΔH_3	exp. saturated:oxidized
1	MeOH	-13.2	6.1	3.7	1:12
2	CH ₂ Cl ₂	-8.7	2.3	13.7	2:1

Table 5

Calculated reaction enthalpy (kcal/mol) and relative rate constants for uncatalyzed and catalyzed acyl transfer reactions

R	ΔH_{rxn} (G3(MP2)B3)	k_{rel} (uncatalyzed)	k_{rel} (catalyzed)
CH ₃	-15.1	526	8025
CH ₂ CH ₃	-14.6	103	4543
CH(CH ₃) ₂	-14.2	40	2852
CH ₂ CH(CH ₃) ₂	-14.4	47	963
C(CH ₃) ₃	-13.9	1	1

Table 6

MP2(FC)/6-31+G(2d, p)//B98/6-31G(d) reaction enthalpies for reaction shown in Scheme 77 and half life for acyl transfer shown in Scheme 78

entry	catalyst	ΔH_{rxn} (calculated)	$t_{1/2}$ (min)
1	pyr	0.0	–
2	DMAP	–14.7	151
3	PPY	–16.2	67
4	24	–18.1	44
5	16	–19.7	15
6	21	–20.4	18

Table 7Relative stabilities of alkyne/allene isomers at $-20\text{ }^{\circ}\text{C}$

R	X	ΔG (allene–alkyne, kcal/mol)	experimental alkyne:allene
H	Ph	-3.7	30:70
H	6-MeO-naphth-2-yl	-4.3	20:80
H	thiophen-2-yl	-3.0	61:39
H	<i>N</i> -phthalimido	-6.5	6:94

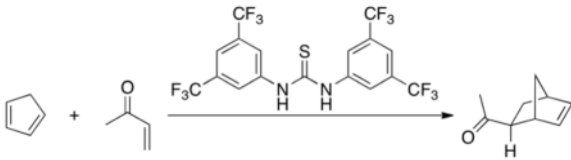
Table 8

TOF and proton affinities of amine catalysts in the Knoevenagel condensation of benzaldehyde and ethyl cyanoacetoacetate

catalyst	proton affinity (kcal/mol)	TOF (min⁻¹)
44	258.8	11.2
43	258.2	1.0
41	251.5	9.6
40	250.9	26.0
39	250.1	8.1
42	241.8	0.6
45	233.3	2.2

Table 9HF/3-21G activation energies (E_a) for the Knoevenagel condensation (with respect to reactants of each step)

catalyst	TS-deprot (kcal/mol)	TS-add (kcal/mol)	TS-prot (kcal/mol)
40	8.8	8.4	no barrier
44	22.4	8.4	4.1

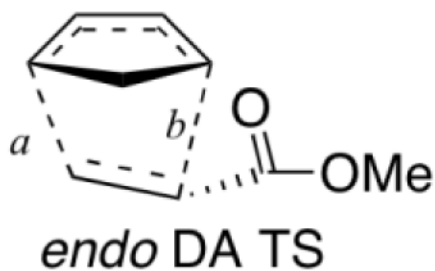
Table 10Methyl vinyl ketone and cyclopentadiene Diels-Alder cycloaddition activation barriers ^a

catalyst	activation barrier
uncatalyzed	19.0
(H ₂ O) ₂	18.5
thiourea catalyst	17.0

^aGas phase, B3LYP/6-31+G(d, p)//AM1

Table 11

Gas phase activation enthalpies^a and bond asynchronicity (b-a)^b of the Diels-Alder between cyclopentadiene and methyl vinyl ketone



	ΔH_{298}^\ddagger	b-a
uncatalyzed	17.9	0.695
thiourea-catalyzed	14.7	0.794
BF ₃ -catalyzed	6.7	1.007

^a B3LYP/6-31+G(d, p) level. Activation barriers are with respect to the catalyst-ketone complex and cyclopentadiene.

^b Bond-forming distance at vinyl carbon α to carbonyl minus bond-forming distance at terminal vinyl carbon.

Table 12

Organocatalytic nucleophilic ring opening of methyl oxirane (+/-) at room temperature

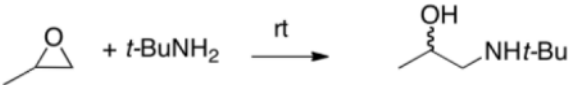
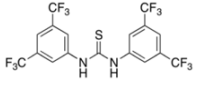
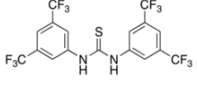
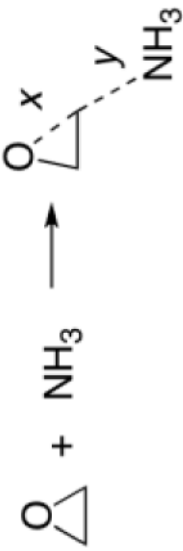
		
solvent	catalyst	% yield
CH ₂ Cl ₂	--	<0.5
CH ₂ Cl ₂		37
water	--	29
water		94

Table 13

Activation energies and bond lengths for the uncatalyzed and thiourea-catalyzed openings of oxirane by NH_3 ^a



entry	solvent	catalyst	E_{act}	x	y
1	gas	—	36.0	2.24	1.65
2	gas	$(\text{NH}_2)_2\text{CS}$	24.4	1.90	1.85
3	CH_2Cl_2	—	23.3	1.97	1.97
4	CH_2Cl_2	$(\text{NH}_2)_2\text{CS}$	17.0	1.88	2.09
5	H_2O	—	21.9	1.94	2.01
6	H_2O	$(\text{NH}_2)_2\text{CS}$	16.2	1.87	2.11

^a $\text{B3LYP/6-311++G(d, p)//B3LYP/6-31G(d)}$ level of theory (SCRF solvent inclusion).

Table 14

Organocatalyzed addition of 1,2-dimethylindole to phenyloxirane

Entry	catalyst	% yield
1		71
2		<2
3		0
4		0
5		56

Table 15

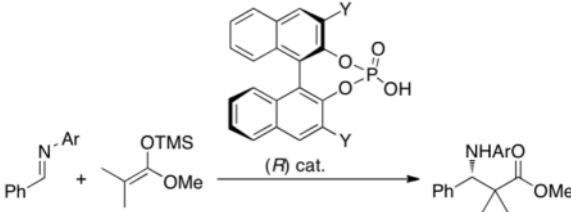
Calculated activation barriers for the nucleophilic opening of oxirane by ammonia

entry	complex	Activation Barrier	
		B3LYP ^a	MP2 ^b
1	uncatalyzed	38.8	38.8
2		14.0	20.1
3	PhOH	22.2	27.5
4	<i>p</i> -Cl-PhOH	20.8	26.7
5	<i>p</i> -CN-PhOH	19.4	25.8
6	<i>p</i> -CHO-PhOH	19.8	26.0
7	<i>p</i> -Me-PhOH	25.8	31.2
8	H ₂ O	26.2	31.9

^aB3LYP/6-31G(d).^bMP2/6-311++G(d, p)//B3LYP/6-31G(d).

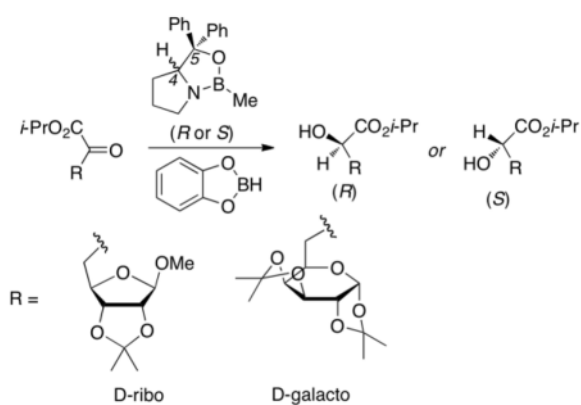
Table 16

Addition of silyl enolate to aldimines, catalyzed by chiral phosphoric acids



entry	Ar	Y	% Yield	% ee
1	2-OH-Ph	H	57	0
2	2-OH-Ph	Ph	100	27
3	2-OH-Ph	2,4,6-Me ₃ C ₆ H ₂	100	60
4	2-OH-Ph	4-MeOC ₆ H ₄	36	32
5	2-OH-Ph	4-NO ₂ C ₆ H ₄	98	89
6	4-OH-Ph	4-NO ₂ C ₆ H ₄	2	20
7	4-OMe-Ph	4-NO ₂ C ₆ H ₄	56	3
8	Ph	4-NO ₂ C ₆ H ₄	76	39

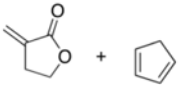
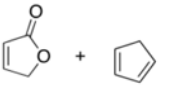
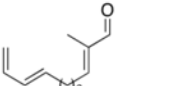
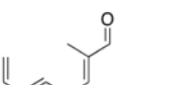
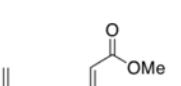
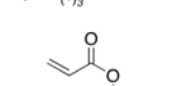
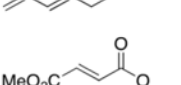
Table 17

Reduction of α -ketoesters by catecholborane

Glycosyl α -ketoester	catalyst configuration	% yield	Major product configuration	% d.e.
D-ribo	<i>S</i>	61	<i>R</i>	70
D-ribo	<i>R</i>	39	<i>S</i>	68
D-galacto	<i>S</i>	94	<i>R</i>	78
D-galacto	<i>R</i>	81	<i>S</i>	90

Table 18

Predicted^a and experimental % *ee* values

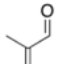

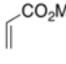
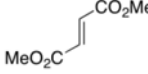
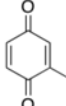
Entry	substrate	Calculated % <i>ee</i>	Experimental % <i>ee</i>
1		85	70
2		77	88
3		94	90
4		36	80
5		87	93 ^b
6		82	53
7		96	86

^aMPW1K/6-31+G(d, p)//B3LYP/6-31G(d) + B3LYP/6-31G(d) thermal corrections and nonspecific solvent effects (dichloromethane) using the PCM model. Values were calculated at 298.15K. The modeled catalyst differs from the experimental catalyst only by substitution of the *o*-tolyl group with a phenyl group.

^bThe $-\text{CO}_2\text{CH}_2\text{CF}_3$ group was used experimentally.

Table 19

Computed^a and experimental Diels-Alder cycloaddition selectivities

entry	dienophile	Calculated er	Experimental er
1		92.4:7.6	98.5:1.5 ^b
2		84:16	84.5:15.5 ^c
3		96.8:3.2	97.5:2.5 ^d
4		94.7:5.3	96.5:3.5 ^e
5		68.6:31.4	95.5:4.5 ^f

^a diene = 1,3-butadiene.^b experimental diene = 2-methyl-1,3-butadiene.^c experimental diene = cyclopentadiene.^d experimental dienophile = 2,2,2-trifluoroethyl acrylate.^e experimental dienophile = *E*-diethyl maleate.^f experimental diene = 2-triisopropylsilyloxy-1,3-butadiene, dienophile = 2-*tert*-butyl-1,4-benzoquinone.

Table 20

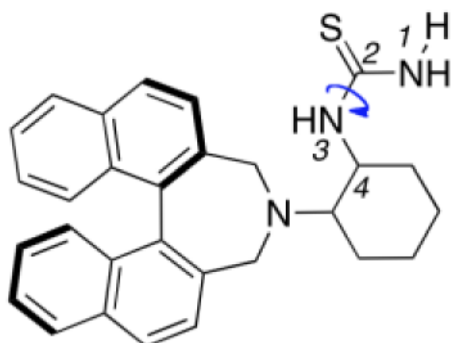
B3LYP/6-311++G(d, p)//B3LYP/6-31G(d) transition state energies with respect to initial catalyst-substrate complexes^a

TS-CC
C-C bond formation TS
(stereochemistry-determining)

TS-PT
proton transfer TS
(rate-determining)

TS	Catalyst	product configuration	E_{act} (kcal/mol)
TS-CC	A	<i>S</i>	10.4
TS-CC	A	<i>R</i>	12.0
TS-CC	B	<i>S</i>	14.7
TS-CC	B	<i>R</i>	13.4
TS-PT	A	<i>S</i>	17.6
TS-PT	A	<i>R</i>	20.3
TS-PT	B	<i>S</i>	26.0
TS-PT	B	<i>R</i>	16.3

^aBold numbers represent favored enantiomer of each step.

Table 21Dihedral angle (N1-C2-N3-C4) change in **TS-CC** with respect to ground state

Catalyst	Product configuration	$\Delta(\text{N1-C2-N3-C4})$
A	<i>S</i>	7
A	<i>R</i>	15
B	<i>S</i>	21
B	<i>R</i>	14

Table 22

Epoxidation of *trans*-chalcone

catalyst	% yield (exper.)	% ee (exper.)	<i>E-trans</i> – <i>E-cis</i> (calc., kcal/mol)
	93	89	0.9
	33	85	2.0
	48	75	0.3
	21	52	0.6